

**CRITICAL CONCENTRATION MODELS FOR THE MECHANICAL
AND ACOUSTIC PROPERTIES OF POROUS MATERIALS**

A DISSERTATION
SUBMITTED TO THE DEPARTMENT OF GEOPHYSICS
AND THE COMMITTEE ON GRADUATE STUDIES
OF STANFORD UNIVERSITY
IN PARTIAL FULFILLMENT OF THE REQUIREMENTS
FOR THE DEGREE OF
DOCTOR OF PHILOSOPHY

By
Qiang Chen
March 1992

©Copyright by Qiang Chen 1992
All Rights Reserved

I certify that I have read this dissertation and that in my opinion it is fully adequate, in scope and quality, as a dissertation for the degree of Doctor of Philosophy.

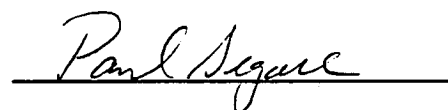


(Principal Advisor)

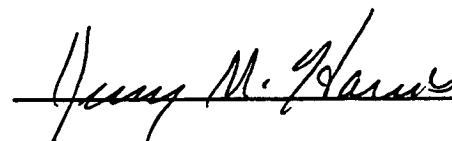
I certify that I have read this dissertation and that in my opinion it is fully adequate, in scope and quality, as a dissertation for the degree of Doctor of Philosophy.



I certify that I have read this dissertation and that in my opinion it is fully adequate, in scope and quality, as a dissertation for the degree of Doctor of Philosophy.



I certify that I have read this dissertation and that in my opinion it is fully adequate, in scope and quality, as a dissertation for the degree of Doctor of Philosophy.



Approved for the University Committee
on Graduate Studies:

Abstract

The knowledge of microstructures and effective properties of porous materials is indispensable to exploration geophysics, tectonophysics, and geological engineering. This dissertation proposes critical concentration models and presents theoretical results for the mechanical and acoustic properties of porous materials. These models and results are significant extensions of the nondilute concentration models and solutions for porous materials with critical porosities or concentrations, are in good agreement with most existing experimental data, and provide physical explanations to several empirical relations.

Porous rocks and sediments have complicated microstructures that result from various pore formation processes. These microstructures make the effective properties such as elastic moduli and wave velocities so distinctive that conventional models like dilute and nondilute concentration models originally developed for composite materials fail in describing them quantitatively. Critical porosity, or critical concentration of porous materials, is an important material constant to quantify those microstructures, and is closely related to the pore geometry and connectivity.

By introducing critical porosity and defining the critical concentration phase, we propose the critical concentration model whose microstructural interpretations are of nonuniform features as indicated by thin section observations and SEM images of porous materials. The critical porosities of porous materials determined by geometrical, theoretical, and experimental approaches are consistent, and are of wide ranges due to the diverse pore size, geometry, and connectivity.

Then a substitution method is proposed to develop critical concentration solutions to the effective moduli and wave velocities of clay-free and clay-bearing porous rocks and sediments. These solutions are extensions of the nondilute concentration solutions to porous materials with critical porosity or concentration, and they can quantitatively describe most available experimental data and provide interpretations to several empirical relations between wave velocity, porosity, and clay content.

The asymmetric self-consistent method (ASCM) is utilized to estimate the critical porosity and evaluate the effective moduli and wave velocities of porous materials.

With the existing ASCM solutions for spherical and cylindrical inclusions, the ASCM solutions for penny-shaped inclusions are found to describe the systematic changes of critical porosities, effective moduli, and wave velocities with pore geometry. By comparing ASCM solutions with the critical concentration solutions, we conclude that the ASCM solutions are accurate almost up to the critical porosity, and that they are exact after the critical porosity.

For sand-clay sediments ranging from clean sands, shaly sands, sandy shales, to pure shales, a special critical concentration model is proposed to evaluate the porosity-clay relation, porosity-permeability relation, effective moduli, and wave velocities. In particular, the intergranular clay and void effects are taken into account. The model results are in good agreement with available experimental data.

The critical concentration model is applied to the effective stress laws of porous rocks and sediments. For isotropic porous materials, it is the critical concentration phase that represents the pore pressure effect, and so the volume fraction of the critical concentration phase is the so called effective stress coefficient. Such results are applicable to elastic and inelastic deformation and failure processes, and they reduce to five different expressions of the effective stress coefficient used mostly in existing effective stress laws. For structurally anisotropic porous materials, the effective stress coefficient is a symmetric second-rank tensor, which indicates that pore pressure affects both the normal and shear stress components. Such anisotropic pore pressure effects are important to the understanding of faulting and earthquake instabilities induced by fluid extraction from subsurface.

Finally the critical concentration model is applied to the strength theory of porous materials. The actual stresses acting on the material skeleton depend on both the contact area between grains and the stress concentration induced by the pores and cracks. The critical concentration strength criteria based on such actual stresses are proposed for uniaxial tensile and compressive, and shear fractures. The results predict systematic decreases of material strengths with pore volume fraction, geometry, and connectivity. Then the strength criterion of transversely-isotropic rocks is studied and applied to the explanation of tectonic block rotations.

Acknowledgements

I wish to express my sincere thanks to Amos Nur, my advisor at Stanford University. The dissertation that follows was greatly inspired by Amos Nur whose physical insights into rock properties, earthquake phenomena, and tectonic processes, make the Stanford Rockphysics & Borehole Geophysics Project very unique and attractive. I am deeply indebted to him for his stimulating advice and communicative enthusiasm, and I am grateful to him for his continuous support throughout my stay at Stanford.

I would like to thank all the Stanford faculty and staff members who have been involved with my work these last five years. Special thanks are due to Gary Mavko for his interesting discussion and continuous encouragement, to David Pollard for introducing me into boundary element research on rock deformation and fracture, and to other dissertation committee members Huajian Gao, Jerry Harris, Mark Zoback, and Paul Segall for their useful discussions and reviews of my dissertation. I wish to express gratitude to Margaret Muir for her kindness, patience, and support during my stay at Stanford.

It has been a unique and enjoyable experience to be part of the Stanford Rockphysics & Borehole Geophysics Project for the last five years because of the stimulating research environment in the Geophysics Department, and in particular the Rock Physics Laboratory. I wish to thank all former and present students of SRB for their help and support. Special thanks go to Hezhu Yin for his resourcefulness at interpreting experimental data.

Finally, I want to thank my wife Dr. Xiaolei Li for her love, confidence, and support throughout these years. Her moral support across the Atlantic Ocean in early years, her courage to leave France for new challenges in the United States, and her love and care for our son Victor, make my stay at Stanford an enjoyable and unforgettable experience.

Contents

1. Introduction	1
1.1 Background	1
1.2 Objective	4
1.3 Plan	5
2. Dilute and nondilute concentration models and solutions	11
2.1 Dilute solutions to effective elastic moduli	12
2.2 Nondilute solutions to effective elastic moduli	15
2.3 Comparison with Gassmann's solution	27
2.4 Specific solutions for dry porous materials	28
2.5 Wave velocity-porosity relations	33
2.6 Conclusions	34
3. Critical concentration models of porous materials	45
3.1 Observation of porosity data	46
3.2 Concept of critical porosity	51
3.3 Critical concentration phase	55
3.4 Microstructural interpretation	56
3.5 Determination of critical porosity	60
3.6 Conclusions	68
4. Substitution method and critical concentration solutions	74
4.1 Substitution method	75
4.2 Critical concentration solutions	76
4.3 Comparison between models and data	88
4.4 Clay effects on effective properties	91
4.5 Conclusions	98
5. Asymmetric self-consistent method and solutions for porous materials	105
5.1 Symmetric and asymmetric self-consistent methods	106
5.2 Existing asymmetric self-consistent solutions	108

5.3	Solution for penny-shaped inclusion model	111
5.4	Velocity-porosity relations and comparison	113
5.5	Clay effects on effective elastic moduli and wave velocities	121
5.6	Conclusions	133
6.	Critical concentration model and solutions	
	for sand-clay sediments	136
6.1	Critical clay concentration	137
6.2	Porosity-clay content relations	137
6.3	Permeability in sand-clay sediments	146
6.4	Evaluation of effective elastic moduli and wave velocities	151
6.5	Conclusions	157
7.	Effective stress laws for fluid-saturated porous materials	163
7.1	Introduction	164
7.2	Critical porosity effects	166
7.3	Microstructural anisotropy effects	170
7.4	Applications	178
7.5	Conclusions	186
8.	Critical concentration strength theory of porous materials	191
8.1	Introduction	192
8.2	Critical porosity and actual stress	192
8.3	Uniaxial strength criteria	195
8.4	Shear strength criteria	199
8.5	Pore pressure effect on strength	203
8.6	Transverse-isotropy effect on strength	205
8.7	Application to tectonic block rotations	209
8.8	Conclusions	216
9.	Discussions and conclusions	222
9.1	Main contributions	222
9.2	Discussions	223
9.3	Further studies	224

List of Tables

Table 2.1: A summary of dilute concentration models and solutions	12
Table 2.2: A summary of nondilute concentration models and solutions	17
Table 4.1: Substitution method to derive critical concentration solutions	75
Table 7.1: A summary of the effective stress coefficient α	165

List of Figures

Figure 2.1: Dilute concentration solution to the effective elastic moduli vs. porosity of dry porous materials	16
Figure 2.2: Comparison between the Mori-Tanaka's solution and dilute concentration solution for cylindrical pore model of water-saturated porous materials	21
Figure 2.3: Comparison between the Mori-Tanaka's solution and dilute concentration solution for penny-shaped pore model of water-saturated porous materials	22
Figure 2.4: Comparison between the HS bounds and Mori-Tanaka's solution for water-saturated porous materials	26
Figure 2.5: Comparison of effective elastic modulus-porosity relations for dry and water-saturated porous materials	29
Figure 2.6: Micromechanical models for the finite-matrix solution, the Mackenzie's solution, and the HS bounds	31
Figure 2.7: Mori-Tanaka's solution to wave velocity vs. porosity and pore aspect ratio for water-saturated porous materials	35

Figure 3.1: Experimental data of strength vs. porosity of mudstones47

Figure 3.2: Experimental data of permeability vs. porosity
of Fontainebleau sandstones 48

Figure 3.3: Comparison between various models and experimental data of
effective Young’s modulus vs. porosity of porous materials 49

Figure 3.4: Experimental data of P wave velocity vs. porosity
of porous geomaterials50

Figure 3.5: Comparison between model results and experimental data of
permeability vs. porosity of porous materials52

Figure 3.6: Schematic section of a solid-fluid material system, representing
a system of porous rocks, sediments, and marine suspensions 54

Figure 3.7: Microstructural interpretation of critical concentration model 58

Figure 3.8: SEM image and microsection of sandstone microstructures59

Figure 3.9: Porosity vs. sound velocity in marine sediments 61

Figure 3.10: Critical porosity range predicted by the regular packing of
monosize inclusions62

Figure 3.11: Critical porosity range predicted by the random packing of
monosize inclusions63

Figure 3.12: Critical porosity range predicted by the self-consistent
solution for water-saturated porous materials 65

Figure 3.13: Experimental data of effective elastic moduli vs. porosity
of dry porous materials66

Figure 3.14: Experimental data of wave velocity vs. porosity
of dry porous materials 67

- Figure 4.1:** P wave velocity-porosity relation predicted by the critical concentration solution extended from Wyllie's relation 78
- Figure 4.2:** Effective elastic modulus-porosity relation predicted by the critical concentration solution extended from Voigt's relation 80
- Figure 4.3:** Wave velocity-porosity relation predicted by the critical concentration solution extended from Voigt's relation 81
- Figure 4.4:** Effective elastic modulus-porosity relation predicted by the critical concentration solution extended from HS relation 83
- Figure 4.5:** Wave velocity-porosity relation predicted by the critical concentration solution extended from HS relation 84
- Figure 4.6:** Comparison between existing models and acoustic velocity vs. porosity of sediments sampled by DSDP 89
- Figure 4.7:** Comparison between existing models and critical concentration model for P wave velocity-porosity relation 90
- Figure 4.8:** Comparison between Raymer's solution and critical concentration solution to P wave velocity-porosity relation 92
- Figure 4.9:** Comparison of several model results with experimental data of wave velocity-porosity relation 93
- Figure 4.10:** Experimental data and empirical relation between P wave velocity, porosity, and clay content of shaly sandstones 94
- Figure 4.11:** Effective elastic modulus-porosity-clay relation predicted by critical concentration solution extended from HS relation 99
- Figure 4.12:** Wave velocity-porosity-clay relation predicted by the critical concentration solution extended from HS relation 100
- Figure 4.13:** Comparison between critical concentration solution and experimental data of P wave velocity-porosity-clay relation 101

Figure 5.1: Asymmetric self-consistent solution to the effective elastic modulus-porosity relations with spherical and cylindrical fluid inclusions	110
Figure 5.2: Asymmetric self-consistent solution to the effective elastic modulus-porosity relations with penny-shaped fluid inclusions ...	114
Figure 5.3: Asymmetric self-consistent solution to the effective elastic modulus-porosity relations with spheroidal fluid inclusions	115
Figure 5.4: Asymmetric self-consistent solution to the wave velocity-porosity relations with spheroidal fluid inclusions	117
Figure 5.5: Comparison of ASCM solution to velocities with Han's experimental data at 5 MPa confining pressure	119
Figure 5.6: Comparison of ASCM solution to velocities with Han's experimental data at 40 MPa confining pressure	120
Figure 5.7: Comparison of ASCM solution with critical concentration solution for spherical fluid inclusions	122
Figure 5.8: Comparison of ASCM solution with critical concentration solution for penny-shaped fluid inclusions	123
Figure 5.9: ASCM solution to the effective elastic modulus-porosity relation with cemented clay phase	128
Figure 5.10: ASCM solution to the effective elastic modulus-porosity relation with uncemented clay phase	130
Figure 5.11: ASCM solution to the effective elastic modulus-porosity relation with varying clay cementation phase	131
Figure 5.12: Comparison between velocity data and ASCM solution with varying clay cementation phase	132

Figure 6.1: Schematic diagram of intergranular clay and void effects in sand-clay sediments	140
Figure 6.2: Porosity-clay content relations with varying intergranular clay and void effects in sand-clay sediments	143
Figure 6.3: Comparison between model results and experimental data of porosity-clay content relations at 0 and 10 MPa pressures	144
Figure 6.4: Comparison between model results and experimental data of porosity-clay content relations at 30 and 50 MPa pressures	145
Figure 6.5: Critical clay concentration vs. confining pressure	147
Figure 6.6: Experimental data of permeability vs. clay content	149
Figure 6.7: Model results of permeability vs. clay content and confining pressure	151
Figure 6.8: Model results of permeability vs. porosity and confining pressure	152
Figure 6.9: Schematization of permeability-porosity relationship in sedimentary rocks	152
Figure 6.10: Effective bulk modulus and P wave velocity vs. clay content for fluid-saturated sand-clay sediments at zero confining pressure	154
Figure 6.11: Effective elastic moduli vs. clay content for fluid-saturated sand-clay sediments at finite confining pressure	158
Figure 6.12: Model results and experimental data of wave velocity vs. clay content for sand-clay sediments at finite confining pressure	159

Figure 7.1: Anisotropic rock model and pore pressure effects 179

Figure 7.2: Mohr circle diagram for pore pressure effects in an orthotropic
rock. (x,y,z) consistent with $(1,2,3)$, respectively 183

Figure 7.3: Mohr circle diagram for pore pressure effects in an orthotropic
rock. (x,y,z) consistent with $(3,2,1)$, respectively 184

Figure 7.4: Mohr circle diagram for pore pressure effects in an orthotropic
rock. (x,y,z) consistent with $(2,1,3)$, respectively 185

Figure 8.1: Model results and experimental data of tensile strength vs. porosity of porous materials 197

Figure 8.2: Experimental data of normalized tensile strength vs. porosity of various porous materials 198

Figure 8.3: Experimental data of compressive strength vs. porosity of carbonates 200

Figure 8.4: Experimental data of shear strength vs. porosity of Nugget sandstones 204

Figure 8.5: Experimental data of shear strength vs. porosity of sandstones with about 35% critical porosity 205

Figure 8.6: Model results of shear strength vs. porosity of sandstones with about 35% critical porosity 206

Figure 8.7: Reference frame of transversely-isotropic porous materials under boundary loading 208

Figure 8.8: A model of tectonic block rotation with sequential fault sets 210

Figure 8.9: Comparison of theoretical and experimental deviatoric stress vs. the inclination of weakness plane 212

Figure 8.10: Generalized critical angle vs. anisotropic strength ratio 215

Figure 8.11: Generalized critical angle vs. principal stress at failure 216

Chapter 1

Introduction

1.1 Background

Porous materials include a variety of pore-containing geomaterials, metallic materials, polymer materials, and ceramic materials, which are encountered everywhere in daily life, in technology, and in nature. Early efforts to understand porous material properties date back to Lucretius, 1st century B.C. (see Kendall (1984)). There are voluminous literatures treating porous material microstructures, mechanical and acoustic properties, and their relationships. Most of these studies are based on a fundamental hypothesis that porous material microstructures and effective properties change smoothly when its porosity increases from zero to 100%. This hypothesis stems from the studies of two-phase or multiphase heterogeneous materials.

There are two catalogs of material models and theories for two-phase or multiphase heterogeneous materials. The first catalog is the mixture model of continua and mixture theory (or theory of interacting continua). The mixture model assumes that each constituent preserves its own identity but is so diffused through the mixture that each point of the continuum is co-occupied by two or more different constituents. Thus, the mixture theory treats each constituent equally and yields the smooth and continuous variation of effective properties for the whole range of any constituent volume fraction (Truesdell, 1962; Green and Naghdi, 1965; Morland, 1971; Atkin and Craine, 1976a, 1976b). With one constituent as void or fluid, some modified mixture

theories take porosity as an internal state variable, and turn out to be equivalent to Biot's theory in porous materials (Biot, 1941, 1956a 1956b; Bowen, 1982; Katsube, 1985, Katsube and Carroll, 1987a, 1987b).

The other catalog of studies takes elastic inclusion models to simulate two-phase or multiphase heterogeneous materials. Extensive reviews of elastic inclusion models have been given by Hashin (1970, 1983), Watt et al. (1976), Mura (1982, 1988), and Hudson and Knopoff (1989). The microstructures of elastic inclusion models are usually described as matrix phase and inclusion phases. For any inclusion concentration or relative volume fraction, the matrix phase exists as a framework connected in space, and the inclusion phase is embedded as isolated inclusions. At low level of inclusion volume fraction, the inclusion phase is in the so-called dilute concentration state; at high level of inclusion volume fraction, the matrix phase occurs as honeycomb-like or foam-like framework with nonzero stiffness. Consequently, when the inclusion phase is void or fluid, the effective properties such as elastic moduli and strengths exhibit smooth and continuous variation from zero to 100% inclusion volume fraction, or porosity.

When the constituent properties of two-phase or multiphase materials are in the same order, as often in the case of engineering composite materials, the constituent volume fraction becomes the sole dominant parameter to influence the effective properties. As indicated by the Hashin-Shtrikman bounds (Hashin and Shtrikman, 1961, 1962, 1963), the upper and lower bounds of effective elastic moduli for engineering composite materials are very narrow and change smoothly when one constituent concentration increases from zero to 100%. Since the upper and lower HS bounds represent very different constituent geometry and connectivity, the narrowness of HS bounds makes it acceptable in most cases of engineering composite materials to neglect the effects of constituent geometry and connectivity. Because much of our knowledge of porous material properties is rendered from the effective properties of

two-phase or multi-phase materials by decreasing the material constants of one constituent to zero for dry porous materials and to fluid properties for fluid-saturated porous materials, it has been customary to take porosity as the primary measure of porous material microstructures, and it has been generally accepted that the porous material properties such as effective moduli, strengths, and wave velocities change smoothly from zero to 100% porosity (Wyllie et al., 1956; Watt et al., 1976; Bourbié et al., 1987; Nobes, 1989).

Most crustal rocks and sediments belong to dry or fluid-saturated porous materials. When the effective properties of such geomaterials in low-porosity domains are concerned, it is verified by a large number of in-situ and laboratory experiments that the direct applications of conventional models and solutions for composite materials to such geomaterials are appropriate. However, in the intermediate and high porosity domains, systematic discrepancies between the data of geomaterial properties and predicted results from the conventional models have been recognized by many researchers, as reported recently by Han (1986), Hudson and Knopoff, (1989), Jizba and Mavko (1990), and Marion (1990). For instance, the Hashin-Shtrikman upper and lower bounds of effective elastic moduli for water-saturated porous materials are far apart, implying that the influence of other pore structure parameters on effective moduli is in the same order as porosity effect. To remedy such discrepancies, several empirical relations have been proposed (Raymer et al., 1980; Han et al., 1986; Marion and Nur, 1991).

Those discrepancies are mainly due to the oversimplified models of porous material microstructures which vary with lithology, pressure, etc.. Porous rocks and sediments have complicated microstructures that result from depositional, diagenetic, and tectonic processes. There is more and more evidence that at some finite values of porosity, the effective properties of porous materials, such as strengths, effective elastic moduli, and wave velocities, change distinctively from previous levels, decreasing sharply

or even reducing to zero. These values of porosity are defined as critical porosities. Critical porosity means a distinctive change of porous material microstructure, and is closely related to the pore size, geometry, and connectivity.

1.2 Objective

The phenomena of critical porosity and associated mechanical and acoustic properties of porous rocks and sediments are not consistent with the fundamental hypothesis stated above. We believe that the relaxation of the fundamental hypothesis and incorporation of more parameters than porosity to describe porous material microstructures can lead to new material model and theory to describe quantitatively the relationships between microstructures and effective properties of various porous materials, especially those of porous rocks and sediments.

During the last two decades, quite a few controversies have been raised on the predicted porous material properties in intermediate and high porosity or crack density domains, especially those vanishing elastic moduli at finite porosities or crack densities derived from the self-consistent method (Hill, 1965; Budiansky, 1965; Walpole, 1969; Hashin, 1970, 1983; O'Connell and Budiansky, 1974, 1976, 1977; Bruner, 1976; Christensen, 1979, 1990; Berryman, 1980; Henyey and Pomphrey, 1982; Hudson and Knopoff, 1989). Essentially, the criticisms upon the effective medium theory or self-consistent method rest on the above fundamental hypothesis or similar arguments, and the advocates base their arguments on physical intuition and very limited data relevant to those of critical porosity in porous rocks and sediments. A better understanding of such phenomena and resolving of these controversies are important in both theory and practice, and this becomes one of motivations to conduct this thesis study.

The knowledge of microstructures and effective properties of porous rocks and sediments is indispensable to exploration geophysics, tectonophysics, earthquake en-

gineering, and environmental protection. The interpretation and modeling of acoustic well logging, seismic reflection, and cross-well tomography in exploration and production require the wave velocity-porosity relations that include the effects of lithology, saturation, confining pressure, and anisotropy. The faulting and earthquake instabilities in the crust are intrinsically related to the mechanical behaviors of rocks that suffer from pore/crack nucleation, growth, and coalescence. The earthquake intensity zonation and hazard assessment are associated with the mechanical behaviors of poorly consolidated rocks and sediments. The environmental pollutions by nuclear waste disposals and subsurface fluid injection and extraction can be minimized only with fully understanding of the transport and mechanical properties on site and in the surrounding areas. These multidisciplinary demands, along with above theoretical considerations, encourage us to develop the material models, methods, and solutions to incorporate the critical porosity, to provide better descriptions of rock and sediment microstructures, and to evaluate the mechanical and acoustic properties such as effective elastic moduli, strengths, and wave velocities. This thesis study is an important step in this needed direction.

1.3 Plan

This dissertation is organized as follows.

Chapter 2 summarizes and complements the conventional dilute and nondilute concentration models and solutions of porous materials in such a way that the effects of microstructural geometry on effective elastic modulus-porosity relations are systematically examined.

Chapter 3 proposes the critical concentration model of porous materials. The concepts of critical porosity and concentration are introduced, and the critical concentration phase is defined. Then the microstructure interpretation of the critical concentration model is provided and compared with thin section observations and

SEM image of porous rocks. The critical porosities of porous materials are determined by geometrical and theoretical approaches, and compared with many experimental results in literatures.

In Chapter 4, a substitution method is proposed to develop critical concentration solutions to the effective elastic moduli and wave velocities of clay-free and clay-bearing porous rocks and sediments described by the critical concentration model. The theoretical results can quantitatively describe many experimental data and give an insight into several empirical relations between wave velocity, porosity, and clay content.

The asymmetric self-consistent method (ASCM) is utilized in Chapter 5 to estimate the critical porosity of porous materials and evaluate the effective elastic moduli and wave velocities. The ASCM solutions for penny-shaped pore/crack models are found, and they, along with the solutions for spherical and cylindrical pore models, describe the systematic changes of critical porosities with pore geometry. The resulting effective elastic moduli and wave velocities are compared with critical concentration solutions, and they are within the ranges predicted by the substitution method.

In Chapter 6, for sand-clay sediments ranging from clean sands, shaly sands, sandy shales, to pure shales, a specific critical concentration model is proposed to evaluate the porosity-clay relation, porosity-permeability relation, effective elastic moduli, and wave velocities. In particular, the intergranular clay and void effects are taken into account.

The critical concentration model is extended to the study of effective stress laws of porous rocks and sediments in Chapter 7. For isotropic porous materials, it is the critical concentration phase that applies the pore pressure on the material skeleton, and so the effective stress coefficient is exactly the volume fraction of the critical concentration phase. For structurally anisotropic porous materials, the effective stress coefficient is a symmetric second-rank tensor, which indicates that pore pressure

affects both the normal and shear stress components. Such anisotropic pore pressure effects are important to the understanding of faulting and earthquake instabilities induced by fluid extraction from subsurface.

In Chapter 8, the critical concentration model is extended to the study of strength criteria of porous materials. The actual stresses acting on the material skeleton depend on both the contact area between grains and the stress concentration induced by the pores and cracks. The uniaxial strength criteria and shear strength criteria based on such actual stresses are proposed, and the anisotropy effect on the strength is studied and applied to the explanation of tectonic block rotations.

Finally, Chapter 9 summarizes the main results of this thesis study, discusses the further applications of proposed models and solutions, and suggests several related topics for further studies.

References

- Atkin, R. J. and R. E. Craine, 1976a, Continuum theories of mixtures: basic theory and historical development, *Quart. J. Mech. Appl. Math.*, **29**, 209-244.
- Atkin, R. J. and R. E. Craine, 1976b, Continuum theories of mixtures: applications, *J. Inst. Math. Appl.*, **17**, 153-207.
- Berryman J. G., 1980, Long-wavelength propagation in composite elastic media I. spherical inclusions, *J. Acoust. Soc. Am.*, **68**, 1809-1819.
- Biot, M. A., 1941, General theory of three-dimensional consolidation, *J. Appl. Phys.*, **12**, 155-164.
- Biot, M. A., 1956a, Theory of propagation of elastic waves in a fluid-saturated porous solid, I. low frequency range, *J. Acoust. Soc. Am.*, **28**, 168-178.
- Biot, M. A., 1956b, Theory of propagation of elastic waves in a fluid-saturated porous solid, II. high frequency range, *J. Acoust. Soc. Am.*, **28**, 179-191.
- Bourbié, T., Coussy, O., and B. Zinszner, 1987, *Acoustics of porous media*, Gulf Publishing Company, Houston, London, Paris, Tokyo, pp.334.
- Bowen, R. M., 1982, Compressible porous models by use of the theory for mixtures, *Int. J. Engng. Sci.*, **20**, 697-735.
- Bruner, W. M., 1976, Comment on "Seismic velocities in dry and saturated cracked solids" by R. J. O'Connell and B. Budiansky, *J. Geophys. Res.*, **81**, 2573-2576.
- Budiansky, B., 1965, On the elastic moduli of some heterogeneous materials: *J. Mech. Phys. Solids*, **13**, 223-227.
- Christensen, R. M., 1979, *Mechanics of Composite Materials*, Wiley, New York, pp.348.
- Christensen, R. M., 1990, A critical evaluation for a class of micromechanical models, *J. Mech. Phys. Solids*, **38**, 379-404.
- Green, A. E. and P. M. Naghdi, 1965, A dynamical theory of interacting continua, *Int. J. Engng. Sci.*, **3**, 231-241.
- Han, D. H., 1986, Effects of porosity and clay content on acoustic properties of sandstones and unconsolidated sediments, PhD dissertation, SRB, **28**, Stanford University.

- Han, D. H., Nur, A., and D. Morgan, 1986, Effects of porosity and clay content on wave velocities in sandstones, *Geophysics*, **51**, 2093-2107.
- Hashin, Z. and S. Shtrikman, 1961, Note on a variational approach to the theory of composite elastic materials, *J. Franklin Inst.*, **271**, 336-341.
- Hashin, Z. and S. Shtrikman, 1962, A variational approach to the theory of the elastic behavior of polycrystals, *J. Mech. Phys. Solids*, **10**, 343-352.
- Hashin, Z. and S. Shtrikman, 1963, A variational approach to the elastic behavior of multiphase materials, *J. Mech. Phys. Solids*, **11**, 127-140.
- Hashin, Z., 1970, Theory of composite materials, in *Mechanics of Composite Materials*, 5th Symposium on Naval Structural Mechanics, edited by Wendt, F. W., H. Liebowitz, and Perrone, N., 201-242. Pergamon, New York.
- Hashin, Z., 1983, Analysis of composite materials – a survey, *J. Appl. Mech.*, **50**, 481-505.
- Henye, F. S. and N. Pomphrey, 1982, Self-consistent elastic moduli of a cracked solid, *Geophys. Res. Lett.*, **9**, 903-906.
- Hill, R., 1965, A self-consistent mechanics of composite materials: *J. Mech. Phys. Solids*, **13**, 213-222.
- Hudson, J. A. and L. Knopoff, 1989, Predicting the overall properties of composite materials with small-scale inclusions or cracks, *PAGEOPH*, **131**, 551-576.
- Jizba, D. and G. Mavko, 1990, The high pressure seismic velocities of sandstones, *SRB*, **40**, Paper B.
- Katsube, N., 1985, The constitutive theory for fluid-saturated porous materials, *ASME J. Appl. Mech.*, **52**, 185-189.
- Katsube, N. and M. M. Carroll, 1987a, The modified mixture theory for fluid-filled porous materials: theory, *ASME J. Appl. Mech.*, **54**, 35-40.
- Katsube, N. and M. M. Carroll, 1987b, The modified mixture theory for fluid-filled porous materials: applications, *ASME J. Appl. Mech.*, **54**, 41-46.
- Kendall, K., 1984, Connection between structure and strength of porous solids, in *Physics and Chemistry of Porous Media*, edited by Johnson, D. L. and P. N. Sen, American Institute of Physics, AIP Conference Proceedings 107, 78-88.
- Marion, D., 1990, Acoustic, mechanical, and transport properties of sediments and

granular materials, PhD dissertation, SRB, **39**, Stanford University.

Marion, D. and A. Nur, 1991, Pore-filling material and its effect on velocity in rocks, *Geophysics*, **56**, 225-230.

Morland, L. W., 1971, A simple constitutive theory for a fluid-saturated porous solid, *J. Geophys. Res.*, **77**, 890-900.

Mura, T., 1982, *Micromechanics of defects in solids*, Martinus Nijhoff, The Hague, pp.494.

Mura, T., 1988, Inclusion problems, *Appl. Mech. Rev.* **41**, 15-20.

Nobes C. David, A test of a simple model of the acoustic velocity in marine sediments, *J. Acoust. Soc. Am.*, **86**, 290-294.

O'Connell, R. J. and B. Budiansky, 1974, Seismic velocities in dry and saturated cracked solids, *J. Geophys. Res.*, **79**, 5412-5426.

O'Connell, R. J. and B. Budiansky, 1976, Reply, *J. Geophys. Res.*, **81**, 2577-2578.

O'Connell, R. J. and B. Budiansky, 1977, Viscoelastic properties of fluid-saturated cracked solids, *J. Geophys. Res.*, **82**, 5719-5735.

Raymer, L. L., Junt, E. R., and J. S. Gardner, 1980, An improved sonic transit time-to-porosity transform, SPWLA, 21st Ann. Logg. Symp., Paper P.

Truesdell, C., 1962, Mechanical basis of diffusion, *J. Chem. Phys.*, **37**, 2336-2344.

Walpole, L. J., 1969, On the overall elastic moduli of composite materials, *J. Mech. Phys. Solids*, **17**, 235-251.

Watt, J. P., G. F. Davies, and R. J. O'Connell, 1976, The elastic properties of composite materials, *Review of Geophysics and Space Physics*, **14**, 541-563.

Wyllie, M. R. J., Gregory, A. R., and L. W. Gardner, 1956, Elastic wave velocities in heterogeneous and porous media, *Geophysics*, **21**, 41-70.

Chapter 2

Dilute and Nondilute Concentration Models and Solutions

Abstract

This chapter summarizes and complements the dilute and nondilute concentration models and solutions for the effective elastic moduli of porous materials. The microstructural geometry effects on the effective elastic moduli are consistent for both the dilute and nondilute solutions. Spherical pore model results in the highest effective elastic moduli, and flat pore or crack model leads to dramatical decrease in effective elastic moduli. The dilute solutions to effective elastic moduli are valid at low porosity, but become unacceptable at high porosity. The nondilute solutions, such as Mori-Tanaka's solution and bounding solutions, yield asymptotic values of the dilute solution at low porosity, but exhibit broad variations at high porosity due to different approximations of porous material microstructures. The Mori-Tanaka's solutions for a series of spheroidal pore models just fully fill the broad domain between the Hashin-Shtrikman upper and lower bounds, and share the saturation feature described by Gassmann's solution for pore models. Based on the dilute and nondilute solutions, a group of solutions with simple forms but sufficient accuracy are proposed for the effective elastic moduli of dry porous materials.

2.1 Dilute Solutions to Effective Elastic Moduli

2.1.1 Model and method

The dilute-concentration solutions to effective elastic moduli of composite materials are based on an assumption that the fractional volume of inclusions is much smaller than unity, which implies that distances between inclusions are so large relative to inclusion sizes that the interactions between inclusions may be neglected. Table 2.1 compares the microstructure models and derivations of typical dilute concentration solutions to the effective elastic moduli of porous materials.

Table 2.1 A summary of dilute concentration models and solutions

Reference	Microstructure model	Derivation and comments
Eshelby (1957)	Ellipsoidal inclusion	S-tensor transformation. For spherical inclusion the S-tensor becomes isotropic and the solution is of simple and explicit form. Applicable to porous materials.
Walsh (1969)	Penny-shaped inclusion	Modification from asymmetric self-consistent solution. Appropriate for inclusions with aspect ratio $\eta \ll 1$. Applicable to porous materials.
Mavko (1980)	Cylindrical pores with circular and triangular sections	Reciprocity theorem and explicit elastic deformation solution. Only for dry porous materials. Invoking Gassmann's relation to extend to fluid-saturated materials.
Chen et al. (1990)	Two-dimensional pores with arbitrary shapes such as tapered pore and star-shaped pore	Numerical modeling by boundary element method. Only for dry porous materials. Invoking Gassmann's relation to extend to fluid-saturated materials.

2.1.2 Spheroidal inclusion materials

The dilute-concentration solution to effective bulk and shear moduli for spherical inclusions was found by Eshelby (1957), which can be rewritten as

$$\frac{K_1}{K} = 1 + \frac{3K_1 + 4\mu_1}{3K_2 + 4\mu_1} \frac{K_1 - K_2}{K_1} \phi_2, \quad (2.1)$$

$$\frac{\mu_1}{\mu} = 1 + \frac{5(3K_1 + 4\mu_1)(\mu_1 - \mu_2)}{(9K_1 + 8\mu_1)\mu_1 + (6K_1 + 12\mu_1)\mu_2} \phi_2. \quad (2.2)$$

where K and μ represent effective bulk and shear moduli, K_1 and μ_1 represent bulk and shear moduli of matrix phase, K_2 and μ_2 represent bulk and shear moduli of inclusion phase, respectively, and ϕ_2 represents the inclusion volume fraction, or porosity for porous materials.

Walsh (1969) simplified the result obtained from the self-consistent method (Wu, 1966), and found the dilute-concentration solution for penny-shaped inclusions whose aspect ratios η are $\eta \ll 1$,

$$\frac{K_1}{K} = 1 + \frac{3K_1 + 4\mu_2}{3K_2 + 4\mu_2 + 3\pi\eta\mu_1(3K_1 + \mu_1)/(3K_1 + 4\mu_1)} \frac{K_1 - K_2}{K_1} \phi_2, \quad (2.3)$$

$$\begin{aligned} \frac{\mu_1}{\mu} = & 1 + \left[1 + \frac{8\mu_1}{4\mu_2 + 3\pi\eta\mu_1(3K_1 + 2\mu_1)/(3K_1 + 4\mu_1)} + \right. \\ & \left. + \frac{2(3K_2 + 2\mu_2 + 2\mu_1)}{3K_2 + 4\mu_2 + 3\pi\eta\mu_1(3K_1 + \mu_1)/(3K_1 + 4\mu_1)} \right] \frac{\mu_1 - \mu_2}{5\mu_1} \phi_2. \end{aligned} \quad (2.4)$$

By using Walsh's procedure, we find the dilute-concentration solution for cylindrical inclusion model (Chen and Nur, 1991),

$$\frac{K_1}{K} = 1 + \frac{3(K_1 + \mu_1) + \mu_2}{3(K_2 + \mu_1) + \mu_2} \frac{K_1 - K_2}{K_1} \phi_2, \quad (2.5)$$

$$\frac{\mu_1}{\mu} = 1 + \left[\frac{4(\mu_1 - \mu_2)}{5(\mu_1 + \mu_2)} + \frac{\mu_1 - \mu_2}{5\mu_1} F_c \right] \phi_2, \quad (2.6)$$

where

$$F_c = \frac{52\mu_1^3 + (48K_1 + 51K_2 + 44\mu_2)\mu_1^2 + (45K_1K_2 + 24K_1\mu_2 + 21\mu_2K_2)\mu_1 + 9K_1K_2\mu_2}{[(3K_1 + \mu_1)\mu_1 + (3K_1 + 7\mu_1)\mu_2][3(K_2 + \mu_1) + \mu_2]}. \quad (2.7)$$

2.1.3 Application to dry porous materials

There is no restriction on inclusion property in deriving above dilute-concentration solutions. By decreasing appropriately the properties of inclusion phase, those solutions are conventionally applied to dry porous materials ($K_2, \mu_2 = 0$) and inviscid fluid-saturated porous materials ($K_2 \neq 0, \mu_2 = 0$). Pores are supposed to orient randomly in three dimensions so that the effective properties are isotropic. If Poisson's ratio ν_1 is used instead of shear modulus μ_1 for the matrix phase, above dilute-concentration solutions reduce to simple expressions for dry porous materials:

For spherical pore model,

$$\frac{K_1}{K} = 1 + \frac{3(1 - \nu_1)}{2(1 - 2\nu_1)} \phi_2, \quad (2.8)$$

$$\frac{\mu_1}{\mu} = 1 + \frac{15(1 - \nu_1)}{7 - 5\nu_1} \phi_2. \quad (2.9)$$

For penny-shaped pore/crack model which is characterized by $\eta \ll 1$,

$$\frac{K_1}{K} = 1 + \frac{4(1 - \nu_1^2)}{3\pi\eta(1 - 2\nu_1)} \phi_2, \quad (2.10)$$

$$\frac{\mu_1}{\mu} = 1 + \frac{1}{5} \left[1 + \frac{8(1 - \nu_1)(5 - \nu_1)}{3\pi\eta(2 - \nu_1)} \right] \phi_2. \quad (2.11)$$

For cylindrical pore model, our solution is identical with Mavko' solution which was derived by a different method (Mavko, 1980),

$$\frac{K_1}{K} = 1 + \frac{5 - 4\nu_1}{3(1 - 2\nu_1)}\phi_2, \quad (2.12)$$

$$\frac{\mu_1}{\mu} = 1 + \frac{40 - 24\nu_1}{15}\phi_2. \quad (2.13)$$

Fig.2.1 shows dilute-concentration solutions to the effective elastic moduli versus porosity for dry porous materials. Spherical and cylindrical pore shapes are of similar effects on effective elastic moduli. Flat pore shapes with smaller aspect ratios lead to more decrease in both effective bulk and shear moduli. This tendency is consistent with fracture mechanics analysis of materials with cracks or flat pores. Given a value of porosity, the smaller the pore aspect ratio is, the larger the pore number in a unit of porous material, and the lower the effective elastic moduli. Thus, porosity is no longer the dominant parameter in such situations.

2.2 Nondilute Solutions to Effective Elastic Moduli

2.2.1 Model and method

Nondilute concentration solutions to effective elastic moduli can be determined by several methods such as statistical treatment, scattering theory, bounding method, and self-consistent method. These solutions are exact at the ending porosities (0% and 100%) and vary smoothly between them, but such variations differ considerably for individual models due to different approximations of the inclusion interaction. Table 2.2 classifies the nondilute concentration models and solutions into four catalogs and gives comments on their applicabilities to porous materials.

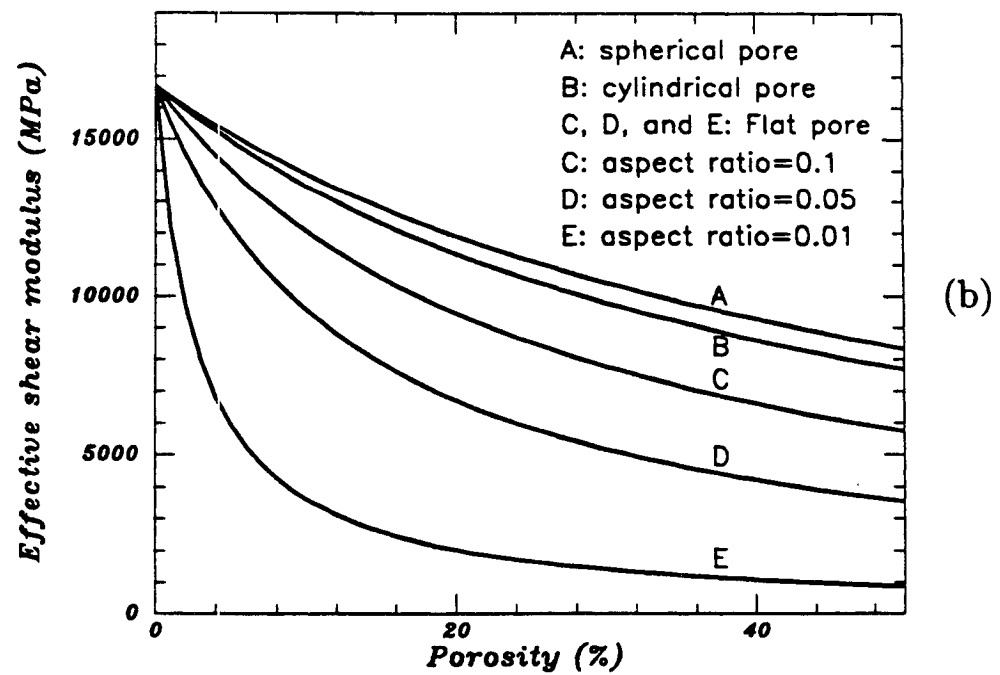
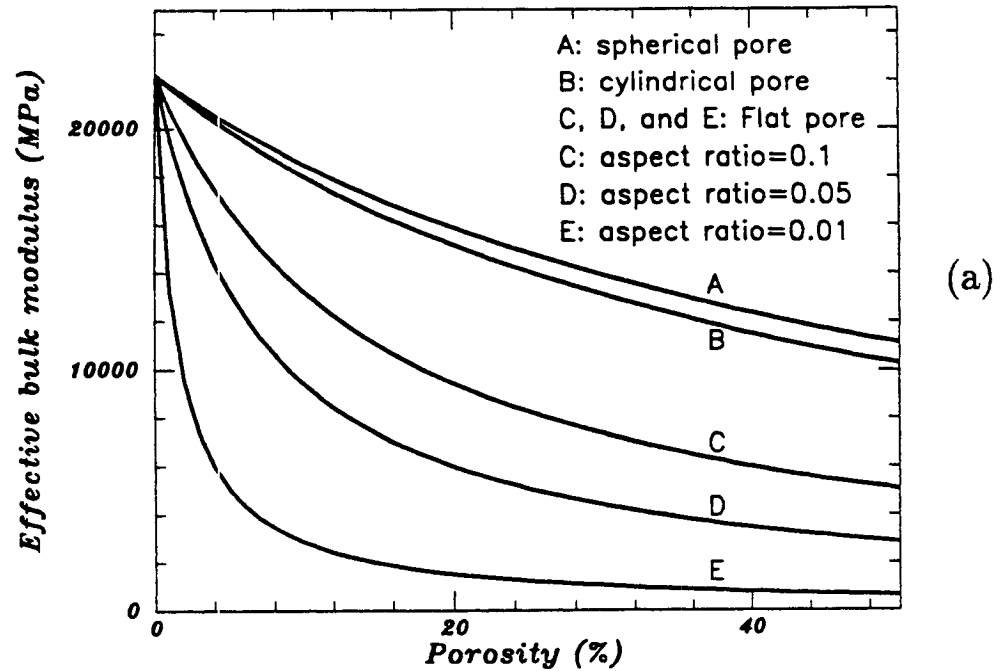


Fig.2.1 Dilute-concentration solutions to the effective elastic moduli versus porosity for dry porous materials. Flat pore shapes are of dramatic effects on both effective bulk and shear moduli. (a) effective bulk modulus-porosity relation, (b) effective shear modulus-porosity relation.

Table 2.2 A summary of nondilute concentration models and solutions

Classification	Reference	Applicability to porous materials
Mori-Tanaka method (Based on Eshelby's S-tensor)	Mori-Tanaka (1973) Weng (1984) Tandon & Weng (1986) Benveniste (1987)	Applicable to porous materials with porosity from zero to 100% and spheroidal pore shapes.
Differential effective medium theory (Add incrementally one phase to the new matrix phase)	Roscoe (1952) Boucher (1976) McLaughlin (1977) Cleary et al. (1980) Sheng & Callegari (1984)	The added phase, assumed as pores, is not connected in space. Applicable to porous materials with porosity from zero to 100% but little specification on pore shapes.
Self-consistent method (Symmetric: treating phases equally. Asymmetric: matrix and inclusion phases differ in shapes and occurrences)	Kroner (1958) Hill (1965) Wu (1966) Walpole (1969) Boucher (1974) Watt et al. (1976) Berryman (1980)	For dry or fluid-saturated porous materials, the solutions predict distinctive change of effective moduli at finite porosities which vary with spheroidal pore shapes (see details in chapter 5).
Bounding method (Upper and lower bounds on effective moduli given the constituents and microstructural properties)	Voigt (1928) Reuss (1929) Hashin & Shtrikman (1961, 1962, 1963) Miller (1969) Corson (1974) Watt et al. (1976) Hashin (1983)	Applicable to porous materials with porosity from zero to 100% but little specification on pore shapes. Narrow bounds for composite materials with same order of constituent properties, but far-apart bounds for fluid-saturated and dry porous materials.

When applied to the study of effective elastic moduli of porous materials, the differential effective medium theory (DEM) is less competitive than others since it does not give a definite description of porous material microstructure regarding the pore shape, connectivity, and orientation. Because the self-consistent method yields controversial predictions on the effective elastic moduli of porous materials, we will give a separate study of self-consistent model and solution in chapter 5. In the following, the Mori-Tanaka method and solution are introduced since they are often used for engineering composite materials but relatively new for porous geomaterials (Mori and Tanaka, 1973; Mura, 1988).

2.2.2 Mori-Tanaka's solution

The Mori-Tanaka's method can be outlined as follows. As the concentration of inclusions increases from dilute state to finite state, the perturbed stress field near the inclusion interfaces no longer dies out completely, giving rise to an average perturbed stress in the matrix which clearly differs from that applied externally. Eshelby's equivalence principle is then used to find the deviation of stress in the inclusions in terms of the average perturbed stress in the matrix. Such average perturbed stress in the matrix can be solved to account for the inclusion interaction. This original procedure has been used to advantage by many researchers, for example, Chow (1978), Taya and Chou (1981), Taya and Mura (1981), Weng (1984), Tandon and Weng (1986), and Benveniste (1987).

For spheroidal inclusions, the aspect ratio η is defined as the ratio of length to diameter of a spheroidal inclusion. The values of η correspond to the inclusion configurations as follows:

$\eta \rightarrow \infty$ — cylindrical;

$\eta \gg 1$ — needle-like;

$\eta > 1$ — prolate;

- $\eta = 1$ — spherical;
 $\eta < 1$ — oblate;
 $\eta \ll 1$ — penny-shaped.

The Mori-Tanaka's solution for spheroidal inclusion materials are expressed as

$$\frac{K_1}{K} = 1 + \frac{f_1}{f_2}\phi_2, \quad \frac{\mu_1}{\mu} = 1 + \frac{f_3}{f_4}\phi_2, \quad (2.14)$$

where

$$f_1 = \frac{a_1 - 2(a_2 - a_3 - a_4)}{3a}, \quad (2.15)$$

$$f_2 = 1 + \phi_2 \frac{2(S_{1122} + S_{2222} + S_{2233} - 1)(a_3 + a_4) + (S_{1111} + 2S_{2211} - 1)(a_1 - 2a_2)}{3a}, \quad (2.16)$$

$$f_3 = -\frac{2}{5} \frac{1}{2S_{1212} + \mu_1/(\mu_2 - \mu_1)} - \frac{1}{3} \frac{1}{2S_{2323} + \mu_1/(\mu_2 - \mu_1)} + \frac{1}{15a} [2(a_1 + a_2 - a_3) + a_4 + a_5a], \quad (2.17)$$

$$f_4 = 1 - \phi_2 \left\{ \frac{2}{5} \frac{2S_{1212} - 1}{2S_{1212} + \mu_1/(\mu_2 - \mu_1)} + \frac{1}{3} \frac{2S_{2323} - 1}{2S_{2323} + \mu_1/(\mu_2 - \mu_1)} - \frac{1}{15a} [(S_{1122} - S_{2233})(2a_3 - a_4 + a_5a) + 2(S_{1111} - S_{2211} - 1)(a_1 + a_2) + (S_{1122} - S_{2222} + 1)(2a_3 - a_4 - a_5a)] \right\}. \quad (2.18)$$

For dry spheroidal pore/crack materials, $K_2 = 0$, $\mu_2 = 0$, above solution reduces to

$$\frac{K_1}{K} = 1 + f_5 \frac{\phi_2}{1 - \phi_2}, \quad \frac{\mu_1}{\mu} = 1 + f_6 \frac{\phi_2}{1 - \phi_2}, \quad (2.19)$$

where

$$f_5 = \frac{1}{3} \frac{(S_{2222} + S_{2233} - 1) + 2(S_{1111} - S_{1122} - S_{2211} - 1)}{2S_{1122}S_{2211} - (S_{1111} - 1)(S_{2222} + S_{2233} - 1)}, \quad (2.20)$$

$$f_6 = -\frac{2}{5(2S_{1212} - 1)} - \frac{1}{3(2S_{2323} - 1)} + \frac{1}{15(S_{2233} - S_{2222} + 1)} + \frac{1}{15} \frac{2(S_{2222} + S_{2323} - 1 + S_{1122}S_{2211}) + (S_{1111} - 1)}{2S_{1122}S_{2211} - (S_{1111} - 1)(S_{2222} + S_{2233} - 1)}, \quad (2.21)$$

and the components of S_{ijkl} and a, a_1, \dots, a_5 , functions of the aspect ratio η , are given in Appendix.

Fig.2.2 and 2.3 compare the Mori-Tanaka's solutions with the dilute-concentration solutions as well as the Voigt's bounds for cylindrical and penny-shaped pore models of water-saturated porous materials, respectively. In computation, $K_2 = 2222MPa$, $\mu_2 = 0$, $(K_1/K_2) = 10$, and $\mu_1 = 16666MPa$ are used. At low porosity (10% or smaller), the Mori-Tanaka's solutions are equivalent to the dilute-concentration solutions. The dilute-concentration solutions at high porosity become unacceptable since they violate the Voigt's bounds (Voigt, 1928; Hill, 1952, 1963). These features hold for other spheroidal pore/crack models. Thus, it is the microstructural interaction that causes difference between these solutions for the same spheroidal model.

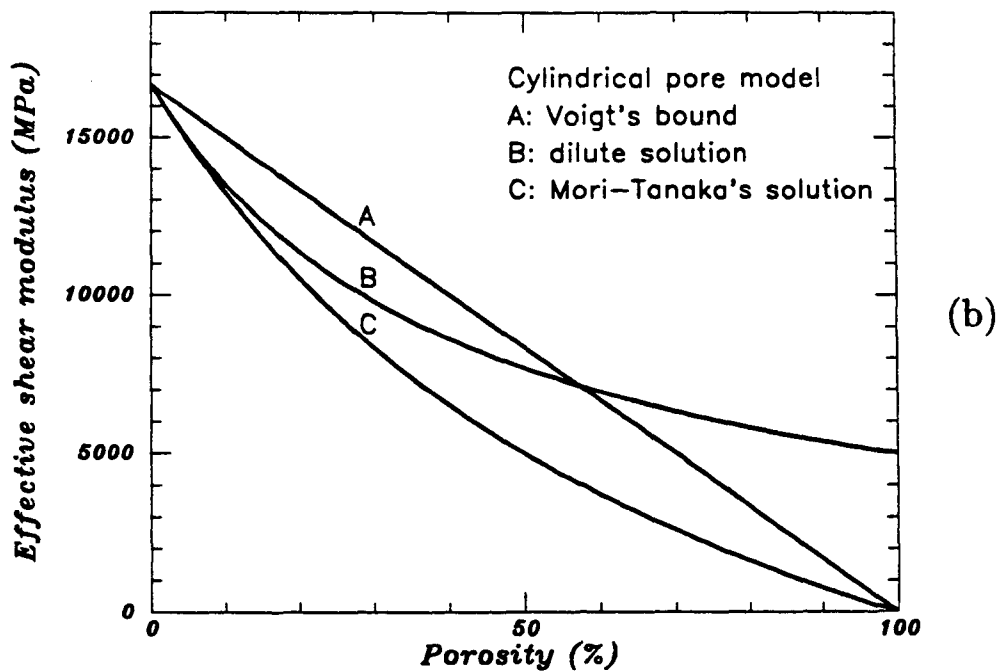
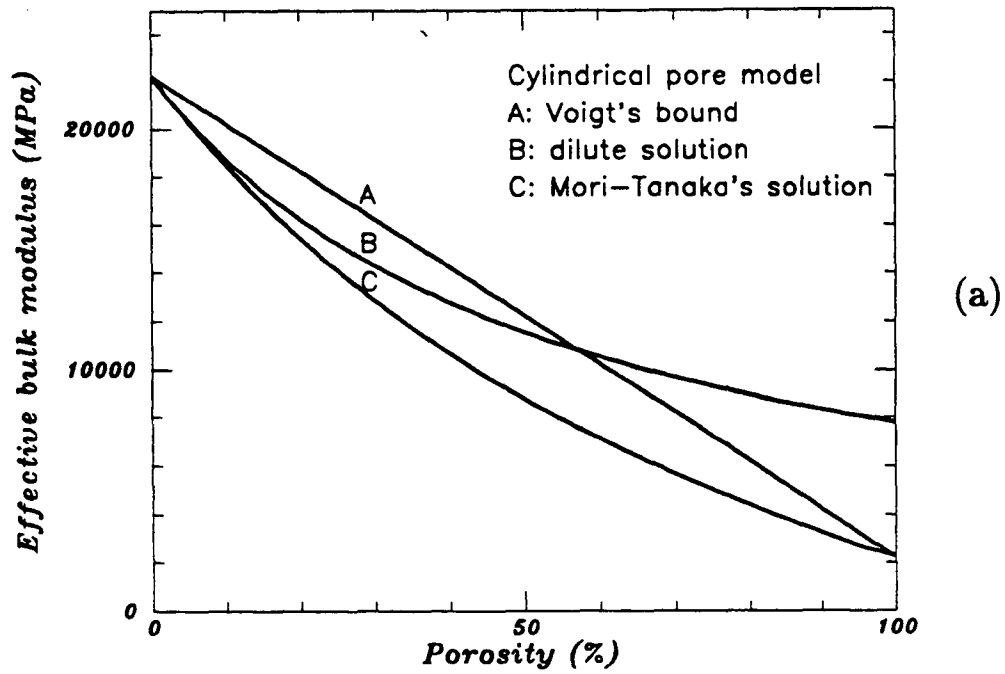


Fig.2.2 Comparison between the Mori-Tanaka's solution and dilute-concentration solution for cylindrical pore model of water-saturated porous materials. (a) effective bulk modulus-porosity relation, (b) effective shear modulus-porosity relation.

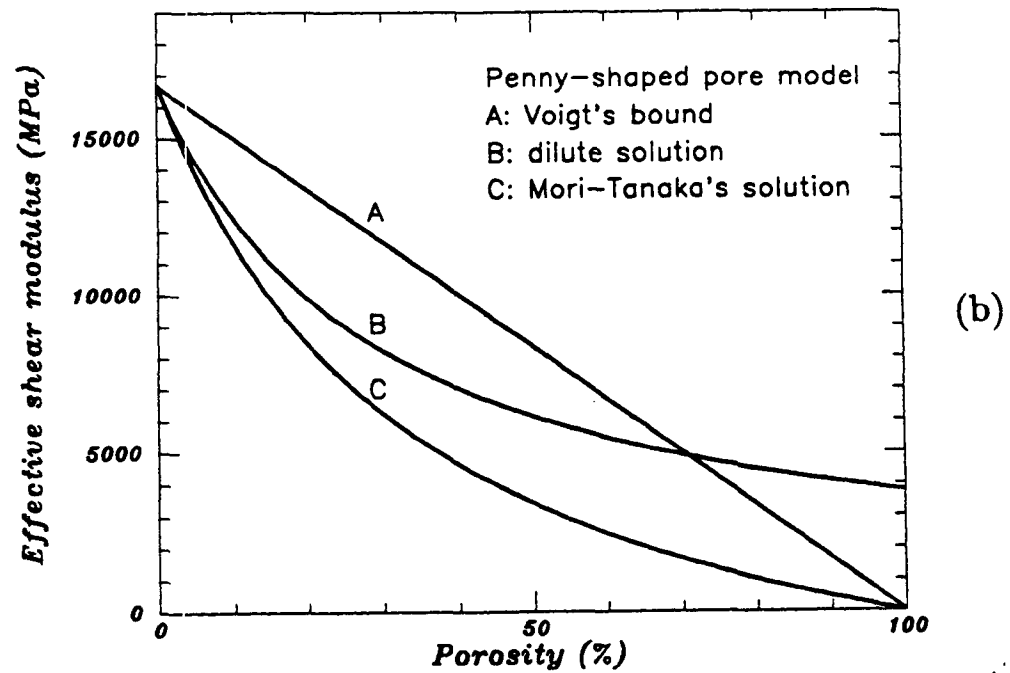
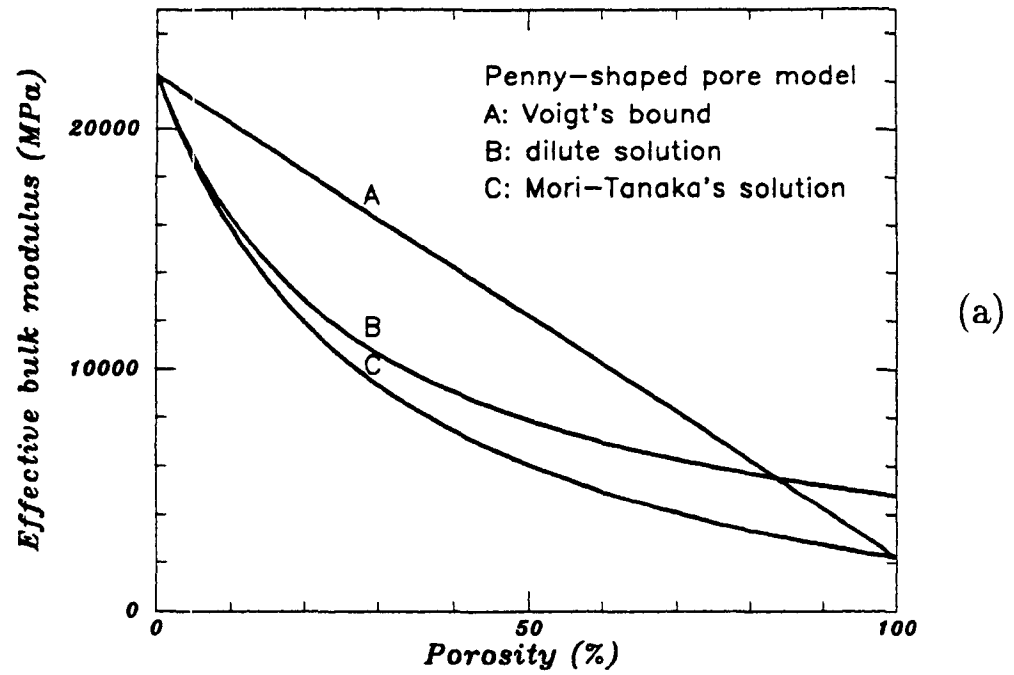


Fig.2.3 Comparison between the Mori-Tanaka's solution and dilute-concentration solution for penny-shaped pore model ($\eta = 0.1$) of water-saturated porous materials. (a) effective bulk modulus-porosity relation, (b) effective shear modulus-porosity relation.

2.2.3 Bounding solutions

While above solutions to effective elastic moduli are inclusion geometry-specific, bounding solutions to effective elastic moduli bear little information about inclusion geometries. Voigt and Reuss bounds are resulted from two simple assumptions, namely, those of uniform strain (isostrain) and uniform stress (isostress) field throughout the composite material (Voigt, 1928; Reuss, 1929). For two-phase composite materials, the effective bulk and shear moduli of Voigt's solution, K_V , μ_V , and Reuss' solution, K_R , μ_R , are expressed respectively as

$$K_V = (1 - \phi_2)K_1 + \phi_2K_2, \quad \mu_V = (1 - \phi_2)\mu_1 + \phi_2\mu_2; \quad (2.22)$$

$$\frac{1}{K_R} = \frac{1 - \phi_2}{K_1} + \frac{\phi_2}{K_2}, \quad \frac{1}{\mu_R} = \frac{1 - \phi_2}{\mu_1} + \frac{\phi_2}{\mu_2}. \quad (2.23)$$

Hill (1952, 1963) verified that (K_V, μ_V) and (K_R, μ_R) are the most general upper and lower bounds on effective elastic moduli K and μ of composite materials. However, no information about the inclusion geometry is specified in the Voigt and Reuss bounds, and so poor agreements often arise between the solutions and experimental data even for engineering composite materials.

To improve the Voigt-Reuss bounds, Hashin and Shtrikman (1961, 1962, 1963) used variational principles to find the bounding of effective elastic moduli of n -phase composite materials. Although no information about the inclusion geometry of multiphase composite is specified in the HS bounds, the physical meaning of the HS bounds in the common case of two-phase composite is quite clear from the work of Hashin (1962, 1970). The so called "composite spheres assemblage" micromechanical model of HS bounds, as in Fig. 2.6c, is composed of an assemblage of size-distributed concentric spheres. Each sphere consists of a spherical inclusion with K_2 and μ_2 , and a concentric spherical shell with K_1 and μ_1 . In the limit the entire volume can be filled out with such spheres and then becomes a composite spheres assemblage. For

soft-inclusion and stiff-matrix materials ($K_1 > K_2$, $\mu_1 > \mu_2$), the HS upper bound can be written as

$$K = K_1 + \frac{(K_2 - K_1)(3K_1 + 4\mu_1)\phi_2}{3K_2 + 4\mu_1 + 3(K_1 - K_2)\phi_2}, \quad (2.24)$$

$$\mu = \mu_1 + \frac{5\mu_1\phi_2(\mu_2 - \mu_1)(3K_1 + 4\mu_1)}{5\mu_1(3K_1 + 4\mu_1) + 6(1 - \phi_2)(\mu_2 - \mu_1)(K_1 + 2\mu_1)} \quad (2.25)$$

The corresponding HS lower bound is of the above forms with the suffix 1 and 2 exchanged.

Some bounding solutions narrower than HS bounds were developed when more specifications on microstructures were added to the material (Beran and Molyneux, 1966; Miller, 1969; McCoy, 1970; Corson, 1974). For asymmetric materials in which matrix and inclusion phases have different geometries, Miller (1969) introduced geometry parameters G_1 and G_2 to describe the average matrix and inclusion geometries. Watt et al. (1976) gave the correct forms of Miller solution to the effective bulk modulus. The reasons why these bounding solutions are not so popular as the HS bounding solution may be attributed to the facts that they usually yield bounds only for effective bulk modulus like Miller bounds, that it is very time-consuming to determine those geometry parameters, and that it is difficult to verify the existence of those microstructural specifications in most composite materials.

When the elastic properties of matrix and inclusion phases are in the same order, the HS bounds are quite narrow, which implies that inclusion volume fraction is the sole dominant parameter to influence the effective elastic moduli. However, for dry and fluid-saturated porous materials, the high contrast of constituent properties causes the HS upper and lower bounds far apart. For inviscid fluid-saturated porous materials, $K_2 \neq 0$, $\mu_2 = 0$, the HS lower bound becomes

$$\mu = 0; \quad K = K_R. \quad (2.26)$$

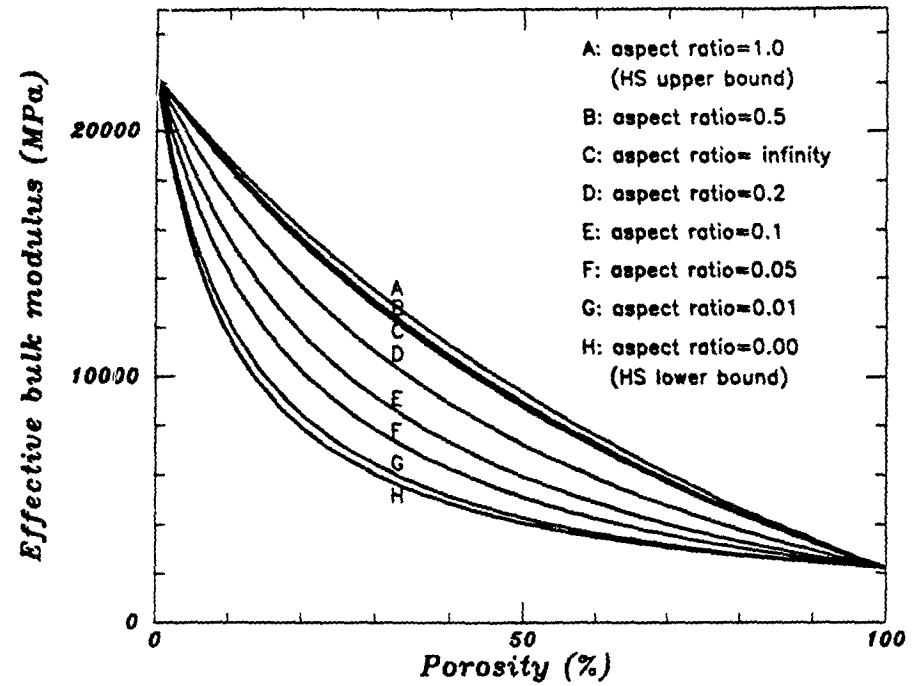
Above analysis thus raises an interesting problem: what factor and how it affects the effective elastic moduli within the far-apart HS upper and lower bounds for porous materials? It is the pore geometry that becomes a major factor affecting the effective elastic moduli of porous materials. Fig.2.4 compares the Mori-Tanaka's solutions with the far-apart HS bounds of effective bulk and shear moduli for water-saturated porous materials. Several conclusions can be drawn as follows:

1. At any level of porosity, Mori-Tanaka's solutions to K and μ for all possible spheroidal pore models just fully fill the domain between the far apart HS upper and lower bounds.

2. The results indicate that the pore geometry effects on effective elastic moduli are consistent with those in dilute-concentration solutions.

3. Mori-Tanaka's solution with spherical pore geometry is the same as HS upper bound. Since the micromechanical model of Mori-Tanaka's solution doesn't define the size distribution and space pattern of spherical inclusions, such consistence of these two solutions implies that the micromechanical model of HS bounds is just a specific model to account for equivalent inclusion interactions.

4. The consistency of HS lower bounds (here $K = K_R$, $\mu = 0$) with Mori-Tanaka's solution for $\eta = 0$ can be understood in the following way. The Reuss' solution K_R is based on the isostress model, with no specification to material microstructure geometry. For inviscid fluid-saturated materials, when the fluid phase is distributed as matrix and the solid phase as isolated inclusions of arbitrary geometry, the materials are perfectly in the isostress state. The HS lower bound is just a solution to such materials when spherical solid inclusions are assumed. Mori-Tanaka's solution with $\eta = 0$ implies that those thin fluid inclusions are somehow connecting each other to form the fluid matrix in the material. Thus it is a solution to such fluid-matrix supported materials when the connecting of infinitesimal-thin inclusions are assumed.



(a)

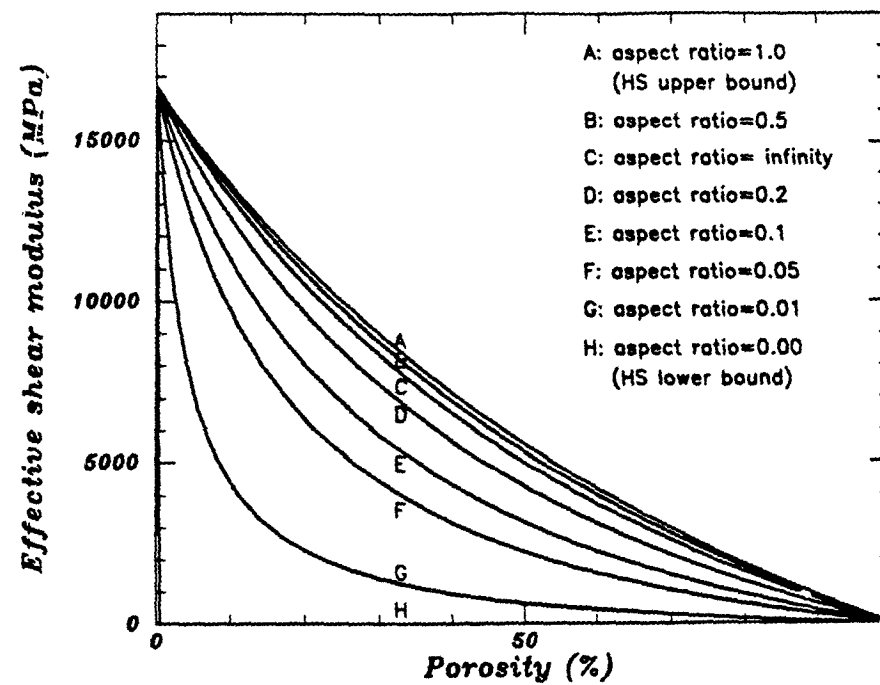


Fig.2.4 Comparison between the HS bounds and Mori-Tanaka's predictions for water-saturated porous material. Mori-Tanaka's predictions for all spheroidal pore models just fully fill the domain between the upper and lower bounds. (a) effective bulk modulus-porosity relations, (b) effective shear modulus-porosity relations.

2.3 Comparison with Gassmann's Solution

As shown above, pores and cracks soften the elastic stiffness of materials, but fluid saturation tends to restore some portions of the elastic stiffness. The relationship between the dry and saturated material elastic moduli depends on several factors such as porosity, microstructural geometry, and wave frequency. Gassmann (1951) assumed the statistical isotropy of rock microstructures and identical moduli of the individual grains, and arrived at quite simple relations between effective elastic moduli of dry rocks (K_{dry} , μ_{dry}) and inviscid fluid-saturated rocks (K_{ifs} , μ_{ifs}),

$$\frac{1}{K_{ifs}} = \frac{1}{K_1} + \frac{(\frac{1}{K_2} - \frac{1}{K_1})}{1 + \phi_2(\frac{1}{K_2} - \frac{1}{K_1})/(\frac{1}{K_{dry}} - \frac{1}{K_1})} \phi_2, \quad (2.27)$$

$$\frac{1}{\mu_{ifs}} = \frac{1}{\mu_{dry}}. \quad (2.28)$$

Since no specific pore geometry is assumed in the derivation of above formulas, it seems that K_{ifs} and μ_{ifs} are completely independent of pore geometry. However, our results above show that K_{dry} and μ_{dry} strongly depend on material microstructural geometries, thus K_{isf} and μ_{isf} are, in fact, related to specific microstructural geometry.

Gassmann's solution predicts that inviscid fluid saturation has no effect on the effective shear modulus. This implies that the perturbed fluid pressure induced by the applied stress is sufficiently equilibrated throughout the material when the external loading is in low frequency. However, the equilibration mechanism is intrinsically related to the material microstructural geometry. In other words, some pore geometries may be favorable to the equilibration, others may not. For various pore geometries such as cylindrical, prolate, and spherical pore models, Mori-Tanaka's solutions to K_{ifs} and μ_{ifs} are consistent with the Gassmann's solution. Fig.2.5a shows Mori-Tanaka's solution to K_{dry} , μ_{dry} , K_{ifs} , and μ_{ifs} for cylindrical pore model. The

saturated shear modulus μ_{ifs} is, in general, equivalent to μ_{dry} . When K_{dry} from Mori-Tanaka's solution is used in Gassmann's solution, the resulting K_{ifs} is identical with the one in Mori-Tanaka's solution.

However, for flat pore and crack models, the equilibration mechanism as implied in Gassmann's solution is not applicable to the Mori-Tanaka's solution. Fig.2.5b shows Mori-Tanaka's solution to effective shear moduli for penny-shaped crack models with $\eta = 0.1, 0.05,$ and $0.01,$ respectively. These results indicate that the crack models, unlike the above pore models, result in fluid stiffening effects not only on K_{ifs} but also on μ_{ifs} .

2.4 Specific Solutions for Dry Porous Materials

2.4.1 Finite-matrix solution

Instead of assuming an infinite elastic matrix and remote applied loading, the finite-matrix model assumes that the interaction between any one pore and all other pores can be approached through a model of a finite matrix with a single pore embedded inside and applied loading on the matrix boundary. Since the interaction between the loaded boundary of the finite matrix and the pore inside the matrix is usually easier to be quantified, and it increases with the fractional volume of the pore, we utilize this kind of interaction to simulate the interaction between pores (Chen et al., 1990).

When the boundary configuration of a finite matrix containing a pore is chosen similar to that of the pore, as shown in Fig.2.6a, some finite-matrix solutions can be obtained by means of the Betti-Rayleigh reciprocity theorem (Timoshenko and Goodier, 1970). For the spherical pore model, such finite-matrix solution is found as

$$\frac{K_1}{K} = 1 + \frac{3(1 - \nu_1)}{2(1 - 2\nu_1)} \frac{\phi_2}{1 - \phi_2}, \quad (2.29)$$

$$\frac{\mu_1}{\mu} = 1 + \frac{15(1 - \nu_1)}{7 - 5\nu_1} \frac{\phi_2}{1 - \phi_2}. \quad (2.30)$$

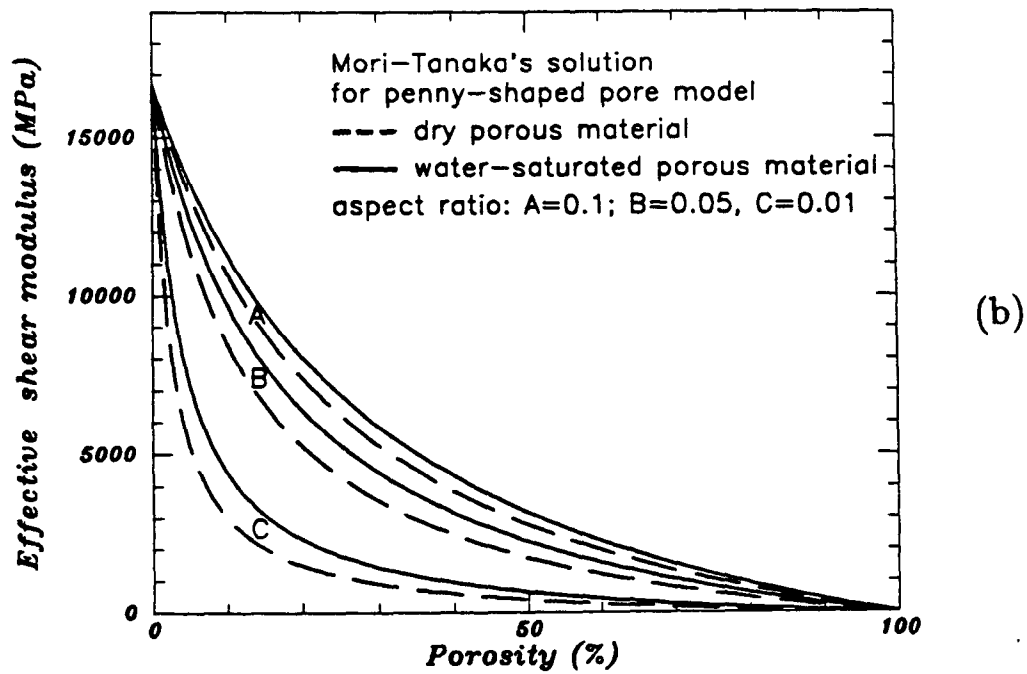
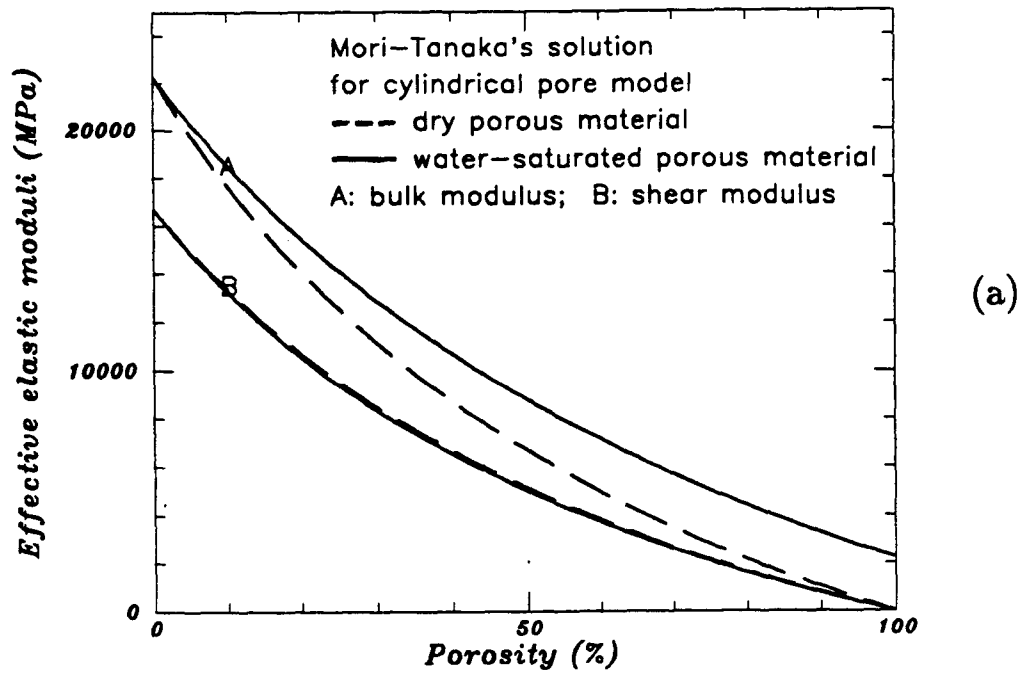


Fig.2.5 (a) comparison of effective elastic modulus-porosity relations for dry and water-saturated materials with cylindrical pores, (b) comparison of effective shear modulus-porosity relations for dry and water-saturated materials with penny-shaped cracks ($\eta = 0.1, 0.05, 0.01$).

2.4.2 Mackenzie's solution

Mackenzie (1950) proposed a microscopic model to calculate the effective elastic moduli of porous rocks. As shown in Fig.2.6b, an element covering one pore is cut out of the rock, and the loading is applied on its outer boundary. Then the element is simulated as three concentric spheres: the inside one represents a single pore; the intermediate one has matrix elastic moduli K_1 and μ_1 ; and the outer one has effective elastic moduli K and μ . Accurate to the first order of ϕ_2 , Mackenzie obtained

$$\frac{1}{K} = \frac{1}{K_1} + \left(\frac{1}{K_1} + \frac{3}{4\mu_1} \right) \frac{\phi_2}{1 - \phi_2}, \quad (2.31)$$

$$\mu = \mu_1 \left(1 - 5\phi_2 \frac{3K_1 + 4\mu_1}{9K_1 + 8\mu_1} \right). \quad (2.32)$$

By algebra the above results become

$$\frac{K_1}{K} = 1 + \frac{3(1 - \nu_1)}{2(1 - 2\nu_1)} \frac{\phi_2}{1 - \phi_2}, \quad (2.33)$$

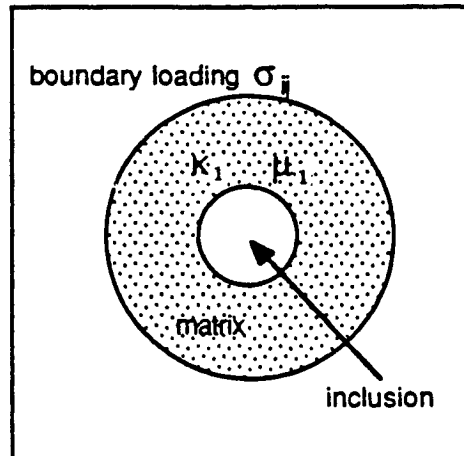
$$\frac{\mu_1}{\mu} = 1 + \frac{\frac{15(1-\nu_1)}{7-5\nu_1} \phi_2}{1 - \frac{15(1-\nu_1)}{7-5\nu_1} \phi_2} \approx 1 + \frac{15(1 - \nu_1)}{7 - 5\nu_1} \frac{\phi_2}{1 - \phi_2}. \quad (2.34)$$

Thus, Mackenzie's solution is equivalent to the finite-matrix solution.

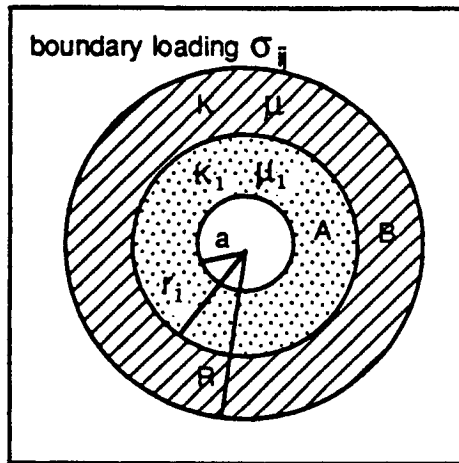
2.4.3 Walsh's solution

Walsh(1965) studied the effect of crack on the compressibility of rock and found the effective compressibility β for a spherical cavity as

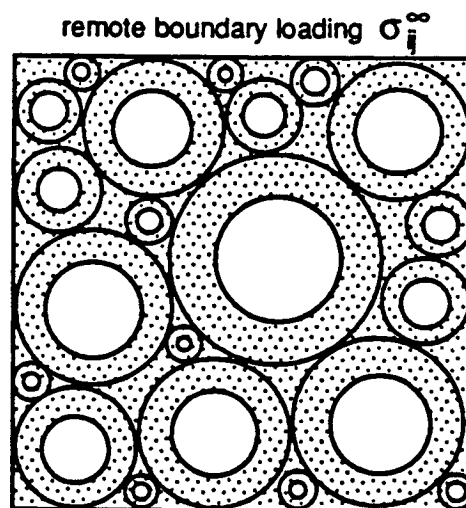
$$\frac{\beta}{\beta_1} = 1 + \frac{3(1 - \nu_1)}{2(1 - 2\nu_1)} \frac{\phi_2}{1 - \phi_2}, \quad (2.35)$$



(a)



(b)



(c)

Fig.2.6 Micromechanical models for (a) the finite-matrix solution, (b) the Mackenzie's solution, and (c) the Hashin-Shtrikman bounds

which is the same as the finite-matrix solution since $K = 1/\beta$ and $K_1 = 1/\beta_1$. Walsh derived the result by presuming the pore concentration in the rock was small, but later he demonstrated with experimental data that the result was valid even for high pore concentration (Walsh et al., 1965).

2.4.4 Hashin-Shtrikman's upper bound

When pores are considered, the HS upper bound becomes

$$\frac{K_1}{K} = \left[1 - \frac{(3K_1 + 4\mu_1)\phi_2}{3K_1\phi_2 + 4\mu_1} \right]^{-1} = 1 + \frac{3(1 - \nu_1)}{2(1 - 2\nu_1)} \frac{\phi_2}{1 - \phi_2}, \quad (2.36)$$

$$\frac{\mu_1}{\mu} = \left[1 - \frac{5\phi_2(3K_1 + 4\mu_1)}{5(3K_1 + 4\mu_1) - 6(1 - \phi_2)(K_1 + 2\mu_1)} \right]^{-1} = 1 + \frac{15(1 - \nu_1)}{7 - 5\nu_1} \frac{\phi_2}{1 - \phi_2}, \quad (2.37)$$

which are also the same as the finite-matrix solution. Furthermore, we already show that Mori-Tanaka's solution for spherical inclusions is identical with HS upper bound. The consistency of all these solutions for porous materials implies that the micromechanical model of the finite-matrix solution in Fig.2.6a is a simple but fundamental one to describe the effective elastic moduli of spherical-pore materials, and that the "composite spheres assemblage" model of the HS bounds in Fig.2.6c is in fact an assemblage of the model in Fig.2.6a.

2.4.5 A group of pore geometry-specific solutions

By comparing the finite-matrix solution with dilute-concentration solution for spherical pore model, we notice that their difference is the factor ϕ_2 being replaced by $\frac{\phi_2}{1 - \phi_2}$. It is this change that accounts for the nondilute concentration pore interaction. To extend this feature to other pore geometries, the dilute-concentration solution for cylindrical pore model can be modified as the nondilute concentration solution for cylindrical pore model,

$$\frac{K_1}{K} = 1 + \frac{5 - 4\nu_1}{3(1 - 2\nu_1)} \frac{\phi_2}{1 - \phi_2}, \quad (2.38)$$

$$\frac{\mu_1}{\mu} = 1 + \frac{40 - 24\nu_1}{15} \frac{\phi_2}{1 - \phi_2}, \quad (2.39)$$

and the dilute-concentration solution for penny-shaped crack model can be modified as the nondilute concentration solution for penny-shaped crack model,

$$\frac{K_1}{K} = 1 + \frac{4(1 - \nu_1^2)}{3\pi\eta(1 - 2\nu_1)} \frac{\phi_2}{1 - \phi_2}, \quad (2.40)$$

$$\frac{\mu_1}{\mu} = 1 + \frac{1}{5} \left[1 + \frac{8(1 - \nu_1)(5 - \nu_1)}{3\pi\eta(2 - \nu_1)} \right] \frac{\phi_2}{1 - \phi_2}. \quad (2.41)$$

Numerical computations show that these simple-form solutions coincide with Mori-Tanaka's solutions for dry porous materials.

2.5 Wave Velocity-Porosity Relations

Since the effective elastic properties of all above material models are isotropic, effective Young's modulus E and uniaxial-strain modulus M are obtained through relations

$$E = \frac{9K\mu}{3K + \mu}, \quad M = \frac{3K + 4\mu}{3}. \quad (2.42)$$

The low-frequency or long-wavelength P-wave and S-wave velocities, V_p , V_s , are then calculated from the relations

$$V_p = \sqrt{\frac{M}{\rho}}, \quad V_s = \sqrt{\frac{\mu}{\rho}}, \quad (2.43)$$

where the effective density ρ is related to rock matrix density ρ_1 and inclusion density ρ_2 by $\rho = (1 - \phi_2)\rho_1 + \phi_2\rho_2$. In the calculation, $\rho_1 = 2600\text{kgm}^{-3}$ for solid phase and $\rho_2 = 1000\text{kgm}^{-3}$ for water fluid are used. Fig.2.7 presents the velocity-porosity-aspect ratio relations for water-saturated materials from Mori-Tanaka's solution. For cylindrical, prolate, spherical, and spheroidally-oblate pore models, the velocity-porosity relations have similar features for both the P and S wave velocities. When the aspect ratio becomes smaller, P and S wave velocities drop sharply at low porosity, thus the penny-shaped crack model yields distinctive velocity-porosity relations from other pore models.

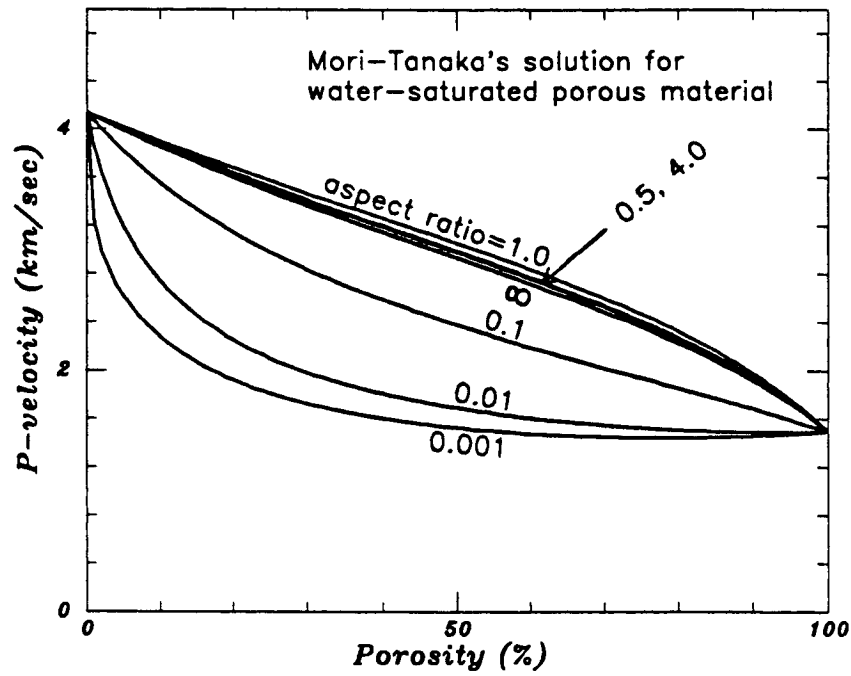
2.6 Conclusions

The microstructural geometry effects on the effective elastic moduli of porous materials are consistent for both dilute and nondilute concentration solutions. Spherical pore model yields high elastic moduli; prolate and cylindrical pore models exhibit minor decrease in elastic moduli compared with the spherical pore model; oblate and penny-shaped crack models lead to dramatic drop in elastic moduli.

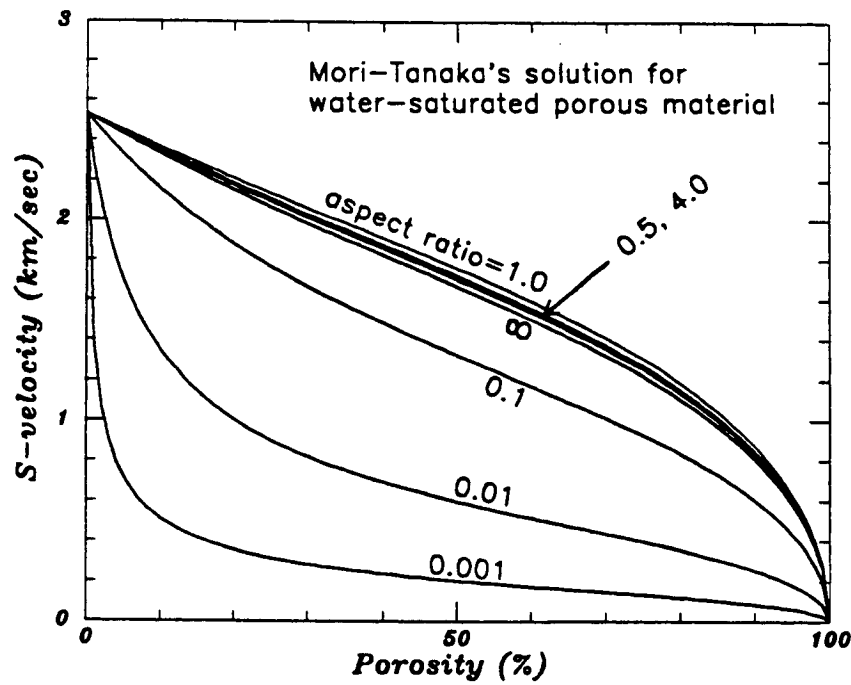
The dilute-concentration solutions to spherical, cylindrical, and penny-shaped pore/crack models are valid at low porosity (10% porosity or smaller), but become unacceptable at high porosity.

The Mori-Tanaka's solutions for a continuous series of spheroidal pore/crack models just fully fill the broad domain between the HS upper and lower bounds, and yield the asymptotic values of dilute-concentration solutions at low porosities. The equilibration mechanism implied in the Gassmann's solution is appropriate only for pore models but fails for crack models according to Mori-Tanaka's solution.

The consistence of finite-matrix solution with other solutions for spherical pore model leads us to propose a group of simple formulations for the effective elastic moduli of dry porous materials.



(a)



(b)

Fig.2.7 Mori-Tanaka's solution to wave velocity versus porosity and pore aspect ratio for water-saturated porous material, (a) P wave velocity-porosity relation, (b) S wave velocity-porosity relation.

However, when applied to porous rocks and sediments, the dilute and nondilute concentration solutions may be appropriate only at low porosity, since they fail in explaining the distinctive change of effective elastic moduli before and after the critical porosity. To solve such a problem, we develop the critical concentration model and solutions for porous materials with critical porosities in the following chapters.

Appendix

Components of Eshelby's S_{ijkl} Tensor

The components of Eshelby's tensor S_{ijkl} for a spheroidal inclusion are:

$$S_{1111} = \frac{1}{2(1-\nu_1)} \left\{ 1 - 2\nu_1 + \frac{3\eta^2-1}{\eta^2-1} - \left[1 - 2\nu_1 + \frac{3\eta^2}{\eta^2-1} \right] g \right\}$$

$$S_{2222} = S_{3333} = \frac{3}{8(1-\nu_1)} \frac{\eta^2}{\eta^2-1} + \frac{1}{4(1-\nu_1)} \left[1 - 2\nu_1 - \frac{9}{4(\eta^2-1)} \right] g$$

$$S_{2233} = S_{3322} = \frac{1}{4(1-\nu_1)} \left\{ \frac{\eta^2}{2(\eta^2-1)} - \left[1 - 2\nu_1 + \frac{3}{4(\eta^2-1)} \right] g \right\}$$

$$S_{2211} = S_{3311} = -\frac{1}{2(1-\nu_1)} \frac{\eta^2}{\eta^2-1} + \frac{1}{4(1-\nu_1)} \left[\frac{3\eta^2}{\eta^2-1} - (1 - 2\nu_1) \right] g$$

$$S_{1122} = S_{1133} = -\frac{1}{2(1-\nu_1)} \left[1 - 2\nu_1 + \frac{1}{\eta^2-1} \right] + \frac{1}{2(1-\nu_1)} \left[1 - 2\nu_1 + \frac{3}{2(\eta^2-1)} \right] g$$

$$S_{2323} = S_{3232} = \frac{1}{4(1-\nu_1)} \left\{ \frac{\eta^2}{2(\eta^2-1)} + \left[1 - 2\nu_1 - \frac{3}{4(\eta^2-1)} \right] g \right\}$$

$$S_{1212} = S_{1313} = \frac{1}{4(1-\nu_1)} \left\{ 1 - 2\nu_1 - \frac{\eta^2+1}{\eta^2-1} - \frac{1}{2} \left[1 - 2\nu_1 - \frac{3(\eta^2+1)}{\eta^2-1} \right] g \right\}$$

where ν_1 and η are Poisson's ratio of the matrix and the aspect ratio of the inclusion, respectively, and g is given by

$$g = \frac{\eta}{(\eta^2-1)^{3/2}} \left[\eta(\eta^2-1)^{1/2} - \cosh^{-1} \eta \right]$$

for prolate shape, and

$$g = \frac{\eta}{(1-\eta^2)^{3/2}} \left[\cos^{-1} \eta - \eta(1-\eta^2)^{1/2} \right]$$

for oblate shape.

For a spherical inclusion($\eta = 1$), they simplify to

$$S_{1111} = S_{2222} = S_{3333} = \frac{7-5\nu_1}{15(1-\nu_1)}$$

$$S_{1122} = S_{2233} = S_{3311} = \frac{5\nu_1-1}{15(1-\nu_1)}$$

$$S_{1212} = S_{2323} = S_{3131} = \frac{4-5\nu_1}{15(1-\nu_1)}$$

For a penny-shape crack with small but finite width($\eta \ll 1$), they become

$$S_{1111} = 1 - \frac{1-2\nu_1}{4(1-\nu_1)}\pi\eta$$

$$S_{2222} = S_{3333} = -\frac{13-8\nu_1}{32(1-\nu_1)}\pi\eta$$

$$S_{2233} = S_{3322} = \frac{8\nu_1-1}{32(1-\nu_1)}\pi\eta$$

$$S_{2211} = S_{3311} = \frac{2\nu_1-1}{8(1-\nu_1)}\pi\eta$$

$$S_{1122} = S_{1133} = \frac{\nu_1}{1-\nu_1}\left[1 - \frac{1+4\nu_1}{8\nu_1}\pi\eta\right]$$

$$S_{2323} = \frac{7-8\nu_1}{32(1-\nu_1)}\pi\eta$$

$$S_{1212} = S_{1313} = \frac{1}{2}\left[1 - \frac{2-\nu_1}{4(1-\nu_1)}\pi\eta\right]$$

For a cylindrical pore ($\eta \rightarrow \infty$), one has

$$S_{1111} = 0$$

$$S_{2222} = S_{3333} = \frac{5-4\nu_1}{8(1-\nu_1)}$$

$$S_{2233} = S_{3322} = \frac{4\nu_1-1}{8(1-\nu_1)}$$

$$S_{2211} = S_{3311} = \frac{\nu_1}{2(1-\nu_1)}$$

$$S_{1122} = S_{1133} = 0$$

$$S_{2323} = \frac{3-4\nu_1}{8(1-\nu_1)}$$

$$S_{1212} = S_{1313} = \frac{1}{4}$$

Parameters $a_1 \dots a_5$ and a

$$a_1 = 6(K_2 - K_1)(\mu_2 - \mu_1)(S_{2222} + S_{2233} - 1) - 2(K_1\mu_2 - K_2\mu_1) + 6K_2(\mu_2 - \mu_1)$$

$$a_2 = 6(K_2 - K_1)(\mu_2 - \mu_1)S_{1133} + 2(K_1\mu_2 - K_2\mu_1)$$

$$a_3 = -6(K_2 - K_1)(\mu_2 - \mu_1)S_{3311} - 2(K_1\mu_2 - K_2\mu_1)$$

$$a_4 = 6(K_2 - K_1)(\mu_2 - \mu_1)(S_{1111} - 1) + 2(K_1\mu_2 - K_2\mu_1) + 6\mu_2(K_2 - K_1)$$

$$a_5 = 1/[S_{3322} - S_{3333} + 1 - \mu_2/(\mu_2 - \mu_1)]$$

$$\begin{aligned}
a = & 6(K_2 - K_1)(\mu_2 - \mu_1)[2S_{1133}S_{3311} - (S_{1111} - 1)(S_{3322} + S_{3333} - 1)] \\
& + 2(K_1\mu_2 - K_2\mu_1)[2(S_{1133} + S_{3311}) + (S_{1111} - S_{3322} - S_{3333})] \\
& - 6K_2(\mu_2 - \mu_1)(S_{1111} - 1) - 6\mu_2(K_2 - K_1)(S_{2222} + S_{2233} - 1) - 6K_2\mu_2
\end{aligned}$$

References

- Benveniste, Y., 1987, A new approach to the application of Mori-Tanaka's theory in composite materials, *Mech. Mater.*, **6**, 147-157.
- Beran, M. J. and J. Molyneux, 1966, Use of classical variational principles to determine bounds for the effective bulk modulus in heterogeneous media, *Quart. Appl. Math.*, **24**, 107-118.
- Berryman, J. G., 1980, Long-wavelength propagation in composite elastic media. I. Spherical Inclusions, *J. Acoust. Soc.*, **68**, 1809-1819; and II. Ellipsoidal inclusions, *J. Acoust. Soc.*, **68**, 1820-1831.
- Boucher, S., 1974, On the effective moduli of isotropic two-phase elastic composites, *J. Compos. Mater.*, **8**, 82-89.
- Boucher, S., 1976, Modules effectifs de materiaux quasi homogenes et quasi isotropes, constitues d'une matrice elastique et d'inclusions elastiques, II Cas des concentrations finies en enclussions, *Revue de Metallurgie*, **22**, 31-36.
- Chen, Q., Nur, A., Mavko, G., and Dvorkin, J., 1990, Modeling effective elastic moduli of porous rocks, *SRB*, **40**, Paper C.
- Chen, Q. and A. Nur, 1991, The effective property-porosity relations of porous geomaterials with critical porosities, *SRB*, **46**, Paper D.
- Chow, T. S., 1978, Effect of particle shape at finite concentration on the elastic moduli of filled polymers, *J. Polymer Science: Polymer Physics Edition*, **16**, 959-965.
- Cleary, M. P., Chen, I. W., and S. M. Lee, 1980, Self-consistent techniques for heterogeneous solids, *ASCE J. Eng. Mech.*, **106**, 861-887.
- Corson, P. B., 1974, Correlation functions for predicting properties of heterogeneous materials, 3, effective elastic moduli of two-phase solids, *J Appl. Phys.*, **45**, 3171-3179.
- Eshelby, J. D., 1957, The determination of the elastic fields of an ellipsoidal inclusion, and related problems, *Proc. Roy. Soc. A* **241**, 376-396.
- Gassmann, G., 1951, Uber die Elastizitat poroser Medien, *Vierteljahresschr., Naturforsch. Ges. Zuerich*, **96**, 1-21.
- Hashin, Z. and S. Shtrikman, 1961, Note on a variational approach to the theory of composite elastic materials, *J. Franklin Inst.*, **271**, 336-341.

- Hashin, Z. and S. Shtrikman, 1962, A variational approach to the theory of the elastic behavior of polycrystals, *J. Mech. Phys. Solids*, **10**, 343-352.
- Hashin, Z. and S. Shtrikman, 1963, A variational approach to the elastic behavior of multiphase materials, *J. Mech. Phys. Solids*, **11**, 127-140.
- Hashin, Z., 1962, The elastic moduli of heterogeneous materials, *J. Appl. Mech.*, **29**, 143-150.
- Hashin, Z., 1970, Theory of composite materials, in *Mechanics of Composite Materials*, 5th Symposium on Naval Structural Mechanics, edited by Wendt, F. W., H. Liebowitz, and Perrone, N., 201-242. Pergamon, New York.
- Hashin, Z., 1983, Analysis of composite materials – a survey, *J. Appl. Mech.*, **50**, 481-505.
- Hill, R., 1952, The elastic behavior of a crystalline aggregate, *Proc. Phys. Soc. London, Sect. A*, **65**, 349-354.
- Hill, R., 1963, Elastic properties of reinforced solids: some theoretical principles, *J. Mech. Phys. Solids*, **11**, 357-372.
- Hill, R., 1965, A self-consistent mechanics of composite materials: *J. Mech. Phys. Solids*, **13**, 213-222.
- Kroner, E., 1958, Berechnung der elastischen Konstanten des Vielkristalls aus den Konstanten der Einkristalls, *Zeitschrift Physik*, **151**, 504-518.
- Mackenzie, J. K., 1950, The elastic constants of a solid containing spherical holes, *Proc. Phys. Soc. London Sect. B*, **63**, 2-11.
- Mavko, G. M., 1980, Velocity and attenuation in partially molten rocks: *J. G. Res.*, **85**, 5173-5189.
- McCoy, J. J., 1970, On the displacement field in an elastic medium with random variations in material properties, in *Recent Advances in Engineering Science*, edited by A. C. Eringen, 235-254, Gordon and Breach, New York.
- McLaughlin, R., 1977, A study of the differential scheme for composite materials, *Int. J. Eng. Sci.*, **15**, 237-244.
- Miller, M. N., 1969, Bounds for effective bulk modulus of heterogeneous materials, *J. Math. Phys.*, **10**, 2005-2013.
- Mori, T. and Tanaka, K., 1973, Average stress in the matrix and average elastic en-

- ergy of materials with misfitting inclusions, *Acta Metallurgica*, **21**, 571-574.
- Mura, T., 1988, Inclusion problems, *Appl. Mech. Rev.* **41**, 15-20.
- Reuss, A., 1929, Berechnung der Fließgrenze von Mischkristallen auf Grund der Plastizitätsbedingung für Einkristalle, *Z. Angew. Math. Mech.*, **9**, 49-58.
- Roscoe, R., 1952, The viscosity of suspensions of rigid spheres, *British J. Appl. Phys.*, **3**, 267-269.
- Sheng, P. and A. J. Callegari, 1984, Differential effective medium theory for sedimentary rocks, in D. L. Johnson and P. N. Sen, eds., *Physics and Chemistry of Porous Media*, AIP Conference Proceedings 197, American Institute of Physics, New York, 144-165.
- Tandon, G. P. and Weng, G. J., 1986, Average stress in the matrix and effective moduli of randomly oriented composites, *Composites Science and Technology*, **27**, 111-132.
- Taya, M. and Chou, T.-W., 1981, On two kinds of ellipsoidal inhomogeneities in an infinite elastic body: an application to a hybrid composite, *Int. J. Solids and Struct.*, **17**, 553-563.
- Taya, M. and Mura, T., 1981, The stiffness and strength of an aligned short-fiber reinforced composite containing fiber-end cracks under uniaxial applied stress, *ASME J. Appl. Mech.*, **43**, 361-367.
- Timoshenko, S. P. and J. N. Goodier, 1970, *Theory of elasticity*: 3rd ed., McGraw-Hill, New York, pp.567.
- Voigt, W., 1928, *Lehrbuch der Kristallphysik*, Teubner, Leipzig, pp.964.
- Walpole, L. J., 1969, On the overall elastic moduli of composite materials, *J. Mech. Phys. Solids*, **17**, 235-251.
- Walsh, J. B., 1965, The effect of cracks on the uniaxial elastic compression of rocks: *J. G. Res.*, **70**, 399-411.
- Walsh, J. B., 1969, New analysis of attenuation in partially melted rock, *J. Geo. Res.*, **74**, 4333-4337.
- Walsh, J. B., W. F. Brace, and England, A. W., 1965, Effect of porosity on compressibility of glass, *J. Amer. Ceramic Soc.*, **48**, 605-608.
- Watt, J. P., G. F. Davies, and R. J. O'Connell, 1976, The elastic properties of com-

posite materials, *Review of Geophysics and Space Physics*, **14**, 541-563.

Weng, G. J., 1984, Some elastic properties of reinforced solids, with special reference to isotropic ones containing spherical inclusions, *Int. J. Eng. Sci.*, **22**, 845-856.

Wu, T. T., 1966, The effect of inclusion shape on the elastic moduli of a two-phase material, *Int. J. Solids Struct.*, **3**, 1-8.

Chapter 3

Critical Concentration Models of Porous Materials

Abstract

Porous rocks and sediments have complicated microstructures that result from depositional, diagenetic, and tectonic processes. These nonuniform microstructures cause the effective properties such as elastic moduli and wave velocities so distinctive from those predicted by conventional models that several empirical formulas have been proposed to remedy the lacking of appropriate models of porous rocks and sediments. We identify that critical porosity is an important parameter to describe the variations of porous material microstructural and effective properties. By introducing the concepts of critical porosity and concentration, and defining the critical concentration phase, we propose the critical concentration model which describes the nonuniform load-bearing capacities of solid grains. The microstructural interpretation of critical concentration model is characterized by nonuniform contact areas and coordination numbers of solid grains throughout the porous material. The critical porosities of porous rocks and sediments determined by geometrical, theoretical, and experimental approaches are consistent, and are of wide ranges due to the diverse pore size, geometry, and connectivity.

3.1 Observation of porosity data

Microstructures affect almost all the physical properties of porous materials. Geomaterial microstructures depend on their origins including depositional, diagenetic, and tectonic processes, and synthetic material microstructures come from thermal history, pressure condition and chemical environment. Several parameters such as pore volume fraction (porosity), pore geometry, pore connectivity, pore size, and pore surface roughness have been used to describe the microstructures or pore structures of various porous materials (Dullien, 1979; Johnson and Sen, 1983; Banavar et al., 1986; Bourbié et al., 1987; Roberts and Skalny, 1989, Shah, 1991). It is generally recognized that porosity is the primary measure of porous material microstructures, and so many analytical and empirical relations between effective properties and porosity have been established and applied to various practical problems (Wyllie et al., 1956; Watt et al., 1976; Raymer et al., 1980; Nobes, 1989). One of the fundamental aspects in these relations is that the effective properties exhibit smooth variations when porosity increases from zero to 100%, which implies that the material framework has nonzero stiffness until the porosity reaches 100%.

However, more and more in-situ and laboratory experimental data indicate that at some finite values of porosity, the effective properties of porous materials change distinctively from previous levels, increasing or decreasing sharply, or even reducing to zero, such as strength data (Schiller, 1958; Rzhovsky and Novik, 1971; Dunn et al., 1973; Hoshino, 1981; Kendall, 1984; Pratt, 1987; Jizba, 1991), permeability and electric conductivity data (Kirkpatrick, 1973; Chelidze, 1979; Bernabe et al., 1982; Teisseyre, 1983; Walder and Nur, 1984, Bourbié et al., 1987), and effective modulus and wave velocity data (Geertsma, 1961; Wyllie et al., 1961; Gregory, 1963; Burns et al., 1973; Benguigui, 1984; Marion, 1988; Chelidze et al., 1988, 1990).

Fig.3.1 shows the experimental data of strength versus porosity of mudstones. At atmospheric pressure, the strength approaches zero at about 50% porosity. At high

confining pressure, the failure mechanism changes from brittle (black circle) to ductile (open circle), and the strength drops to the level of given confining pressure at about 50% porosity. In general, the strength properties of all natural and synthetic porous materials terminate at finite values of porosity, not the 100% porosity.

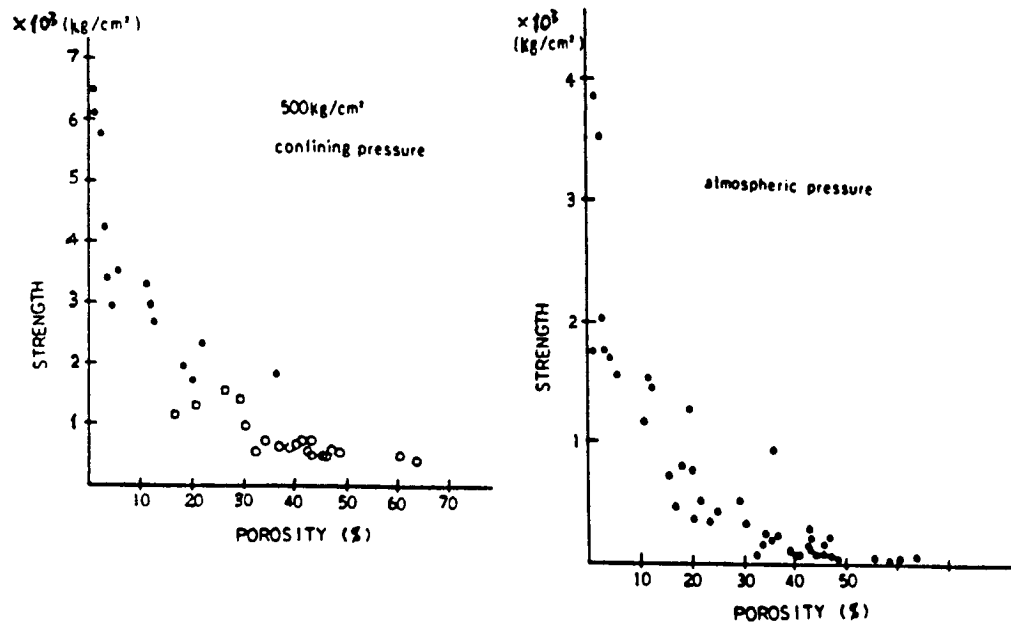


Fig.3.1 The experimental data of strength versus porosity of mudstones. Black circles: brittle failure; open squares: transitional failure; open circles: ductile failure. The strengths terminate at about 50% porosity (after Hoshino, 1981).

Fig. 3.2 shows the experimental data of permeability versus porosity of Fontainebleau sandstones. At about 5% porosity, the classic cubic law of permeability-porosity relationship is insufficient to describe the decrease of permeability with porosity. The permeability terminates at about 3% porosity, not zero porosity, which is certainly related to the distinctive change in the sandstone pore structures.

Fig.3.3 compares various models and experimental data of effective Young's modulus versus porosity of porous materials. Some data indicate that the effective Young's modulus terminates at about 50% porosity. The diverse data imply that other pore

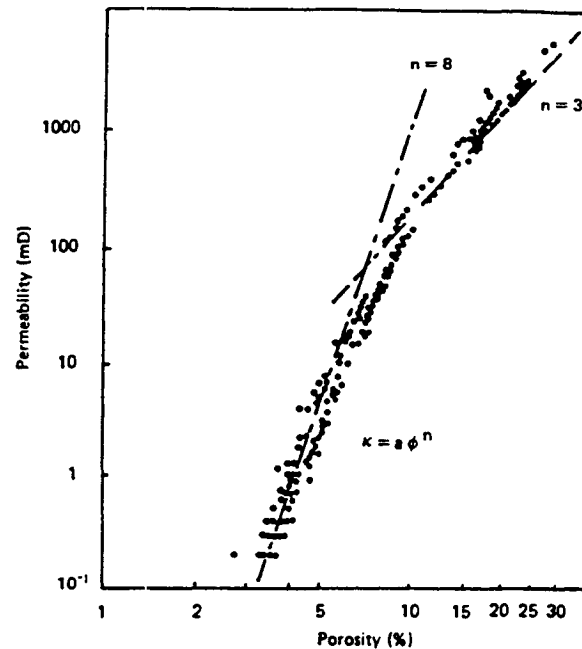


Fig.3.2 The experimental data of permeability versus porosity of Fontainebleau sandstones. The permeability terminates at about 3% porosity, not zero porosity (after Bourbié et al., 1987).

structure parameters such as pore size, geometry, and connection play considerable roles in determining mechanical properties of porous materials.

Fig.3.4 shows the experimental data of P wave velocity versus porosity, collected by Marion (1990). Obviously, clay content causes the decrease of P wave velocity. There is a distinctive change in P wave velocity before and after about 40% porosity. The suspension data are well explained by the Wood's relation, but the other data depart from the Wood's relation. No existing model or theory can fully explain such velocity data.

In summary, many experimental data are not consistent with the fundamental hypothesis that porous material microstructures and effective properties vary smoothly when the porosity ranges from zero to 100%. Not only porosity, but also other pore structure parameters should be taken into account so as to evaluate quantitatively the mechanical and acoustic properties of porous materials.

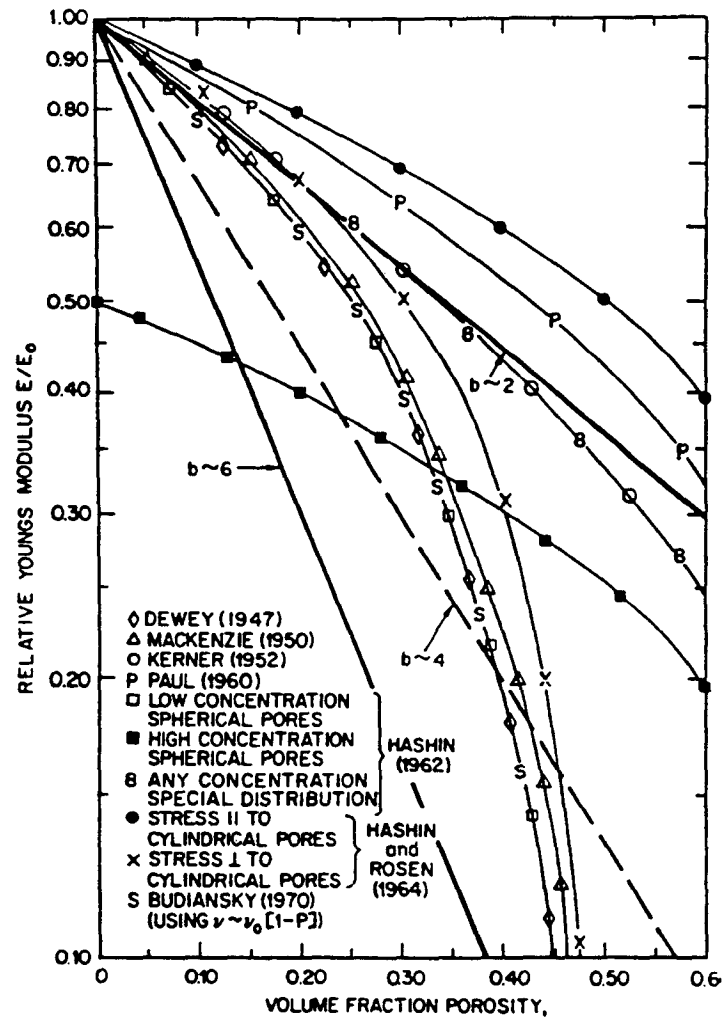


Fig.3.3 The comparison between various models and experimental data of effective Young's modulus versus porosity of porous materials. Empirical exponential relation $E/E_0 = e^{-b\phi}$ with $b = 2, 4, \text{ and } 6$ is used to fit the data (after Pereira et al., 1989).

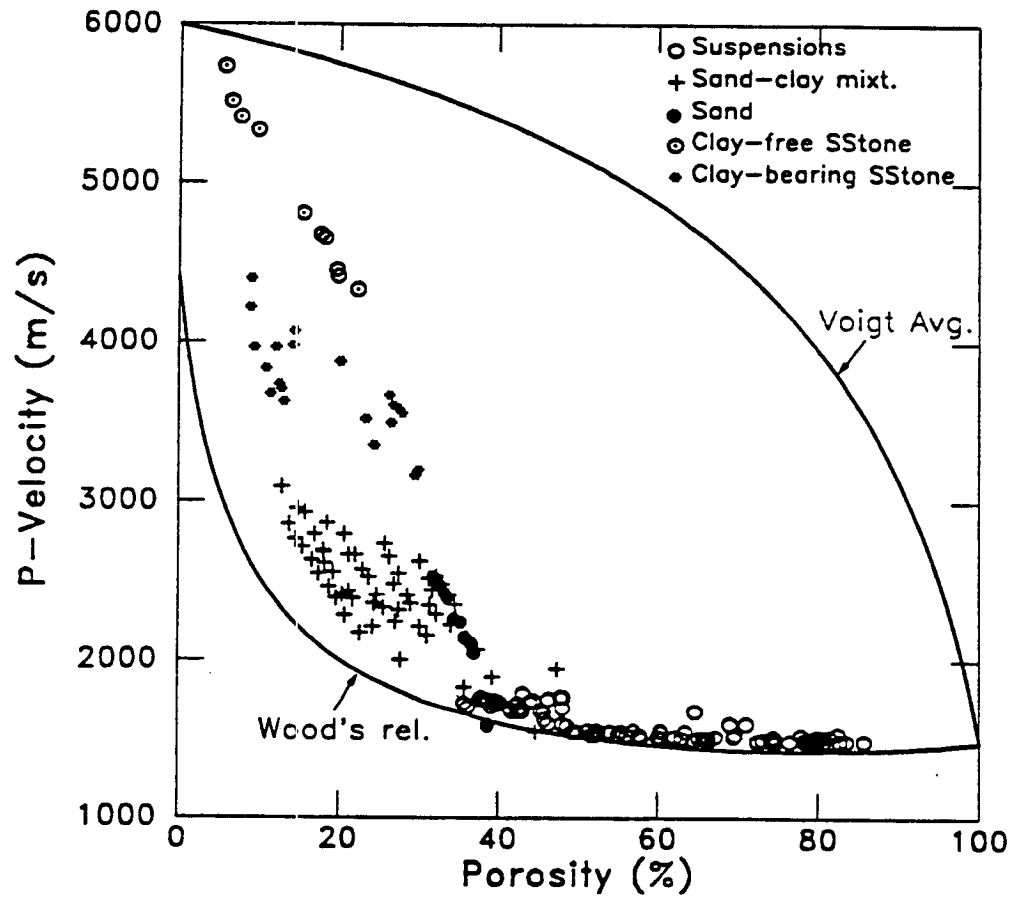


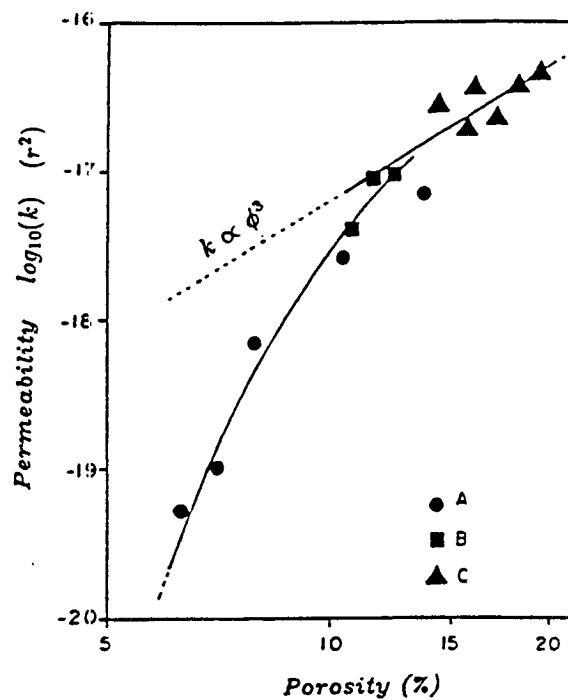
Fig.3.4 Experimental data of P wave velocity versus porosity of porous geomaterials. Clay-free and clay-bearing data from Hamilton (1956), Han et al. (1986), and Yin et al. (1988) were collected by Marion (1990). There is a distinctive change in P wave velocity before and after about 40% porosity (after Marion, 1990).

3.2 Concept of Critical Porosity

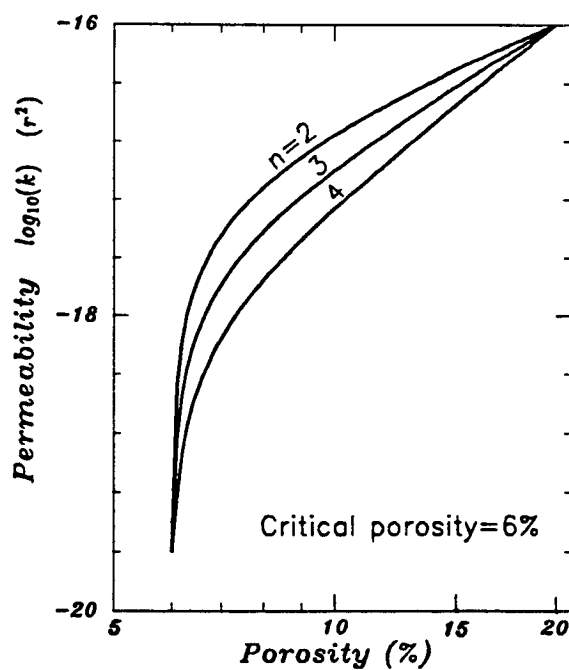
Above section shows the distinctive changes of physical properties of porous materials at some finite values of porosity. Such phenomena are similar to the critical phenomena related to phase transitions or transformations in heterogeneous materials (Dora et al., 1980; Stanley, 1987; Baker, 1990). These finite values of porosity are hereby defined as critical porosities which mean distinctive changes in pore material microstructures. As studied in later sections, critical porosity is closely related to other pore structure parameters such as pore size, geometry, and connectivity. The incorporation of critical porosity into effective property-porosity relations of porous materials will certainly be useful in both theory and practice.

The well-known percolation phenomenon is a good example of critical porosity. The critical porosity with respect to permeability is defined as the transition porosity between totally-isolated pores and at least a complete path of connected pores across the material. Such critical porosity can be determined experimentally by measuring the so-called “total porosity” and “effective porosity”. Some porous materials, such as lava, may have a high value of total porosity but a low effective porosity, resulting in considerable critical porosity. Fig.3.5a indicates that as porosity decreases to about 11%, the classic cubic power law of permeability-porosity relationship becomes insufficient to describe permeability data. By observation we infer that the critical porosity is about 6%. When the critical porosity is incorporated into the evaluation of permeability, as first proposed by Walder and Nur (1984), the theoretical result in Fig.3.5b can quantitatively describe the experimental permeability data.

When effective elastic moduli or wave velocities in a solid-fluid material system are concerned, critical porosity is defined as the transition porosity between solid-matrix and fluid-matrix supported subsystems. As a special case for dry porous materials, critical porosity is the maximum porosity at which the material collapses. Critical concentration is the generalization of critical porosity concept for general materials.



(a)



(b)

Fig.3.5 (a) The experimental data of permeability versus porosity for hot-pressing calcites, where r is the hydraulic radius (after Bernabe et al., 1982), (b) The theoretical result of permeability versus porosity in porous materials. 6% critical porosity and exponent $n = 2, 3, 4$ are used in the formula proposed by Walder and Nur (1984).

For example, when the third phase material is dispersed in the fluid, it is rigorous to use critical concentration to represent the transition between the subsystems, and then the critical porosity decreases with the increase of the third phase material. On the other hand, a porous material with very low porosity and flat pores may be taken as a cracked material. If infinitesimal-thin cracks are assumed for a cracked material, it is appropriate to define the critical concentration as the critical crack density, as implied in the study by O'Connell and Budiansky (1974, 1977).

To illustrate the concept of critical porosity with respect to effective elastic moduli, let us analyze the changes of material microstructures and effective properties of a solid-fluid material system in Fig.3.6. When the porosity or fluid volume fraction ϕ_2 is higher than the critical porosity ϕ_{cr} , the fluid phase becomes the matrix, and the solid grains become the isolated inclusions. Since the inviscid fluid only bears normal stress, no shear stress will be transmitted to those isolated solid inclusions. Thus the stress state of this fluid-matrix supported subsystem is in a uniform stress state. Consequently, the effective elastic modulus-porosity and (low frequency) wave velocity-porosity relations can be analytically described by the isostress material model (Reuss, 1929; Wood, 1941),

$$\frac{1}{K} = \frac{1 - \phi_2}{K_1} + \frac{\phi_2}{K_2}, \quad (3.1)$$

$$\mu = 0 \quad (3.2)$$

$$V_P^2 = \frac{\left(\frac{1-\phi_2}{K_1} + \frac{\phi_2}{K_2}\right)^{-1}}{\rho_1(1 - \phi_2) + \rho_2\phi_2}, \quad (3.3)$$

$$V_S = 0. \quad (3.4)$$

where K and μ are effective bulk and shear moduli, K_1 and ρ_1 are solid bulk modulus

and density, K_2 and ρ_2 are fluid bulk modulus and density, V_P and V_S are P and S wave velocities, respectively.

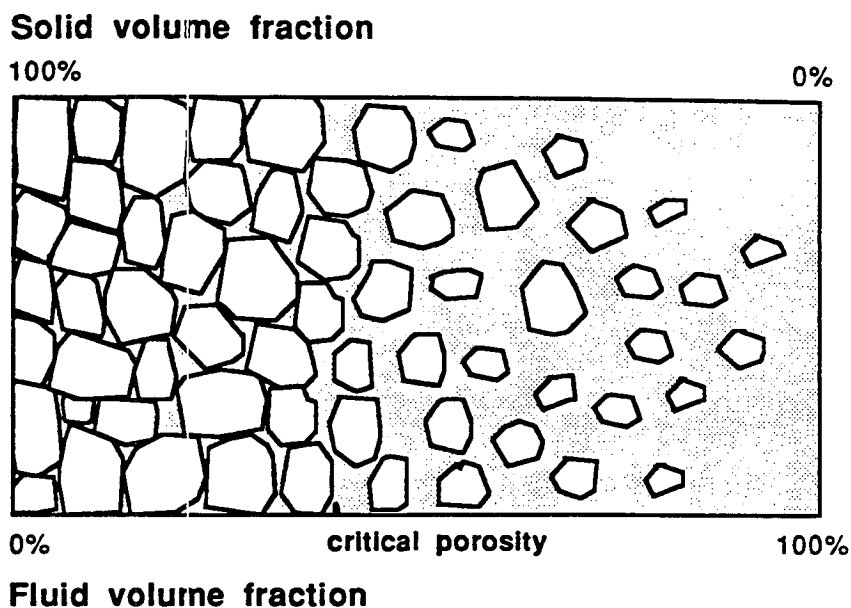


Fig.3.6 Schematic section of a solid-fluid material system, representing a system of porous rocks, sediments, and marine suspensions. The critical porosity is defined as the transition porosity between solid-matrix and fluid-matrix supported subsystems

In the solid-matrix supported subsystem such as porous rocks and sediments, the effective bulk modulus K and shear modulus μ decrease with porosity. In general, the complicated microstructures lead to the departure from the isostrain state or Voigt's model. At the critical porosity ϕ_{cr} , the solid matrix disappears and fluid matrix emerges. Thus K and μ at critical porosity should reduce to those in (3.1) and (3.2), respectively. As a special case for dry porous materials, both K and μ should reduce to zero at the critical porosity at which the material collapses.

Porous rocks and sediments have complicated microstructures that result from depositional, diagenetic, and tectonic processes (Cohen, 1987; Thompson et al., 1987; Krohn, 1988). Existing material models can only partially describe the changes of

microstructures and effective properties in the solid-matrix supported subsystem. For example, the inclusion material model originally developed for most composite materials, is only appropriate at low porosity range since no pore connectivity is taken into account. On the other hand, the model for a grain-packing or granular material is only applicable to narrow porosity ranges for sediments. To remedy the lacking of appropriate models for porous rocks and sediments, several empirical relations between velocity, porosity, and clay content have been proposed (Tosaya and Nur, 1982; Castagna et al., 1985; Han et al., 1986, Marion and Nur, 1991).

From above analysis it is clear that an appropriate model for porous rocks and sediments should meet the following conditions: (1) to describe the critical porosity effect on the variations of microstructural and effective properties; (2) to be consistent with Reuss' and Wood's models at $\phi_2 = \phi_{cr}$.

3.3 Critical Concentration Phase

The essential of a critical concentration model is to redefine the constituents of a material system, and to relax the conventional hypothesis that a porous material framework has nonzero stiffness until 100% porosity. Critical concentration phase is defined as the material state of whole system at critical porosity. Thus, at zero porosity, the material is a pure solid phase with ρ_1 , K_1 , and μ_1 ; at critical porosity, the material is a critical concentration phase. In order to be consistent with Reuss' model at critical porosity, the critical concentration phase is of following critical physical properties ρ_{cr} , K_{cr} , μ_{cr} , V_{Pcr} , and V_{Scr} :

$$\rho_{cr} = \rho_1(1 - \phi_{cr}) + \rho_2\phi_{cr}, \quad (3.5)$$

$$K_{cr} = \left(\frac{1 - \phi_{cr}}{K_1} + \frac{\phi_{cr}}{K_2} \right)^{-1}, \quad (3.6)$$

$$\mu_{cr} = 0, \quad (3.7)$$

$$V_{Pcr} = \left(\frac{K_{cr}}{\rho_{cr}}\right)^{1/2}, \quad (3.8)$$

$$V_{Scr} = 0. \quad (3.9)$$

From the effective density ρ we know that the critical concentration phase is a mixture of fluid and solid at critical porosity. From the effective elastic moduli we see that the critical concentration phase is in isostress state.

The critical concentration model possesses following functions for $0 \leq \phi_2 \leq \phi_{cr}$:

- A. The critical concentration phase with volume fraction (ϕ_2/ϕ_{cr}) serves as weakly load-bearing “composite inclusions”.
- B. The pure solid phase with volume fraction $(1 - \frac{\phi_2}{\phi_{cr}})$ serves as highly load-bearing material framework.
- C. Such material model has the so-called space-filling feature, that is, the framework has nonzero stiffness until the material is fully occupied by the critical concentration phase.

3.4 Microstructural Interpretation

According to the critical concentration model, The load-bearing capacities of solid grains in a porous material differ from one grain to another. Consequently, the contact areas and coordination numbers of solid grains are nonuniform throughout the material. For porous rocks and sediments, three kinds of pore formation processes may be responsible for such nonuniform microstructural features:

- (1) Depositional — The deposit of grains with different size, shape, and surface roughness.

(2) Diagenetic — Even the sediments are composed of regular packing of mono-size grains, the cementation, growth and dissolution of minerals, may lead to the nonuniformity of pore structures.

(3) Tectonic — Stress-induced cracks, dislocations, and gouges.

Are such nonuniform microstructures **fractal**? There have been many fractal analysis of pore structures of sedimentary rocks (Mandelbrot, 1983; Katz and Thompson, 1985; Krohn and Thompson, 1986; Thompson et al., 1987; Krohn, 1988; Nolte et al., 1989). In general, above pore formation processes lead to fractal pore structures. Thus it is very possible that some of the nonuniform microstructures are of fractal features.

These nonuniform microstructures may differ from one porous material to another, but the fundamental feature is that a portion of solid grains is highly load-bearing as framework, and the other portion in critical concentration phase is weakly load-bearing. One extreme case is the random packing of monosize grains. A portion of random-packing grains may be in random close packing, serving as the highly load-bearing framework, and the other portion may be in random loose packing, being in isostress state with fluid. Here we give one microstructural interpretation of the critical concentration model as in Fig.3.7. At a certain porosity, some bigger grains often serve as framework, other grains and fluid of critical concentration phase, are embedded as composite inclusions. The contact areas and coordination numbers of solid grains are thus of nonuniform feature. Such interpretation is very close to the sandstone microstructures often observed from thin sections and scanning electron microscopic images (Wilkins et al., 1986; Bourbié et al., 1987; Doyen, 1988; Burns et al., 1990), as in Fig.3.8.

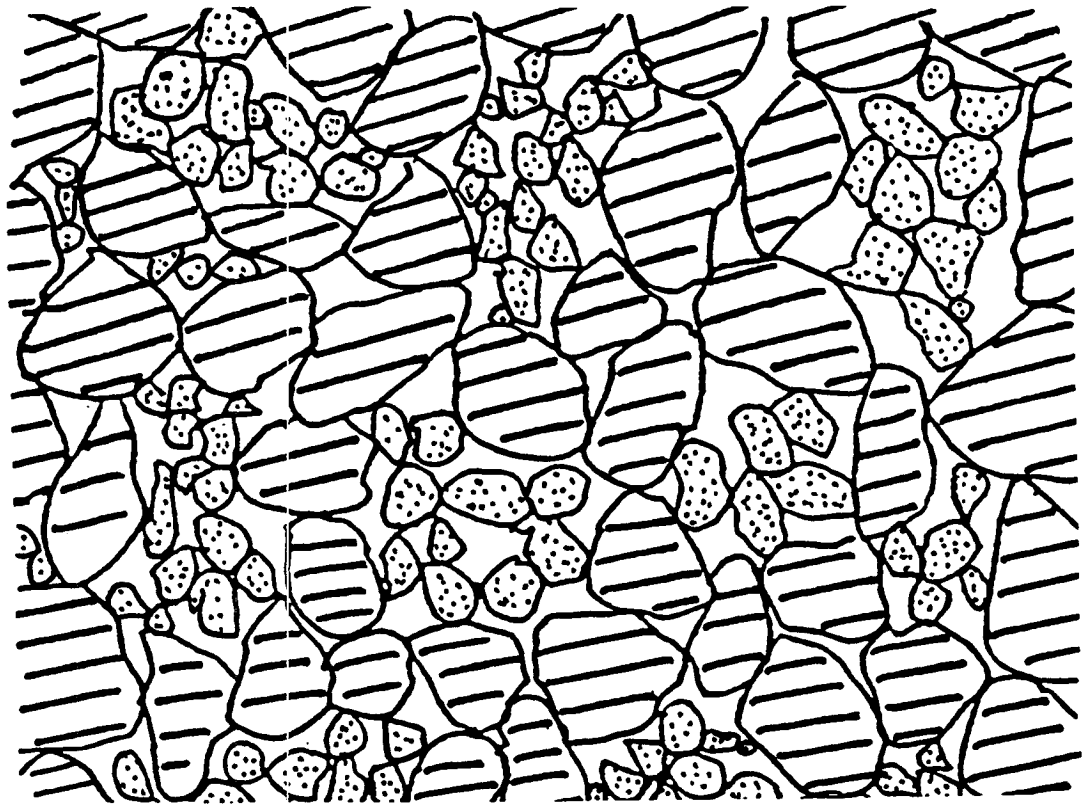
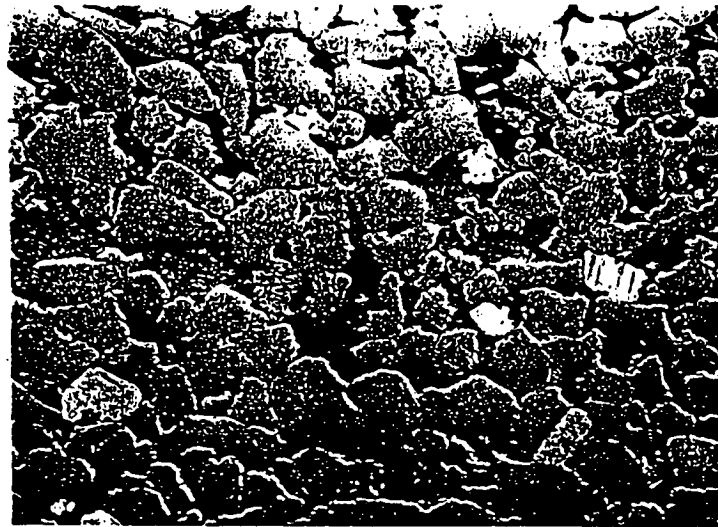
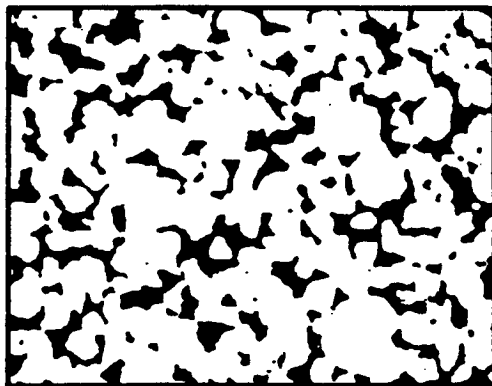


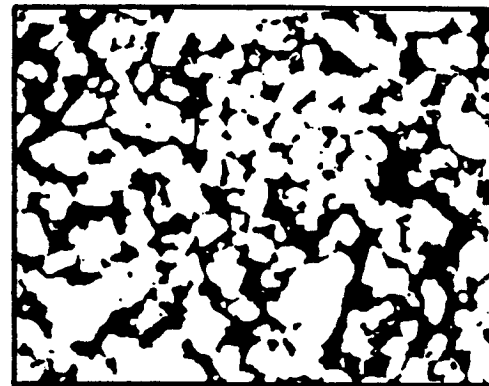
Fig.3.7 One microstructural interpretation of the critical concentration model. Some bigger solid grains serve as the highly load-bearing framework, and other grains with fluid are embedded as composite inclusions. The contact areas and coordination numbers of solid grains thus differ from one grain to another.



(a)



$$\phi_2 = 15.2\%$$



$$\phi_2 = 22.1\%$$

(b)

Fig.3.8 (a) Scanning electron microscopic image of sandstone microstructures. The black areas are the pore spaces (after Wilkens et al., 1986). (b) Microsections of Fontainebleau sandstone microstructures. The black areas are the pore spaces which become more connected to each other with the increase of porosity (after Doyen, 1988).

3.5 Determination of Critical Porosity

There are several ways to determine the critical porosities of porous materials with respect to effective elastic moduli and wave velocities.

3.5.1 Experimental approach

The direct approach is to conduct experiments to observe and measure how the effective properties change with porosity. The experimental data in Fig.3.1, Fig.3.3 and Fig.3.4 indicate about 40% ~ 50% critical porosity. For marine sediments, many borehole logging and laboratory experiments show that the critical porosity is about 70% ~ 80% in such unconsolidated materials (Hamilton and Bachman, 1982; Taylor and Leonard, 1990; Wilkens et al., 1990). Fig.3.9 presents the sound velocity-porosity relationship of marine sediments obtained by Hamilton and Bachman (1982), which clearly indicates about 80% critical porosity.

3.5.2 Geometrical approach

Let us first consider the regular packings of monosize inclusions. On the one hand, those inclusions are assumed as spherical pores or fluid inclusions. When porosity is approaching the critical porosity, they merge and connect to each other as the material matrix. As a result, the critical porosity changes with regular packing style, ranging from 52.36% to 74.05%. On the other hand, when spherical grains are considered, we obtain another set of critical porosities for flat and irregular pores, ranging from 25.95% to 47.64% (Fig.3.10). Similarly, when random packings of monosize inclusions are considered, random close and loose packings yield 36% ~ 40% critical porosity for the spherical grain model, and 60% ~ 64% critical porosity for the spherical pore model (Fig.3.11). In general, pore geometries of porous materials with either regular or random packing styles, may vary between these spherical pore and grain models, and so the critical porosities change between these two sets of critical

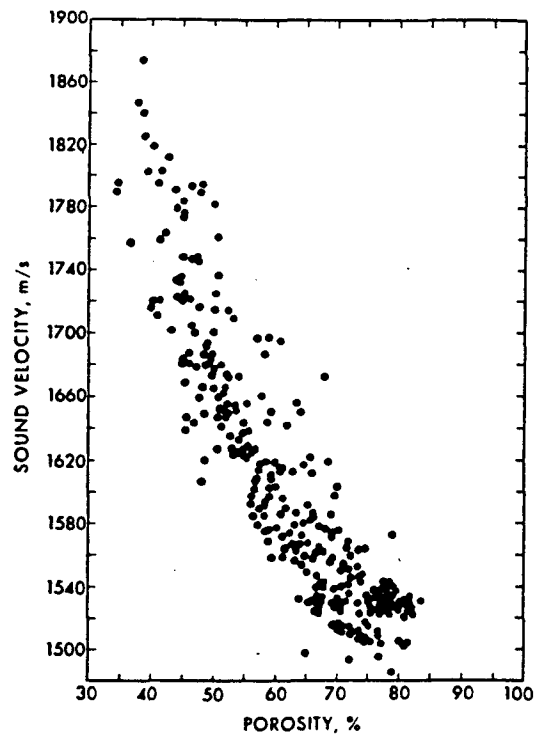


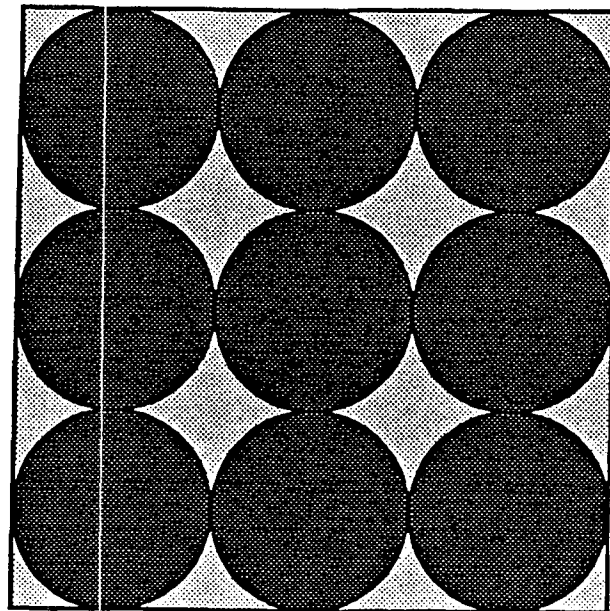
Fig.3.9 Porosity versus sound velocity in marine sediments. As porosity increases to 70% ~ 80%, the sound velocity drops to 1500 m/s for suspensions (after Hamilton and Bachman, 1982).

porosities, ranging from 74.05% to 25.95%. Furthermore, when the packing of grains with different sizes is considered, the critical porosity may range from 80% to 20% between spherical pore and grain models.

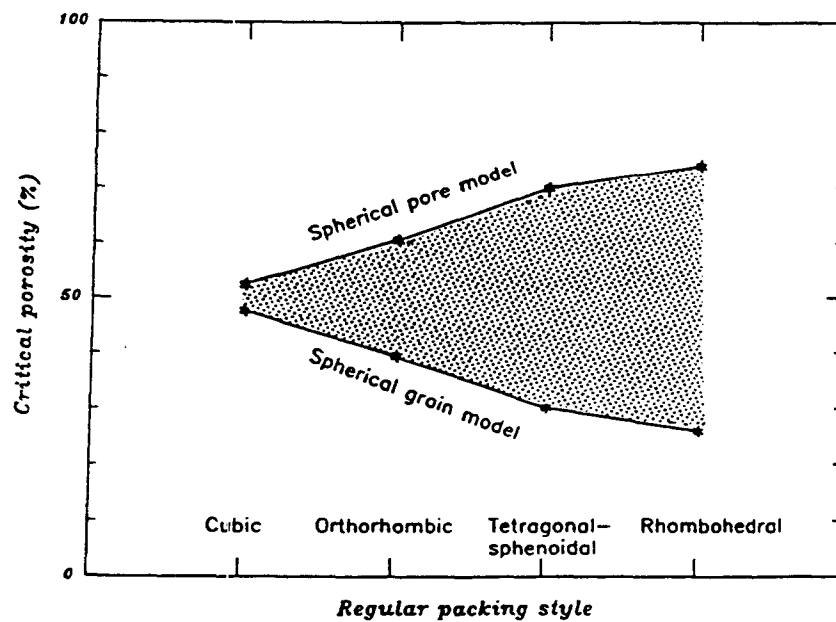
3.5.3 Theoretical approach

By examining all existing methods, only the asymmetric self-consistent method (ASCM) can describe the critical porosity as defined above for dry and inviscid fluid-saturated porous materials. The symmetric self-consistent method (SSCM) developed by Kroner (1958) and Berryman (1980) treats constituent phases symmetrically, that is, same geometry for each phase, and no distinction of matrix or inclusion phase. As a result, there should be no transition between solid and fluid matrix-supported domains, and so no critical porosity.

There is a detailed presentation of ASCM in chapter 5. Here we show ASCM so-

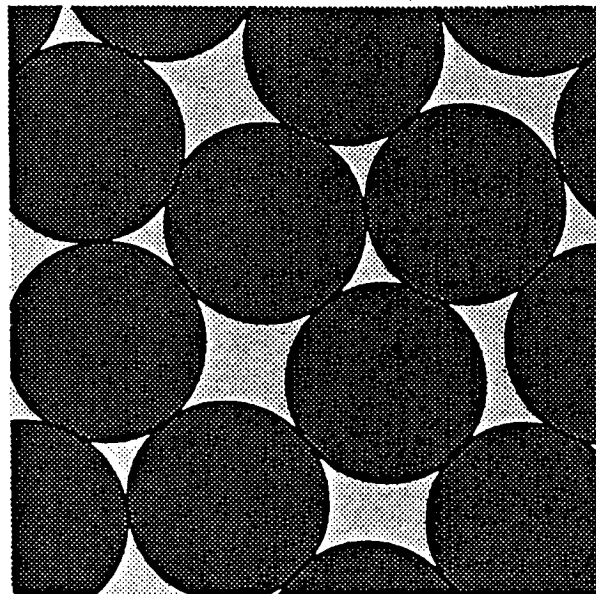


(a)

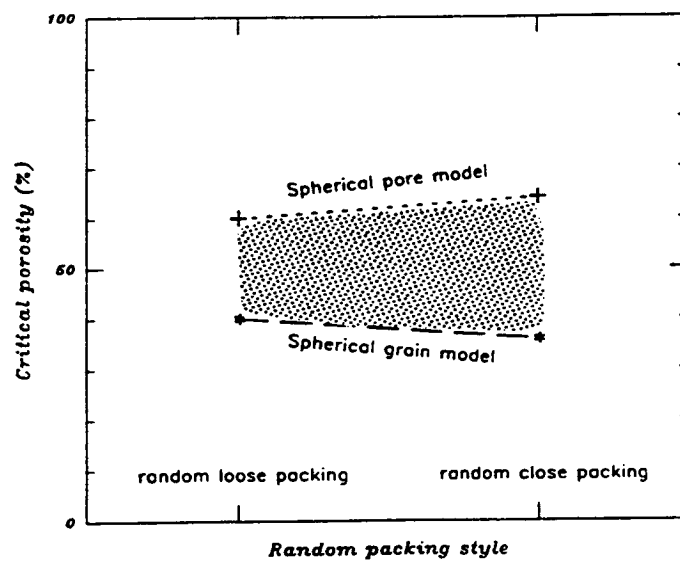


(b)

Fig.3.10 (a) A two-dimensional section of cubic packing of monosize inclusions, (b) Critical porosity ranges predicted by the regular packing of monosize inclusion with different packing styles.



(a)



(b)

Fig.3.11 (a) A two-dimensional section of random packing of monosize inclusions, (b) Critical porosity ranges predicted by the random loose and close packings of monosize inclusions.

lution to effective bulk and shear moduli for spherical, cylindrical, and penny-shaped inclusions (Fig.3.12). For water-saturated porous materials, the critical porosity is about 60% for spherical pores, 55% for cylindrical pores, and 30% ~ 40% when 10^{-1} aspect ratio is considered. These values of critical porosity are within the ranges predicted by the geometrical approach.

3.5.4 Comparison between data and model result

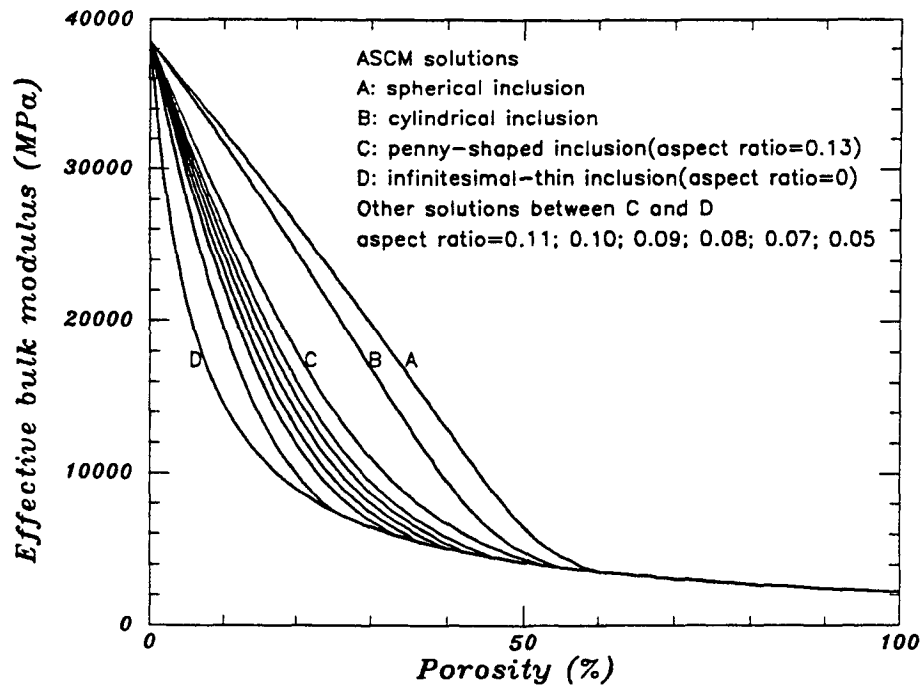
There are a lot of published experimental results indicating the critical porosity of porous materials. Fig.3.1, 3.3, 3.4, and 3.9 are only a few of them. Here we select some more to compare with above model results.

Fig.3.13a shows that, when a thin elastic plate is punched randomly with circular pores and loaded at the ends, the critical porosity for effective modulus is between 50% ~ 60% (Benguigui, 1984). Fig.3.13b shows the dynamic bulk and shear moduli versus porosity for dry sandstones (Gregory, 1963), and the critical porosity is about 45%.

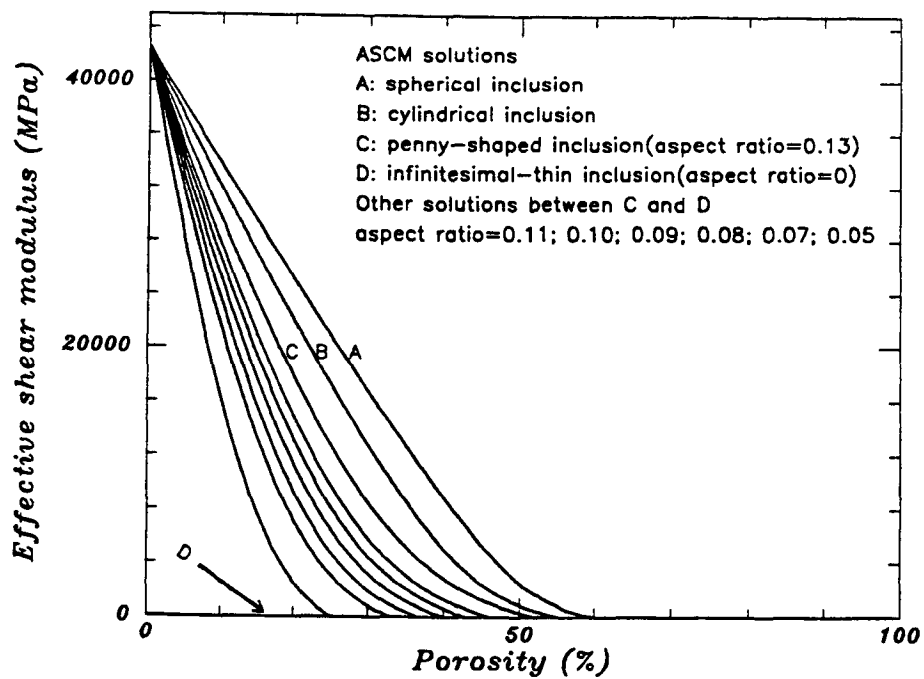
Marion (1988, 1990) conducted experiments with random packing of spherical grains to observe the changes of P wave velocity, pressure, and electric conductivity. At 39% critical porosity, the P-velocity, as well as conductivity and pressure, changes distinctively from previous levels.

Fig.3.14 presents data of wave velocity versus porosity in dry rocks. For dry carbonates, the ultrasonic wave velocities approach zero at about 30% critical porosity (Geertsma, 1961). Another set of data obtained by Wyllie et al. (1961) indicate about 75% critical porosity. The time-average equation can not explain such feature.

In summary, various experimental data indicate a wide range of critical porosity, from 25% ~ 75%, which is generally consistent with above model results.



(a)



(b)

Fig.3.12 ASCM solutions to effective elastic moduli versus porosity. The critical porosity decreases when the pore shape departs from the spherical shape. (a) effective bulk modulus versus porosity, (b) effective shear modulus versus porosity.

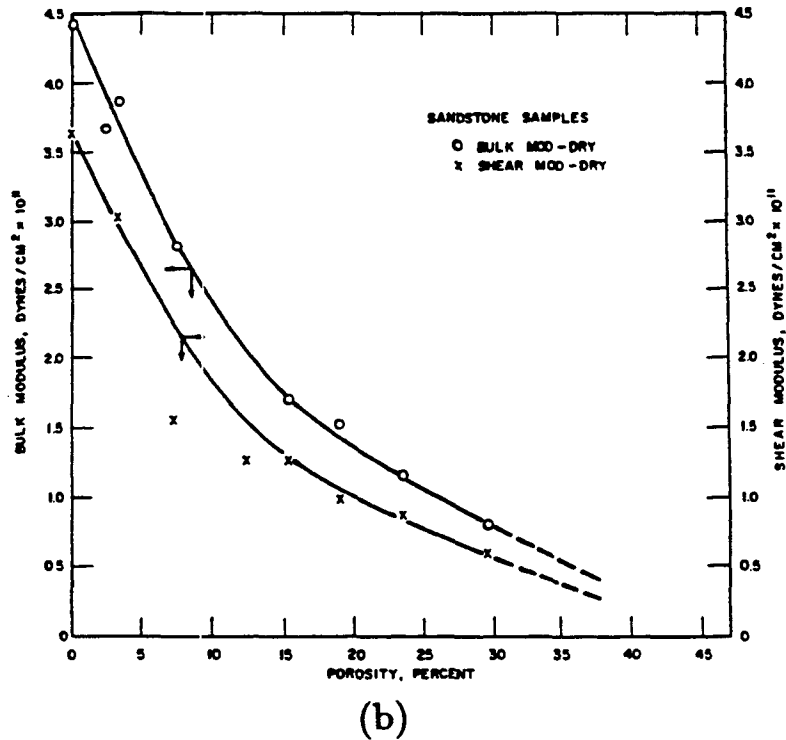
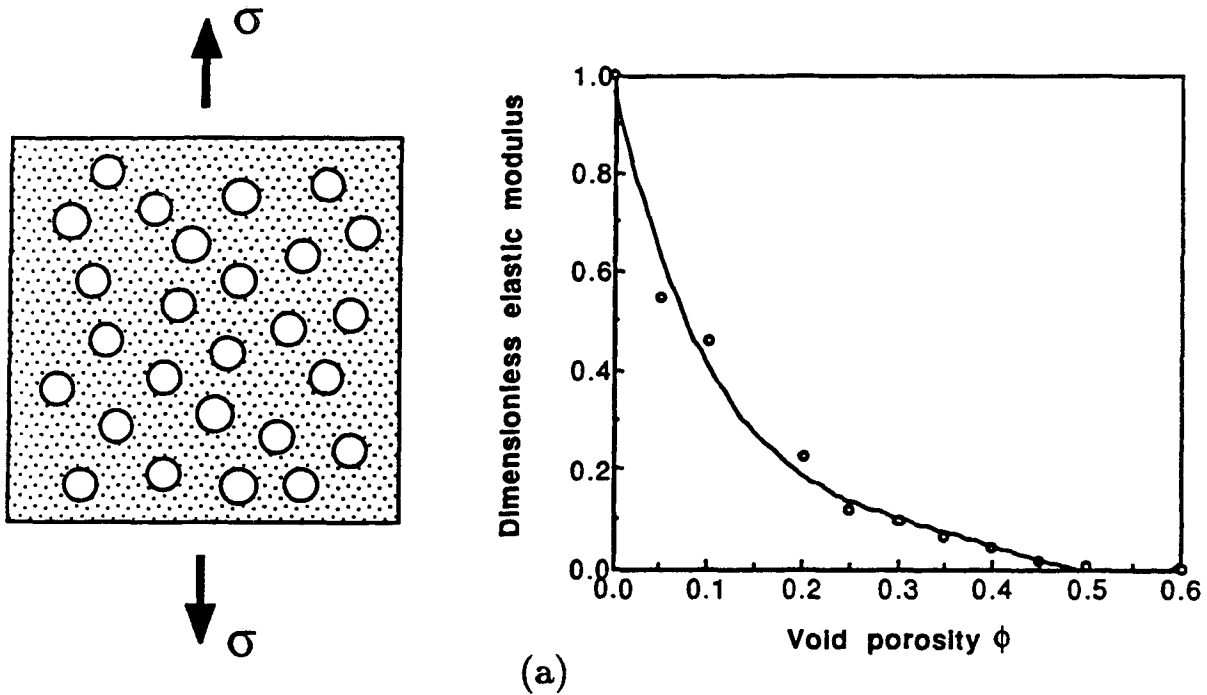
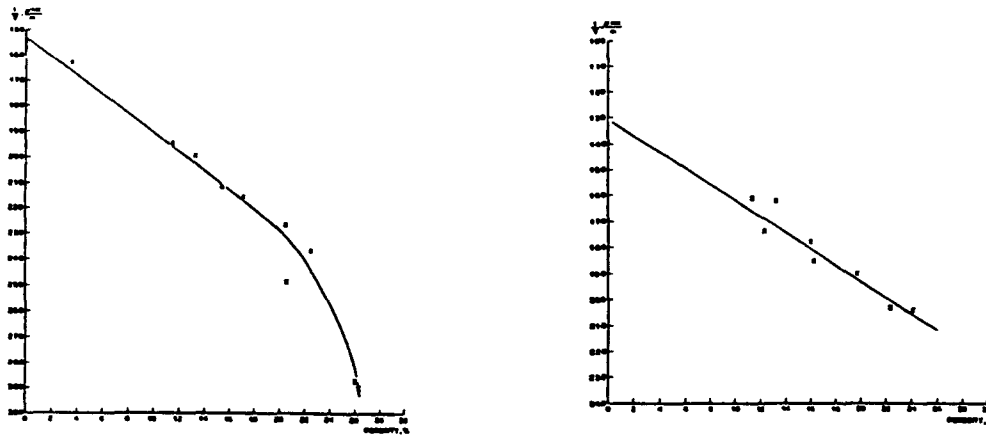
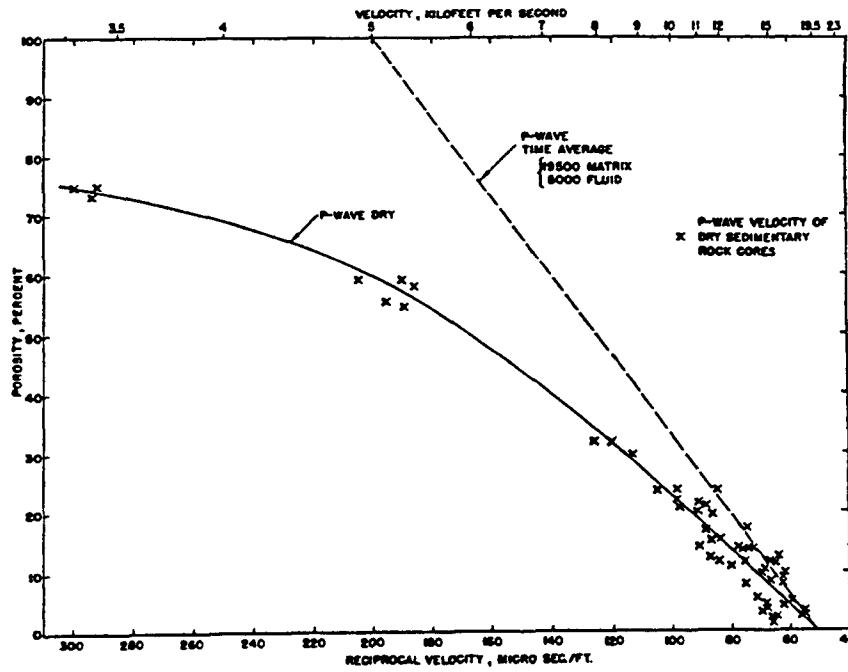


Fig.3.13 Experimental data of effective elastic moduli versus porosity. (a) For a thin elastic plate punched with circular pores, the critical porosity is between 50% ~ 60% (after Benguigui, 1984). (b) For dry sandstones, the critical porosity is about 45%. (after Gregory, 1963).



(a)



(b)

Fig.3.14 Experimental data of wave velocity versus porosity in dry rocks. (a) For dry carbonates, the critical porosity is about 30% (after Geertsma, 1961). (b) For sedimentary rocks, the critical porosity is about 75% (after Wyllie et al., 1961).

3.6 Conclusions

Critical porosity is an important parameter to describe the variations of porous material microstructural and effective properties.

The critical concentration model describes the nonuniform load-bearing capacities of solid grains. The microstructural interpretation of critical concentration model is characterized by nonuniform contact areas and coordination numbers of solid grains throughout the porous material.

The critical porosities of sedimentary rocks and sediments determined by geometrical, theoretical, and experimental approaches are consistent, and are of wide ranges due to the diverse pore size, geometry, and connectivity.

References

- Baker, G. A., 1990, Quantitative theory of critical phenomena, Boston, Academic Press, pp.366.
- Banavar, J. R., Koplik, J., and K. W. Winkler, 1986, Physics and chemistry of porous media II, American Institute of Physics, AIP Conference Proceedings **154**, pp.318.
- Benguigui, L., 1984, Experimental study of the elastic properties of a percolating system, Physical Review Letters, **53**, 2028-2030.
- Bernabe, Y., W. F. Brace, and B. Evans, 1982, Permeability, porosity and pore geometry of hot-pressed calcite, Mech. Materials, **1**, 173-183.
- Berryman, J. G., 1980, Long-wavelength propagation in composite elastic media. I. Spherical Inclusions, J. Acoust. Soc., **68**, 1809-1819; and II. Ellipsoidal inclusions, J. Acoust. Soc., **68**, 1820-1831.
- Bourbié, T., Coussy, O., and B. Zinszner, 1987, Acoustics of porous media, Gulf Publishing Company, Houston, London, Paris, Tokyo, pp.334.
- Burns, D. R., C. H. Cheng, and R. H. Wilkens, 1990, Sandstone pore aspect ratio spectra from direct observations and velocity inversion, Int. J. Rock Mech. Min. Soc. & Geomech. Abstr., **27**, 316-323.
- Burns, R. E. et al., 1973, Initial report of the deep sea drilling project, **21**, Washington(U.S. government printing office), 495-507.
- Castagna, J. P., Batzle, M. L., and R. L. Eastwood, 1985, Relationships between compressional wave and shear wave velocities in clastic silicate rocks, Geophysics, **50**, 571-581.
- Chelidze, T. L., 1979, Percolation model of electric conductivity of minerals, Ivest. Akad. Nauk SSSR, Fizika Zemli, **11**, 97-99.
- Chelidze, T. L., Gueguen, V., Darot, M., and T. Roehle, 1988, On the elastic properties of depleted refilled solids near percolation, J. Phys., **C21**, L1007-L1010.
- Chelidze, T. L., Spetzler, H., Getting, I. C., and Z. A. Avaliani, 1990, Experimental investigation of the elastic modulus of a fractal system-a model of fractured rocks, PAGEOPH, **134**, 31-43.
- Cohen, M. H., 1987, The morphology of porous sedimentary rocks, in Physics and Chemistry of Porous Media II, edited by J. R. Banavar, J. Koplik, and K. W. Winkler, 3-16, American Institute of Physics, New York.

- Dora, J. D., Demongeot, J., and B. Lacolle, 1980, Numerical methods in the study of critical phenomena, Berlin, Heidelberg, New York, Springer-Verlag, pp.267.
- Doyen, P. M., 1988, Permeability, conductivity, and pore geometry of sandstones, *J. Geophys. Res.*, **93**, 7729-7740.
- Dullien, F. A. L., 1979, Porous media: fluid transport and pore structure, Academic Press, New York, London, Toronto, Sydney, San Francisco, pp.396.
- Dunn, D. E., La Fountain, L. J., and R. E. Jackson, 1973, Porosity dependence and mechanism of brittle fracture in sandstones, *J. Geophys. Res.*, **78**, 2403-2417.
- Geertsma, J., 1961, Velocity-log interpretation: the effect of rock bulk compressibility, *SPE Jour.*, **1**, 235-248.
- Gregory, A. R., 1963, Shear wave velocity measurements of sedimentary rock samples under compression, in Fairhurst, C. (eds.) *Rock Mechanics*, 439-472, Pergamon Press, New York.
- Hamilton, E. L., 1956, Low sound velocities in high porosity sediments, *J. Acoust. Soc. Am.*, **28**, 16-19.
- Hamilton, E. L. and R. T. Bachman, 1982, Sound velocity and related properties of marine sediments, *J. Acoust. Soc. Am.*, **72**, 1891-1904.
- Han, D. H., Nur, A., and D. Morgan, 1986, Effects of porosity and clay content on wave velocities in sandstones: *Geophysics*, **51**, 2093-2107.
- Hoshino, K., 1981, Consolidation and strength of the soft sedimentary rocks, *Proc. Int. Symp. Weak Rock*, edited by Akai, K., Hayashi, M., and Y. Nishimatsu, **1**, 155-160.
- Jizba, D., 1991, Mechanical and acoustical properties of sandstones and shales, PhD dissertation, Stanford University, California.
- Johnson, D. L. and P. N. Sen, 1984, Physics and chemistry of porous media, *American Institute of Physics, AIP Conference Proceedings* **107**, 78-88.
- Katz, A. J. and A. H. Thompson, 1985, Fractal sandstone pores: implications for conductivity and pore formation, *Phys. Rev. Lett.*, **54**, 12, 1325-1328.
- Kendall, K., 1984, Connection between structure and strength of porous solids, in *Physics and Chemistry of Porous Media*, edited by Johnson, D. L. and P. N. Sen, *American Institute of Physics, AIP Conference Proceedings* **107**, 78-88.

- Kirkpatrick, S., 1973, Percolation and conduction, *Review of Modern Phys.*, **45**, 574-588.
- Krohn, C. E., 1988, Fractal measurements of sandstones, shales, and carbonates, *J. Geophys. Res.*, **93**, B4, 3297-3305.
- Krohn, C. E. and A. H. Thompson, 1986. Fractal sandstone pores: automated measurements using scanning-electron-microscope images, *Phys. Rev., Sec. B*, **33**, 6366-6374.
- Kroner, E., 1958, Berechnung der elastischen Konstanten des Vielkristalls aus den Konstanten der Einkristalls, *Zeitschrift Physik*, **151**, 504-518.
- Mandelbrot, B. B., 1983, *The Fractal Geometry of Nature*, W. H. Freeman, San Francisco, pp.468.
- Marion, D., 1988, Sensitivity of compressional waves to the transition from a suspension to compacted sediments, *Stanford Rock & Borehole Project*, **33**, 317-338.
- Marion, D., 1990, Acoustic, mechanical, and transport properties of sediments and granular materials, PhD dissertation, SRB, **39**, Stanford University.
- Marion, D. and A. Nur, 1991, Pore-filling material and its effect on velocity in rocks, *Geophysics*, **56**, 225-230.
- Nobes, D. C., 1989, A test of a simple model of the acoustic velocity in marine sediments, *J. Acoust. Soc. Am.*, **86**, 290-294.
- Nolte, D. D., Pyrak-Nolte, L. J., and N. G. W. Cook, 1989, The fractal geometry of flow paths in natural fractures in rocks and the approach to percolation, *PA-GEOPH*, **131**, 111-138.
- O'Connell, R. J. and B. Budiansky, 1974, Seismic velocities in dry and saturated cracked solids, *J. Geophys. Res.*, **79**, 5412-5426.
- O'Connell, R. J. and B. Budiansky, 1977, Viscoelastic properties of fluid-saturated cracked solids, *J. Geophys. Res.*, **82**, 5719-5735.
- Pereira, C. J., Rice, R. W., and J. P. Skalny, Pore structure and its relationship to properties of materials, in *Pore Structure and Permeability of Cementitious Materials*, edited by Roberts, L. R. and J. P. Skalny, Materials Research Society Symposium Proceedings **137**, 3-21.
- Pratt, P. L., 1987, Relationships between microstructure and engineering properties,

- in Microstructural Development During Hydration of Cement, Materials Research Society Symposium Proceedings **85**, edited by Struble, L. J. and P. W. Brown, 145-155.
- Raymer, L. L., Junt, E. R., and J. S. Gardner, 1980, An improved sonic transit time-to-porosity transform, SPWLA, 21st Ann. Logg. Symp., Paper P.
- Reuss, A., 1929, Berechnung der Fließgrenze von Mischkristallen auf Grund der Plastizitätsbedingung für Einkristalle, *Z. Angew. Math. Mech.*, **9**, 49-58.
- Roberts, L. R. and I. P. Skalny, 1989, Pore structure and permeability of cementitious materials, Materials Research Society, Symposium Proceedings **137**, pp.467.
- Rzhevsky, V. and G. Novik, 1971, *The Physics of Rocks*, Moscow, MIR Publishers, pp.320.
- Schiller, K. K., 1958, Porosity and strength of brittle solids (with particular reference to gypsum), *Proc. Conf. Mech. Prop. Non-metallic Brittle Materials*, London, 35-45.
- Shah, S. P., 1991, Toughening mechanisms in quasi-brittle materials, NATO ASI Series, Series E: Applied Sciences **195**, pp.612.
- Stanley, H. E., 1987, *Introduction to phase transitions and critical phenomena*, New York, Oxford University Press, pp.308.
- Taylor, E. and J. Leonard, 1990, Sediment consolidation and permeability at the Barbados Forearc, in *Proc. Ocean Drilling Program, Sci. Results*, **110**, edited by Moore, J. C., Mascle, A., et al., 289-308.
- Teisseyre, R., 1983, Premonitory mechanism and resistivity variations related to earthquake, *PAGEOPH*, **121**, 297-315.
- Thompson, A. H., Katz, A. J., and C. E. Krohn, 1987, The microgeometry and transport properties of sedimentary rocks, *Advance in Physics*, **36**, 5, 625-694.
- Tosaya, C. and A. Nur, 1982, Effects of diagenesis and clays on compressional velocities in rocks, *Geophys. Res. Lett.*, **9**, 5-8.
- Walder, J. and A. Nur, 1984, Porosity reduction and crustal pore pressure development, *J. Geophys. Res.*, **89**, B13, 11,539-11,548.
- Watt, J. P., G. F. Davies, and R. J. O'Connell, 1976, The elastic properties of composite materials, *Review of Geophysics and Space Physics*, **14**, 541-563.

- Wilkins, R. H., G. Simmons, T. M. Wisler, and L. Caruso, 1986, The physical properties of a set of sandstones - Part III, the effects of fine-grained pore-filling material on compressional wave velocity, *Int. J. Rock Mech. Min. Sci. & Geomech. Abstr.*, **23**, 313-325.
- Wilkins, R., et al., Diagenesis and dewatering of clay-rich sediments, Barbados Accretionary Prism, in *Proc. Ocean Drilling Program, Sci. Results*, **110**, edited by Moore, J. C., Masle, A., et al., 309-320.
- Wood, A. B., 1941, *A Textbook of Sound*, Macmillan, New York, pp.519.
- Wyllie, M. R. J., Gregory, A. R., and L. W. Gardner, 1956, Elastic wave velocities in heterogeneous and porous media, *Geophysics*, **21**, 41-70.
- Wyllie, M. R. J., Gardner, L. W., and A. R. Gregory, 1961, Some phenomena pertinent to velocity logging, *J. Petr. Phys.*, **13**, 629-636.
- Yin, H., Han, D., and A. Nur, 1988, Study of velocity and compaction on sand-clay mixtures, *SRB*, **33**, 265-302.

Chapter 4

Substitution Method and Critical Concentration Solutions

Abstract

In order to evaluate the effective properties predicted by the critical concentration model of porous materials, a substitution method is proposed to develop critical concentration solutions which are based on existing analytical and empirical formulas of conventional porous material models. The critical concentration solutions extended from Wyllie's, Voigt's, and Hashin-Shtrikman's relations give better description of experimental data of wave velocities in rocks and sediments such as clean sandstones, and are compared with Nobes' and Raymer's relations. The critical concentration model is then generalized to take into account the effects of pore-filling and dispersed clays on effective properties of porous materials. The resulting critical concentration solutions are in good agreement with available experimental data of clay-bearing effective elastic moduli and wave velocities, and provide insights into several empirical relations between velocity, porosity, and clay content.

4.1 Substitution Method

The critical porosity of porous materials in cases of effective property-porosity relations can be of considerable fundamental importance both in theory and practice, and may prove to be the rule rather than exception. In fact, conventional porous material models such as nondilute concentration models in chapter 2, can be taken as critical concentration models of porous materials with 100% critical porosity. Consequently, the effective properties predicted by the critical concentration model of porous materials should reduce to those predicted by conventional porous material models when 100% critical porosity is considered. In order to find the critical concentration solutions which meet with above basic requirement, we propose a substitution method to extend existing analytical and empirical formulas of conventional porous material models to general porous materials with critical porosities (Table 4.1).

Table 4.1 Substitution method to derive critical concentration solutions

Material Model	Conventional Model	Critical Concentration Model
Space-filling	Yes	Yes
Porosity range	$\phi_2: 0\% \sim 100\%$	$\phi_2: 0\% \sim \phi_{cr}$
Matrix Phase	$(1 - \phi_2), \rho_1, K_1, \mu_1, V_{P1}, V_{S1}$	$(1 - \phi_2/\phi_{cr}), \rho_1, K_1, \mu_1, V_{P1}, V_{S1}$
Nonmatrix Phase	Inclusion Phase $\phi_2, \rho_2, K_2, \mu_2, V_{P2}, V_{S2}$	Critical Concentration Phase $\phi_2/\phi_{cr}, \rho_{cr}, K_{cr}, \mu_{cr}, V_{Pcr}, V_{Scr}$
Solutions to moduli and velocities	Nondilute solutions, Time-average equation, etc.	Critical concentration solutions by substituting matrix and nonmatrix phases

There are physical or mechanical assumptions behind each of the analytical and empirical formulas of conventional porous material models. These assumptions, such as time average assumption in Wyllie's relation, are adopted in the critical concentration model with respect to the solid matrix phase and critical concentration phase.

In principle, the substitution method is implemented by (a) substituting $(1 - \frac{\phi_2}{\phi_{cr}})$ instead of $(1 - \phi_2)$ for matrix phase, and (b) replacing *inclusion phase* by *critical concentration phase*.

4.2 Critical Concentration Solutions

4.2.1 Extension from Wyllie's relation

Wyllie et al. (1956) proposed the time-average equation to estimate P wave velocity-porosity relations of fluid-saturated porous rocks,

$$\frac{1}{V_P} = \frac{1 - \phi_2}{V_1} + \frac{\phi_2}{V_2}, \quad (4.1)$$

where V_1 and V_2 , respectively, are P wave velocity in the solid matrix and pore fluid. No information of porous material microstructures is specified in the time-average equation. Many studies indicate that for unconsolidated or poorly-consolidated materials, the time-average equation may be appropriate up to 30% porosity, but overestimates considerably the velocity in high porosity domains.

When this time average assumption is applied to the critical concentration model, the fluid phase is now replaced by the critical concentration phase with volume fraction ϕ_2/ϕ_{cr} and P wave velocity V_{Pcr} , and the matrix phase has volume fraction $(1 - \phi_2/\phi_{cr})$. Therefore we obtain the critical concentration solution as

$$\frac{1}{V_P} = \frac{1 - \frac{\phi_2}{\phi_{cr}}}{V_1} + \frac{\frac{\phi_2}{\phi_{cr}}}{V_{Pcr}}, \quad \text{for } 0 \leq \phi_2 \leq \phi_{cr} \quad (4.2)$$

$$\frac{1}{V_P} = \left[\frac{\rho_1(1 - \phi_2) + \rho_2\phi_2}{\left(\frac{1-\phi_2}{K_1} + \frac{\phi_2}{K_2}\right)^{-1}} \right]^{1/2}, \quad \text{for } \phi_{cr} \leq \phi_2 \leq 1 \quad (4.3)$$

Obviously, above solution is always between the results of time-average equation (with $\phi_{cr} = 100\%$) and Wood's equation (with $\phi_{cr} = 0\%$). Since the critical porosity ϕ_{cr} is closely related to the pore size, geometry, and connectivity of porous materials, such critical concentration solution provides a better relationship between velocity and porous material microstructure, and will be useful in acoustic logging analysis of marine sediments.

Given the critical porosity ranging from 30% to 60%, the critical concentration solution yields lower P wave velocity as in Fig.4.1. $K_1 = 38500\text{MPa}$, $\mu_1 = 42500\text{MPa}$, $\rho_1 = 2650\text{kg/m}^3$, and $\rho_2 = 1000\text{kg/m}^3$ are used in the calculation. The time-average equation, in fact, can be reduced from the critical concentration solution with 100% critical porosity.

4.2.2 Extension from Voigt's relation

Voigt's bounds K_V and μ_V are derived from the so-called isostrain assumption (Voigt, 1928). With the critical concentration model, the isostrain state means that both the critical concentration phase and solid matrix phase are in the same strain state. To reach such an isostrain state, the critical concentration phase is required in parallel to boundary loading. This, of course, is just an approximation of porous material microstructures. Since the strain state in heterogeneous materials such as fluid-saturated porous materials is always more or less departed from the isostrain state, it is appropriate to take the critical concentration solution extended from Voigt's relation as the upper bounds for the effective elastic moduli of porous materials with critical porosity. This is consistent with the meaning of Voigt's bounds since they can be reduced from the solution with 100% critical porosity.

The critical concentration solution is

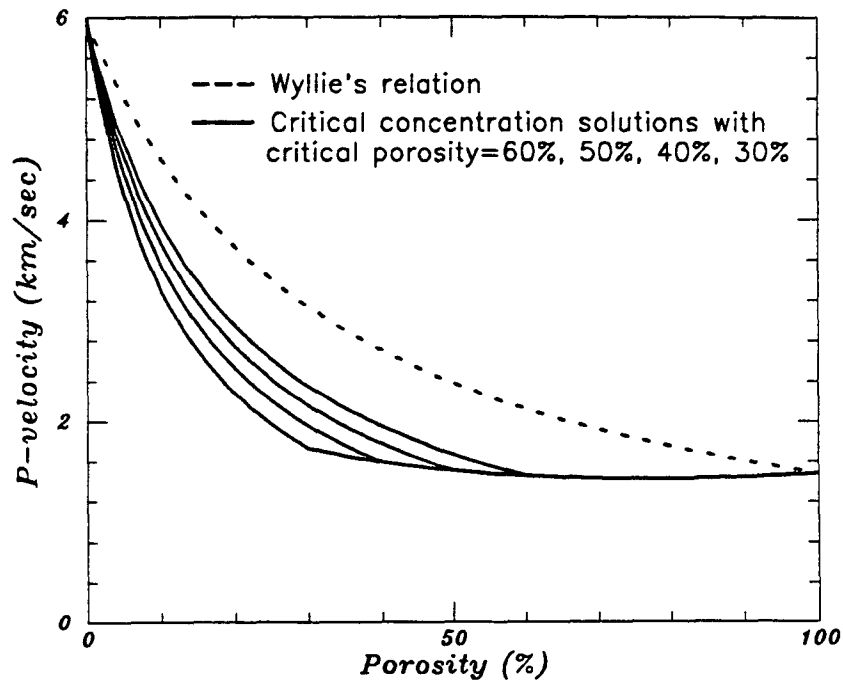


Fig.4.1 P wave velocity-porosity relations predicted by the critical concentration solution in (4.2) and (4.3) with critical porosity ranging from 30% to 60%. The time average equation can be reduced from the solution with 100% critical porosity.

$$K = \left(1 - \frac{\phi_2}{\phi_{cr}}\right)K_1, \quad \mu = \left(1 - \frac{\phi_2}{\phi_{cr}}\right)\mu_1, \quad 0 \leq \phi_2 \leq \phi_{cr}, \quad (4.4)$$

for dry porous materials, and

$$K = \left(1 - \frac{\phi_2}{\phi_{cr}}\right)K_1 + \frac{\phi_2}{\phi_{cr}}K_{cr}, \quad \mu = \left(1 - \frac{\phi_2}{\phi_{cr}}\right)\mu_1, \quad 0 \leq \phi_2 \leq \phi_{cr}, \quad (4.5)$$

$$K = \left(\frac{1 - \phi_2}{K_1} + \frac{\phi_2}{K_2}\right)^{-1}, \quad \mu = 0, \quad \phi_{cr} \leq \phi_2 \leq 1, \quad (4.6)$$

for inviscid fluid-saturated porous materials. The corresponding wave velocities are

$$V_P = \left[\frac{K + 4\mu/3}{\rho_1(1 - \phi_2) + \rho_2\phi_2}\right]^{1/2}, \quad V_S = \left[\frac{\mu}{\rho_1(1 - \phi_2) + \rho_2\phi_2}\right]^{1/2}. \quad (4.7)$$

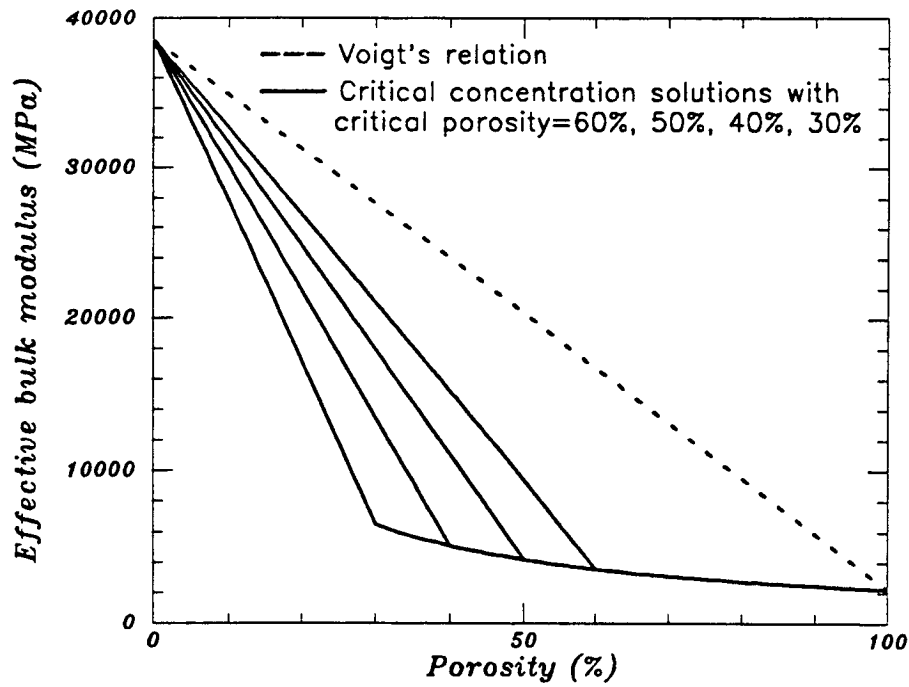
Fig.4.2 presents the effective elastic moduli versus porosity predicted by the critical concentration solution. Since Voigt' bounds are extreme upper bounds of K and μ , the critical concentration solution results in substantial improvements on the evaluation of effective elastic moduli of porous materials. The corresponding wave velocity versus porosity in water-saturated porous materials are given in Fig.4.3.

4.2.3 Extension from Hashin-Shtrikman' relation

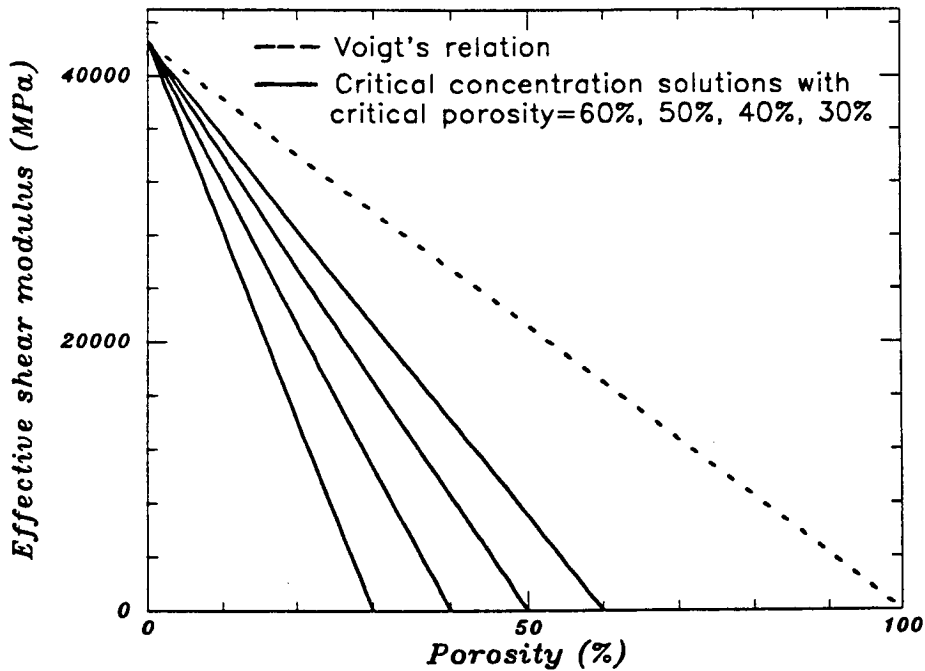
Since the solid matrix phase is always stiffer than the critical concentration phase in the critical concentration model, the critical concentration solution is extended from Hashin-Shtrikman's upper bound.

For dry porous materials, $0 \leq \phi_2 \leq \phi_{cr}$, the critical concentration solution is

$$K = K_1 \left[1 - \frac{(3K_1 + 4\mu_1)\frac{\phi_2}{\phi_{cr}}}{4\mu_1 + 3K_1\frac{\phi_2}{\phi_{cr}}}\right], \quad (4.8)$$



(a)



(b)

Fig.4.2 Effective elastic modulus-porosity relations predicted by the critical concentration solution (4.5) and (4.6) with critical porosity ranging from 30% to 60%, (a) effective bulk modulus-porosity relations, (b) effective shear modulus-porosity relations.

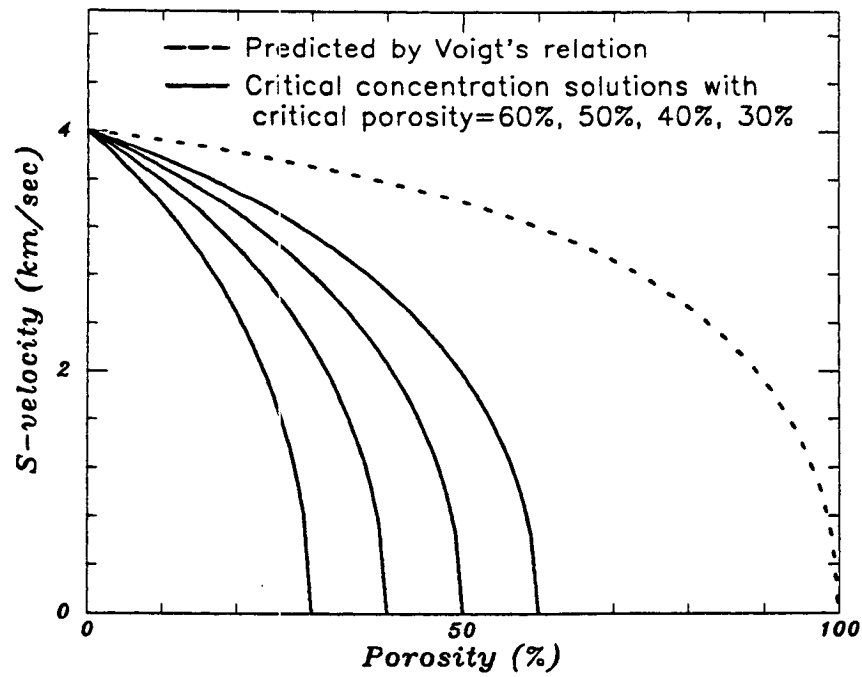
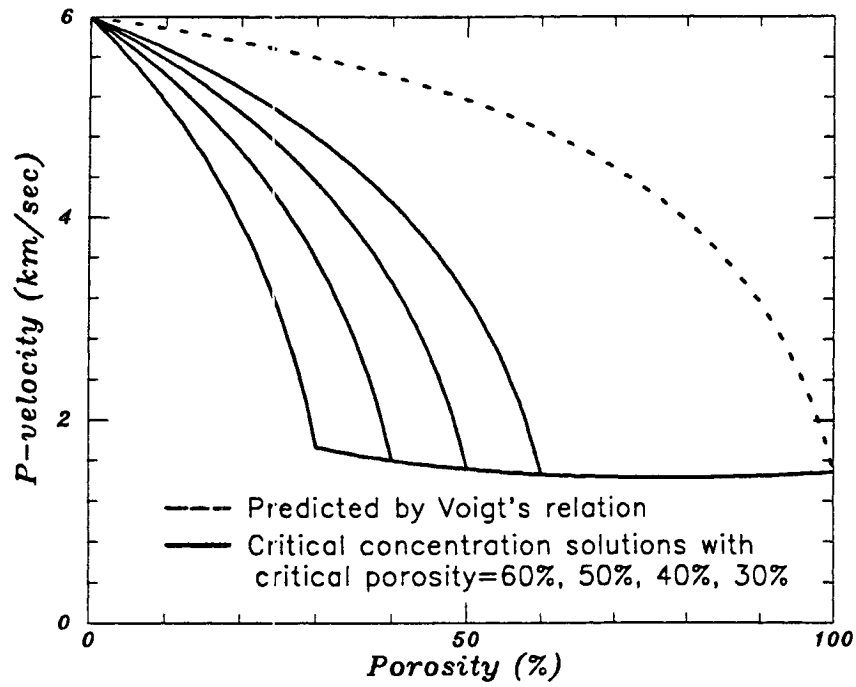


Fig.4.3 Wave velocity-porosity relations predicted by the critical concentration solution (4.5) to (4.7) with critical porosity ranging from 30% to 60%, (a) P wave velocity-porosity relations, (b) S wave velocity-porosity relations.

$$\mu = \mu_1 + \frac{5\mu_1(3K_1 + 4\mu_1)\frac{\phi_2}{\phi_{cr}}}{6(K_1 + 2\mu_1)(1 - \frac{\phi_2}{\phi_{cr}}) - 5(3K_1 + 4\mu_1)}. \quad (4.9)$$

For inviscid fluid-saturated porous materials, the critical concentration solution is

$$K = K_1 + \frac{(K_{cr} - K_1)(3K_1 + 4\mu_1)\frac{\phi_2}{\phi_{cr}}}{3K_{cr} + 4\mu_1 + 3(K_1 - K_{cr})\frac{\phi_2}{\phi_{cr}}}, \quad (4.10)$$

$$\mu = \mu_1 + \frac{5\mu_1(3K_1 + 4\mu_1)\frac{\phi_2}{\phi_{cr}}}{6(K_1 + 2\mu_1)(1 - \frac{\phi_2}{\phi_{cr}}) - 5(3K_1 + 4\mu_1)}, \quad (4.11)$$

for $0 \leq \phi_2 \leq \phi_{cr}$, and

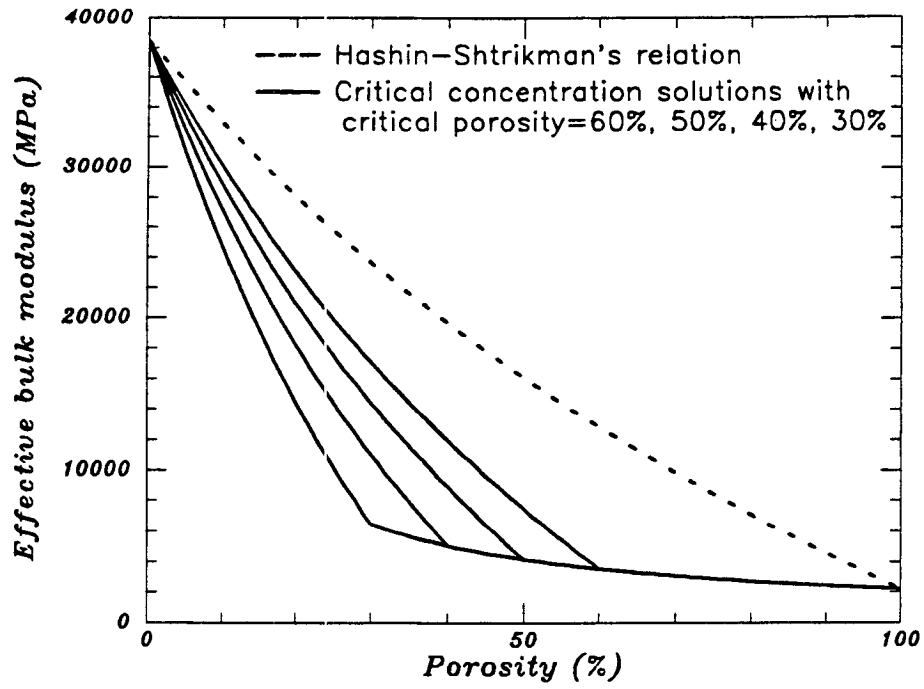
$$K = \left(\frac{1 - \phi_2}{K_1} + \frac{\phi_2}{K_2}\right)^{-1}, \quad \mu = 0, \quad (4.12)$$

for $\phi_{cr} \leq \phi_2 \leq 1$. The corresponding wave velocities are also in the form of equation (4.7).

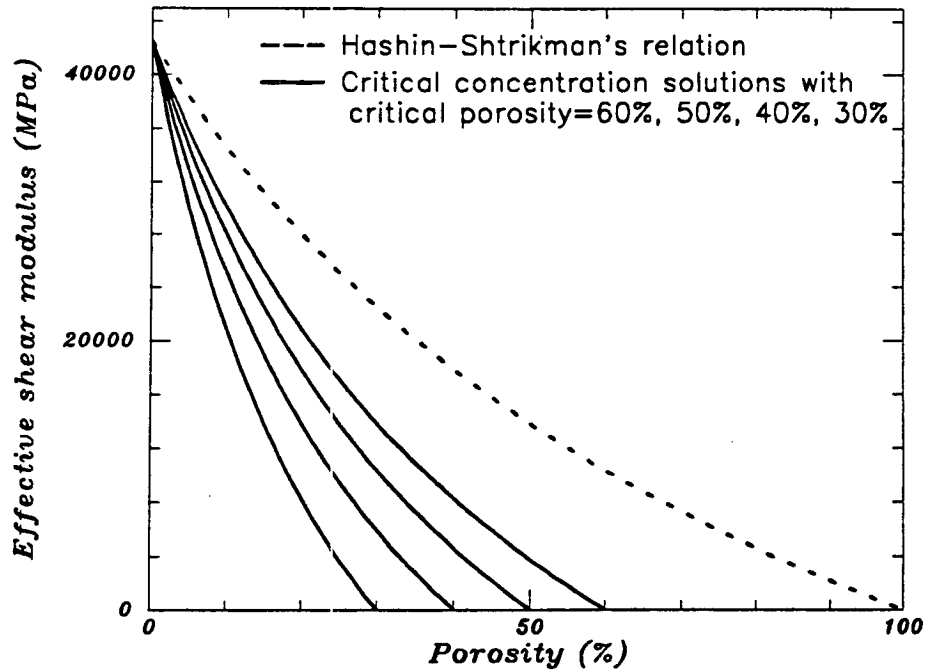
Fig.4.4 and 4.5 present the effective elastic moduli and wave velocities versus porosity predicted by the critical concentration solution. The Hashin-Shtrikman upper bounds can be reduced from the solution with 100% critical porosity. By comparing them with Fig.4.2 and 4.3, we notice that, given a critical porosity, the effective elastic moduli and wave velocities in Fig.4.4 and 4.5 are always lower than those in Fig.4.2 and 4.3, respectively.

Similarly, another critical concentration solution can be extended from the Mori-Tanaka's solution which is given in chapter 2.

Since the effective shear modulus is the same for dry and fluid-saturated porous materials as indicated in (4.4) and (4.5), and (4.9) and (4.11), the pore fluid properties have greater effects on P wave velocity than on shear velocity. The P wave velocities are higher in fluid-saturate porous materials than in dry porous materials, but the

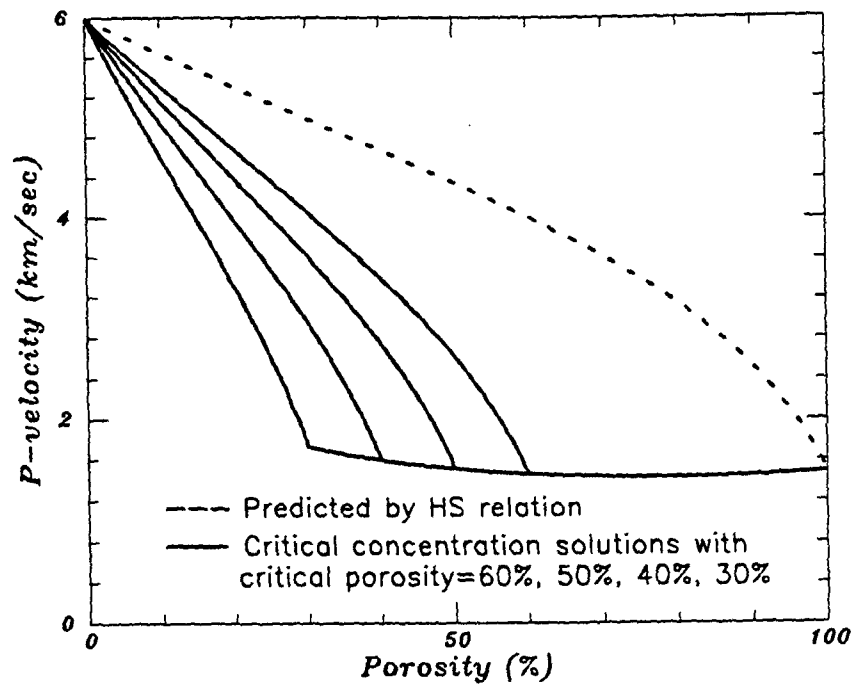


(a)

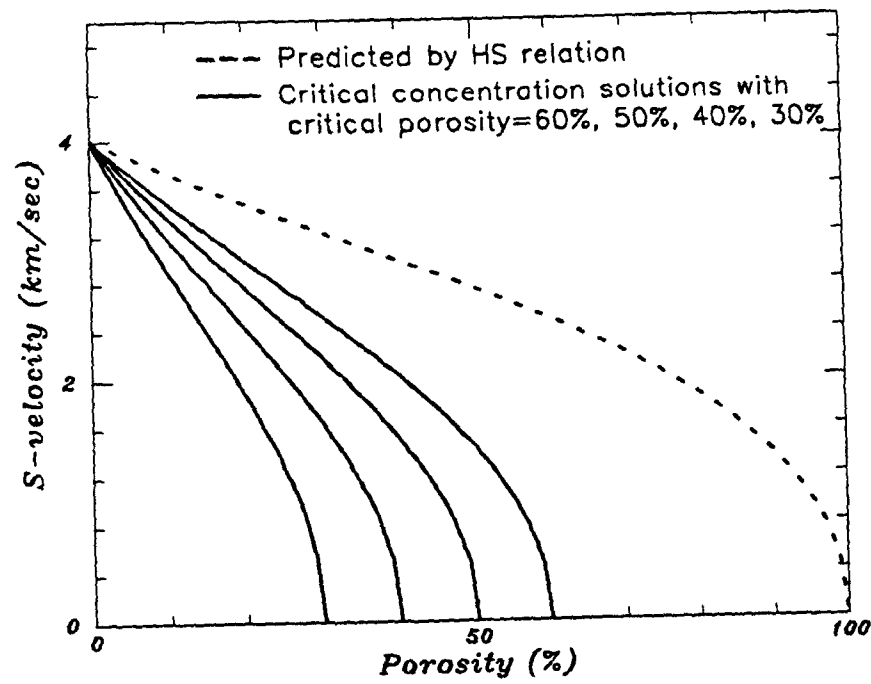


(b)

Fig.4.4 Effective elastic modulus-porosity relations predicted by the critical concentration solution extended from HS relation with critical porosity ranging from 30% to 60%, (a) effective bulk modulus-porosity relations, (b) effective shear modulus-porosity relations.



(a)



(b)

Fig.4.5 Wave velocity-porosity relations predicted by the critical concentration solution extended from HS relation with critical porosity ranging from 30% to 60%, (a) P wave velocity-porosity relations, (b) S wave velocity-porosity relations.

behavior is opposite for S wave velocities. With the same effective shear modulus, the density effect leads to higher S wave velocities in dry porous materials than in fluid-saturated porous materials. Such features of critical concentration solutions are consistent with those derived from Gassmann's relation and scattering theories (Gassmann, 1951; Kuster and Toksöz, 1974; Toksöz et al., 1976).

4.2.4 Extension from percolation solution

When dry porous materials are concerned, both K_{cr} and μ_{cr} are zero, and the critical concentration model terminates at the critical porosity. The effective elastic moduli of such materials can be also estimated on the basis of percolation theory. During the last decade there has been important progress in the theoretical analysis of effective elastic properties near the percolation threshold (Feng and Sen, 1984; Kantor and Webman, 1984; Bergman and Kantor, 1984; Benguigui, 1984; Bergman, 1985; Stauffer, 1985; Roux and Guyon, 1985; Deptuck et al., 1985; Sahimi, 1986; Chelidze et al., 1988, 1990).

For two or three-dimensional percolation systems, the effective elastic bulk and shear moduli are usually expressed as

$$K, \mu \propto (\varpi - \varpi_{pt})^T, \quad (4.13)$$

where ϖ is the volume fraction of bonds or sites occupied, ϖ_{pt} is the percolation threshold value of ϖ , and T is called critical elasticity exponent.

When the percolation method is applied to the critical concentration model of dry porous materials, it follows that

$$\phi_2 + \varpi = 1; \quad \phi_{cr} + \varpi_{pt} = 1, \quad (4.14)$$

and the basic conditions are

$$K = K_1, \quad \mu = \mu_1, \quad \text{when } \phi_2 = 0, \quad (4.15)$$

$$K = K_{cr} = 0, \quad \mu = \mu_{cr} = 0, \quad \text{when } \phi_2 = \phi_{cr}. \quad (4.16)$$

Following the conventional expression in percolation solution, we construct a critical concentration solution to K and μ of dry porous materials as

$$K = K_1 \left(1 - \frac{\phi_2}{\phi_{cr}}\right)^{T_K}, \quad \mu = \mu_1 \left(1 - \frac{\phi_2}{\phi_{cr}}\right)^{T_\mu}, \quad (4.17)$$

where T_K and T_μ are critical elasticity exponents for bulk and shear moduli, respectively. For two and three dimensional elastic percolating *lattice* models, the critical elasticity exponent T ranges from 3.2 to 3.96. However, for percolating *solid* models, T becomes smaller. Chelidze et al. (1988) used a depleted solid model consisting of a polymethyl methacrylate plate punched randomly with circular holes, and found $T = 2.13$ for Young's modulus. Furthermore, for refilled holes, T for Young's modulus drops to 0.9. For porous materials such as rocks and sediments, it is expected the values of T are related to pore geometry and connectivity, and much lower than those for percolating lattice models.

When the critical elasticity exponents in above critical concentration solution are chosen as $T_K = 1$ and $T_\mu = 1$, the predicted elastic modulus-porosity relations are identical with those predicted by the critical concentration solution extended from Voigt's relation. On the other hand, when $T_K = T_\mu = 1.6$ are used, the results are very close to those predicted by the critical concentration solution extended from Hashin-Shtrikman's relation.

The geometry effect of the critical concentration phase on the effective elastic moduli of porous materials is believed similar to the pore geometry effect as indicated by the comparison between Mori-Tanaka's solution and HS bounds in chapter 2.

Above percolation solution doesn't include explicitly such effect. By utilizing the nondilute concentration solutions to K and μ of dry porous materials we proposed in chapter 2, we construct another critical concentration solution that meets the above basic conditions and takes into account the geometry effect of the critical concentration phase:

For spherical critical concentration phase, the solution is

$$\frac{K_1}{K} = 1 + \frac{3(1 - \nu_1)}{2(1 - 2\nu_1)} \frac{\frac{\phi_2}{\phi_{cr}}}{1 - \frac{\phi_2}{\phi_{cr}}}, \quad (4.18)$$

$$\frac{\mu_1}{\mu} = 1 + \frac{15(1 - \nu_1)}{7 - 5\nu_1} \frac{\frac{\phi_2}{\phi_{cr}}}{1 - \frac{\phi_2}{\phi_{cr}}}. \quad (4.19)$$

For cylindrical critical concentration phase, the solution is

$$\frac{K_1}{K} = 1 + \frac{5 - 4\nu_1}{3(1 - 2\nu_1)} \frac{\frac{\phi_2}{\phi_{cr}}}{1 - \frac{\phi_2}{\phi_{cr}}}, \quad (4.20)$$

$$\frac{\mu_1}{\mu} = 1 + \frac{40 - 24\nu_1}{15} \frac{\frac{\phi_2}{\phi_{cr}}}{1 - \frac{\phi_2}{\phi_{cr}}}. \quad (4.21)$$

For penny-shaped critical concentration phase with aspect ratio η , the solution is

$$\frac{K_1}{K} = 1 + \frac{4(1 - \nu_1^2)}{3\pi\eta(1 - 2\nu_1)} \frac{\frac{\phi_2}{\phi_{cr}}}{1 - \frac{\phi_2}{\phi_{cr}}}, \quad (4.22)$$

$$\frac{\mu_1}{\mu} = 1 + \frac{1}{5} \left[1 + \frac{8(1 - \nu_1)(5 - \nu_1)}{3\pi\eta(2 - \nu_1)} \right] \frac{\frac{\phi_2}{\phi_{cr}}}{1 - \frac{\phi_2}{\phi_{cr}}}. \quad (4.23)$$

4.3 Comparison between models and data

4.3.1 Comparison with Nobes' relation

Nobes et al. (1986) noted that Wood's relation is approximately valid for high porosities and Wyllie's relation for low porosities. Then they compute the compressive wave velocity from the weighted mean slowness using the relation

$$\frac{1}{V_P} = \frac{w\phi_2}{V_{Wood}} + \frac{(1-w\phi_2)}{V_{Wyllie}}, \quad (4.24)$$

where V_{Wood} is the Wood velocity as in equation (3.3) and V_{Wyllie} is the Wyllie velocity as in equation (4.1). The empirical weighting factor w is introduced to take into account the lack of consolidation. Nobes (1989) set equal weighting ($w = 1$) for the Wood and Wyllie velocities and used the relation

$$\frac{1}{V_P} = \frac{\phi_2}{V_{Wood}} + \frac{(1-\phi_2)}{V_{Wyllie}} \quad (4.25)$$

to describe a physical model that sediments are assumed to be mixtures of slurry and rigid components. In describing the acoustic velocity data in sediments sampled by the Deep Sea Drilling Project (DSDP), as in Fig.4.6, Nobes et al. (1986) found $w = 1.2$ in equation (4.24), and interpreted it as the indication of underconsolidation. The scatter in the data may be due to variations in grain size and mineralogy.

When we apply the concept of critical porosity to Nobes' relation with $w = 1.2$, we see that w is related to critical porosity ϕ_{cr} by $\phi_{cr} \sim 1/w$, and that ϕ_{cr} ranging from 60% to 80% is common for ocean sediments as reported in the Scientific Results of Ocean Drilling Program (Taylor and Leonard, 1990; Wilkens et al., 1990). By comparing Nobes' relation with the critical concentration solution extended from Wyllie's relation, as in Fig.4.7, we conclude that the critical concentration solutions with 60% ~ 80% critical porosities are equivalent to Nobes' relation, and that they

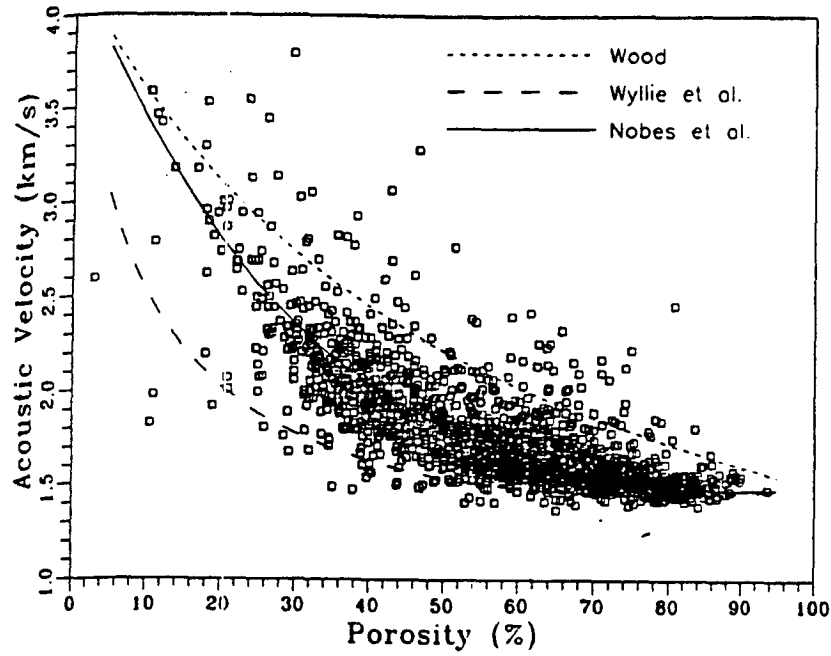


Fig. 4.6 Acoustic velocity versus porosity for sediments sampled by DSDP. Wyllie's relation, Wood's relation, and Nobes' relation are used to compare with the data (after Nobes et al., 1986).

are able to quantitatively describe most sediment data as in Fig.4.6.

4.3.2 Comparison with Raymer's relation

Based on extensive field measurements and observations of transit time versus porosity in various rocks and sediments, Raymer et al. (1980) proposed a set of relations between P wave velocity and porosity over the entire porosity range,

$$V_P = (1 - \phi_2)^2 V_1 + \phi_2 V_2 \quad (0 \leq \phi_2 \leq 0.37) \quad (4.26)$$

$$V_P = \frac{0.1V_{37}V_{47}}{V_{37}(\phi_2 - 0.37) - V_{47}(\phi_2 - 0.47)} \quad (0.37 \leq \phi_2 \leq 0.47) \quad (4.27)$$

$$\frac{1}{\rho V_P^2} = \frac{1 - \phi_2}{\rho_1 V_1^2} + \frac{\phi_2}{\rho_2 V_2^2} \quad (\phi_2 > 0.47) \quad (4.28)$$

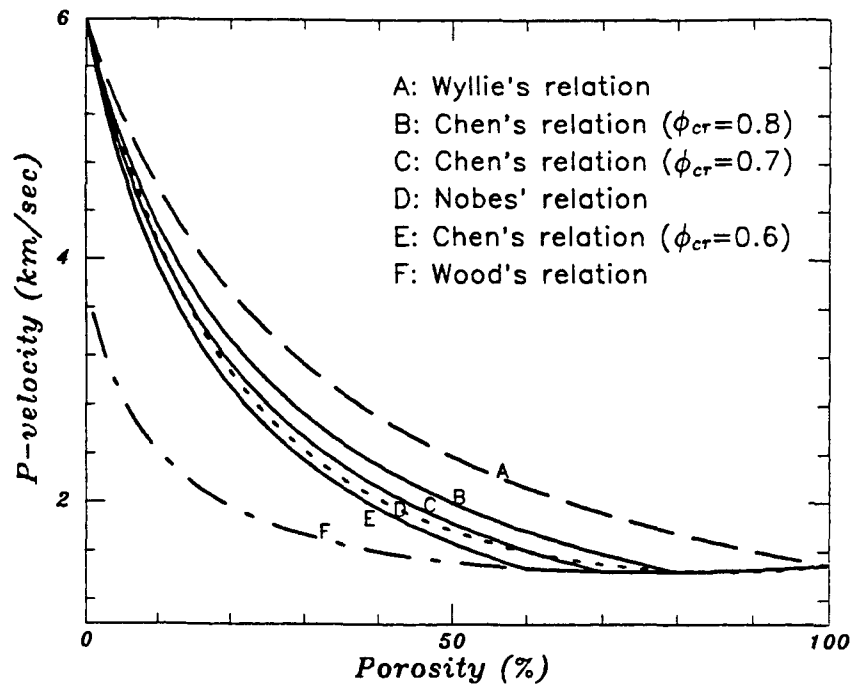


Fig.4.7 Comparison between critical concentration solutions with other model results. Nobes' relation is bracketed by the critical concentration solutions with 60% ~ 80% critical porosities.

where V_{37} and V_{47} are the P wave velocities in the fluid-saturated material with 37% and 47% porosities, respectively.

Although above relations are empirical, Raymer et al. (1980) did give a qualitative interpretation of their material models. Equation (4.26) is a modification from Voigt's relation implying that rock matrix and fluid-filled pores constitute a more parallel network for acoustic transmission. Equation (4.28) is Wood's relation for suspension materials. And equation (4.27) represent the transition between these two material models. Fig.4.8a compares Raymer's relation with Wyllie's and Wood's relations. At porosity up to 37%, Raymer's relation yields higher velocity than Wyllie's.

It is appropriate to say that the critical concentration model in this thesis study roots in the similar observation and logic to those for Raymer's relation. For example, the transition porosities 37% ~ 47% in Raymer's relation are indeed the typical values of critical porosity for limestones and sandstones. The critical concentration solutions

so developed are theoretical extension and formulation of Raymer's empirical relation. One of features in Raymer's relation is the abrupt change of wave velocity at 37% porosity as seen in Fig.4.8a, which stems from the empirical forms and is criticized as unphysical. Fig.4.8b compares Raymer's relation with the critical concentration solution extended from Hashin-Shtrikman's relation. Raymer's relation is completely bracketed by the critical concentration solution with 40% and 50% critical porosities.

4.3.3 Wave velocity-porosity relations in sandstones

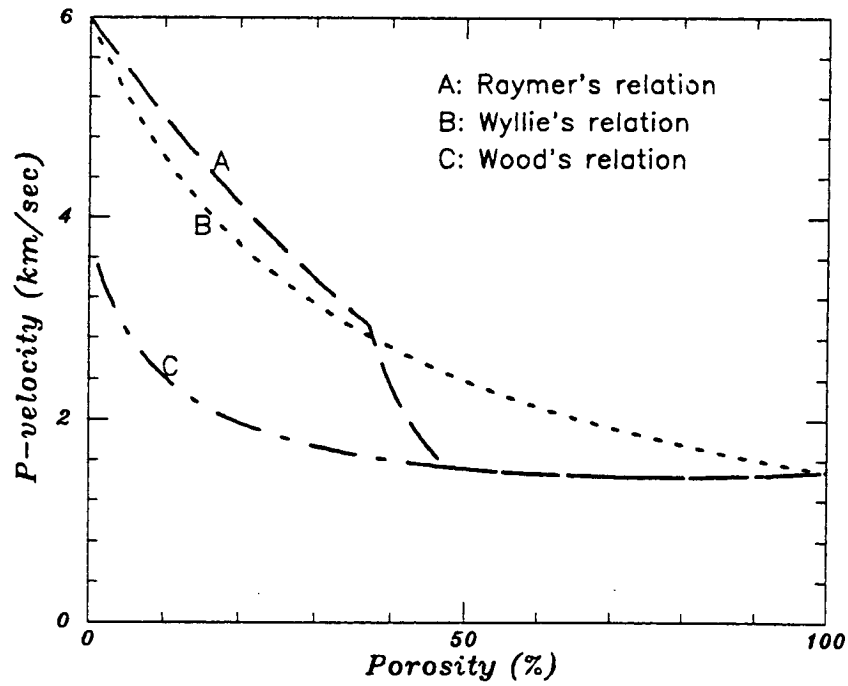
Fig.4.9 compares several theoretical results with experimental data of wave velocities in clean sandstones obtained by Han (1986). 40% critical porosity is used in the critical concentration solutions. For both P and S wave velocities, the data are completely bracketed by the critical concentration solutions extended from Voigt's and Hashin-Shtrikman's relations. If the exact critical porosity of such porous materials is available, one can easily fit the velocity data with one of the critical concentration solutions. In general, critical concentration solutions give better evaluations compared with self-consistent spherical and cylindrical pore models and original Voigt's and HS bounds.

4.4 Clay Effects on Effective Properties

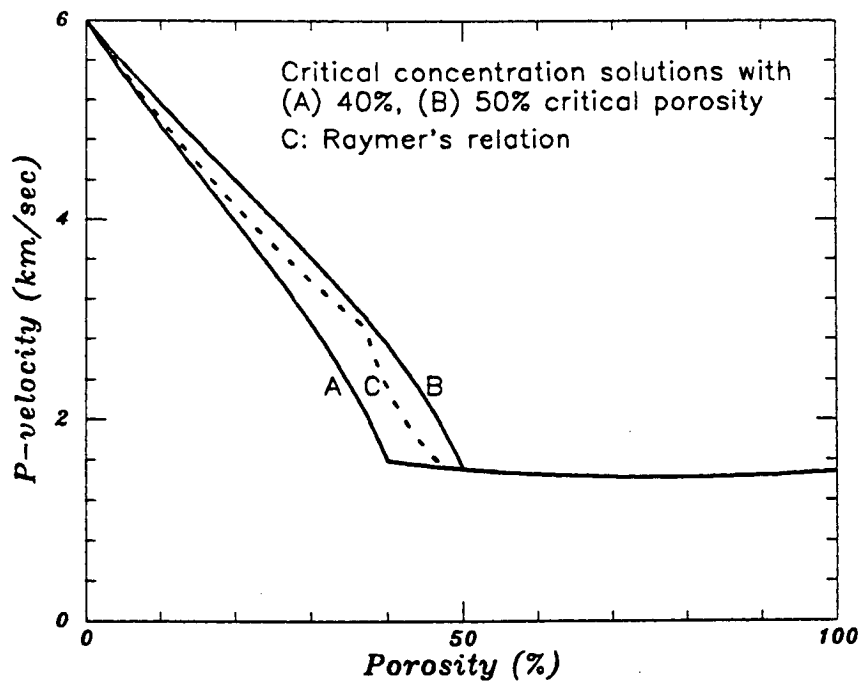
4.4.1 Experimental data and empirical relations

Clay content in shaly sandstones has been recognized by experiments as the second factor after porosity to influence P and S wave velocities. Tosaya and Nur (1982), based on their experiments, proposed an empirical relation that P wave velocity (km/sec) is a linear function of porosity ϕ_2 and clay volume fraction ϕ_3 of fully-saturated rocks,

$$V_P = 5.8 - 8.6\phi_2 - 2.4\phi_3. \quad (4.29)$$

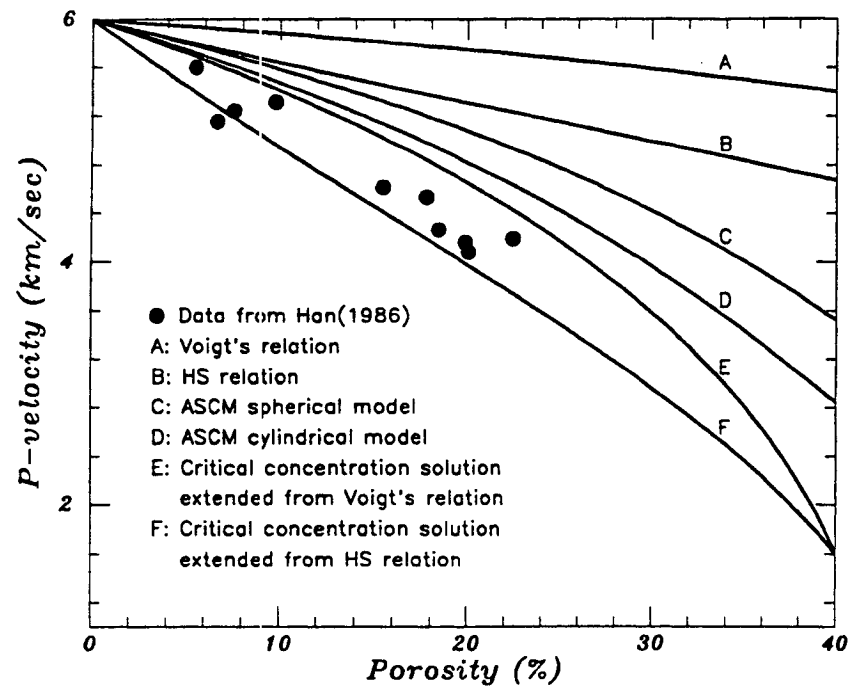


(a)

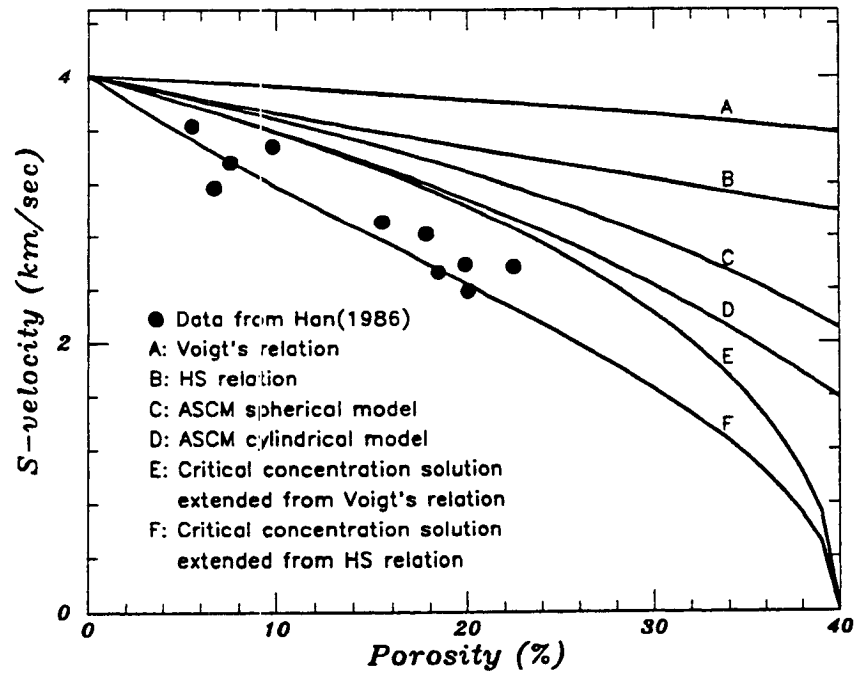


(b)

Fig.4.8 (a) Comparison between Raymer's relation and Wyllie's and Wood's relations, (b) comparison between Raymer's relation and the critical concentration solutions with 40% ~ 50% critical porosities.



(a)



(b)

Fig. 4.9 Comparison of several model results with experimental data of wave velocity-porosity relations. Han's clean sandstone data under 5 MPa confining pressure are used. 40% critical porosity is used for the critical concentration solution, (a) P wave velocity-porosity relations, (b) S wave velocity-porosity relations.

Kowallis et al. (1984) examined this empirical relation by collecting broad ranges of experimental data from DeMartini et al. (1976), Tosaya and Nur (1982), and their own, and found that the empirical relation is generally consistent with available data, as in Fig.4.10.

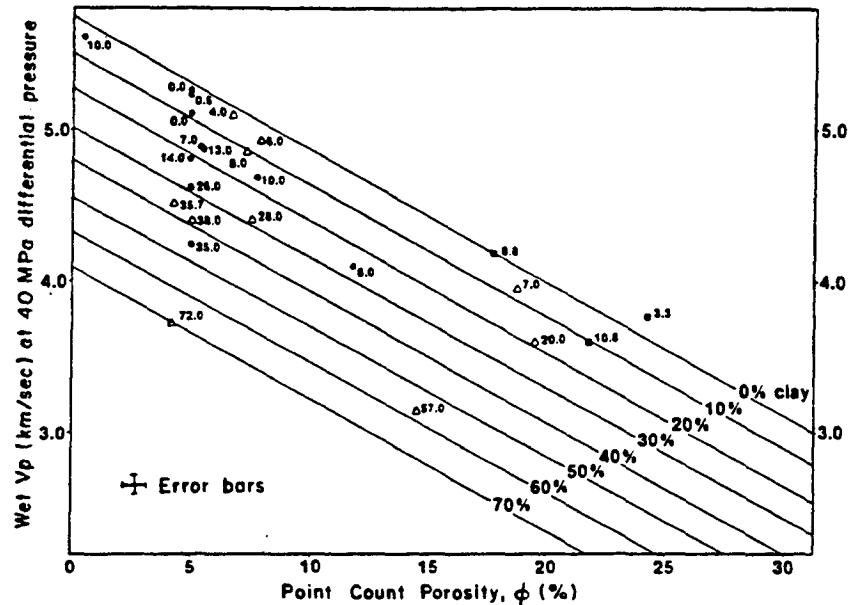


Fig.4.10 Experimental data and empirical relation between P wave velocity, porosity, and clay volume fraction of shaly sandstones. The solid lines are predicted by the empirical relation (4.24). The experimental data are from DeMartini et al. (1976) (circles), Tosaya and Nur (1982) (triangles), and Kowallis et al. (1984) (squares). (after Kowallis et al., 1984)

Han et al. (1986) conducted extensive experiments on shaly sandstones and arrived at both P and S velocity-porosity-clay content relations,

$$V_P = 5.59 - 6.93\phi_2 - 2.18\phi_3, \quad V_S = 3.52 - 4.91\phi_2 - 1.89\phi_3, \quad (4.30)$$

at 40MPa confining pressure and 1MPa pore pressure. In particular, they observed that clay content affects shear modulus μ much more than bulk modulus K .

Wilkins et al. (1986) conducted aspect ratio modeling to investigate clay effects on the compressional wave velocity of dry sandstones with varying clay contents. They concluded that the effect of clays in sandstone pores is simply to reduce the porosity without changing the non-framework (void + clay) volume fraction.

In the following we extend the critical concentration model to include the pore-filling and dispersed clay effects. The critical concentration solutions are then compared with available experimental data.

4.4.2 Pore-filling and dispersed clay effects

For fluid-saturated porous rocks and sediments with pore-filling clay which has microporosity ϕ_{cm} , the pore-filling clay volume fraction ϕ_3 is limited by the supposed pore volume fraction $(1 - \phi_1)$ as $0 \leq \phi_3 \leq (1 - \phi_1)$, and $(1 - \phi_1)$ may change from zero to 1 throughout a porous material system. Thus, it is practical and analytically-convenient to define the pore-filling volume fraction ϕ_3 as some percentage of $(1 - \phi_1)$. Let $\phi_3 = \chi(1 - \phi_1)$, the material porosity ϕ_2 is given by

$$\phi_2 = (1 - \phi_1)[1 - \chi(1 - \phi_{cm})]. \quad (4.31)$$

For example, given a sample with 15% porosity, 8% pore-filling clay, and 25% microporosity, from equations $\phi_2 = 1 - \phi_1 - \phi_3(1 - \phi_{cm})$ and $\phi_3 = \chi(1 - \phi_1)$ one finds $\phi_1 = 0.79$ and $\chi = 0.381$. For marine suspensions, the clay state is not pore-filling clay but dispersed clay, but the porosity is also given by above formula.

When the critical concentration model is extended to clay-bearing porous materials, it is believed that pore-filling clay particles do not disturb the highly load-bearing matrix phase, that is, the clay particles are totally included in the critical concentration phase. Now it is rigorous to use critical concentration C_{cr} to represent the transition from solid-matrix supported and fluid-matrix supported subsystems, and the critical porosity ϕ_{cr} decreases with the increase in pore-filling clay volume fraction,

$$\phi_{cr} = C_{cr}[1 - \chi(1 - \phi_{cm})]. \quad (4.32)$$

4.4.3 Critical concentration solutions

In the fluid-matrix supported subsystem ($C_{cr} \leq \frac{\phi_2}{1-\chi(1-\phi_{cm})} \leq 1$) where clay particles are in dispersed state, the effective elastic modulus-porosity and wave velocity-porosity relations can be analytically described by the isostress material model (Reuss, 1929; Wood, 1941; Hill, 1963),

$$\begin{aligned} \frac{1}{K} &= \frac{\phi_1}{K_1} + \frac{\phi_2}{K_2} + \frac{\phi_3(1 - \phi_{cm})}{K_3} \\ &= \frac{\frac{1-\chi(1-\phi_{cm})-\phi_2}{1-\chi(1-\phi_{cm})}}{K_1} + \frac{\phi_2}{K_2} + \frac{\frac{\phi_2\chi(1-\phi_{cm})}{1-\chi(1-\phi_{cm})}}{K_3}, \end{aligned} \quad (4.33)$$

$$\mu = 0, \quad (4.34)$$

$$V_P^2 = \frac{\left[\frac{\frac{1-\chi(1-\phi_{cm})-\phi_2}{1-\chi(1-\phi_{cm})}}{K_1} + \frac{\phi_2}{K_2} + \frac{\frac{\phi_2\chi(1-\phi_{cm})}{1-\chi(1-\phi_{cm})}}{K_3} \right]^{-1}}{\rho_1 \left[\frac{1-\chi(1-\phi_{cm})-\phi_2}{1-\chi(1-\phi_{cm})} \right] + \rho_2 \phi_2 + \rho_3 \left[\frac{\phi_2\chi(1-\phi_{cm})}{1-\chi(1-\phi_{cm})} \right]}, \quad (4.35)$$

$$V_S = 0. \quad (4.36)$$

where K_3 and ρ_3 are clay bulk modulus and density, respectively.

In the solid-matrix supported subsystem ($0 \leq \frac{\phi_2}{1-\chi(1-\phi_{cm})} \leq C_{cr}$), when Voigt's relation is applied to the critical concentration model, the critical concentration solution to effective elastic moduli is

$$K = \left\{ 1 - \frac{\phi_2}{C_{cr}[1 - \chi(1 - \phi_{cm})]} \right\} K_1 + \frac{\phi_2}{C_{cr}[1 - \chi(1 - \phi_{cm})]} K_{cr}, \quad (4.37)$$

$$\mu = \left\{ 1 - \frac{\phi_2}{C_{cr}[1 - \chi(1 - \phi_{cm})]} \right\} \mu_1, \quad (4.38)$$

where

$$K_{cr} = \left\{ \frac{1 - C_{cr}}{K_1} + \frac{C_{cr}[1 - \chi(1 - \phi_{cm})]}{K_2} + \frac{C_{cr}\chi(1 - \phi_{cm})}{K_3} \right\}^{-1}. \quad (4.39)$$

When Hashin-Shtrikman upper bound is applied to the critical concentration model, the effective elastic moduli for $0 \leq \frac{\phi_2}{1 - \chi(1 - \phi_{cm})} \leq C_{cr}$ are given by

$$K = K_1 + \frac{(K_{cr} - K_1)(3K_1 + 4\mu_1) \frac{\phi_2}{C_{cr}[1 - \chi(1 - \phi_{cm})]}}{3K_{cr} + 4\mu_1 + 3(K_1 - K_{cr}) \frac{\phi_2}{C_{cr}[1 - \chi(1 - \phi_{cm})]}}, \quad (4.40)$$

$$\mu = \mu_1 + \frac{5\mu_1(3K_1 + 4\mu_1) \frac{\phi_2}{C_{cr}[1 - \chi(1 - \phi_{cm})]}}{6(K_1 + 2\mu_1)(1 - \frac{\phi_2}{C_{cr}[1 - \chi(1 - \phi_{cm})]}) - 5(3K_1 + 4\mu_1)}. \quad (4.41)$$

The corresponding wave velocities for $0 \leq \frac{\phi_2}{1 - \chi(1 - \phi_{cm})} \leq 1$, are expressed as

$$V_P = \left\{ \frac{K + 4\mu/3}{\rho_1 \left[\frac{1 - \chi(1 - \phi_{cm}) - \phi_2}{1 - \chi(1 - \phi_{cm})} \right] + \rho_2 \phi_2 + \rho_3 \left[\frac{\phi_2 \chi(1 - \phi_{cm})}{1 - \chi(1 - \phi_{cm})} \right]} \right\}^{1/2}, \quad (4.42)$$

$$V_S = \left\{ \frac{\mu}{\rho_1 \left[\frac{1 - \chi(1 - \phi_{cm}) - \phi_2}{1 - \chi(1 - \phi_{cm})} \right] + \rho_2 \phi_2 + \rho_3 \left[\frac{\phi_2 \chi(1 - \phi_{cm})}{1 - \chi(1 - \phi_{cm})} \right]} \right\}^{1/2}. \quad (4.43)$$

Fig.4.11 shows effective elastic modulus-porosity relations with different levels of pore-filling and dispersed clay. The effect of pore-filling clay is stronger on effective shear modulus than on effective bulk modulus, consistent with the experimental observation (Han et al., 1986). The dispersed clay has little effect on the effective bulk modulus. The critical porosity decreases from 40% to 22% as the parameter χ increases from zero to 0.6.

Fig.4.12 presents the wave velocity-porosity relations with different levels of pore-filling and dispersed clay. At porosities up to 20% ~ 30%, the P and S wave

velocities decrease almost linearly with porosity and parameter χ indicating the clay content. This feature is consistent with the linear empirical relations between velocity, porosity, and clay content proposed by Tosaya and Nur (1982) and Han et al. (1986).

Recently, Marion (1990) collected experimental data of P wave velocity from Hamilton (1956), Han et al. (1986), and Yin et al. (1988). For clean sandstones and sands, the P wave velocity data indicate about 40% critical porosity. With the increase in clay content, P wave velocity data scatter very much. Neither predictions from existing analytical models like HS bounds nor empirical relations can match the feature of such wave velocity-porosity-clay relations. When we compare the critical concentration solution as in Fig.4.12 with such data, we find that our theoretical results can explain all features in such data (Fig.4.13). We use the parameter χ to characterize the clay content in the data and draw the lines with $\chi = 0.0, 0.2, 0.4, 0.6$. As predicted by our model result, the critical porosity decreases with clay content, and P wave velocity drops dramatically with clay content.

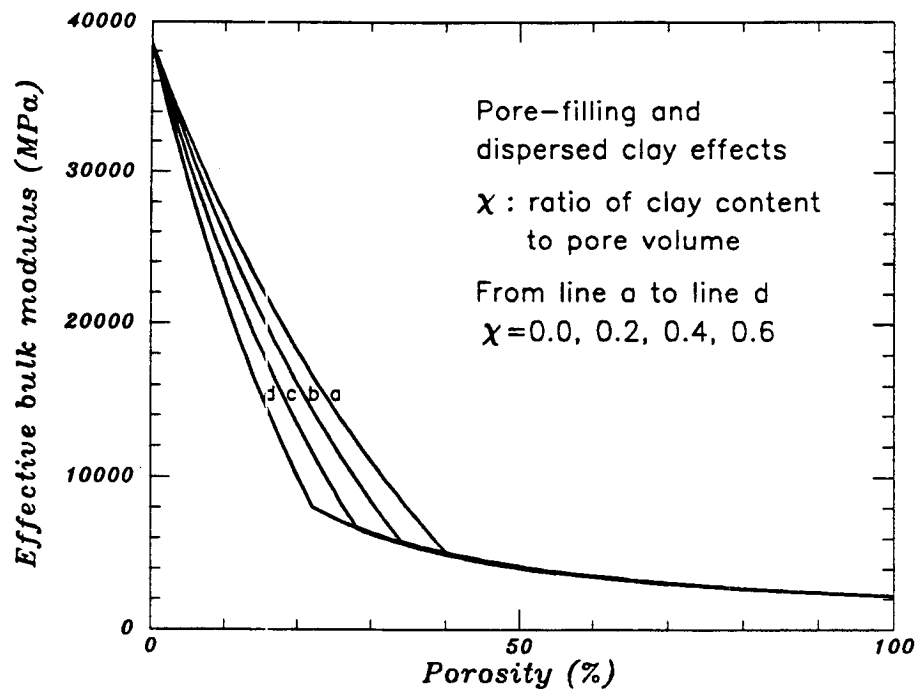
4.5 Conclusions

Conventional porous material models can be taken as specific critical concentration models with 100% critical porosity.

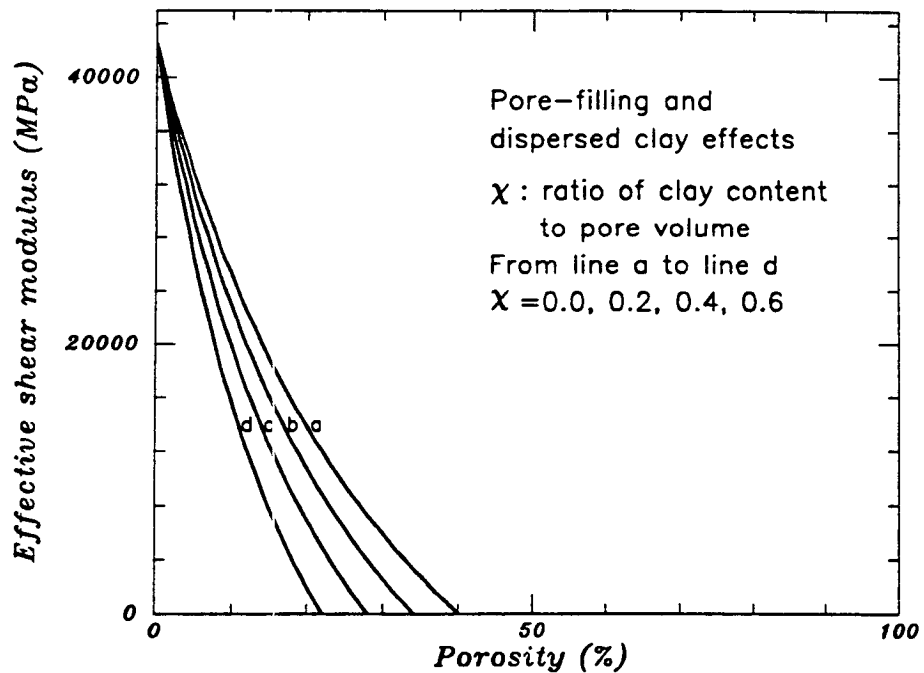
The substitution method is useful for deriving critical concentration solutions on the basis of existing analytical and empirical formulas of conventional porous material models.

The critical concentration solutions extended from Wyllie's, Voigt's, and HS relations give better description of available experimental data for both clay-free and clay-bearing porous materials.

Our theoretical results provide insights into several empirical relations between velocity, porosity, and clay content.

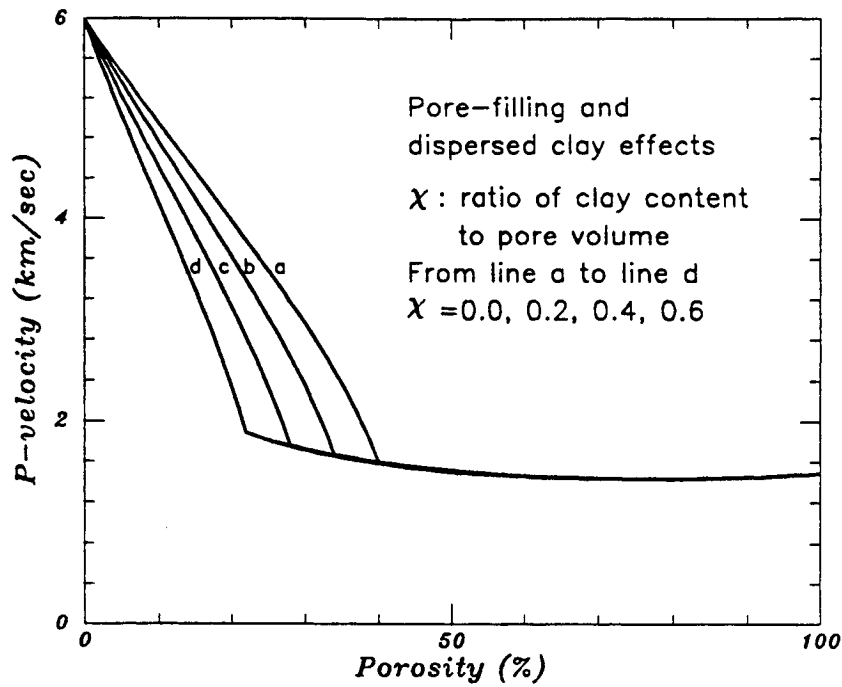


(a)

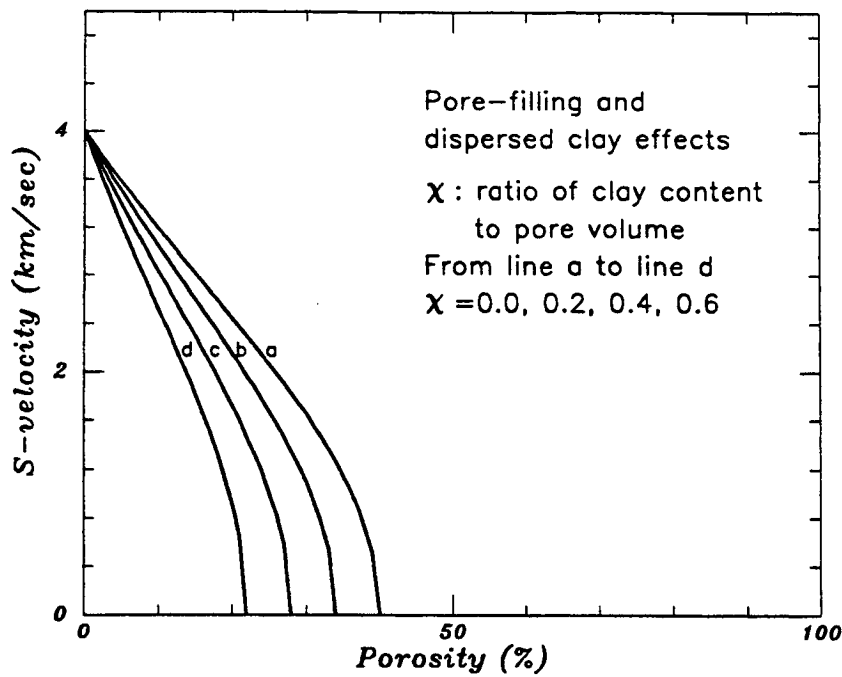


(b)

Fig.4.11 Effective elastic modulus-porosity-clay relations predicted by the critical concentration solution extended from HS bounds. $\phi_{cm} = 25\%$ and $\chi = 0.0, 0.2, 0.4, 0.6$ are used in calculation. Critical porosity decreases from 40% to 22% as clay content increases. (a) effective bulk modulus versus porosity and clay content, (b) effective shear modulus versus porosity and clay content.



(a)



(b)

Fig.4.12 Wave velocity-porosity-clay relations predicted by the critical concentration solution extended from HS bounds. $\phi_{cm} = 25\%$ and $\chi = 0.0, 0.2, 0.4, 0.6$ are used in calculation. (a) P wave velocity versus porosity and clay content, (b) S wave velocity versus porosity and clay content.

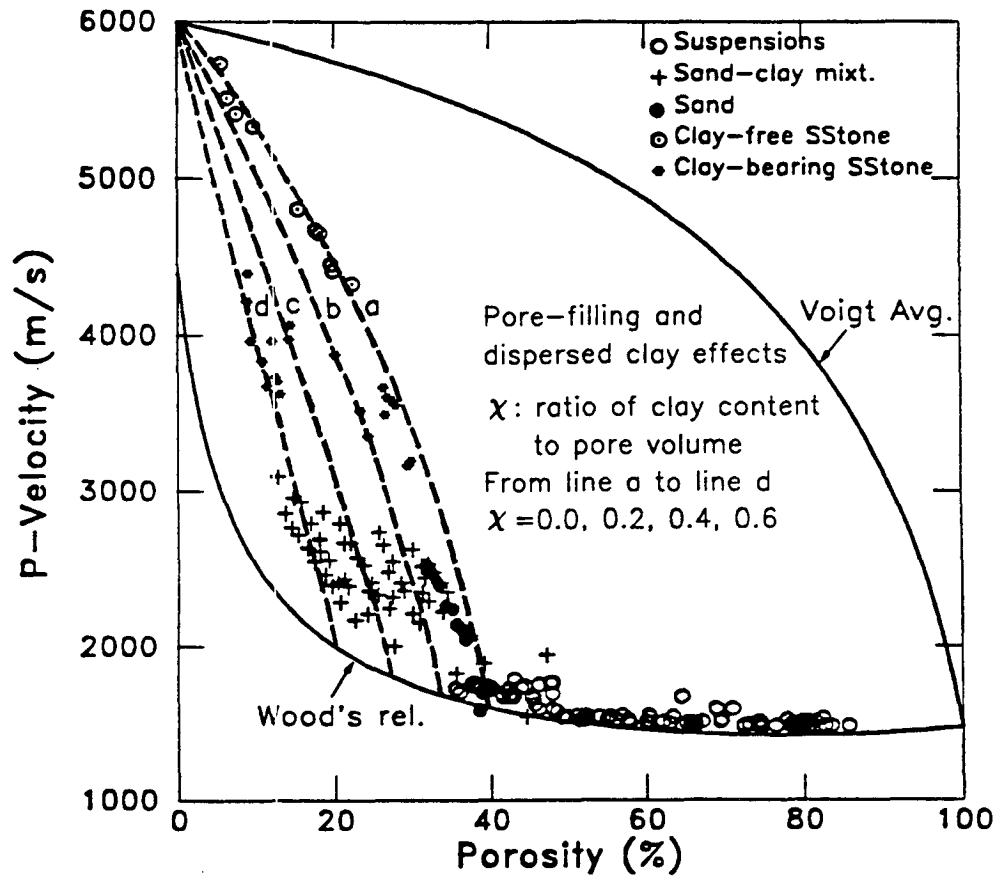


Fig.4.13 Comparison between critical concentration solution as in Fig.4.12(a) and experimental data of P wave velocity-porosity relations in clastic sediments and rock (data collected by Marion, 1990).

References

- Benguigui, L., 1984, Experimental study of the elastic properties of a percolating system, *Physical Review Letters*, **53**, 2028-2030.
- Bergman, D. J. and Y. Kantor, 1984, Critical properties of an elastic fractal, *Phys. Rev. Lett.*, **53**, 511-514.
- Bergman, D. J., 1985, Elastic moduli near percolation, *Phys. Rev.*, **B31**, 1696-1699.
- Chelidze, T. L., Gueguen, V., Darot, M., and T. Roehle, 1988, On the elastic properties of depleted refilled solids near percolation, *J. Phys.*, **C21**, L1007-L1010.
- Chelidze, T. L., Spetzler, H., Getting, I. C., and Z. A. Avaliani, 1990, Experimental investigation of the elastic modulus of a fractal system—a model of fractured rocks, *PAGEOPH*, **134**, 31-43.
- DeMartini, D. C., D. C. Beard, J. S. Danburg, and J. H. Robinson, 1976, Variations of seismic velocities in sandstones and limestones with lithology and pore fluid at simulated in situ conditions, paper presented at the Egyptian General Petroleum Corporation Exploration Seminar, Cairo.
- Deptuck, D., J. P. Harrison, and P. Zawadzki, 1985, Measurement of elasticity and conductivity of a three-dimensional percolation system, *Phys. Rev. Lett.*, **54**, 913-915.
- Feng, S. and P. N. Sen, 1984, Percolation on elastic networks: new exponent and threshold, *Phys. Rev. Lett.*, **52**, 216-219.
- Gassmann, G., 1951, *Über die Elastizität poröser Medien*, *Vierteljahresschr., Naturforsch. Ges. Zuerich*, **96**, 1-21.
- Hamilton, E. L., 1956, Low sound velocities in high porosity sediments, *J. Acoust. Soc. Am.*, **28**, 16-19.
- Han, D. H., 1986, Effects of porosity and clay content on acoustic properties of sandstones and unconsolidated sediments, PhD dissertation, SRB, **28**, Stanford University.
- Han, D. H., Nur, A., and D. Morgan, 1986, Effects of porosity and clay content on wave velocities in sandstones: *Geophysics*, **51**, 2093-2107.
- Hill, R., 1963, Elastic properties of reinforced solids: some theoretical principles, *J. Mech. Phys. Solids*, **11**, 357-372.

- Kantor, Y. and I. Webman, 1984, Elastic properties of random percolating systems, *Phys. Rev. Lett.*, **52**, 1891-1894.
- Kowallis, B., Jones, L. E. A., and H. F. Wang, 1984, Velocity-porosity-clay content; systematics of poorly consolidated sandstones, *J. Geophys. Res.*, **89**, 10355-10364.
- Kuster, G. and M. N. Toksöz, 1974, Velocity and attenuation of seismic waves in two-phase media: I. Theoretical formulation and II. Experimental results, *Geophysics*, **39**, 587-618.
- Marion, D., 1990, Acoustic, mechanical, and transport properties of sediments and granular materials, PhD dissertation, SRB, **39**, Stanford University.
- Raymer, L. L., Junt, E. R., and J. S. Gardner, 1980, An improved sonic transit time-to-porosity transform, SPWLA, 21st Ann. Logg. Symp., Paper P.
- Reuss, A., 1929, Berechnung der Fließgrenze von Mischkristallen auf Grund der Plastizitätsbedingung für Einkristalle, *Z. Angew. Math. Mech.*, **9**, 49-58.
- Roux, S. and E. Guyon, 1985, Mechanical percolation: a small beam lattice study, *J. Phys. Lett.*, **46**, L999-L1004.
- Sahimi, M., 1986, Relation between the critical exponent of elastic percolation networks and the conductivity and geometrical exponents, *J. Phys. C: Solid State Phys.*, **19**, L79-L83.
- Stauffer, D., 1985, Introduction to percolation theory, Taylor and Francis, pp.124.
- Taylor, E. and J. Leonard, 1990, Sediment consolidation and permeability at the Barbados Forearc, in *Proc. Ocean Drilling Program, Sci. Results*, **110**, edited by Moore, J. C., Mascle, A., et al., 289-308.
- Toksöz, M. N., Cheng, C. H., and A. Timur, 1976, Velocities of seismic waves in porous rocks, *Geophysics*, **41**, 621-645.
- Tosaya, C. and A. Nur, 1982, Effects of diagenesis and clays on compressional velocities in rocks, *Geophys. Res. Lett.*, **9**, 5-8.
- Voigt, W., 1928, *Lehrbuch der Kristallphysik*, Teubner, Leipzig, pp.964.
- Wilkens, R., et al., Diagenesis and dewatering of clay-rich sediments, Barbados Accretionary Prism, in *Proc. Ocean Drilling Program, Sci. Results*, **110**, edited by Moore, J. C., Mascle, A., et al., 309-320.
- Wilkens, R.H., G. Simmons, T. M. Wissler, and L. Caruso, 1986, The physical proper-

ties of a set of sandstones – Part III, the effects of fine-grained pore-filling material on compressional wave velocity, *Int. J. Rock Mech. Min. Sci. & Geomech. Abstr.*, **23**, 313-325.

Wood, A. B., 1941, *A Textbook of Sound*, Macmillan, New York, pp.519.

Wyllie, M. R. J., Gregory, A. R., and L. W. Gardner, 1956, Elastic wave velocities in heterogeneous and porous media, *Geophysics*, **21**, 41-70.

Yin, H., Han, D., and A. Nur, 1988, Study of velocity and compaction on sand-clay mixtures, *SRB*, **33**, 265-302.

Chapter 5

Asymmetric Self-consistent Method and Solution for Porous Materials

Abstract

This chapter examines and explores self-consistent methods and solutions for the effective properties of porous materials. Although both symmetric and asymmetric self-consistent methods yield the vanishing elastic moduli at finite porosity for porous materials, only the latter is conceptually consistent with the critical porosity phenomena of porous materials. Asymmetric self-consistent solution for penny-shaped inclusions is found and is compared with experimental data of wave velocity-porosity relation. By comparing the asymmetric self-consistent solutions with the critical concentration solutions of fluid-saturated porous materials, we conclude that the asymmetric self-consistent method and solution can be taken to advantage for evaluating effective properties of porous materials almost up to the critical porosity. Then the clay effects on effective moduli and wave velocities of porous materials are investigated by extending the asymmetric self-consistent solutions to clay-bearing porous materials with varying clay cementation states. The results indicate that clay effect is stronger on effective shear modulus than on effective bulk modulus, and that uncemented clay effect is stronger than cemented clay effect, which are consistent with the observations from clay-bearing sandstone experiments.

5.1 Symmetric and Asymmetric Self-consistent Methods

As pointed out in chapter 1 and 2, only the self-consistent method can yield vanishing effective moduli at finite porosity for porous materials, which seems relevant to the critical porosity as studied in chapter 3 and 4, and has been a controversial issue in effective medium theories. By taking a positive attitude over the issue, this chapter examines and explores asymmetric self-consistent solutions, compares them with the critical concentration solutions, and ascertain how much the self-consistent method and solution can be taken to advantage for evaluating effective properties of porous materials.

According to Berryman (1980) and Thorpe and Sen (1985), there are symmetric and asymmetric self-consistent methods which differ in the role treatments of material constituents. The symmetric self-consistent method (SSCM) treats all material constituents symmetrically or equally, in other words, there are no distinctions of matrix and inclusion phases, and all constituents are assumed to have the same shape and distribution. In Berryman's version of symmetric self-consistent method (Berryman, 1980), the constituents of a multiphase material are embedded equally in a matrix composed of the effective material, and the basic requirement that the scattered, long-wavelength displacement field vanishes on the average leads to a general form of symmetric self-consistent solution.

The asymmetric self-consistent method (ASCM) treats one constituent as matrix or host and the others as embedded inclusions. Thus matrix phase and inclusion phase have quite different geometry and connectivity. The derivations of asymmetric self-consistent solutions for composite materials are often involved with an auxiliary problem that a single inclusion is embedded in an infinite matrix composed of the effective material. Typical asymmetric self-consistent solutions have been found by Hill (1965), Budiansky (1965), Wu (1966), Walpole (1969), Boucher (1974), O'Connell

and Budiansky (1974, 1977), and others.

For composite materials whose constituent properties are in the same order, both the symmetric and asymmetric self-consistent solutions to effective elastic moduli are within the narrow Hashin-Shtrikman bounds, and the shape and connectivity effects of constituents are actually negligible (Berryman, 1980). For dry and fluid-saturated porous materials, however, both solutions yield the feature of vanishing elastic moduli at finite porosity. For spherical pores in three-dimension problems and circular pores in two-dimension problems, both solutions predict the same finite porosity at which the effective elastic moduli vanish. But the solutions predict different finite porosities for all other pore shapes. Thus, which self-consistent solution is conceptually consistent with the critical porosity phenomena of porous materials such as rocks and sediments?

We believe that the asymmetric self-consistent method and solution are more appropriate to describe the microstructural geometry and connectivity effects, and the critical porosity phenomena of porous materials. For porous materials, the microstructural geometry effect on effective moduli is considerable, leading to far-apart HS bounds as illustrated in chapter 2. As indicated in chapter 3, the matrix phase of a porous material has dominant effects on the effective moduli compared with the inclusion phase. SSCM assumes the same shape for every constituent and no distinction of matrix or inclusion phase. These assumptions are unrealistic for porous materials especially rocks and sediments. For a fluid-saturated porous material, ASCM assumes the solid matrix and fluid inclusion, and ASCM solution for 0 ~ 100% porosities contains the vanishing shear moduli at finite porosity. This is conceptually consistent with the porous material system as illustrated in Fig.3.6 where critical porosity is just the transition porosity between the solid-matrix supported and fluid-matrix supported subsystems.

5.2 Existing Asymmetric Self-consistent Solutions

Given a geometrical model of the inclusion phase, the asymmetric self-consistent solutions always turn out as a set of nonlinear simultaneous equations with the unknowns K and μ . An iteration method is generally needed to solve the equation set. We compile a numerical program based on the incorporation of Newton-Raphson method and Conjugate Gradient method (Press et al., 1989) in order to warrant the convergence and accelerate the convergent speed. We rewrite the existing solutions in such forms that all these simultaneous equation sets can be solved stably and accurately by the numerical program to yield the effective bulk and shear moduli. In the following computation, typical values for the fluid-saturated rocks are given as: (1) sand grain phase, $K_1 = 38500 \text{ MPa}$, $\mu_1 = 42500 \text{ MPa}$; (2) fluid phase (water), $K_2 = 2200 \text{ MPa}$, $\mu_2 = 0$.

5.2.1 Spherical inclusion model

Hill (1965) obtained

$$\frac{1 - \phi_2}{K - K_2} + \frac{\phi_2}{K - K_1} = \frac{3}{3K + 4\mu}, \quad (5.1)$$

$$\frac{1 - \phi_2}{\mu - \mu_2} + \frac{\phi_2}{\mu - \mu_1} = \frac{6}{5} \frac{K + 2\mu}{(3K + 4\mu)\mu}, \quad (5.2)$$

which can be rewritten in the following form

$$\frac{K_1}{K} = 1 + \frac{(K_1 - K_2)(3K_1 + 4\mu)\phi_2}{K_1(3K_2 + 4\mu) + 4\mu\phi_2(K_2 - K_1)}, \quad (5.3)$$

$$\frac{\mu_1}{\mu} = \frac{5\mu_1(3K + 4\mu)(\mu - \mu_1 + \mu_1\phi_2 - \mu_2\phi_2)}{6(K + 2\mu)(\mu - \mu_1)(\mu - \mu_2)}. \quad (5.4)$$

For inviscid fluid saturation, the numerical results in Fig.5.1(a) show that μ becomes zero at about 60% porosity, and that K reduces to Reuss' bound K_R at about 60% porosity. In fact, this latter feature can be proved analytically. Since $\mu = 0$ begins at porosity 60%, we substitute $\mu = 0$ and $\mu_2 = 0$ into (5.3) and find that it just reduces to the Reuss' bound K_R ,

$$\begin{aligned}\frac{1}{K} &= \frac{1}{K_1} + \frac{(K_1 - K_2)\phi_2}{K_1 K_2} \\ &= \frac{1 - \phi_2}{K_1} + \frac{\phi_2}{K_2} \\ &= \frac{1}{K_R}.\end{aligned}\tag{5.5}$$

Compared with the definition of critical porosity, the asymmetric self-consistent solution yields about 60% critical porosity for inviscid spherical fluid inclusions.

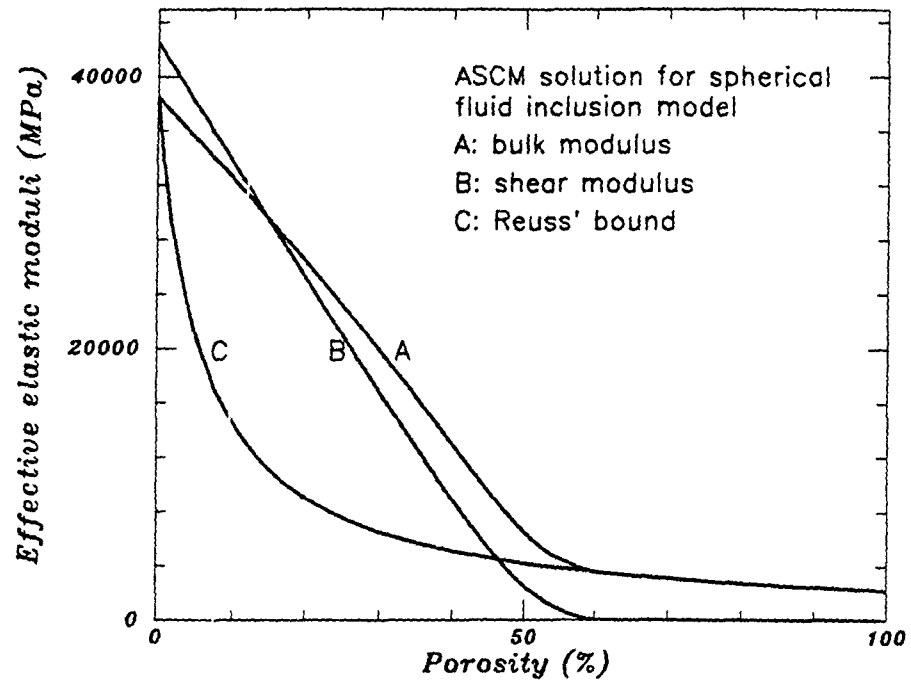
5.2.2 Cylindrical inclusion model

When cylindrical inclusions are randomly oriented in space, the effective elastic moduli are isotropic. The asymmetric self-consistent solution obtained by Walpole (1969) can be rewritten as

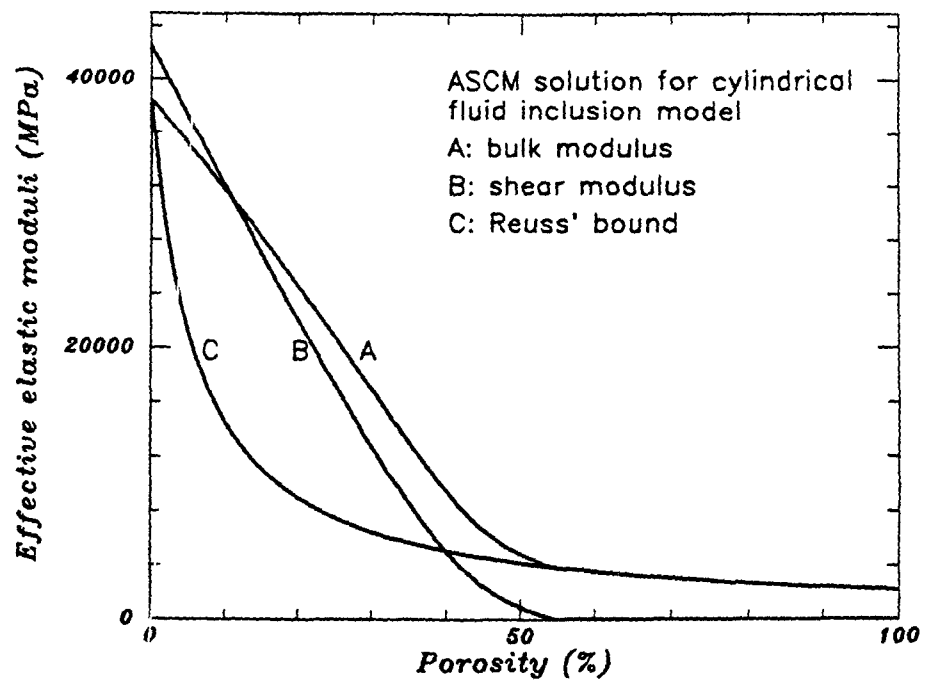
$$\frac{K_1 - K_2}{K - K_2} = 1 + \left[1 + \frac{3(K_1 - K_2)}{3K_2 + \mu_2 + 3\mu}\right] \frac{\phi_2}{1 - \phi_2},\tag{5.6}$$

$$\begin{aligned}\frac{\mu_1 - \mu_2}{\mu - \mu_2} &= 1 + \left[1 + \frac{\mu_1 - \mu_2}{5} \left(\frac{6K_2 + 3\mu_2 + 7\mu}{(\mu_2 + \mu)(3K_2 + \mu_2 + 3\mu)} + \right. \right. \\ &\quad \left. \left. + \frac{2(3K + 7\mu)}{\mu(3K + \mu) + \mu_2(3K + 7\mu)} \right) \right] \frac{\phi_2}{1 - \phi_2}.\end{aligned}\tag{5.7}$$

For inviscid fluid saturation, the numerical results in Fig.5.1(b) indicate about 55% critical porosity for cylindrical fluid inclusions.



(a)



(b)

Fig.5.1 Effective elastic modulus-porosity relations of a fluid-saturated material predicted by the asymmetric self-consistent solutions. (a) spherical fluid inclusion model, (b) cylindrical fluid inclusion model.

5.2.3 Infinitesimal-thin disk inclusion model

Under the condition $K_2 \neq 0$ and $\mu_2 \neq 0$ simultaneously, the asymmetric self-consistent solution obtained by Walpole (1969) can be rewritten as

$$\frac{K_1 - K_2}{K - K_2} = 1 + \left[1 + \frac{3(K_1 - K_2)}{3K_2 + 4\mu_2} \right] \frac{\phi_2}{1 - \phi_2}, \quad (5.8)$$

$$\frac{\mu_1 - \mu_2}{\mu - \mu_2} = 1 + \left[1 + \frac{4(\mu_1 - \mu_2)}{5(3K + 4\mu_2)} + \frac{2(\mu_1 - \mu_2)}{5\mu_2} \right] \frac{\phi_2}{1 - \phi_2}. \quad (5.9)$$

Since the inclusion is assumed infinitesimal thin, the inclusion volume fraction ϕ_2 should be replaced by some other parameter such as inclusion density. Theoretically, μ becomes zero at 0% porosity, and $k = K_R$ beginning at 0% porosity for inviscid fluid saturation.

5.3 Solution for penny-shaped inclusion model

From the nondilute concentration solutions in chapter 2 we know the inclusion geometry effects as follows: prolate inclusions result in effective elastic moduli between those of spherical and cylindrical inclusions; oblate inclusions with about $\eta = 0.5$ yields effective elastic moduli equivalent to those of cylindrical inclusions; with smaller aspect ratio, the penny-shaped inclusions yield effective elastic moduli lower than those of cylindrical inclusions. It is reasonable to believe that such inclusion geometry effects hold in either the dilute solutions or the asymmetric self-consistent solutions. But in the literature we haven't seen any presentation of asymmetric self-consistent solution for penny-shaped inclusion model (Watt et al., 1976; Jizba and Mavko, 1990). On the other hand, almost all experimental data of wave velocities in fluid-saturated rocks and sediments fall within the domain bounded by the asymmetric self-consistent solutions of cylindrical and infinitesimal-thin disk inclusions (Tosaya, 1982; Han, 1986;

Jizba and Mavko, 1990). Consequently, there is a need to find the asymmetric self-consistent solution for penny-shaped inclusion model.

Walsh (1969) found the dilute solution for penny-shaped inclusions by simplifying a self-consistent procedure adapted from Wu's study (Wu, 1966). We examine Walsh's derivation, correct the misprint in one of his formulas, and obtain the asymmetric self-consistent solution for flat-oblate inclusion model,

$$\begin{aligned}\frac{K_1}{K} &= 1 + T_{iijj} \left(\frac{K_1 - K_2}{3K} \phi_2 \right) \\ &= 1 + \frac{3K + 4\mu_2}{3K_2 + 4\mu_2 + 3\pi\eta\mu(3K + \mu)/(3K + 4\mu)} \frac{K_1 - K_2}{K} \phi_2, \quad (5.10)\end{aligned}$$

$$\begin{aligned}\frac{\mu_1}{\mu} &= 1 + (3T_{ijij} - T_{iijj}) \left(\frac{\mu_1 - \mu_2}{15\mu} \phi_2 \right) \\ &= 1 + \left[1 + \frac{8\mu}{4\mu_2 + 3\pi\eta\mu(3K + 2\mu)/(3K + 4\mu)} + \right. \\ &\quad \left. + \frac{2(3K_2 + 2\mu_2 + 2\mu)}{3K_2 + 4\mu_2 + 3\pi\eta\mu(3K + \mu)/(3K + 4\mu)} \right] \frac{\mu_1 - \mu_2}{5\mu} \phi_2, \quad (5.11)\end{aligned}$$

where

$$T_{iijj} = \frac{3(3K + 4\mu_2)}{3K_2 + 4\mu_2 + 3\pi\eta\mu(3K + \mu)/(3K + 4\mu)}, \quad (5.12)$$

$$\begin{aligned}T_{ijij} &= 1 + \frac{8\mu}{4\mu_2 + 3\pi\eta\mu(3K + 2\mu)/(3K + 4\mu)} + \\ &\quad + \frac{2(3K_2 + 4\mu_2) + 3K + 4\mu}{3K_2 + 4\mu_2 + 3\pi\eta\mu(3K + \mu)/(3K + 4\mu)}. \quad (5.13)\end{aligned}$$

When the inviscid fluid inclusions are considered, $K_2 \neq 0$, $\mu_2 = 0$, the above solution reduces to

$$\frac{K_1}{K} = 1 + \frac{(K_1 - K_2)(3K + 4\mu)}{K_2(3K + 4\mu) + \pi\eta\mu(3K + \mu)}\phi_2, \quad (5.14)$$

$$\frac{\mu_1}{\mu} = 1 + \left[1 + \frac{8(3K + 4\mu)}{3\pi\eta(3K + 2\mu)} + \frac{2(3K_2 + 2\mu)(3K + 4\mu)}{3K_2(3K + 4\mu) + 3\pi\eta\mu(3K + \mu)}\right]\frac{\mu_1\phi_2}{5\mu}. \quad (5.15)$$

Let $\eta = 0$, above equations reduce to solution for the infinitesimal-thin disk inclusion model.

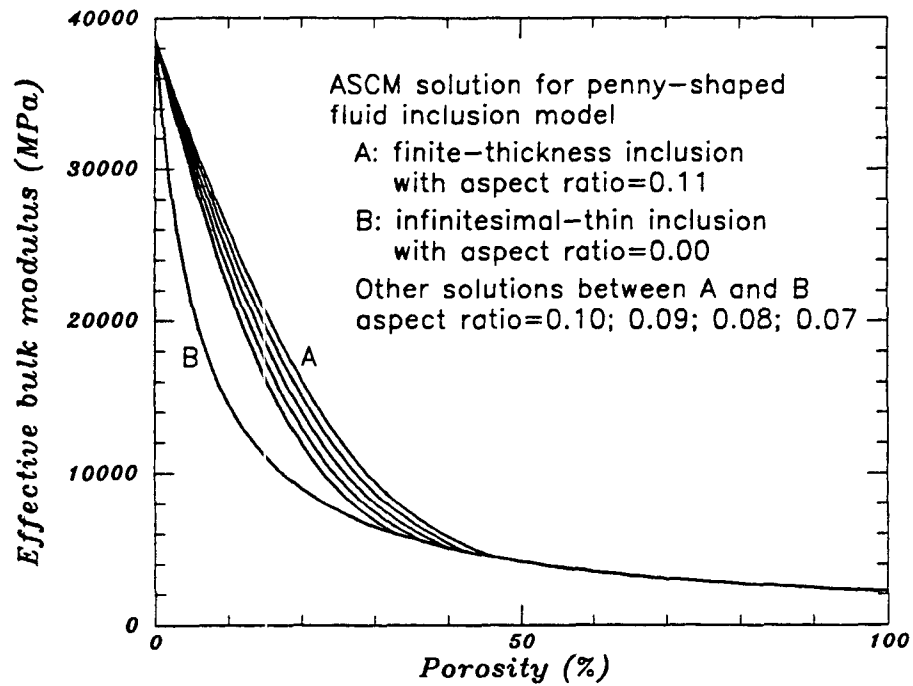
For flat-oblate or finite-thickness penny-shaped inclusions, we find that the above solution is appropriate to describe inclusions with the aspect ratio around 10^{-1} . Fig. 5.2(a) and (b) show the effective bulk and shear moduli versus porosity with aspect ratios ranging $0.07 \sim 0.11$. The critical porosities for each value of the aspect ratio can be clearly seen from Fig.5.2(b). After the critical porosity, the effective bulk modulus K reduces to K_R . Fig.5.3 shows the asymmetric self-consistent solution for a broader range of aspect ratios, including the spherical and cylindrical inclusions. Thus we complete a series of asymmetric self-consistent solutions especially useful for fluid-saturated porous materials.

5.4 Velocity-porosity Relations and Comparison

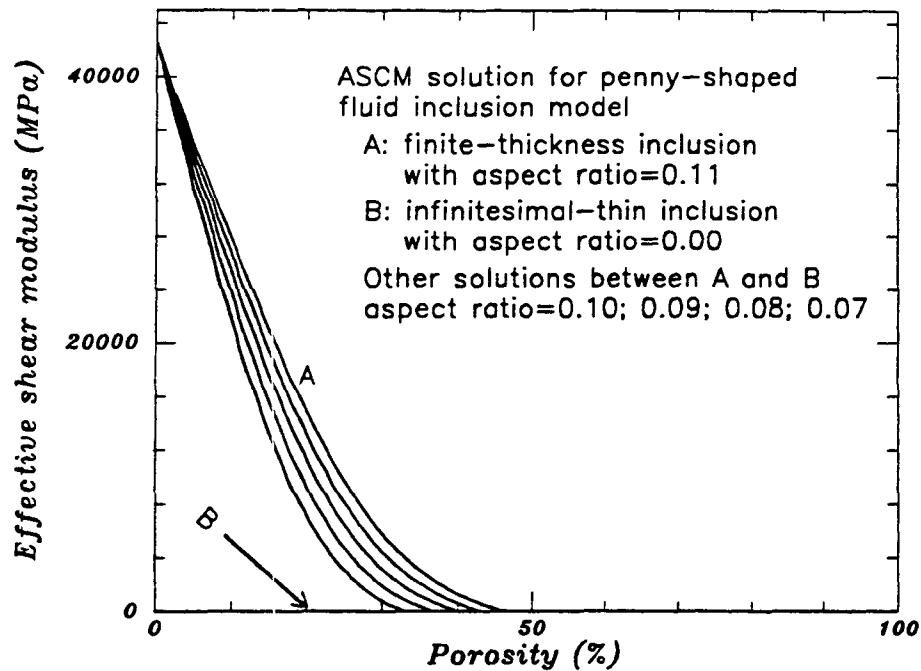
5.4.1 ASCM wave velocity-porosity relations

Given the effective elastic moduli of a fluid-saturated material predicted by the asymmetric self-consistent solution, the low-frequency or long-wavelength P-wave and S-wave velocities, V_p , V_s , are then calculated from the relations

$$V_p = \sqrt{\frac{K + \frac{4\mu}{3}}{\rho}}, \quad V_s = \sqrt{\frac{\mu}{\rho}}, \quad (5.16)$$

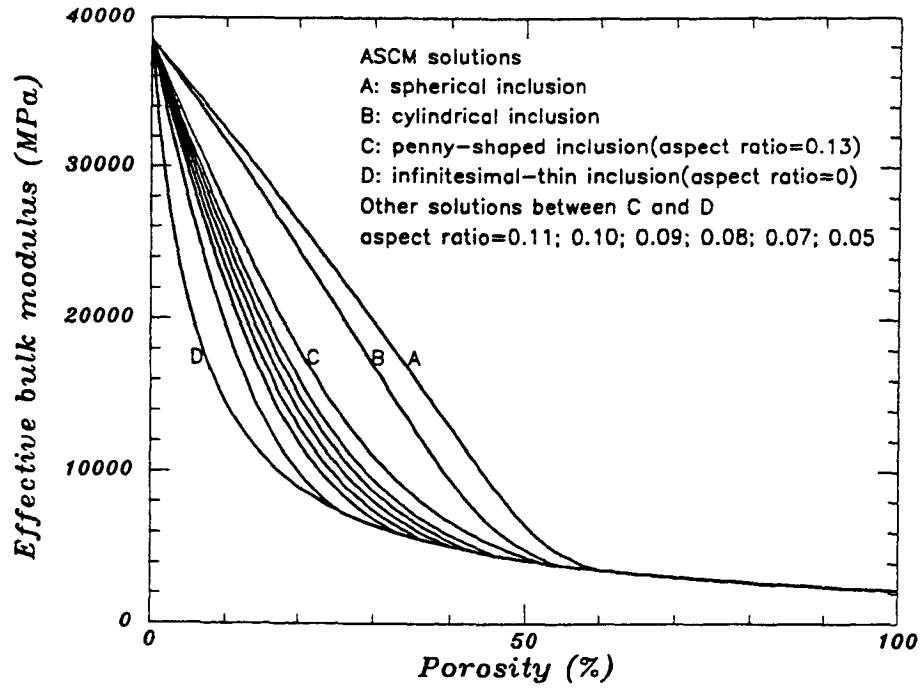


(a)

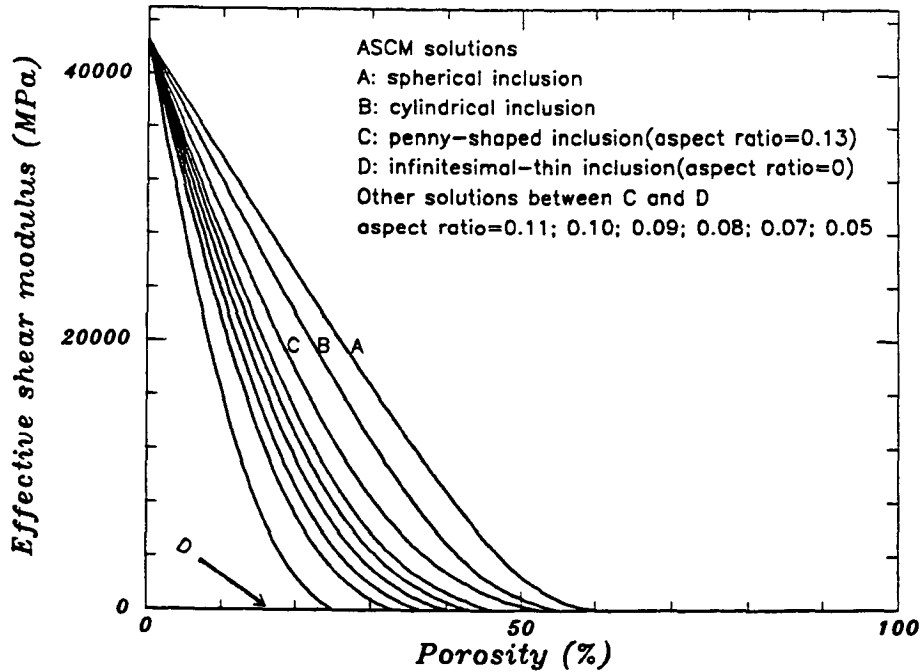


(b)

Fig.5.2 Effective elastic modulus-porosity relations of a fluid-saturated material predicted by the asymmetric self-consistent solution with penny-shaped inclusions. (a) effective bulk modulus-porosity relation, (b) effective shear modulus-porosity relation.



(a)



(b)

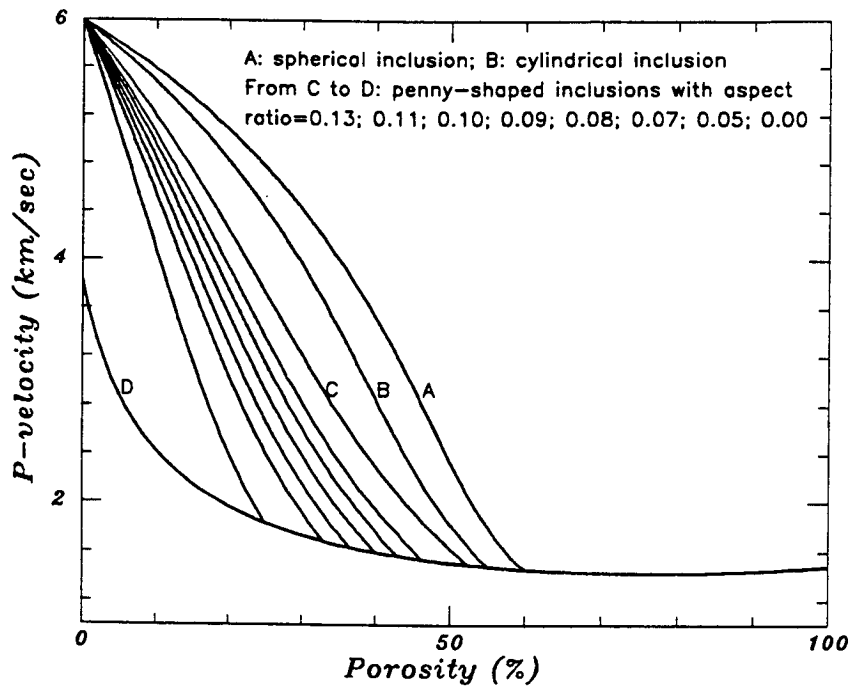
Fig.5.3 Effective elastic modulus-porosity relations of a fluid-saturated material predicted by the asymmetric self-consistent solutions with spheroidal inclusions. (a) effective bulk modulus-porosity relation, (b) effective shear modulus-porosity relation.

where the effective density ρ is related to sand grain density ρ_1 and fluid inclusion density ρ_2 by $\rho = (1 - \phi_2)\rho_1 + \phi_2\rho_2$. In the following calculation, $\rho_1 = 2650\text{kgm}^{-3}$ for sand grains and $\rho_2 = 1000\text{kgm}^{-3}$ for water are used.

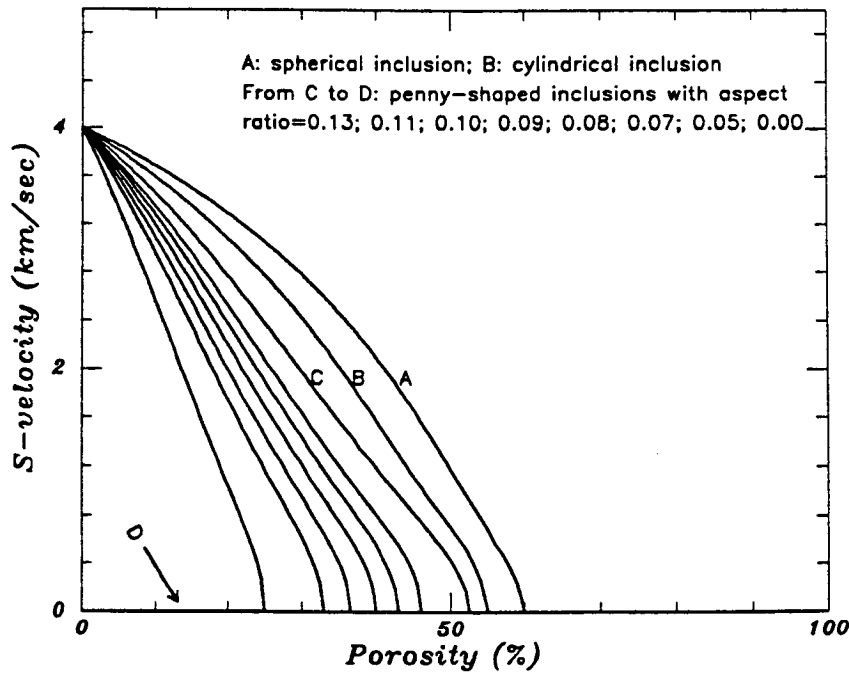
Fig.5.4 shows the wave velocity-porosity relations for water-saturated materials with spheroidal inclusion geometries. The critical porosity ranges from zero to 60% depending on the inclusion aspect ratio. The neighboring domains of the cylindrical inclusion solution are characterized by the aspect ratio around 10^{-1} . After the critical porosity, all solutions reduce to the Reuss' bound $K = K_R$, $\mu = \mu_R = 0$, and so it follows that wave velocities in the fluid matrix-supported materials are independent of the solid inclusion geometries.

5.4.2 Comparison with experimental data

For the solid matrix-supported materials like most fluid-saturated rocks, numerous experimental studies indicate that the confining pressure changes the density, porosity, the effective elastic moduli, and so the wave velocities. Although the asymmetric self-consistent solutions in the above do not take into account those pressure-dependent effects, they still provide some explanations of the pressure-dependent wave velocities through the assumption that the confining pressure effect can be reflected by the varying of inclusion aspect ratios. Han et al. (1986) obtained wave velocity data of 10 clay-free sandstone samples in the confining pressure ranging from 5 to 40MPa. Fig.5.5 compares the P and S wave velocity data at 5MPa confining pressure with the ASCM solution for penny-shaped inclusion models. We see that the models with aspect ratios 0.11 ~ 0.13 best fit the data, corresponding to 46% ~ 52% critical porosities. However, in Fig.5.6 where wave velocity data at 40MPa confining pressure are compared, the appropriate model seem to be the penny-shaped inclusion model with aspect ratios 0.14 ~ 0.15, When these pore aspect ratios are understood as the meaning of "average" and "initial value" of microstructure features, it is reasonable to infer that higher confining pressure leads to the partial or complete closure of those



(a)



(b)

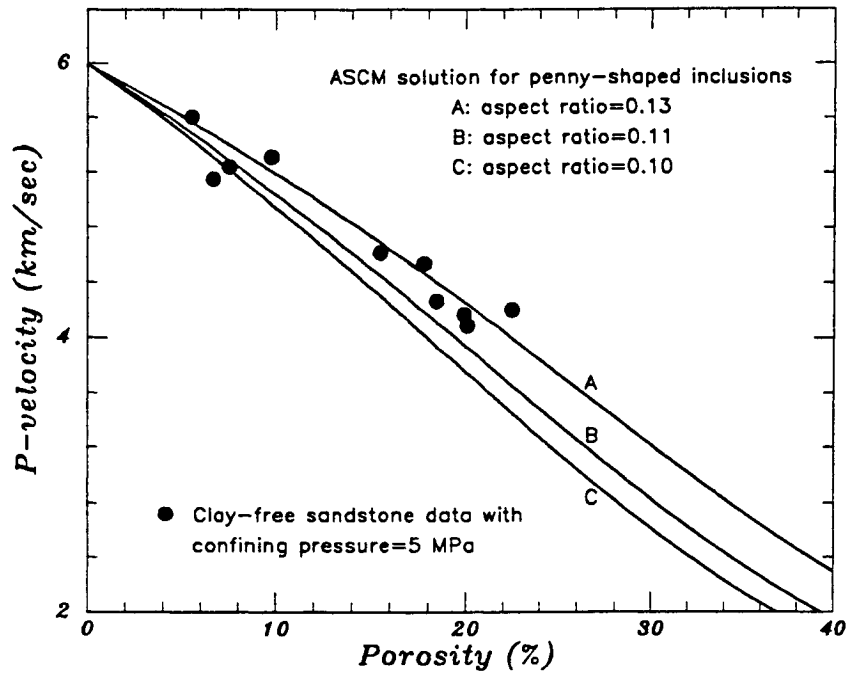
Fig.5.4 Wave velocity-porosity relations of a fluid-saturated material predicted by the asymmetric self-consistent solutions with spheroidal inclusions. (a) P wave velocity-porosity relation, (b) S wave velocity-porosity relation.

inclusions with smaller aspect ratios, and so the remaining inclusions yield a larger value of “average” aspect ratio and also the critical porosity.

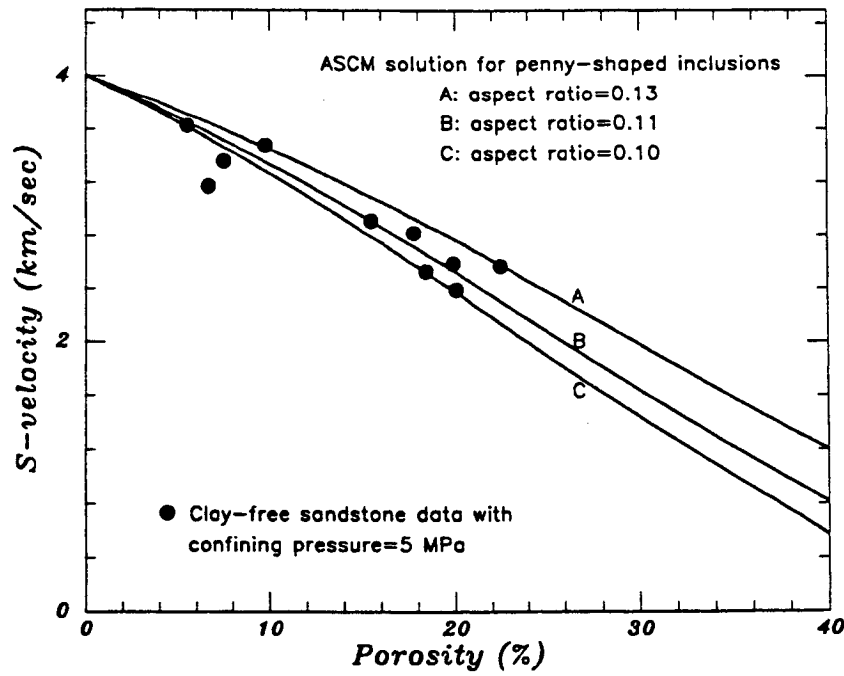
5.4.3 Comparison with critical concentration solutions

In chapters 3 and 4, critical porosity can be determined by several approaches and it is an input parameter for the critical concentration solution of porous materials. In chapter 5 the inclusion aspect ratio is an input parameter for the asymmetric self-consistent solution and the critical porosity turns out as a unique feature of the solution. When these two types of critical porosities are set as same value for a given porous material, what will be the effective modulus-porosity and velocity-porosity relations predicted by the critical concentration solution and the asymmetric self-consistent solution?

Fig.5.7 compares these two types of solutions to effective bulk modulus-porosity and P wave velocity-porosity relations for a fluid-saturated porous material. Spherical fluid inclusions are used in the asymmetric self-consistent solution which yields 60% critical porosity. Then 60% critical porosity is used in the critical concentration solutions extended from Voigt's, Hashin-Shtrikman's and Mori-Tanaka's relations. When spherical fluid inclusions are used in the Mori-Tanaka's relation, the resulting critical concentration solutions from Hashin-Shtrikman's and Mori-Tanaka's relations become identical to each other. Fig.5.7(a) indicates that at porosities up to 20%, the asymmetric self-consistent solution is equivalent to the critical concentration solution extended from Voigt's relation, that at porosities between 20% ~ 45%, the asymmetric self-consistent solution is between the critical concentration solutions extended from Voigt's and Hashin-Shtrikman's relations, that at porosities between 45% ~ *critical porosity*, the asymmetric self-consistent solution is lower than the solution extended from Hashin-Shtrikman's relation, and that after the critical porosity, all solutions become the same. Those solutions have similar features for effective shear modulus. As a result, for P wave velocity-porosity relations in Fig.5.7(b), the asym-

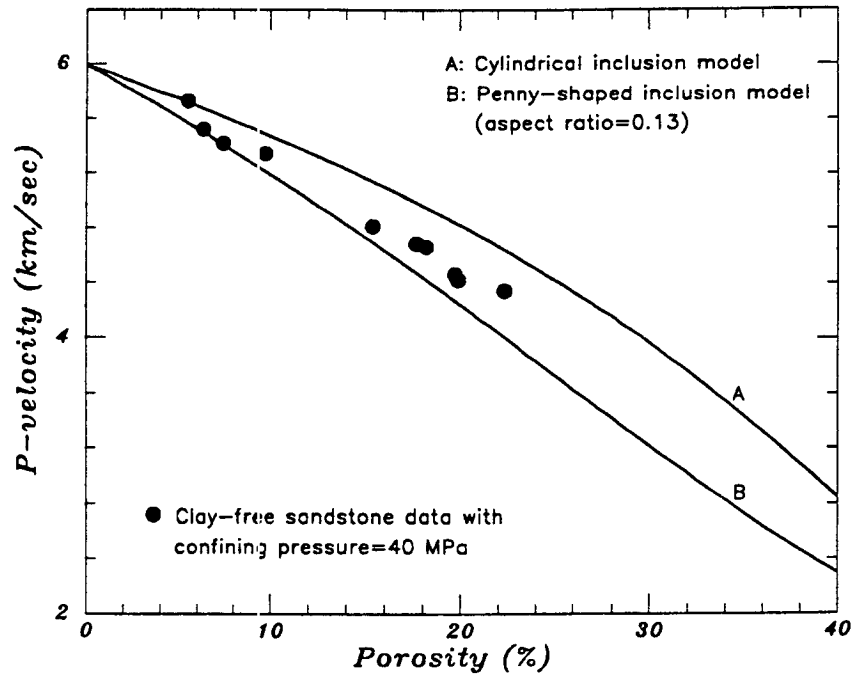


(a)

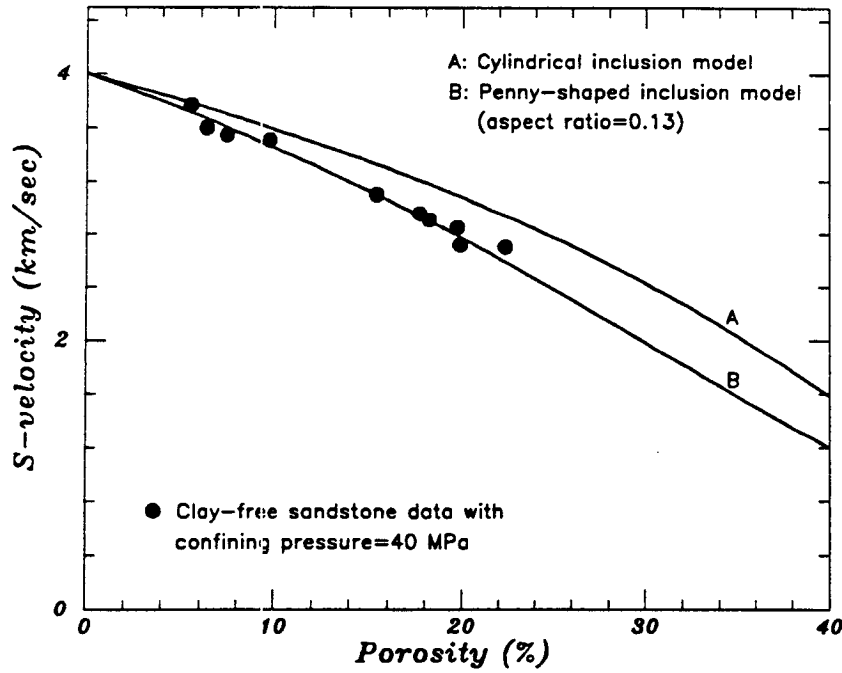


(b)

Fig.5.5 Comparison of wave velocity-porosity relations between Han's experimental data at 5 MPa confining pressure and predicted result from asymmetric self-consistent solution with penny-shaped inclusions. (a) P wave velocity-porosity relation, (b) S wave velocity-porosity relation.



(a)



(b)

Fig.5.6 Comparison of wave velocity-porosity relations between Han's experimental data at 40 MPa confining pressure and predicted result from asymmetric self-consistent solution with penny-shaped inclusions. (a) P wave velocity-porosity relation, (b) S wave velocity-porosity relation.

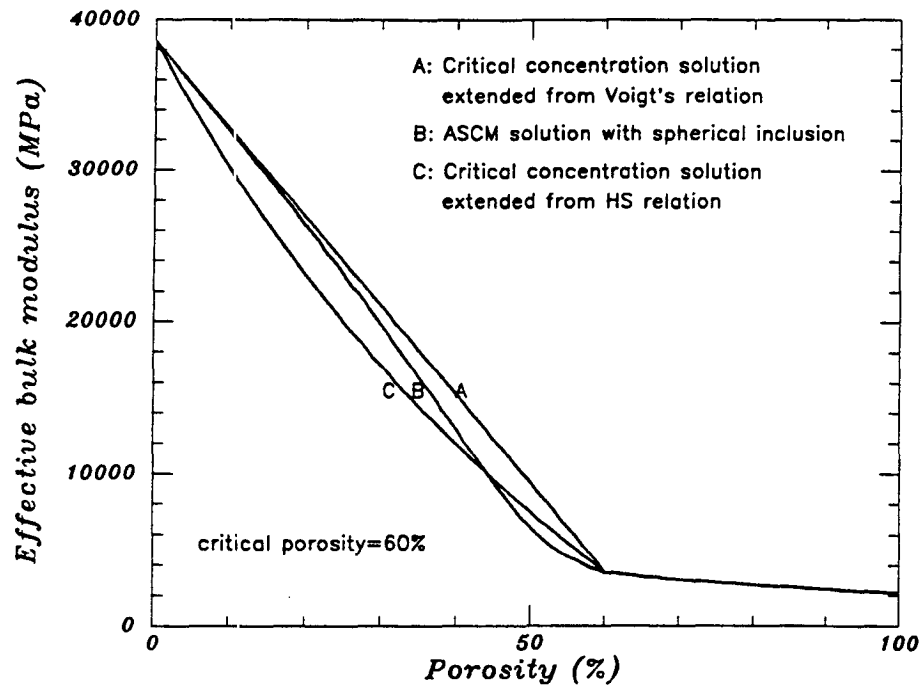
metric self-consistent solutions is between the solutions extended from Voigt's and Hashin-Shtrikman's relations up to 45% porosity, and they become identical after the critical porosity. These results lead to following conclusions: although the asymmetric self-consistent solution for spherical inclusions may not be very accurate near the critical porosity, it works quite well for a broad range of porosity, almost up to the critical porosity, and it is exact after the critical porosity.

Penny-shaped pore and cracks have been used frequently as a class of microstructural models for porous rocks like sandstones. Fig.5.8 compares the effective bulk modulus-porosity and P wave velocity-porosity relations predicted by the critical concentration solution and the asymmetric self-consistent solution with penny-shaped inclusions. Penny-shaped fluid inclusions with aspect ratio $\eta = 10^{-1}$ are used in the asymmetric self-consistent solution which yields 43% critical porosity. Then such critical porosity is used in the critical concentration solutions. With the aspect ratio $\eta = 10^{-1}$ in Mori-Tanaka's relation, the critical concentration solutions extended from Hashin-Shtrikman's and Mori-Tanaka's relations are now different. For both the effective bulk modulus-porosity and P wave velocity-porosity relations, the asymmetric self-consistent solutions are always between the solution extended from Hashin-Shtrikman's and Mori-Tanaka's relations.

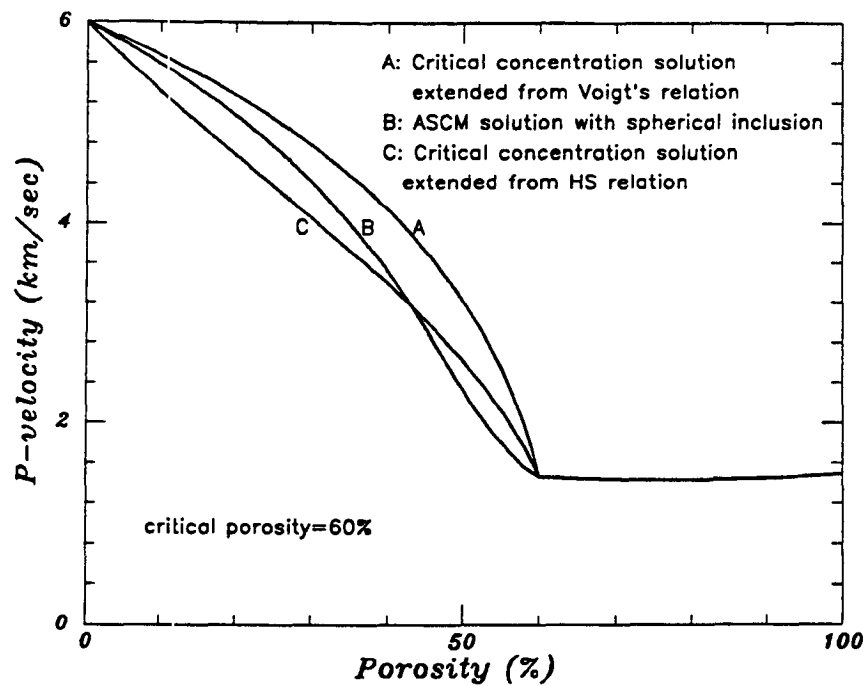
5.5 Clay Effects on Effective Elastic Moduli and Wave Velocities

5.5.1 Clay cementation and material porosity

Clay-bearing fluid-saturated materials can be taken as three-phase materials with sand grain phase, clay phase, and fluid phase. The effect of clay phase on the effective moduli and wave velocities can be evaluated through the mechanical interaction between clay phase and other phases. To describe such an interaction, the cementation state of the clay with other phases is an important parameter to be considered.

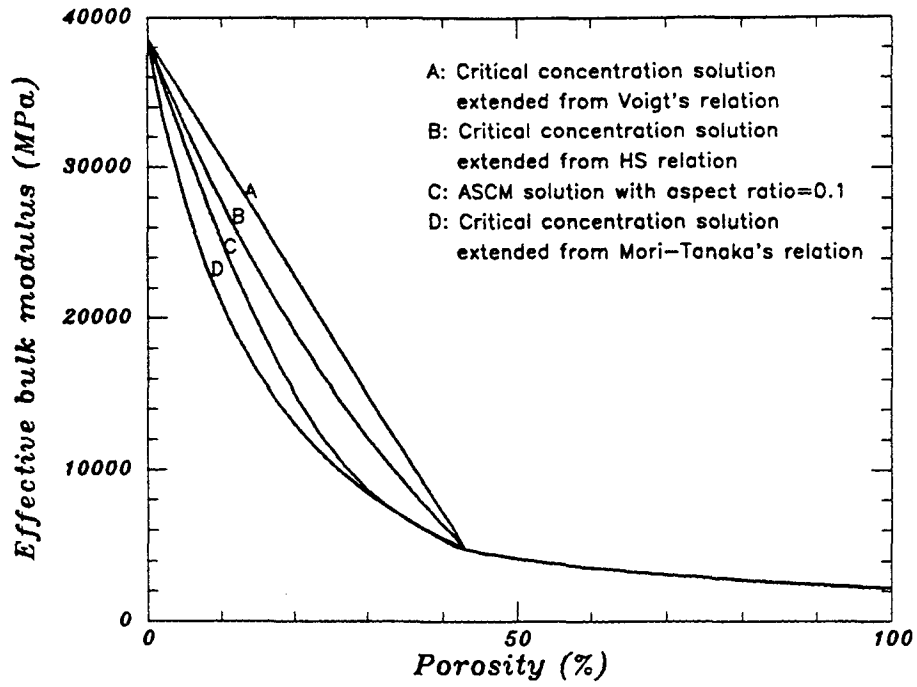


(a)

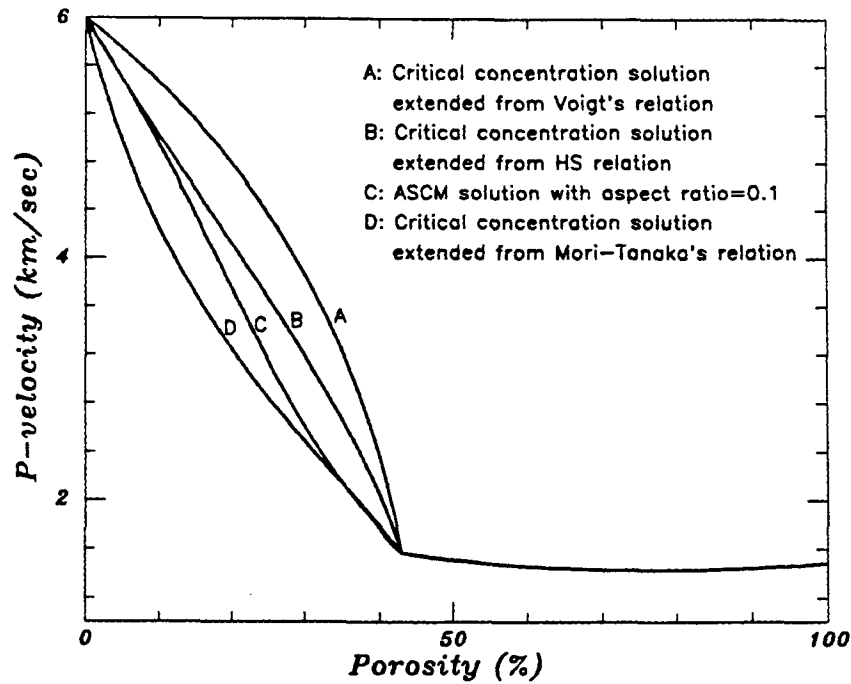


(b)

Fig.5.7 Effective bulk modulus-porosity and P wave velocity-porosity relations predicted by the critical concentration solutions and the asymmetric self-consistent solution for spherical fluid inclusions. (a) effective bulk modulus-porosity relation, (b) P wave velocity-porosity relation.



(a)



(b)

Fig.5.8 Effective bulk modulus-porosity and P wave velocity-porosity relations predicted by the critical concentration solutions and the asymmetric self-consistent solution for penny-shaped fluid inclusions. (a) effective bulk modulus-porosity relation, (b) P wave velocity-porosity relation.

Here we extend the asymmetric self-consistent solutions from two-phase materials to three-phase materials by incorporating the clay volume fraction ϕ_3 , clay cementation coefficient λ , and clay microporosity ϕ_{cm} into a unified model.

The clay cementation coefficient λ is defined as follows. Given a clay volume fraction ϕ_3 , a portion of the clay is cemented with the sand grains, with the volume fraction ϕ'_3 , and the other portion ϕ''_3 is in uncemented state. Then we have

$$\phi_3 = \phi'_3 + \phi''_3, \quad \lambda = \frac{\phi'_3}{\phi_3}, \quad 0 \leq \lambda \leq 1. \quad (5.17)$$

Accordingly, $\lambda = 1$ means complete cementation of the clay phase, and $\lambda = 0$ means the completely-uncemented state of the clay phase.

For the cemented clay, the powder particle assemblages or clusters are supposed to fill with cements, which means that the clay microporosity ϕ_{cm} should be zero, or negligible. In the situation of complete cementation of the clay phase ($\lambda = 1$), only one parameter ϕ_3 of the clay phase is involved into the determination of porosity ϕ_2 ,

$$\phi_2 = 1 - \phi_1 - \phi_3. \quad (5.18)$$

In the situation of completely-uncemented clay phase ($\lambda = 0$), the porosity ϕ_2 depends on two parameters describing the clay phase: clay volume fraction ϕ_3 and clay microporosity ϕ_{cm} ,

$$\phi_2 = 1 - \phi_1 - \phi_3(1 - \phi_{cm}). \quad (5.19)$$

The concept of pore-filling clay, as used in chapter 4, is equivalent to the completely-uncemented clay. If χ is used to represent the ratio of clay volume fraction ϕ_3 to the supposed pore volume fraction ($1 - \phi_1$), the porosity is given by

$$\phi_2 = (1 - \phi_1)[1 - \chi(1 - \phi_{cm})]. \quad (5.20)$$

Generally the porosity of material with $0 \leq \lambda \leq 1$ is given by three parameters describing the clay phase,

$$\phi_2 = 1 - \phi_1 - \phi_3[1 - (1 - \lambda)\phi_{cm}]. \quad (5.21)$$

5.5.2 Asymmetric self-consistent solutions with clay phase

When the clay phase is in complete cementation state, the solid phase of a fluid-saturated material is composed of the sand grain phase and cemented clay phase. Suppose that the overall elastic moduli of the solid phase are represented by K_{13} and μ_{13} , then the asymmetric self-consistent solution for the penny-shaped pore model is

$$\frac{K_{13}}{K} = 1 + \frac{3K + 4\mu_2}{3K_2 + 4\mu_2 + 3\pi\eta\mu(3K + \mu)/(3K + 4\mu)} \frac{K_{13} - K_2}{K} \phi_2, \quad (5.22)$$

$$\begin{aligned} \frac{\mu_{13}}{\mu} = & 1 + \left[1 + \frac{8\mu}{4\mu_2 + 3\pi\eta\mu(3K + 2\mu)/(3K + 4\mu)} + \right. \\ & \left. + \frac{2(3K_2 + 2\mu_2 + 2\mu)}{3K_2 + 4\mu_2 + 3\pi\eta\mu(3K + \mu)/(3K + 4\mu)} \right] \frac{\mu_{13} - \mu_2}{5\mu} \phi_2. \end{aligned} \quad (5.23)$$

When the clay phase is in completely-uncemented state, the clay particles may be in the form of isolated cluster with a certain microporosity, along with the fluid phase, to fill in the space among sand grains. Suppose that the subsystem of clay phase and fluid phase are described by the overall elastic moduli K_{23} and μ_{23} , the asymmetric self-consistent solution for the penny-shaped pore model is

$$\frac{K_1}{K} = 1 + \frac{3K + 4\mu_{23}}{3K_{23} + 4\mu_{23} + 3\pi\eta\mu(3K + \mu)/(3K + 4\mu)} \frac{K_1 - K_{23}}{K} (1 - \phi_1), \quad (5.24)$$

$$\begin{aligned} \frac{\mu_1}{\mu} = & 1 + \left[1 + \frac{8\mu}{4\mu_{23} + 3\pi\eta\mu(3K + 2\mu)/(3K + 4\mu)} + \right. \\ & \left. + \frac{2(3K_{23} + 2\mu_{23} + 2\mu)}{3K_{23} + 4\mu_{23} + 3\pi\eta\mu(3K + \mu)/(3K + 4\mu)} \right] \frac{\mu_1 - \mu_{23}}{5\mu} (1 - \phi_1). \end{aligned} \quad (5.25)$$

where the factor $(1 - \phi_1)$ can be replaced by $[\phi_2 + \phi_3(1 - \phi_{cm})]$.

Based on above analysis, the asymmetric self-consistent solution with penny-shaped pore model for a fluid-saturated material with cemented clay $\lambda\phi_3$ and uncemented clay $(1 - \lambda)\phi_3$ is given by

$$\frac{K_{13}}{K} = 1 + \frac{3K + 4\mu_{23}}{3K_{23} + 4\mu_{23} + 3\pi\eta\mu(3K + \mu)/(3K + 4\mu)} \frac{K_{13} - K_{23}}{K} [\phi_2 + \phi_3(1 - \lambda)(1 - \phi_{cm})], \quad (5.26)$$

$$\begin{aligned} \frac{\mu_{13}}{\mu} = & 1 + \left[1 + \frac{8\mu}{4\mu_{23} + 3\pi\eta\mu(3K + 2\mu)/(3K + 4\mu)} + \right. \\ & \left. + \frac{2(3K_{23} + 2\mu_{23} + 2\mu)}{3K_{23} + 4\mu_{23} + 3\pi\eta\mu(3K + \mu)/(3K + 4\mu)} \right] \frac{\mu_{13} - \mu_{23}}{5\mu} [\phi_2 + \phi_3(1 - \lambda)(1 - \phi_{cm})]. \end{aligned} \quad (5.27)$$

where K_{13} , μ_{13} , K_{23} , and μ_{23} for a material system of porous rocks, sediments, and marine suspensions can be determined as

$$\frac{K_1}{K_{13}} = 1 + \frac{3K_{13} + 4\mu_3}{3K_3 + 4\mu_3 + 3\pi\eta\mu_{13}(3K_{13} + \mu_{13})/(3K_{13} + 4\mu_{13})} \frac{K_1 - K_3}{K_{13}} \frac{\lambda\phi_3}{\phi_1 + \lambda\phi_3}, \quad (5.28)$$

$$\begin{aligned} \frac{\mu_1}{\mu_{13}} = & 1 + \left[1 + \frac{8\mu_{13}}{4\mu_3 + 3\pi\eta\mu_{13}(3K_{13} + 2\mu_{13})/(3K_{13} + 4\mu_{13})} + \right. \\ & \left. + \frac{2(3K_3 + 2\mu_3 + 2\mu_{13})}{3K_3 + 4\mu_3 + 3\pi\eta\mu_{13}(3K_{13} + \mu_{13})/(3K_{13} + 4\mu_{13})} \right] \frac{\mu_1 - \mu_3}{5\mu_{13}} \frac{\lambda\phi_3}{\phi_1 + \lambda\phi_3}, \end{aligned} \quad (5.29)$$

$$\begin{aligned} \frac{1 - \phi_1 - \lambda\phi_3}{K_{23}} &= \frac{\phi_2 + \phi_3(1 - \lambda)(1 - \phi_{cm})}{K_{23}} \\ &= \frac{\phi_2}{K_2} + \frac{\phi_3(1 - \lambda)(1 - \phi_{cm})}{K_3}, \end{aligned} \quad (5.30)$$

$$\mu_{23} = 0. \quad (5.31)$$

For inviscid fluid saturation, above solutions will reduce to a generalized Reuss' bound after the critical porosity,

$$\frac{1}{K} = \frac{1 - [\phi_2 + \phi_3(1 - \lambda)(1 - \phi_{cm})]}{K_{13}} + \frac{\phi_2 + \phi_3(1 - \lambda)(1 - \phi_{cm})}{K_{23}}, \quad (5.32)$$

$$\mu = 0. \quad (5.33)$$

Fig.5.9 presents the asymmetric self-consistent solution to the effective modulus-porosity-clay relations for a fluid-saturated material with cemented clay phase. Since the shear modulus of the clay phase is much smaller than that of sand grains, the effective shear modulus μ drops much more compared with the effective bulk modulus. At low level of clay volume fraction, μ decreases more compared with the situation of high level of clay volume fraction.

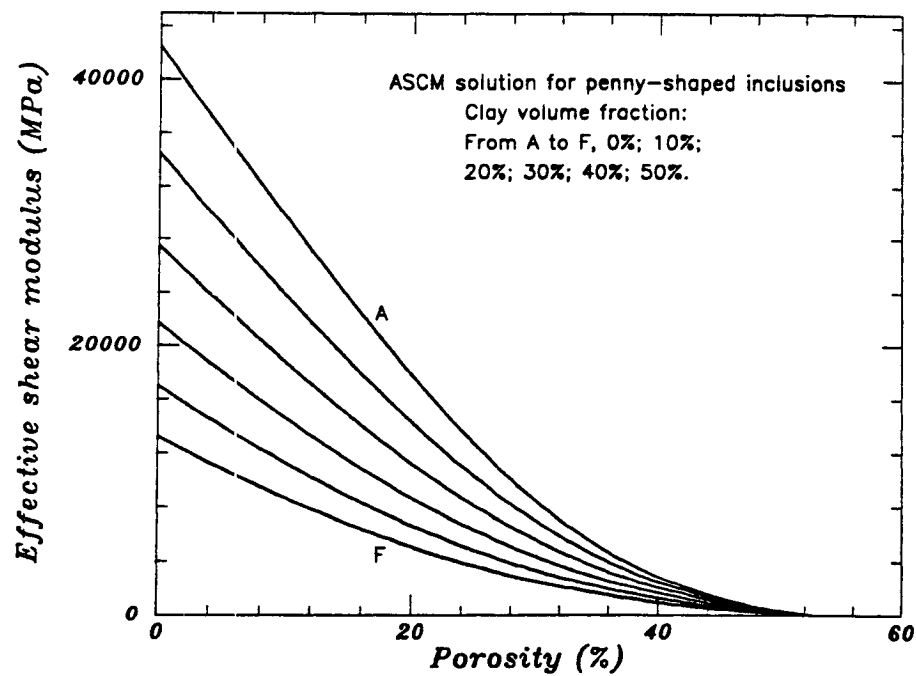
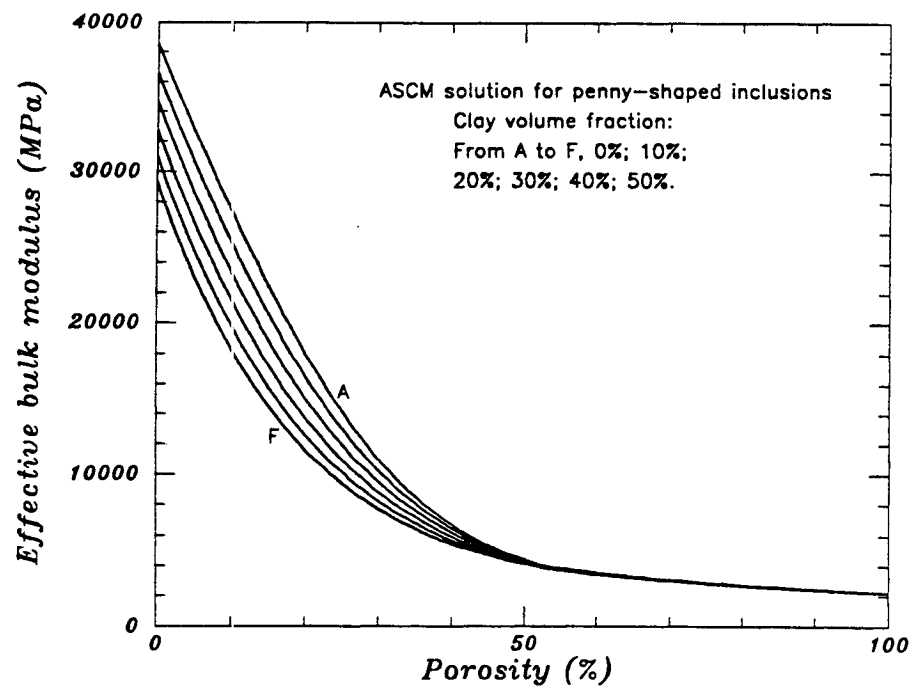


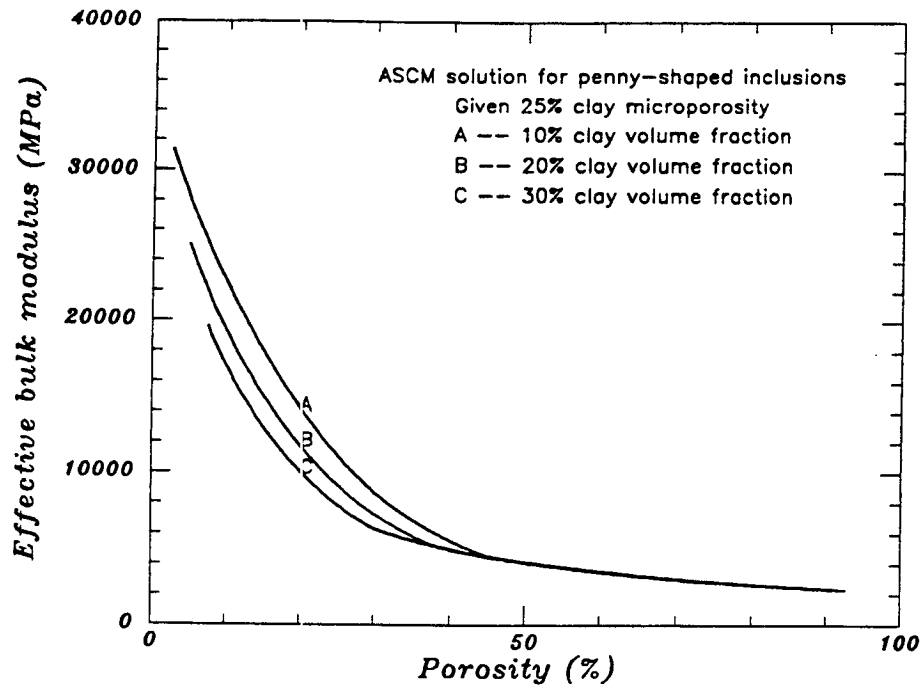
Fig.5.9 Asymmetric self-consistent solution to effective modulus-porosity-clay relations for a fluid-saturated material with cemented clay phase. (a) effective bulk modulus-porosity-clay relation, (b) effective shear modulus-porosity-clay relation.

Fig.5.10 shows the asymmetric self-consistent solution to effective modulus-porosity-clay relations for a fluid-saturated material with uncemented clay phase. Since the uncemented clay particles fill in sand grain spaces, the critical porosity decreases with the increase in clay content. The critical porosities for situations of 10%, 20%, and 30% clay volume fractions are 45.1%, 37.6%, and 30.2%, respectively. Once again, the clay effect on effective shear modulus is stronger than that on effective bulk modulus.

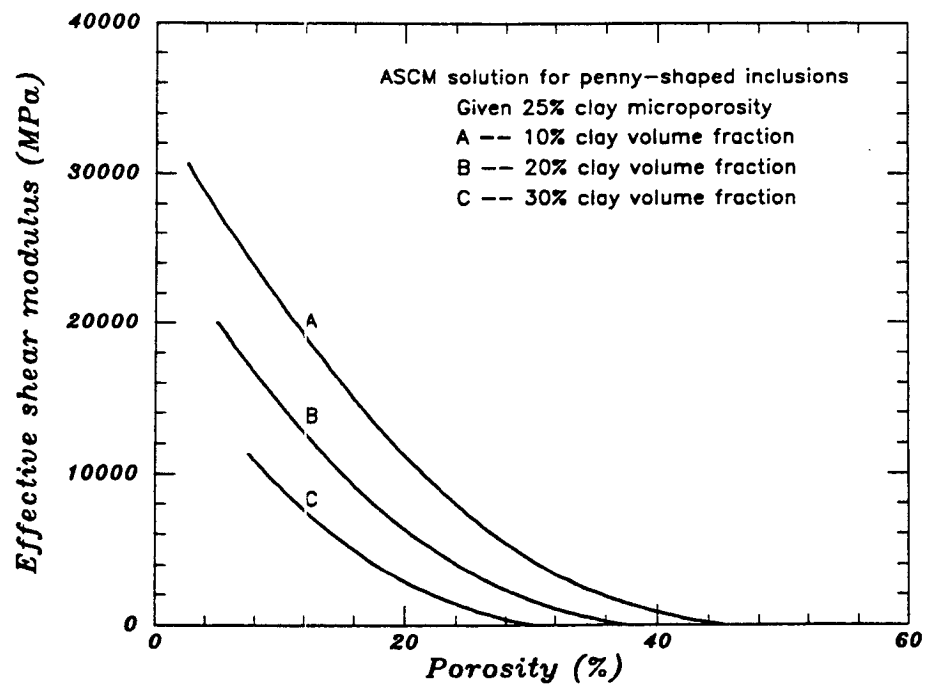
5.5.3 Comparison with velocity data

Han (1986) conducted extensive experiments of clay-bearing sandstones and observed that a few percent of clay can dramatically reduce the effective moduli and wave velocities of the rock. Han described this phenomenon as “bound clay effect”, and his explanation is that a few percent of tiny clay particles will be sufficient to cover all surfaces and boundaries of sand grains, which reduces the elastic moduli and wave velocities.

The bound clay effect can be better understood in terms of the clay cementation state. As indicated in Fig.5.11, given a clay content such as 10%, the uncemented clay causes the strongest decrease in effective moduli. In contrast with the intermediate and high levels of clay particles which may be just half-cemented or incompletely uncemented, the initial clay content such as a few percent may be in completely-uncemented state. Fig.5.12 compares the asymmetric self-consistent solution and experimental data of wave velocities with the cementation coefficient λ ranging from zero to one. Experimental data with clay volume fraction $0 \sim 10\%$ are used for comparison, and they are more close to the model results of completely-uncemented clay phase.

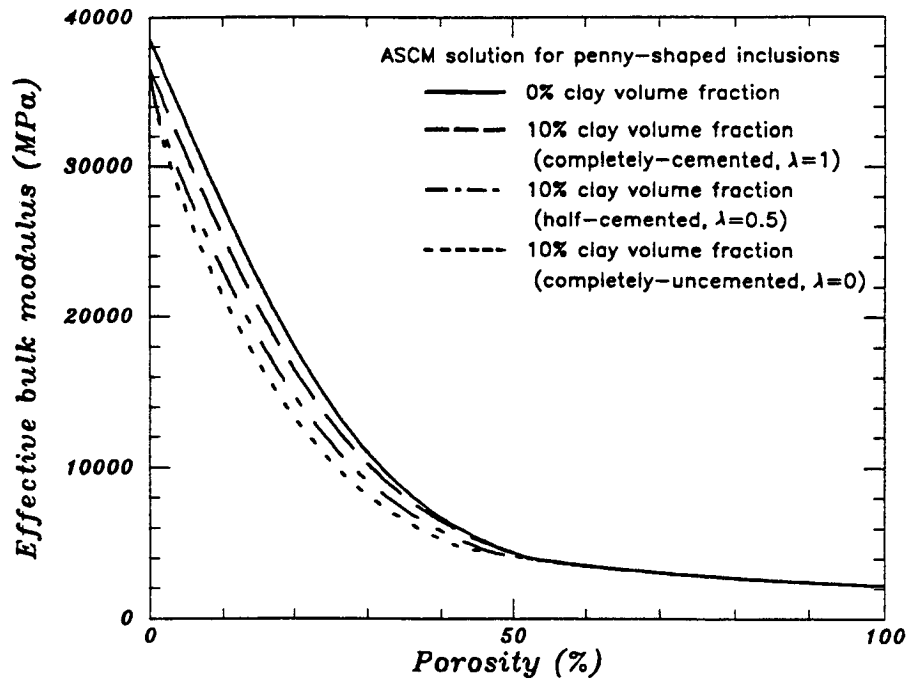


(a)

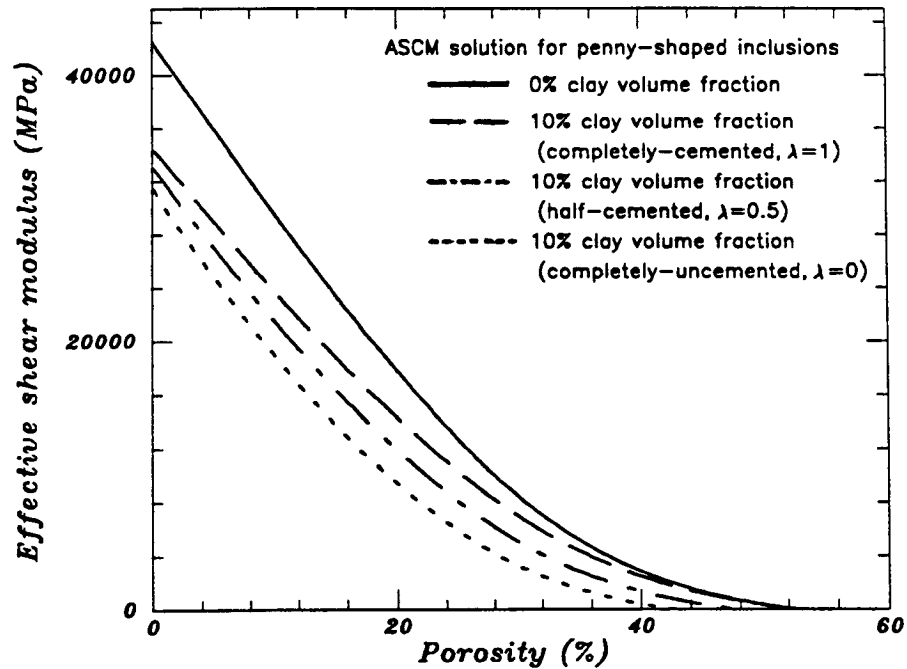


(b)

Fig.5.10 Asymmetric self-consistent solution to effective modulus-porosity-clay relations for a fluid-saturated material with un cemented clay phase. (a) effective bulk modulus-porosity-clay relation, (b) effective shear modulus-porosity-clay relation.

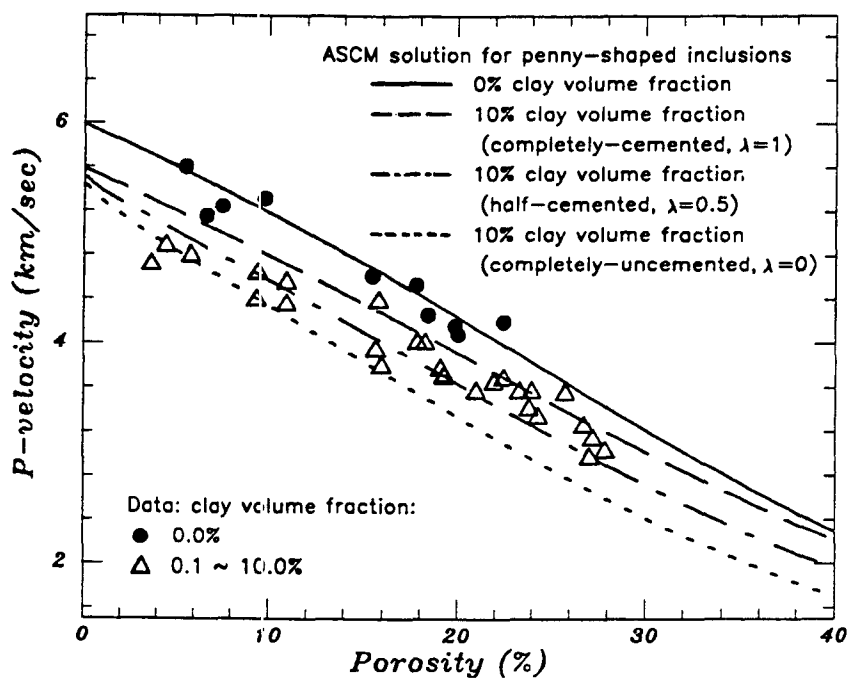


(a)

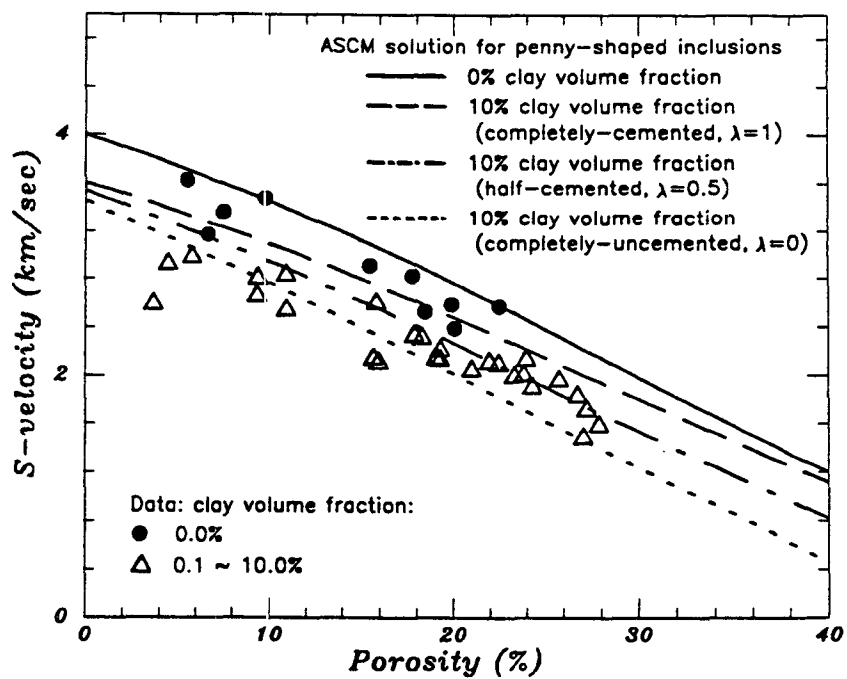


(b)

Fig.5.11 Asymmetric self-consistent solution to effective modulus-porosity-clay relations with varying clay cementation state. (a) effective bulk modulus-porosity-clay relation, (b) effective shear modulus.-porosity-clay relation.



(a)



(b)

Fig.5.12 Comparison between asymmetric self-consistent solution and experimental data of wave velocity-porosity-clay relations with varying clay cementation state. (a) P wave velocity-porosity-clay relation, (b) S wave velocity-porosity-clay relation.

5.6 Conclusions

Although both symmetric and asymmetric self-consistent methods yield the vanishing elastic moduli at finite porosity for porous materials, the latter is conceptually consistent with the critical porosity phenomena of porous materials. Asymmetric self-consistent solution for penny-shaped inclusions is found and is in agreement with experimental data of wave velocity-porosity relation.

By comparing the asymmetric self-consistent solutions with the critical concentration solutions of fluid-saturated porous materials, we conclude that the asymmetric self-consistent method and solution can be taken to advantage for evaluating effective properties of porous materials almost up to the critical porosity.

The clay effects on effective moduli and wave velocities of porous materials are investigated by extending the asymmetric self-consistent solutions to the incorporation of clay phase with varying cementation states. The results indicate that clay effect is stronger on effective shear modulus than on effective bulk modulus, and that uncemented clay effect is stronger than cemented clay effect, which are consistent with the experimental observations.

References

- Benguigui, L., 1984, Experimental study of the elastic properties of a percolating system, *Physical Review Letters*, **53**, 2028-2030.
- Berryman J. G., 1980, Long-wavelength propagation in composite elastic media I. spherical inclusions, *J. Acoust. Soc. Am.*, **68**, 1809-1819.
- Boucher, S., 1874, On the effective moduli of isotropic two-phase elastic composites, *J. Compos. Mater.*, **8**, 82-89.
- Budiansky, B., 1965, On the elastic moduli of some heterogeneous materials: *J. Mech. Phys. Solids*, **13**, 223-227.
- Hamilton, E. L., 1978, Sound velocity-density relations in sea-floor sediments and rocks, *J. Acoust. Soc. Am.*, **63**, 366-377.
- Han, D. H., 1986, Effects of porosity and clay content on acoustic properties of sandstones and unconsolidated sediments, PhD dissertation, SRB, **28**, Stanford University.
- Han, D. H., Nur, A., and D. Morgan, 1986, Effects of porosity and clay content on wave velocities in sandstones, *Geophysics*, **51**, 2093-2107.
- Hill, R., 1965, A self-consistent mechanics of composite materials: *J. Mech. Phys. Solids*, **13**, 213-222.
- Jizba, D. and G. Mavko, 1990, The high pressure seismic velocities of sandstones, SRB, **40**, Paper B.
- Marion, D., 1990, Acoustic, mechanical, and transport properties of sediments and granular materials, PhD dissertation, SRB, **39**, Stanford University.
- O'Connell, R. J. and B. Budiansky, 1974, Seismic velocities in dry and saturated cracked solids, *J. Geophys. Res.*, **79**, 5412-5426.
- O'Connell, R. J. and B. Budiansky, 1977, Viscoelastic properties of fluid-saturated cracked solids, *J. Geophys. Res.*, **82**, 5719-5735.
- Press, W. H., Flannery, B. P., Teukolsky, S. A., and W. T. Vetterling, 1989, *Numerical recipes*, Cambridge University Press, pp.702.
- Thorpe, M. F. and P. N. Sen, 1985, Elastic moduli of two-dimensional composite continua with elliptical inclusions, *J. Acoust. Soc. Am.*, **77**, 1674-1680.

- Tosaya, C. and A. Nur, 1982, Effects of diagenesis and clays on compressional velocities in rocks, *Geophys. Res. Lett.*, **9**, 5-8.
- Walpole, L. J., 1969, On the overall elastic moduli of composite materials, *J. Mech. Phys. Solids*, **17**, 235-251.
- Walsh, J. B., 1969, New analysis of attenuation in partially melted rock, *J. Geo. Res.*, **74**, 4333-4337.
- Watt, J. P., G. F. Davies, and R. J. O'Connell, 1976, The elastic properties of composite materials, *Review of Geophysics and Space Physics*, **14**, 541-563.
- Wu, T. T., 1966, The effect of inclusion shape on the elastic moduli of a two-phase material, *Int. J. Solids Struct.*, **3**, 1-8.

Chapter 6

Critical Concentration Model and Solution for Sand-clay Sediments

Abstract

For sand-clay sediments ranging from clean sands, shaly sands, sandy shales, to pure shales, the concept of critical concentration in porous materials is applied to the evaluation of the porosity-clay content relation, permeability-porosity-clay relation, and effective elastic moduli and wave velocities. The model of complete clay filling yields the lower bound of porosity-clay content relation. With the intergranular clay and void effects taken into account, our model results can quantitatively describe the porosity-clay content relation in experimental data. By applying Kozeny-Carman equation to sand-clay sediments and using experimental data of clean sand porosity and clay microporosity, we present the relationships between permeability, porosity, clay content and location, and confining pressure, which exhibit distinctive change from shaly sands to sandy shales. Then the critical concentration phase is defined on the basis of mechanical implications of the intergranular clay effect. The substitution method is used to evaluate the effective elastic moduli and wave velocities, and the model results are in agreement with available experimental data.

6.1 Critical clay concentration

Sand-clay sediments can be taken as a porous material system ranging from clean sands, shaly sands, sandy shales, to pure shales. There is a distinctive change in microstructures of sand-clay sediments from shaly sands to sandy shales, that is, the transition from sand skeleton-supported to clay matrix-supported subsystems. The clay content at this transition is defined as the critical clay concentration which is related to the porosity of clean sands, and the filling and packing of clay particles with sand grains. The porosity, permeability, effective elastic moduli, and wave velocities change distinctively before and after the critical clay concentration, as indicated in the experimental studies (Han, 1986; Yin et al., 1988). The model studies of effective elastic moduli and wave velocities by Marion and Yin (1988), Marion (1990), and Nur et al. (1991), in general, are qualitatively consistent with the experimental data.

By applying the concept of critical concentration to sand-clay sediments, this chapter provides some quantitative descriptions of the microstructure variations and effective properties of sand-clay sediments.

6.2 Porosity-clay content relations

6.2.1 Complete clay filling

For sand-clay sediments ranging from clean sands, shaly sands, sandy shales, to pure shales, material porosity ϕ_2 depends on sand volume fraction ϕ_1 , clay volume fraction ϕ_3 , and clay microporosity ϕ_{cm} ,

$$\phi_2 = 1 - \phi_1 - \phi_3(1 - \phi_{cm}). \quad (6.1)$$

The clay volume fraction of such a porous material system ranges from zero to 100%, and the porosity distribution depends on how the clay particles fill and pack with sand grains.

In the study of binary mixture properties, many people used the assumption of complete filling, which leads to no clay disturbance on sand grain skeleton for sand-clay sediments (Thomas and Stieber, 1975; Clarke, 1979; Cargill, 1984; Marion and Yin, 1988; Marion, 1990). Consequently, with completely-filling clay particles, there is a constant sand grain volume fraction ϕ_1 from clean sands to shaly sands, and a linear decrease of ϕ_1 from sandy shales to pure shales. Thus the porosity distribution is based on equation (6.1) and has the following form,

$$\text{For } 0 \leq \phi_3 \leq \phi_{cs}, \quad \phi_1 = \text{const.}, \quad \phi_2 = 1 - \phi_1 - \phi_3(1 - \phi_{cm}) = \phi_{cs} - \phi_3(1 - \phi_{cm}), \quad (6.2)$$

$$\text{For } \phi_{cs} \leq \phi_3 \leq 1, \quad \phi_1 = 1 - \phi_3, \quad \phi_2 = 1 - \phi_1 - \phi_3(1 - \phi_{cm}) = \phi_3\phi_{cm}. \quad (6.3)$$

where ϕ_{cs} is the porosity of clean sands. Thus, the critical clay concentration is simply the same as ϕ_{cs} .

6.2.2 Intergranular clay and void effects

For sand-clay sediments, the sand grains are not cemented and depositional clay particles may participate in the load-bearing skeleton of the material. When such clay disturbance is concerned, a portion of clay particles will fill and pack in the sediment as intergranular clay particles, expanding the pure sand skeleton. Consequently, in a unit volume of sand-clay sediment, the intergranular clay effect is to decrease the sand volume fraction ϕ_1 , or increase the porosity of sand-clay sediments. To quantify the additional porosity gained from the intergranular clay effect, a linear decrease of ϕ_1 with ϕ_3 is proposed from clean sands to shaly sands,

$$\phi_1 = 1 - \phi_{cs} - c_1\phi_3, \quad (6.4)$$

where c_1 is the intergranular clay coefficient, indicating the degree of porosity increase due to the expanding skeleton under the intergranular clay effect. For instance, when a cubic packing of spherical sand grains are disturbed by tiny clay particles at contact points, as illustrated in Fig.6.1(a), the intergranular clay effect c_1 depends on the radius ratio of sand grain to clay particle. When the radius ratio is 15, 20, 25, 30, a simple calculation yields the value of c_1 as 0.194, 0.150, 0.122, and 0.103, respectively. In reality, it is not a single clay particle, but a cluster of clay particles that fill and pack between the contact area of sand grains, thus the radius ratio may be much higher.

From sandy shales to pure shales, the existence of sand grains in clay matrix often creates intergranular voids as illustrated in Fig.6.1(b), leading to a considerable increase of porosity. These intergranular voids are equivalent to the so-called air bubbles in marine sediments. When the sand grain volume fraction decreases to zero, such intergranular voids tend to disappear. A linear relation is proposed to describe the intergranular void effect,

$$\phi_1 = 1 - \phi_3 - c_2(1 - \phi_3), \quad (6.5)$$

where c_2 is the intergranular void coefficient, a parameter sensitive to the confining pressure as will be discussed later.

As a result of above analysis, the porosity ϕ_2 is calculated from equation (6.1) with the intergranular clay and void effects taken into account. The porosity-clay content relation for the whole system of sand-clay sediment is thus given by

$$\text{For } 0 \leq \phi_3 \leq \frac{\phi_{cs} - c_2}{1 - c_1 - c_2},$$

$$\begin{aligned} \phi_2 &= 1 - \phi_1 - \phi_3(1 - \phi_{cm}) \\ &= \phi_{cs} - \phi_3(1 - \phi_{cm}) + c_1\phi_3. \end{aligned} \quad (6.6)$$

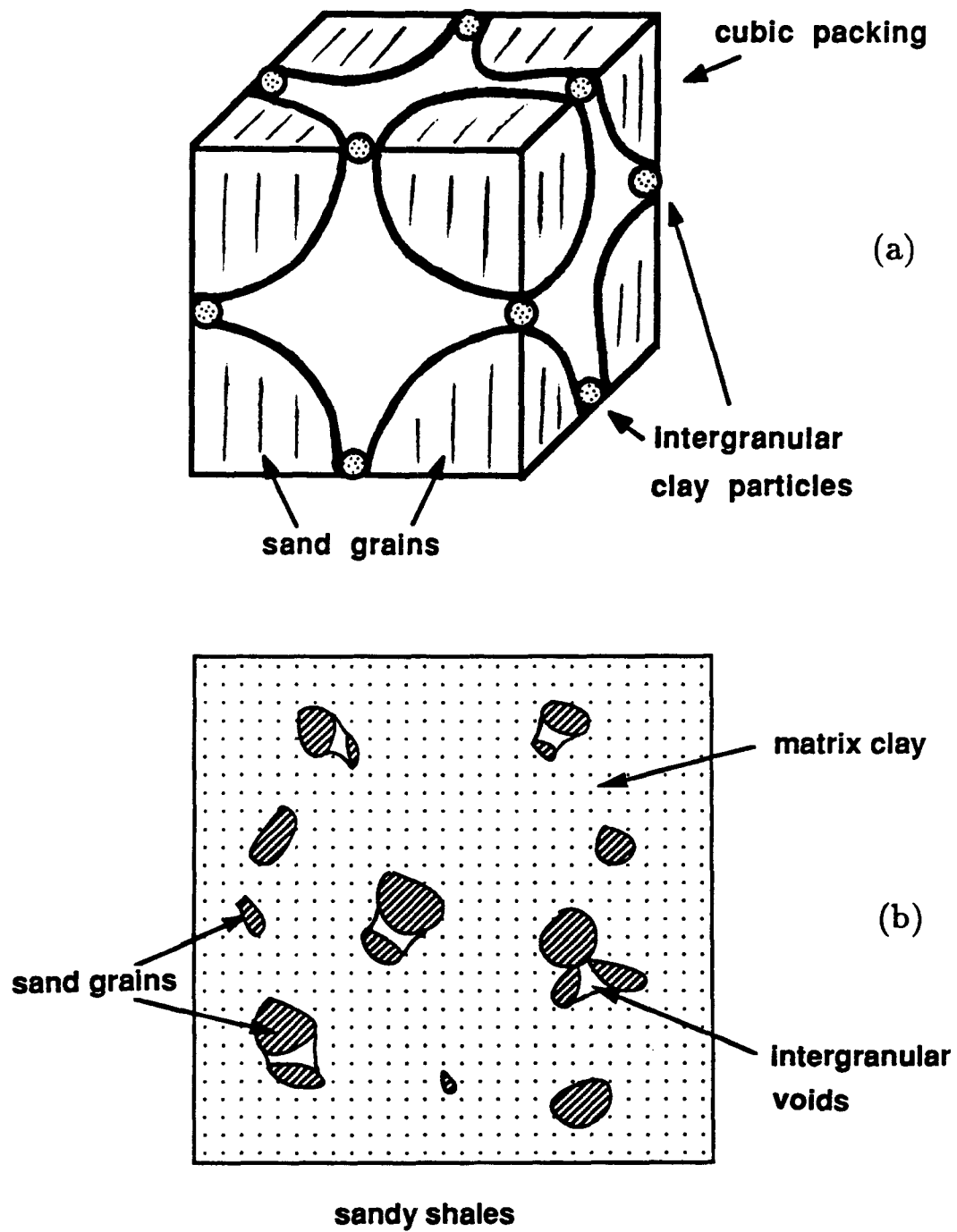


Fig.6.1 (a) Schematic diagram of intergranular clay particles in shaly sands, (b) Schematic diagram of intergranular voids in sandy shales.

For $\frac{\phi_{cs}-c_2}{1-c_1-c_2} \leq \phi_3 \leq 1$,

$$\begin{aligned}\phi_2 &= 1 - \phi_1 - \phi_3(1 - \phi_{cm}) \\ &= \phi_3\phi_{cm} + c_2(1 - \phi_3).\end{aligned}\quad (6.7)$$

Thus, the critical clay concentration is $\frac{\phi_{cs}-c_2}{1-c_1-c_2}$, depending on the porosity of clean sands, and the intergranular clay and void effects.

The clay content can be also described by clay weight fraction. The clay weight fraction measured from dry samples of sand-clay sediments w_3 can be converted from the clay volume fraction ϕ_3 by the formula

$$w_3 = \frac{\phi_3(1 - \phi_{cm})\rho_3}{(1 - \phi_{cs} - c_1\phi_3)\rho_1 + \phi_3(1 - \phi_{cm})\rho_3}, \quad \text{for } 0 \leq \phi_3 \leq \frac{\phi_{cs} - c_2}{1 - c_1 - c_2}, \quad (6.8)$$

$$w_3 = \frac{\phi_3(1 - \phi_{cm})\rho_3}{[1 - \phi_3 - c_2(1 - \phi_3)]\rho_1 + \phi_3(1 - \phi_{cm})\rho_3}, \quad \text{for } \frac{\phi_{cs} - c_2}{1 - c_1 - c_2} \leq \phi_3 \leq 1, \quad (6.9)$$

where ρ_1 and ρ_3 are sand and clay density, respectively.

Obviously, when no intergranular clay and void effects are taken into account, $c_1 = 0$ and $c_2 = 0$, equations (6.6) and (6.7) reduce to those with the assumption of complete clay filling.

6.2.3 Comparison with experimental data

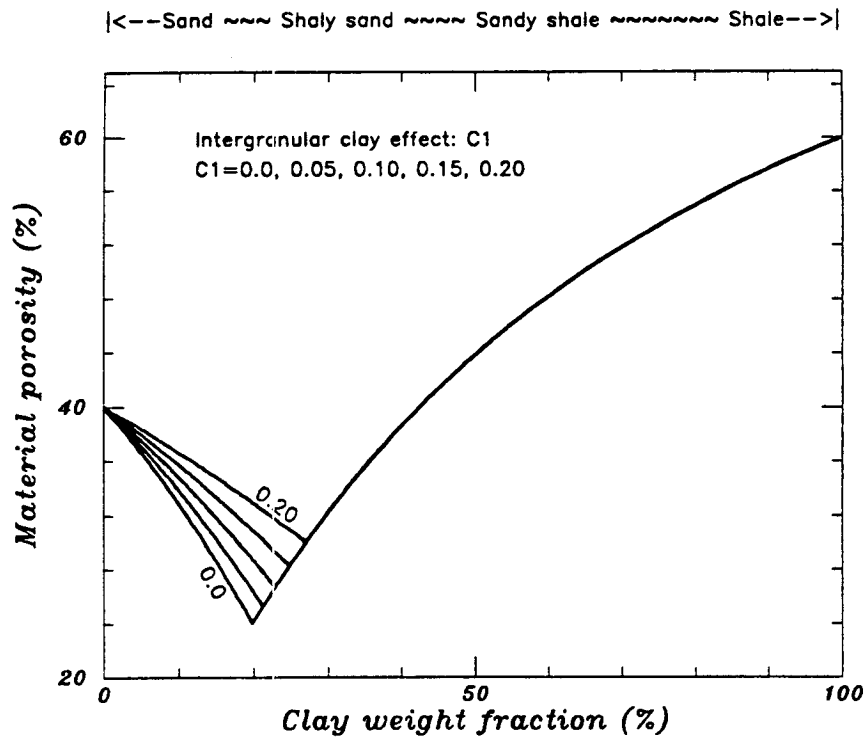
Both ϕ_{cs} and ϕ_{cm} of marine sediments decrease with depth. The depth effect on ϕ_{cs} , ϕ_{cm} , and the porosity-clay content relations can be determined experimentally by loading different confining pressures on sand-clay mixture samples (Yin et al., 1988). Marion and Yin (1988) and Marion (1990) used the porosity-clay content relation based on the complete clay filling of a binary mixture to explain experimental data. However, there are considerable discrepancies between the data and their model

results as regards the minimum porosity points and corresponding porosities of shaly sands and sandy shales.

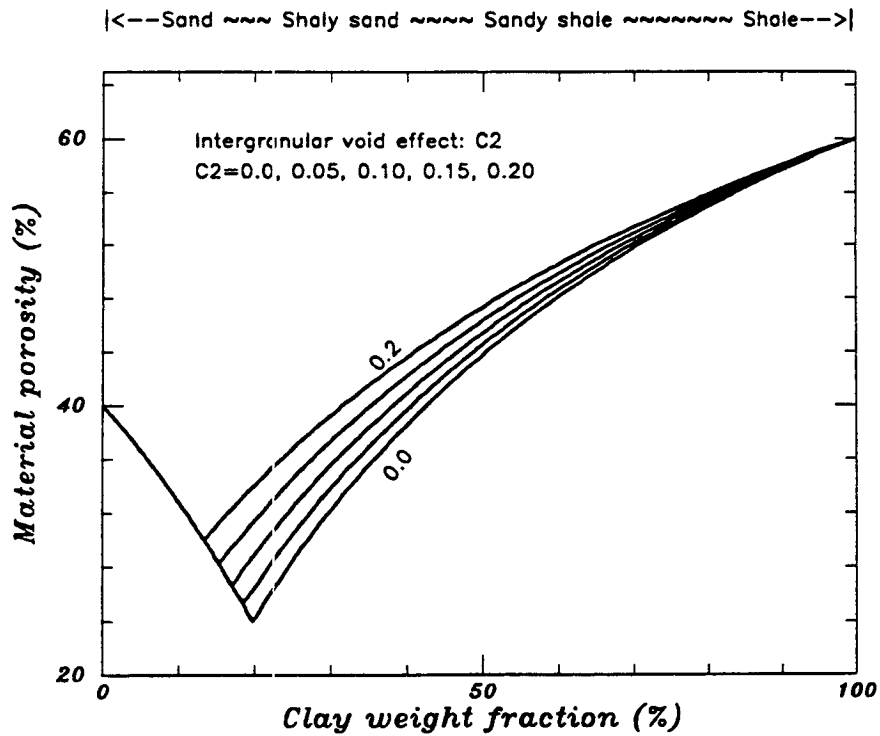
Our analysis in the above indicates that the model results with complete clay filling assumption are actually the lower bound of porosity-clay content relation, and that intergranular clay and void effects result in additional porosity increase in shaly sands and sandy shales. To visualize how intergranular clay and void effects influence the minimum porosity point in each porosity distribution, Fig.6.2(a) shows the porosity-clay weight fraction relations for $c_2 = 0$ and different degrees of intergranular clay effect ($c_1 = 0 \sim 0.2$), and Fig.6.2(b) shows the porosity-clay weight fraction relations for $c_1 = 0$ and different degrees of intergranular void effect ($c_2 = 0 \sim 0.2$). We notice that the minimum porosity points migrate from low to high clay weight fraction with the increase of intergranular clay effect, and that they migrate from high to low clay weight fraction with the increase of intergranular void effect. As a result, the porosities around the minimum points increase considerably.

Fig.6.3 and 6.4 present comparisons between our model results and experimental data obtained by Yin et al. (1988). The model results with intergranular clay and void effects taken into account are in very good agreement with the experimental data. For sand-clay samples at zero confining pressure, both intergranular clay and void effects have their maximum values. With the increase of confining pressure, the porosity of the whole system decreases considerably, but most intergranular clay particles will be still in function, resulting in minor decrease of c_1 . However, intergranular voids are quite sensitive to confining pressure, and high pressure will squeeze more clay particles into the intergranular voids, leading to low values of c_2 .

In summary, the porosity and sand volume fraction distributions of sand-clay sediments can be accurately described by equations (6.4) ~ (6.7); intergranular clay and void effects can systematically account for the porosity changes due to confining pressure and other factors, and the model results are in good agreement with exper-



(a)



(b)

Fig.6.2 (a). Porosity versus clay weight fraction for different degrees of intergranular clay effect, (b). Porosity versus clay weight fraction for different degrees of intergranular void effect.

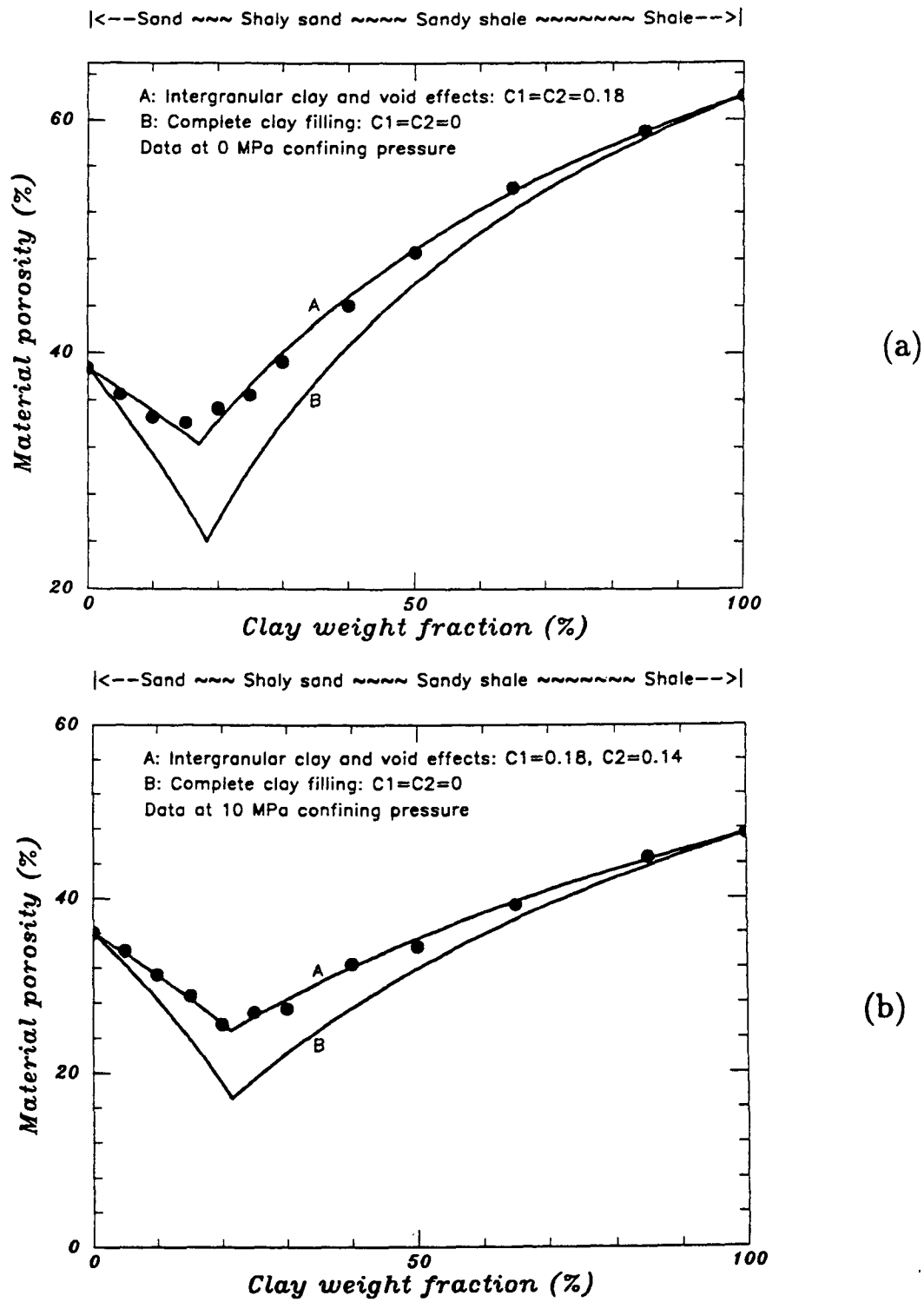


Fig.6.3 Comparison between our model results and experimental data of porosity versus clay weight fraction. (a) at 0 MPa confining pressure, (b) at 10 MPa confining pressure.

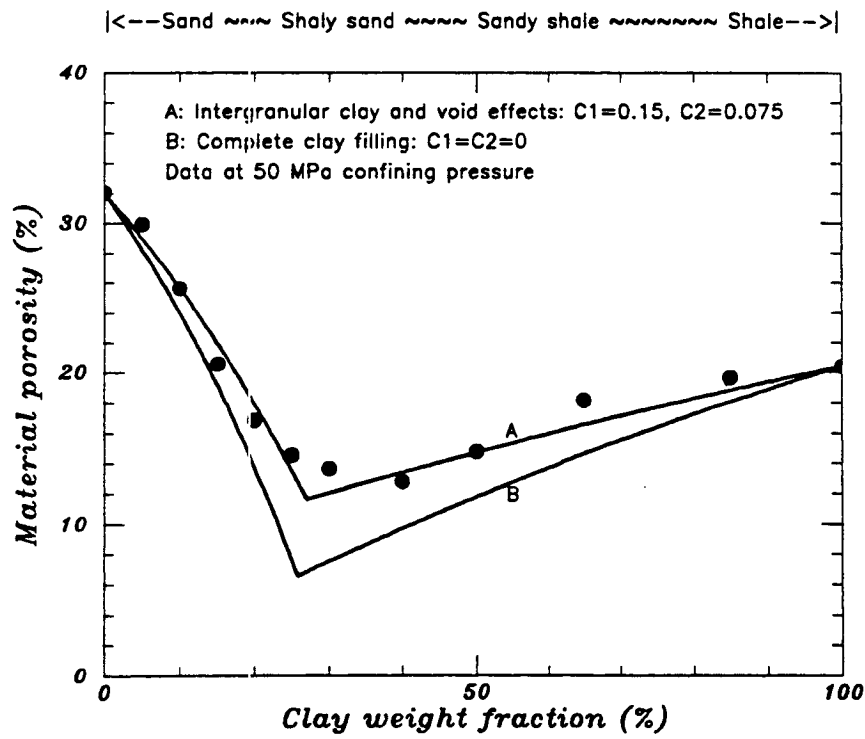
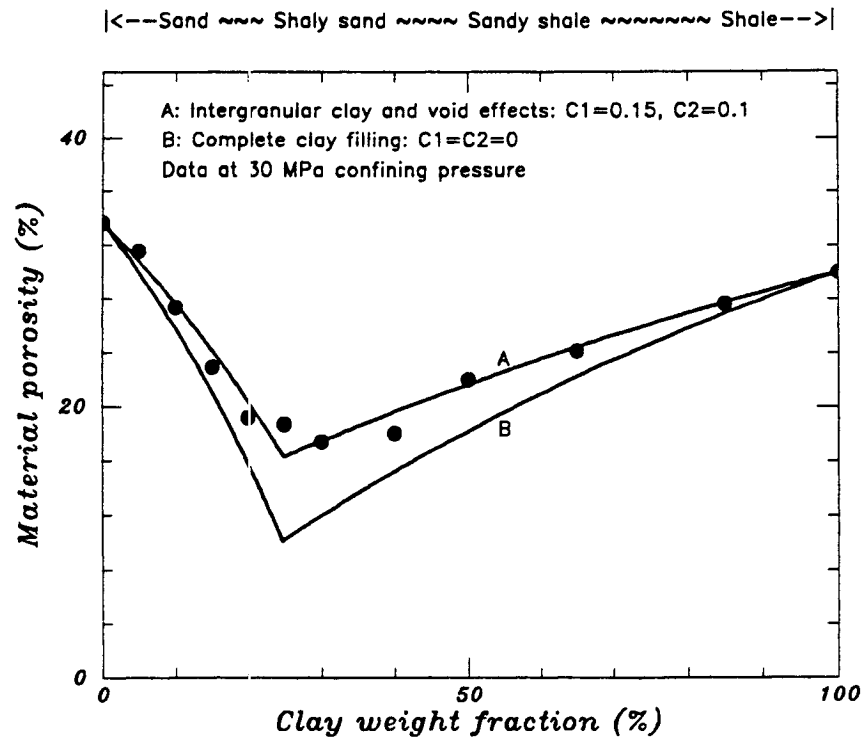


Fig.6.4 Comparison between our model results and experimental data of porosity versus clay weight fraction. (a) at 30 MPa confining pressure, (b) at 50 MPa confining pressure.

imental data; when no intergranular clay and void effects are taken into account, the model results reduce to those with complete clay filling assumption, serving as the lower bound of porosity-clay content relation of a binary mixture.

6.2.4 Pressure effect on critical clay concentration

Above porosity analysis indicates that, when the intergranular clay and void effects are introduced to explain the microstructure variation of sand-clay sediments, the transition from sand skeleton-supported to clay matrix supported subsystems is characterized by the critical clay concentration ϕ_{3cr} ,

$$\phi_{3cr} = \frac{\phi_{cs} - c_2}{1 - c_1 - c_2}. \quad (6.10)$$

From the experimental data obtained by Yin et al. (1988) and above porosity analysis, the critical clay concentration versus confining pressure is presented in Fig.6.5. With increase in confining pressure, there is only minor variation of the critical clay concentration, which is different from the monotonous decrease of clean sand porosity ϕ_{cs} with the increase of confining pressure.

6.3 Permeability in sand-clay sediments

Since porosity data are more easily obtained than permeability data both in laboratory and in-situ measurements, it is useful to estimate the permeability of a porous material by utilizing the relationship between permeability and porosity.

6.3.1 Kozeny-Carman equation

There are many versions of Kozeny-Carman equation available to relate the permeability k to the porosity ϕ_2 of a porous material. According to Carman (1956), the equation is of the form

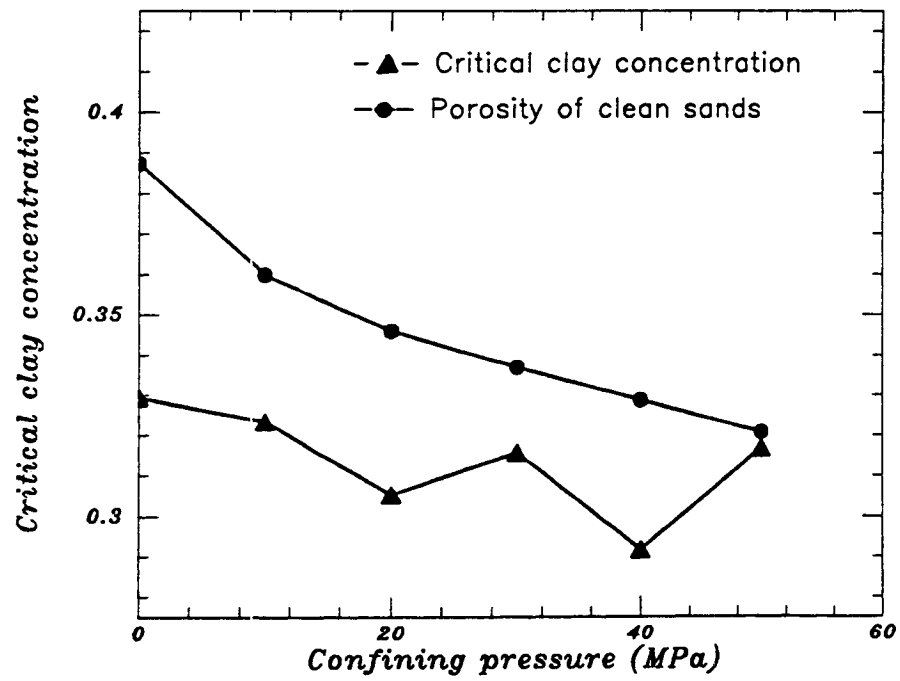


Fig.6.5 Critical clay concentration versus confining pressure. With the increase of confining pressure, ϕ_{cs} decrease monotonously but ϕ_{3cr} exhibits minor variation.

$$k = \frac{\phi_2^3}{k_0 T^2 S^2}, \quad (6.11)$$

where T and S are the tortuosity and specific surface area of a porous material, and k_0 is an empirical constant.

Bear (1972) proposed another form of Kozeny-Carman equation,

$$k = \frac{\phi_2^3 / (1 - \phi_2)^2}{5S^2}. \quad (6.12)$$

For sediments composed of sphere grains with uniform radius r ,

$$S = \frac{4\pi r^2}{\frac{4}{3}\pi r^3} = \frac{3}{r}. \quad (6.13)$$

Brace (1977) arrived at

$$k = \frac{m^2 \phi^3}{C}, \quad (6.14)$$

where C is a constant number ranging between 2 and 3, and m is the hydraulic radius, the ratio of the volume of pores to the void-solid interface area.

Marion (1990) applied equation (6.11) to Gulf Coast sandstone data, and the result provides one possible explanation to the permeability data as in Fig.6.6.

6.3.2 Pressure and clay-dependent Permeability

Sand-clay sediments are quite sensitive to confining pressure. It is very useful for reservoir exploration and production to find how the permeability of sand-clay sediments depends on porosity, clay content, and confining pressure. For sand-clay sediments, both the porosity and the specific surface area will change with variations in sand and clay contents and their relative locations. The porosity variation can be accurately

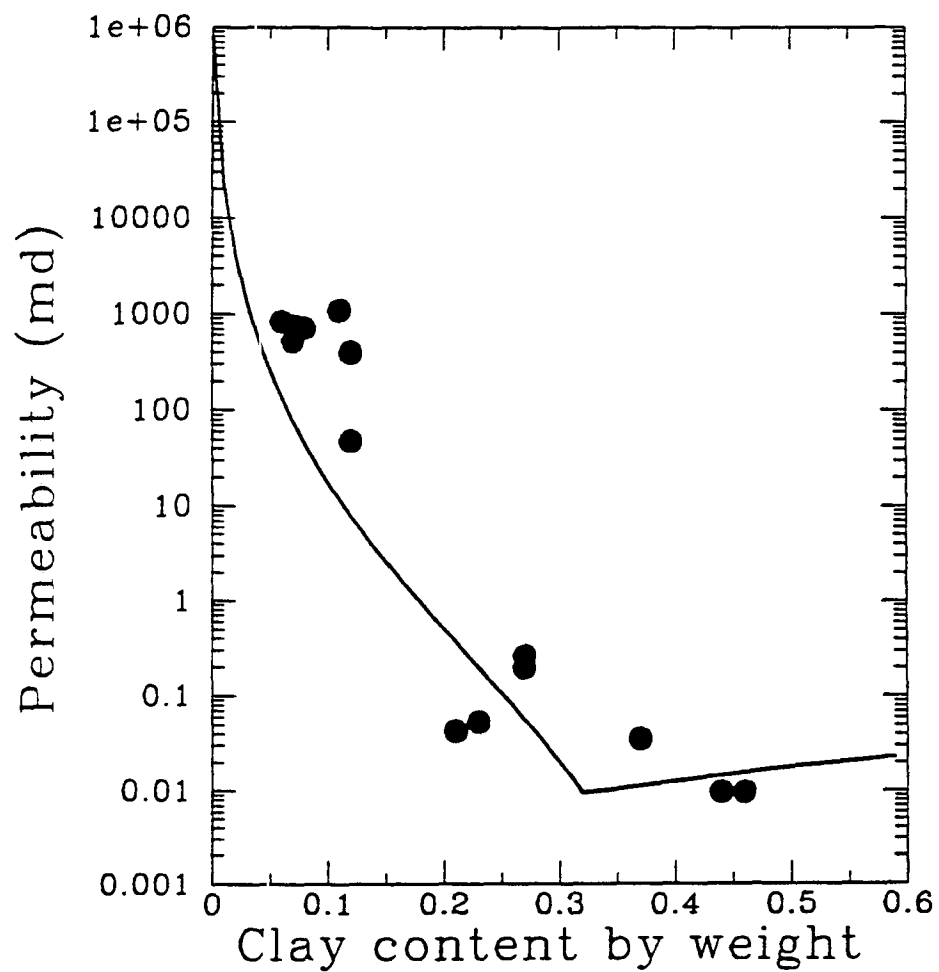


Fig.6.6 Permeability versus clay concentration: comparison of model result (solid line) and Gulf Coast sandstone data (after Marion, 1990).

estimated by the model in above section, but the variation in specific surface area involves the different grain sizes in sand and clay.

As suggested by Bear (1972), the uniform radius r in equation (6.13) may be replaced by the harmonic mean radius \bar{r} for binary reservoir rocks and sediments. Given sand grain radius as r_1 , and clay grain radius as r_3 , one has

$$\bar{r} = \frac{1}{\frac{\phi_1}{r_1} + \frac{\phi_3}{r_3}}, \quad (6.15)$$

and equation (6.12) becomes

$$k = \frac{\phi_2^3 / (1 - \phi_2)^2}{5[3(\frac{\phi_1}{r_1} + \frac{\phi_3}{r_3})]^2}, \quad (6.16)$$

where the relationships between ϕ_1 , ϕ_2 , and ϕ_3 are given by equations (6.6) and (6.7).

For sand-clay mixtures used in Yin's experiments (Yin et al., 1988), the sand and clay grain sizes are characterized by $r_1 = 0.015 \text{ cm}$, $r_3 = 0.0001 \text{ cm}$. Equation (6.16) gives permeability k in cgs system as cm^2 , and $1 \text{ md} = 0.987 \times 10^{-11} \text{ cm}^2$. When the intergranular clay and void effects are taken into account, equations (6.4) ~ (6.7) are used in equation (6.16) to give relationships between permeability, porosity, clay, and confining pressure, as in Fig.6.7 and Fig.6.8.

Fig.6.7 shows that for shaly sands the permeability is very sensitive to clay content but not confining pressure, and that for sandy shales the permeability depends on confining pressure much more than clay content. Thus the clay effects are quite different for shaly sands and sandy shales. Fig.6.8 presents the permeability versus porosity for different confining pressures and clay contents. The increase in confining pressure leads to general decrease in permeability especially in sandy shales. The increase in clay content causes distinctive changes in both the porosity and permeability from shaly sands to sandy shales. The domain bounded by the permeability curves for shaly sands and sandy shales represents the microstructural variation especially

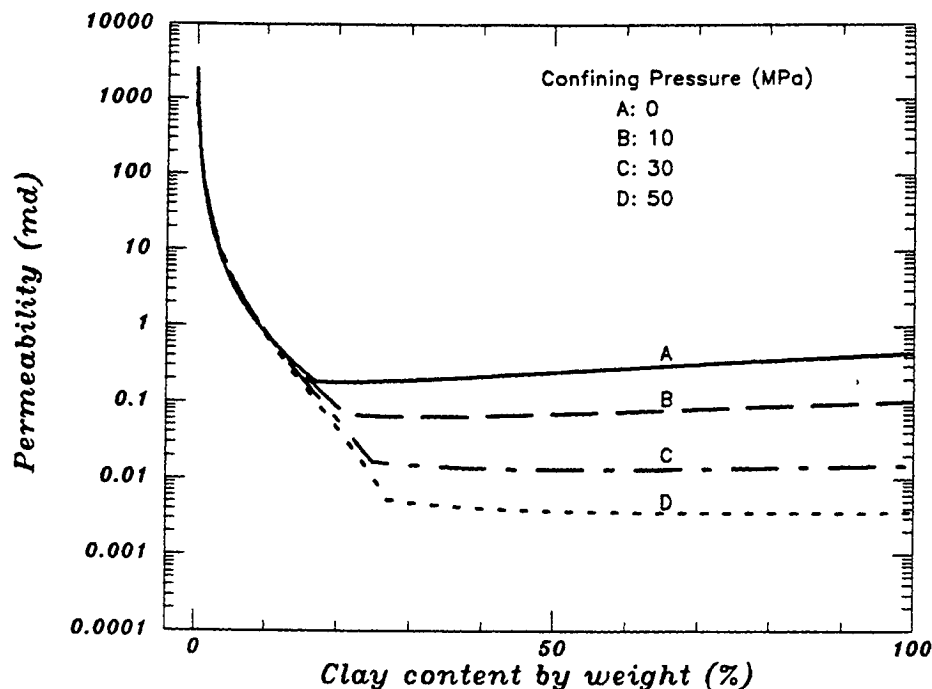


Fig.6.7 Permeability versus clay content at different levels of confining pressures. Yin's experimental data of clean sand porosity and clay microporosity are used in calculation.

particle size variation from medium to fine scales. Such feature is also true from coarse to medium scales for sedimentary rocks. As indicated by the data in Fig.6.9, the permeability-porosity curves show gradual variations from clean coarse-grained sandstones to micritic sandstones.

6.4 Evaluation of Effective Elastic Moduli and Wave Velocities

6.4.1 Sediments at zero confining pressure

Fluid-saturated sand-clay sediments are typical unconsolidated materials. It is well known that unconsolidated materials at zero confining pressure are of zero shear modulus or shear wave velocity. The effective bulk modulus and compressive wave velocity in such materials can be described by the isostress model, or generalized

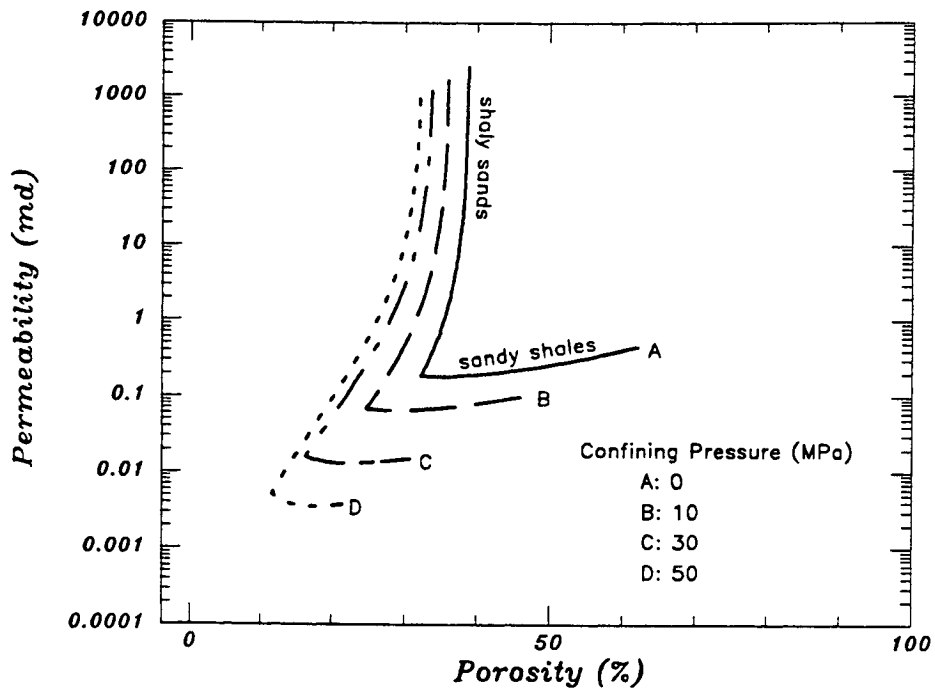


Fig.6.8 Permeability versus porosity at different levels of confining pressures. Yin's experimental data of clean sand porosity and clay microporosity are used in calculation.

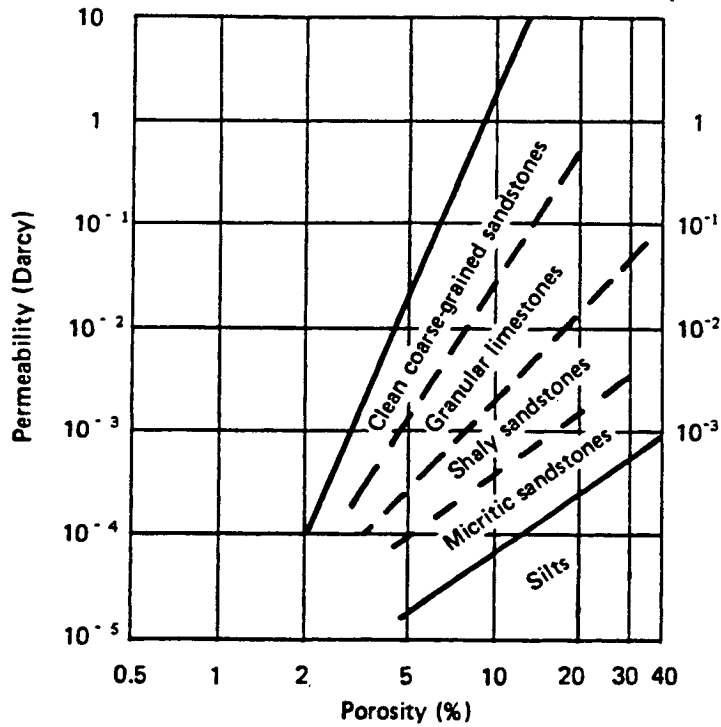


Fig.6.9 Schematization of permeability-porosity relationship in sedimentary rocks (after Bourbié, et al., 1987).

Reuss' and Wood's relations for multiphase materials. When the intergranular clay and void effects are taken into account, the effective bulk modulus K and compressive wave velocity V_P are given by

$$\frac{1}{K} = \frac{1 - \phi_{cs} - c_1\phi_3}{K_1} + \frac{\phi_{cs} - \phi_3(1 - \phi_{cm}) + c_1\phi_3}{K_2} + \frac{\phi_3(1 - \phi_{cm})}{K_3}, \quad (6.17)$$

$$V_P = \left[\frac{K}{(1 - \phi_{cs} - c_1\phi_3)\rho_1 + (\phi_{cs} - \phi_3(1 - \phi_{cm}) + c_1\phi_3)\rho_2 + \phi_3(1 - \phi_{cm})\rho_3} \right]^{1/2}, \quad (6.18)$$

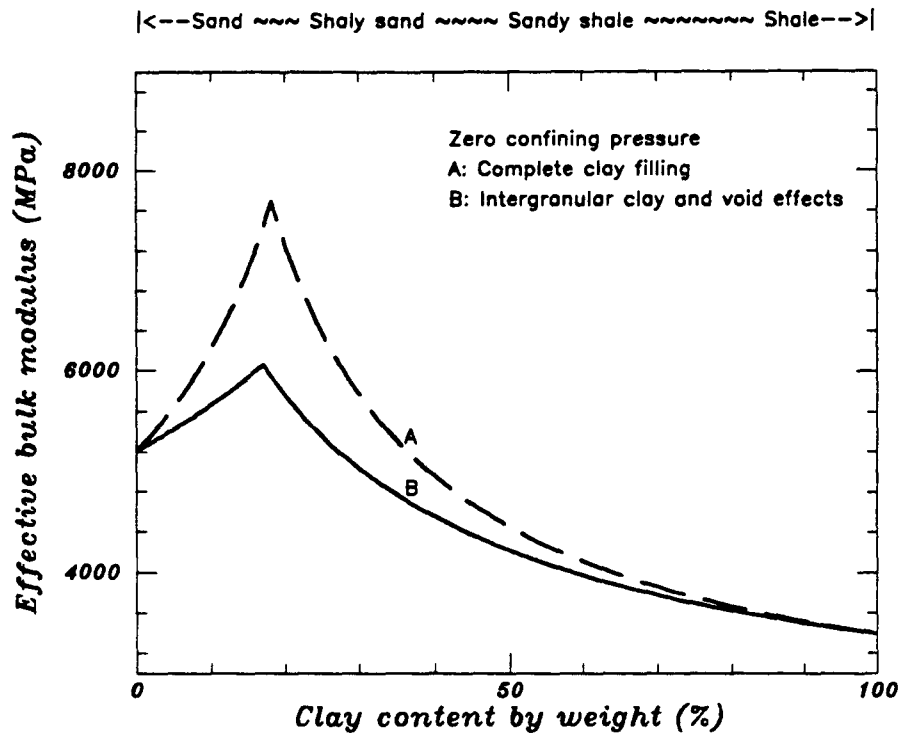
for $0 \leq \phi_3 \leq \phi_{3cr}$, and

$$\frac{1}{K} = \frac{(1 - \phi_3)(1 - c_2)}{K_1} + \frac{\phi_3\phi_{cm} + c_2(1 - \phi_3)}{K_2} + \frac{\phi_3(1 - \phi_{cm})}{K_3}, \quad (6.19)$$

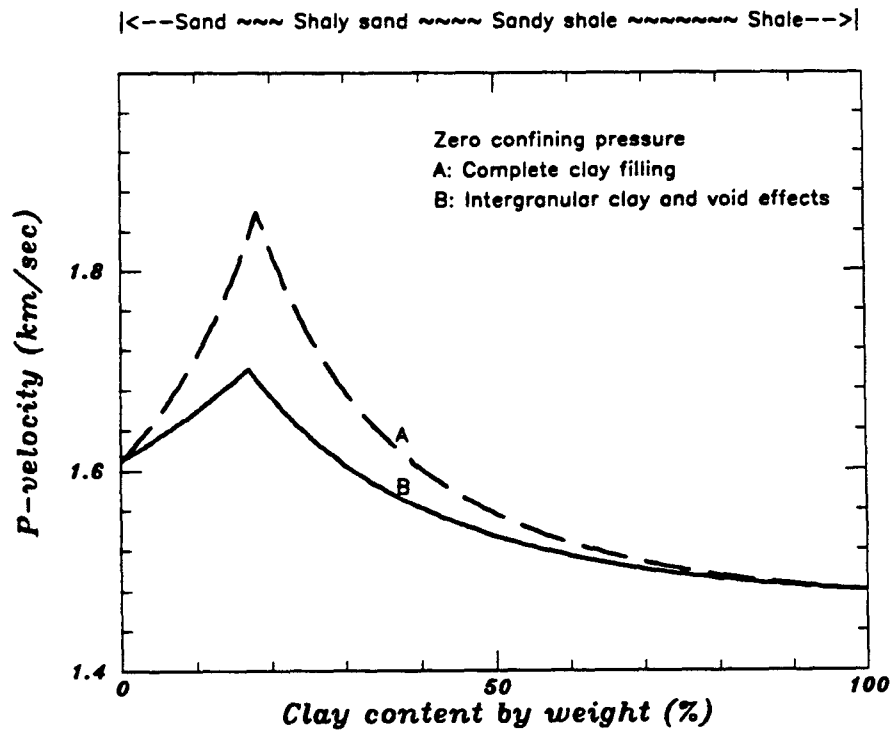
$$V_P = \left[\frac{K}{(1 - \phi_3)(1 - c_2)\rho_1 + (\phi_3\phi_{cm} + c_2(1 - \phi_3))\rho_2 + \phi_3(1 - \phi_{cm})\rho_3} \right]^{1/2}, \quad (6.20)$$

for $\phi_{3cr} \leq \phi_3 \leq 1$.

Fig.6.10 presents the effective bulk modulus and compressive wave velocity versus clay content for fluid-saturated sand-clay sediments. The intergranular clay and void coefficients $c_1 = c_2 = 0.18$ determined above for zero confining pressure condition are used in calculation to compare with the situation of complete clay filling ($c_1 = c_2 = 0$). Since the complete clay filling leads to the lower bound of porosity-clay relation for sand-clay sediments, it leads to the upper bounds of effective bulk modulus and compressive wave velocity as in Fig.6.10a and 6.10b. The peak values in the curves correspond to the critical clay concentration.



(a)



(b)

Fig.6.10 (a) Effective bulk modulus versus clay content and (b) compressive wave velocity versus clay content for fluid-saturated sand-clay sediments at zero confining pressure.

6.4.2 Critical concentration phase

When a finite confining pressure is applied upon the sand-clay sediments, shear wave velocity is observed and so above formulation for zero confining pressure is not applicable. The critical concentration model and solution developed in Chapter 3 and 4 are here applied to the evaluation of both the compressive and shear wave velocities in fluid-saturated sand-clay sediments.

Similar to chapter 3, the critical concentration phase of a fluid-saturated sand-clay sediment is defined as the material state at critical clay concentration ϕ_{3cr} . Its density ρ_{cr} is given by

$$\rho_{cr} = (1 - \phi_{3cr})(1 - c_2)\rho_1 + [\phi_{3cr}\phi_{cm} + c_2(1 - \phi_{3cr})]\rho_2 + \phi_{3cr}(1 - \phi_{cm})\rho_3, \quad (6.21)$$

which indicates that the critical concentration phase is a mixture of fluid, sand grains, and clay particles. The effective bulk modulus of critical concentration phase K_{cr} is given by

$$\frac{1}{K_{cr}} = \frac{(1 - \phi_{3cr})(1 - c_2)}{K_1} + \frac{\phi_{3cr}\phi_{cm} + c_2(1 - \phi_{3cr})}{K_2} + \frac{\phi_{3cr}(1 - \phi_{cm})}{K_3}. \quad (6.22)$$

The elastic shear modulus of critical concentration phase μ_{cr} can be approximated by Reuss average in terms of elastic moduli of saturated clays and sands (Reuss, 1929; Kuster and Toksoz, 1974; Purnell, 1986),

$$\frac{1}{\mu_{cr}} = \frac{(1 - \phi_{3cr})(1 - c_2)}{\mu_1^s} + \frac{\phi_{3cr} + c_2(1 - \phi_{3cr})}{\mu_3^s}, \quad (6.23)$$

where μ_1^s and μ_3^s are the shear moduli of fluid-saturated sands and clays, respectively.

The intergranular clay effect proposed above not only accounts for the variation of geometrical packing of sand gains and clay particles, resulting in porosity increase, but

also implies the gradual increase of clay particles in the highly load-bearing material skeleton with the increase in clay content. Such mechanical interactions between sand grains and clay particles lead to the considerable contribution of clay phase to the effective moduli and wave velocities of sand-clay sediments.

At zero clay content, the effective elastic moduli of clean sand can be evaluated by the critical concentration model and solutions in chapter 3 and 4. Let K_{cs} and μ_{cs} represent the effective elastic bulk and shear moduli of clean sands, respectively, and ρ_{cs} be its density. Then the constituents or end members of the critical concentration model are the sand skeleton phase with K_{cs} , μ_{cs} , and ρ_{cs} , and the critical concentration phase with K_{cr} , μ_{cr} , and ρ_{cr} , respectively. Consequently, the microstructure variation of shaly sands due to the intergranular clay effect is interpreted as the variation from the sand skeleton phase to the critical concentration phase.

6.4.3 Critical concentration solutions

In principle, the substitution method developed in Chapter 4 can be used to find the critical concentration solution to effective elastic moduli of sand-clay sediments. Here we give one critical concentration solution extended from Voigt's relation to illustrate the basic features of effective elastic moduli and wave velocities of sand-clay sediments.

For $0 \leq \phi_3 \leq \phi_{3cr}$, the effective elastic moduli and wave velocities are given by

$$K = \left(1 - \frac{\phi_3}{\phi_{3cr}}\right)K_{cs} + \frac{\phi_3}{\phi_{3cr}}K_{cr}, \quad (6.24)$$

$$\mu = \left(1 - \frac{\phi_3}{\phi_{3cr}}\right)\mu_{cs} + \frac{\phi_3}{\phi_{3cr}}\mu_{cr}, \quad (6.25)$$

$$V_P = \left[\frac{K + 4\mu/3}{(1 - \phi_{cs} - c_1\phi_3)\rho_1 + (\phi_{cs} - \phi_3(1 - \phi_{cm}) + c_1\phi_3)\rho_2 + \phi_3(1 - \phi_{cm})\rho_3} \right]^{1/2}, \quad (6.26)$$

$$V_S = \left[\frac{\mu}{(1 - \phi_{cs} - c_1\phi_3)\rho_1 + (\phi_{cs} - \phi_3(1 - \phi_{cm}) + c_1\phi_3)\rho_2 + \phi_3(1 - \phi_{cm})\rho_3} \right]^{1/2}. \quad (6.27)$$

For $\phi_{3cr} \leq \phi_3 \leq 1$, the effective elastic moduli and wave velocities are given by

$$\frac{1}{K} = \frac{(1 - \phi_3)(1 - c_2)}{K_1} + \frac{\phi_3\phi_{cm} + c_2(1 - \phi_3)}{K_2} + \frac{\phi_3(1 - \phi_{cm})}{K_3}, \quad (6.28)$$

$$\frac{1}{\mu} = \frac{(1 - \phi_3)(1 - c_2)}{\mu_1^s} + \frac{\phi_3 + c_2(1 - \phi_3)}{\mu_3^s}, \quad (6.29)$$

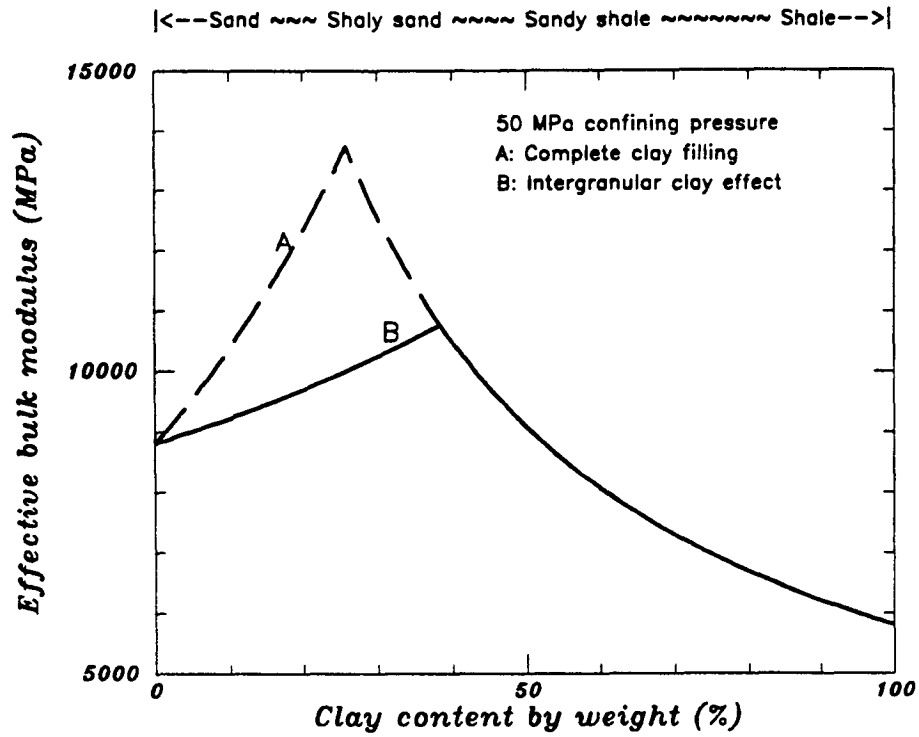
$$V_P = \left[\frac{K + 4\mu/3}{(1 - \phi_3)(1 - c_2)\rho_1 + (\phi_3\phi_{cm} + c_2(1 - \phi_3))\rho_2 + \phi_3(1 - \phi_{cm})\rho_3} \right]^{1/2}, \quad (6.30)$$

$$V_S = \left[\frac{\mu}{(1 - \phi_3)(1 - c_2)\rho_1 + (\phi_3\phi_{cm} + c_2(1 - \phi_3))\rho_2 + \phi_3(1 - \phi_{cm})\rho_3} \right]^{1/2}. \quad (6.31)$$

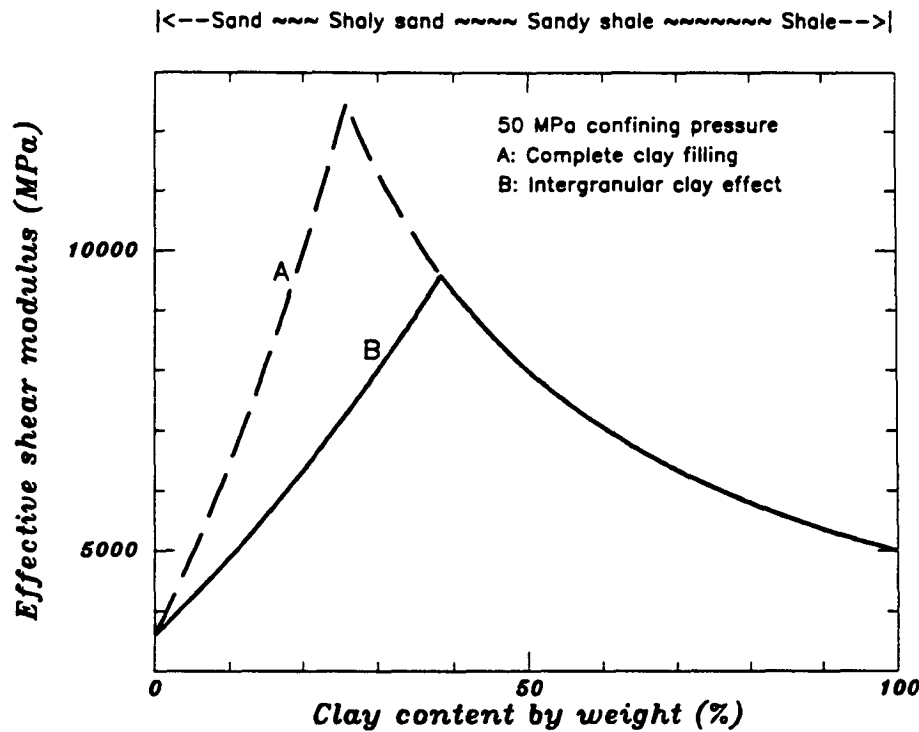
Fig.6.11 shows the effective elastic moduli versus clay content of fluid-saturated sand-clay sediments. The intergranular clay effect at 50 MPa confining pressure is used in calculation. Both bulk and shear moduli of shaly sands decrease considerably as the result of the intergranular clay effect. Fig.6.12 presents the corresponding wave velocities versus clay content. The experimental data obtained by Yin et al. (1988) at 50 MPa confining pressure are compared with the model results. When the intergranular clay effect is taken into account, the model result is in good agreement with the data.

6.5 Conclusions

The conventional model of complete clay filling yields the lower bound of porosity-clay content relation. With the intergranular clay and void effects taken into account,

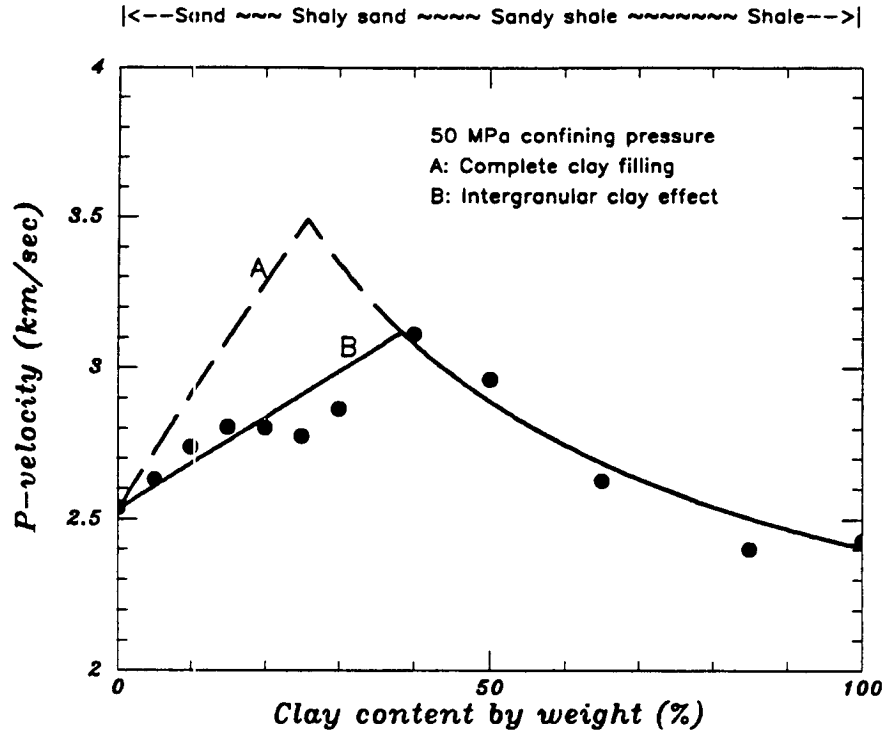


(a)

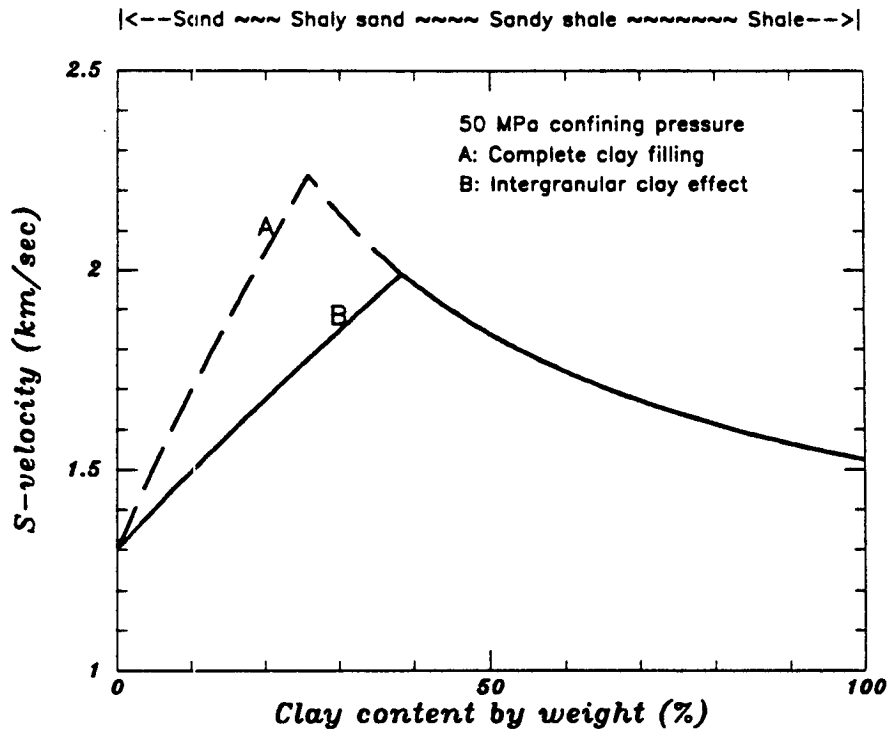


(b)

Fig.6.11 (a) Effective bulk modulus versus clay content and (b) effective shear modulus versus clay content of fluid-saturated sand-clay sediments.



(a)



(b)

Fig.6.12 (a) Compressive wave velocity versus clay content and (b) shear wave velocity versus clay content of fluid-saturated sand-clay sediments. The model result with intergranular clay effect taken into account is in good agreement with Yin's experimental data.

our model results can quantitatively describe the porosity-clay content relation in experimental data.

By applying Kozeny-Carman equation to sand-clay sediments and using experimental data of clean sand porosity and clay microporosity, we determine the relationships between permeability, porosity, clay content and location, and confining pressure, which are very useful in reservoir property evaluation.

The mechanical implications of intergranular clay effect lead to definition of critical concentration phase. The critical concentration solution with intergranular clay effect is in good agreement with experimental data of wave velocity.

References

- Bear, J., 1972, Dynamics of fluids in porous media, New York, American Elsevier Pub. Co., pp.764.
- Bourbié, T., Coussy, O., and B. Zinszner, 1987, Acoustics of porous media, Gulf Publishing Company, Houston, London, Paris, Tokyo, pp.334.
- Brace, W. F., 1977, Permeability from resistivity and pore shape, *J. Geophys. Res.*, **82**, 3343-3349.
- Cargill III, G. S., 1984, Radial distribution functions and microgeometry of dense random packing of hard spheres, in *Physics and Chemistry and Porous Media*, edited by Johnson, D. L. and P. N. Sen, AIP Conference Proceedings, **107**, 20-36.
- Carman, P. C., 1956, Flow of gasses through porous media, New York, Academic Press, pp.182.
- Clarke, R. H., 1979, Reservoir properties of conglomerates and conglomeratic sandstones, *AAPG Bull.*, **63**, 799-803.
- Han, D. H., 1986, Effects of porosity and clay content on acoustic properties of sandstones and unconsolidated sediments, PhD thesis, SRB, **28**, Stanford University.
- Kuster, G. and M. N. Toksöz, 1974, Velocity and attenuation of seismic waves in two-phase media: I. Theoretical formulation and II. Experimental results, *Geophysics*, **39**, 587-618.
- Marion, D., 1990, Acoustic, mechanical, and transport properties of sediments and granular materials, PhD dissertation, SRB, **39**, Stanford University.
- Marion, D. and H. Yin, 1988, A model of porosity and velocity for sand-clay mixtures, *Stanford Rock & Borehole Project*, **33**, 303-316.
- Nur, A., Marion, D., and H. Yin, 1990, Wave velocities in sediments, (in press)
- Purnell, G. W., 1986, Observation of wave velocity and attenuation in two-phase media, *Geophysics*, **51**, 2193-2199.
- Reuss, A., 1929, Berechnung der Fließgrenze von Mischkristallen auf Grund der Plastizitätsbedingung für Einkristalle, *Z. Angew. Math. Mech.*, **9** 49-58.
- Thomas, E. C. and S. J. Stieber, 1975, The distribution of shale in sandstones and its effect upon porosity, *SPWLA Conference*, Paper T.

Wood, A. B., 1941, A Textbook of Sound, Macmillan, New York, pp.519.

Wyllie, M. R. J., Gregory, A. R., and L. W. Gardner, 1956, Elastic wave velocities in heterogeneous and porous media, *Geophysics*, **21**, 41-70.

Yin, H., Han, D., and A. Nur, 1988, Study of velocity and compaction on sand-clay mixtures, *SRB*, **33**, 265-302.

Chapter 7

Effective Stress Laws for Fluid-Saturated Porous Materials

Abstract

The general effective stress law for anisotropic porous materials is defined as $\bar{\sigma}_{ij} = \sigma_{ij} - P_p \alpha_{ij}$, where the pore pressure coefficient α_{ij} is a symmetric second-rank tensor. For isotropic porous materials, $\alpha_{ij} = \alpha \delta_{ij}$, but the value of scalar quantity α has been controversial. According to the critical concentration model of porous materials, α is exactly the volume fraction of the critical concentration phase, $\alpha = \phi_2 / \phi_{cr}$, and this relation is generally applicable to various elastic/inelastic deformation processes and failure state of fluid-saturated isotropic porous materials.

For anisotropic porous materials, we propose $\alpha_{ij} = \alpha_0 \delta_{ij} + A_{ij}$, where A_{ij} quantifies the pore structure anisotropy, and is closely related to the fabric tensor recently proposed in rock mechanics and composite material studies. For the linearly elastic deformation in transversely-isotropic and orthotropic porous rocks, we determine α_{ij} and A_{ij} in terms of directly-measurable elastic constants, and find that the directions and magnitude sequences of effective principal stresses may differ from those of total principal stresses since the pore pressure affects both the normal and shear stress components. In particular, not only the buildup but also the decline of pore pressure in anisotropic porous rocks may lead to faulting and earthquake instabilities.

7.1 Introduction

Pore fluid effects have been proposed as playing a role in a variety of geological processes. The concept of effective stress is the most familiar way to describe the pore pressure effect. The general effective stress law for fluid-saturated isotropic porous materials is

$$\bar{\sigma}_{ij} = \sigma_{ij} - \alpha P_p \delta_{ij}, \quad (7.1)$$

where $\bar{\sigma}_{ij}$ is an effective stress tensor, σ_{ij} is an applied or total stress tensor, P_p is the pore fluid pressure, δ_{ij} is the Kronecker delta, and α is a scalar to quantify the pore pressure effect.

The exact value of α has been controversial. It seems that different elastic and inelastic processes can be controlled by different effective stress laws (Nur and Byerlee, 1971; Robin, 1973; Paterson, 1978; Zimmerman et al., 1986). For an isotropic porous material, let ϕ_2 be the porosity, S_c be the area of contact between the particles in any cross-sectional area S , K be the effective bulk modulus, and K_s be the bulk modulus of the solid phase, Table 7.1 lists the different values of α used mostly in existing effective stress laws and gives short comments on their implications or applicabilities. With these different expressions of α , the first problem we confront with is whether there are fundamental material constants to describe α for different processes.

Equation (7.1) indicates that for isotropic porous materials the pore pressure only affects the normal stress components. Consequently, pore pressure buildup will decrease the effective stress and so destabilize faulting and earthquakes. However, there are more and more reports that pore pressure decline due to fluid extraction from subsurface also destabilizes faulting and earthquakes (Yerkes and Castle, 1976; Segall, 1985, 1989; Wetmiller, 1986; Pennington et al., 1986; Grasso and Wittlinger, 1990; Teufel et al., 1991). How does the pore pressure decline induce rock failure

and faulting? Based on existing studies, this may be attributed to the structural anisotropy of rocks that contain numerous aligned pores, cracks, and fractures.

From the following section it will be evident that the critical concentration model of porous materials can provide a unique way to describe α for different processes. For general anisotropic porous rocks, the effective stress coefficient, a symmetric second-rank tensor, is determined in terms of directly-measurable elastic constants for transversely-isotropic and orthotropic porous rocks. Finally the results are applied to the explanation of the variation of fault slipping, focal stress axis rotation, and especially earthquake instabilities induced by fluid extraction.

Table 7.1 A summary of the effective stress coefficient α

The value of α	References	Comments
$\alpha \approx 1$	Terzaghi (1923, 1936) Hubbert & Rubey (1959) Skempton (1961) Murrell (1963) Brace and Martin (1968)	Based on soil mechanics experiments; agreement with failure/strength data of various rocks.
$\alpha = \phi_2$	Terzaghi (1923, 1942) Schiffman (1970) Manolis & Beskos (1989)	Geometrically consistent; physically identical with solid stress of a porous material.
$\alpha = 1 - \frac{S_c}{S}$	Skempton (1961) Jaeger and Cook (1976)	Being the intergranular stress acting between the particles serving as the material skeleton.
$\alpha = 1 - \frac{K}{K_s}$	Biot and Willis (1957) Geertsma (1957) Skempton (1961) Nur and Byerlee (1971) Rice and Cleary (1976) Zimmerman et al. (1986)	Precise for linear elastic and interconnected-pore materials; with respect to the bulk elastic strain of porous materials.
$\alpha = 1 - \frac{\phi_2 K}{K_s - K}$	Robin (1973) Paterson (1978) Zimmerman et al. (1986)	With respect to the pore volume strain of porous materials.

7.2 Critical Porosity Effects

The critical concentration model of porous materials in Chapter 3 can describe the material microstructural changes from zero porosity to critical porosity ϕ_{cr} . When the concept of effective stress is based on the critical concentration model, the critical porosity, a material constant related to pore geometry and connectivity, plays an important role in quantifying the effective stress.

For isotropic porous materials, the effective stress can be defined as a deformation-producing solid stress which equals the applied stress reduced by a hydrostatic component representing the pore pressure effect. The formula $\alpha = \phi_2$ proposed by Terzaghi (1923) is mainly based on two arguments, (a) the pore pressure effect depends on the fluid volume fraction; (b) in particular, the pore pressure effect should vanish as porosity equals zero. But this formula fails in explaining soil mechanics experimental results that $\alpha \approx 1$ while ϕ_2 of soils is far from unity.

When the critical concentration model is used to analyze the pore pressure effect, we notice that, for $0 \leq \phi_2 \leq \phi_{cr}$, it is the critical concentration phase with volume fraction (ϕ_2/ϕ_{cr}) that applies the pore pressure P_p on the highly load-bearing solid phase with volume fraction $(1 - \phi_2/\phi_{cr})$. Consequently, the value of α is

$$\alpha = \frac{\phi_2}{\phi_{cr}}. \quad (7.2)$$

Equation (7.2) predicts that α is related to pore volume fraction, geometry, and connectivity. It indicates that the pore pressure effect vanishes as porosity approaches zero, consistent with Terzaghi's second argument. More importantly, it predicts $\alpha \approx 1$ when porosity approaches the critical porosity. According to the critical concentration model, as porosity approaches the critical porosity, the material microstructure is like that of a granular material. Thus the effective stress is the intergranular stress acting between the particles serving as the material skeleton. The formula $\alpha = \frac{S-S_c}{S}$

proposed by Skempton (1961) just describes such a situation in terms of the boundary porosity $\frac{S-S_c}{S}$. For statistically isotropic materials, as S_c , the area of contact between skeleton particles, becomes infinitesimal, the material enters the transition between solid and fluid matrix supported states, and the effective stress coefficient α reaches its upper bound, the unity. Therefore we conclude that $\frac{\phi_2}{\phi_{cr}} = \frac{S-S_c}{S}$ for isotropic porous materials.

It is important to point out that equation (7.2) is established without any assumption of linearly/nonlinearly elastic or inelastic materials. Thus it should be applicable to various deformation and failure processes of porous materials, and consistent with other expressions of α under specific circumstances. In rock strength experiments, the increasing loading leads to nucleation of new cracks and merge of existing pores and cracks, thus increasing pore connectivity and decrease the value of critical porosity. The macroscopic failure occurs as the porosity reaches the critical porosity. Consequently, the value of α is close to unity, as often observed in failure/strength experiments of rocks with different porosities (Robinson, 1959; Handin et al., 1963; Murrell, 1963; Brace and Martin, 1968; Bernabe, 1986; Boitnott and Scholz, 1990).

The formulas $\alpha = 1 - \frac{K}{K_s}$ and $\alpha = 1 - \frac{\phi_2 K}{K_s - K}$ are derived for isotropic, linearly elastic, and interconnected-pore materials, with respect to the bulk elastic strain and pore volume strain, respectively (Nur and Byerlee, 1971; Robin, 1973). With the critical concentration model, the effective bulk modulus K of a dry porous material is a function of (ϕ_2/ϕ_{cr}) and K_s , and the factor ϕ_2 in the formula $\alpha = 1 - \frac{\phi_2 K}{K_s - K}$ is now replaced by (ϕ_2/ϕ_{cr}) since the porosity range of porous materials is from zero to ϕ_{cr} . Thus we have

$$\alpha = 1 - \frac{K}{K_s}, \quad (7.3)$$

with respect to the bulk elastic strain, and

$$\alpha = 1 - \frac{\frac{\phi_2}{\phi_{cr}} K}{K_s - K}, \quad (7.4)$$

with respect to the pore volume strain, and in general

$$K = K\left(\frac{\phi_2}{\phi_{cr}}, K_s\right). \quad (7.5)$$

In Chapter 4 we found several expressions of the function $K(\frac{\phi_2}{\phi_{cr}}, K_s)$. One of them is in the form of general percolation solutions,

$$K = \left(1 - \frac{\phi_2}{\phi_{cr}}\right)^T K_s, \quad (7.6)$$

where T is the critical elasticity exponent that can be determined experimentally. When $T = 1$, the solution is identical with the modified Voigt's relation,

$$K = \left(1 - \frac{\phi_2}{\phi_{cr}}\right) K_s, \quad (7.7)$$

Substituting from (7.7) into (7.3) yields

$$\alpha = 1 - \frac{K}{K_s} = 1 - \frac{\left(1 - \frac{\phi_2}{\phi_{cr}}\right) K_s}{K_s} = \frac{\phi_2}{\phi_{cr}}, \quad (7.8)$$

and substituting from (7.7) into (7.4) results in

$$\alpha = 1 - \frac{\frac{\phi_2}{\phi_{cr}} K}{K_s - K} = 1 - \frac{\frac{\phi_2}{\phi_{cr}} \left(1 - \frac{\phi_2}{\phi_{cr}}\right) K_s}{K_s - \left(1 - \frac{\phi_2}{\phi_{cr}}\right) K_s} = \frac{\phi_2}{\phi_{cr}}. \quad (7.9)$$

Why do equations (7.7) and (7.8) become identical to each other? Because the mechanical assumption behind the modified Voigt's relation is the isostrain state

throughout the interconnected-pore material, and so the bulk elastic strain is the same as the pore volume strain.

Finally we notice that equation (7.2) are applicable to not only two-component porous materials, but also multi-component porous materials such as clay-bearing sandstones and gouge-bearing granites.

Clays are often the primary pore-filling particles in sedimentary rocks. Gouges, as a product of sliding and wearing on crack and fracture surfaces, are commonly poorly cemented detrital particles. Gouges are nearly always present in crustal rocks and their effects on fault friction and sliding have been studied in detail (Byerlee, 1967; Dieterich, 1972; Paterson, 1978). Gouges in a rock mass can be taken as secondary pore-filling particles.

We extended the critical concentration model to include pore-filling particles in Chapter 3. Assume that the clay and/or gouge particles do not disturb the solid skeleton of a fluid-saturated material. Let C_2 be the concentration of fluid and a portion of solid not serving as the material skeleton, and C_{cr} be the critical concentration, then the critical concentration phase of clay- and/or gouge-bearing porous materials is of volume fraction C_2/C_{cr} . To quantify the effect of clay and/or gouge particles, let χ be the ratio of the volume fraction of clay and/or gouge particles to the supposed pore volume fraction, and ϕ_{cm} be the particle microporosity. Then the relationship between the critical porosity ϕ_{cr} and critical concentration C_{cr} is

$$\phi_{cr} = C_{cr}[1 - \chi(1 - \phi_{cm})], \quad (7.10)$$

and the value of α is given by

$$\alpha = \frac{C_2}{C_{cr}} = \frac{\phi_2[1 - \chi(1 - \phi_{cm})]}{\phi_{cr}[1 - \chi(1 - \phi_{cm})]} = \frac{\phi_2}{\phi_{cr}}. \quad (7.11)$$

In summary, above analysis shows that the equation (7.2) is indeed a general

expression of the effective stress coefficient for isotropic porous materials. Any of the expressions in Table 7.1 is a specific case reduced from the general expression.

7.3 Microstructural Anisotropy Effects

Recently we have studied the pore pressure effects in anisotropic porous rocks (Chen and Nur, 1991). The remaining of this chapter presents the main results of such theoretical consideration and practical application.

7.3.1 From isotropy to anisotropy

The orientation and distribution of pores and cracks in porous materials may constitute various structural anisotropies, and macroscopic isotropy is one of their specific types with three-dimensional random orientation of pores and cracks. Generalized from equation (7.1), the effective stress law for general anisotropic porous materials can be expressed as

$$\bar{\sigma}_{ij} = \sigma_{ij} - P_p \alpha_{ij}, \quad (7.12)$$

where the effective stress coefficient is a symmetric second-rank tensor α_{ij} . α_{ij} is related to the fabric tensor recently proposed in the studies of rock mechanics and composite materials. The precise definition of a fabric tensor varies with the material microstructure models (Satake, 1978, 1982; Kachanov, 1982; Oda et al., 1982; Oda, 1983; Harrigan and Mann, 1984; Kanatani, 1984). We propose the general expression of α_{ij} as

$$\alpha_{ij} = \alpha_0 \delta_{ij} + A_{ij}, \quad (7.13)$$

where the first term on the right represents the hydrostatic effect of a portion of pore pressure, and the second term A_{ij} , quantifying the pore structure anisotropy,

is closely related to the fabric tensor defined by Sakate (1978). As a special case for isotropic porous materials, A_{ij} is the zero tensor, and $\alpha_0 = \phi_2/\phi_{cr}$. Equations (7.12) and (7.13) are applicable to various elastic and inelastic deformation processes of anisotropic porous materials.

7.3.2 Governing equations for linearly elastic deformation

Most crustal rocks can be taken as homogeneous solid matrix containing anisotropic microstructures such as aligned pores, cracks, and fractures. Let ϵ_{ij} represent the solid strain tensor, m be the fluid mass content per unit volume, and ρ be the pore fluid density, the governing equations for a linearly elastic fluid-saturated rock, according to Biot (1941), Rice and Cleary (1976), and Rudnicki (1985), are expressed as

$$\sigma_{ij} = M_{ijkl}\epsilon_{kl} + P_p N_{ij}, \quad (7.14)$$

$$m - m_0 = \rho N_{ij}\epsilon_{ij} + \eta P_p, \quad (7.15)$$

where M_{ijkl} is the tensor of effective elastic moduli, N_{ij} is an additional elastic constant tensor, and η is a scalar quantity. In an undrained deformation state, $m = m_0$, η can be determined as

$$\eta = -\frac{\rho N_{ij}\epsilon_{ij}}{P_p}. \quad (7.16)$$

When the effective stress is introduced to describe the mechanical behaviors of fluid-saturated rocks, the effective stress-strain relation is

$$\bar{\sigma}_{ij} = M_{ijkl}\epsilon_{kl}, \quad \epsilon_{ij} = C_{ijkl}\bar{\sigma}_{kl}, \quad (7.17)$$

where C_{ijkl} is the effective compliance tensor. Substituting from equation (7.14) into equation (7.17), we arrive at the effective stress law,

$$\bar{\sigma}_{ij} = \sigma_{ij} - P_p N_{ij}. \quad (7.18)$$

By comparing (7.12) with (7.18), we see that the additional elastic constant tensor N_{ij} is the so-called effective stress coefficient α_{ij} .

For linearly elastic deformation of fluid-saturated rocks, α_{ij} can be determined by following the superposition procedure used by Nur and Byerlee (1971) and Carroll (1979),

$$\alpha_{ij} = \delta_{ij} - M_{ijkl} C_{klmm}^s, \quad (7.19)$$

where C_{ijkl}^s is the elastic compliance tensor of rock matrix material.

The intrinsic anisotropy of rocks is governed by the form of C_{klmm}^s , and the structural anisotropy is described by the form of M_{ijkl} . We assume that the rock matrix is isotropic, and so we focus on the structural anisotropy induced by the aligned cracks and fractures embedded in an isotropic rock matrix.

The elastic properties of an isotropic rock matrix are described by only two independent elastic constants, such as bulk modulus K_s and Poisson's ratio ν_s , or Lamé constants μ_s and λ_s . The elastic modulus tensor of an isotropic rock matrix is thus

$$M_{ijkl}^s = \mu_s (\delta_{ik} \delta_{jl} + \delta_{il} \delta_{jk}) + \lambda_s \delta_{ij} \delta_{kl}, \quad (7.20)$$

and then

$$M_{ijkk}^s = 3K_s \delta_{ij}, \quad C_{ijkk}^s = \frac{1 - 2\nu_s}{E_s} \delta_{ij} = \frac{1}{3K_s} \delta_{ij}, \quad (7.21)$$

where E_s is the Young's modulus of isotropic rock matrix. Therefore, the general effective stress law for linearly elastic deformation in structurally-anisotropic rocks can be expressed as

$$\begin{aligned}\bar{\sigma}_{ij} &= \sigma_{ij} - P_p(\delta_{ij} - M_{ijkl}C_{klmm}^s) \\ &= \sigma_{ij} - P_p(\delta_{ij} - \frac{M_{ijkk}}{3K_s}).\end{aligned}\quad (7.22)$$

For isotropic porous rocks, $M_{ijkk} = 3K\delta_{ij}$, then $\alpha_{ij} = (1 - \frac{K}{K_s})\delta_{ij}$, as determined by Skempton(1961), and Nur and Byerlee (1971).

7.3.3 Effective stress coefficients for transversely-isotropic and orthotropic rocks

Transversely-isotropic and orthotropic porous rocks are the main practical models of anisotropic geomaterials. Transverse isotropy may be induced by unidirectionally-aligned spheroidal pores and cracks, or two-dimension randomly oriented cracks and fractures. Orthotropy may come from unidirectionally-aligned ellipsoidal cracks and fractures, or orthogonally conjugate cracks and fractures, or three-dimension orthogonally-oriented cracks and fractures.

When the rock with transverse isotropy is considered, the tensor of effective elastic moduli M_{ijkl} is

$$\begin{aligned}M_{ijkl} &= \mu(\delta_{ik}\delta_{jl} + \delta_{il}\delta_{jk}) + \lambda\delta_{ij}\delta_{kl} + \\ &\quad + \alpha(\delta_{ik}h_jh_l + \delta_{jl}h_ih_k + \delta_{il}h_jh_k + \delta_{jk}h_ih_l) + \\ &\quad + \beta(\delta_{ij}h_kh_l + \delta_{kl}h_ih_j) + \gamma h_ih_jh_kh_l,\end{aligned}\quad (7.23)$$

where $\mu, \lambda, \alpha, \beta$, and γ are elastic constants and h_i are direction cosines of the axis of symmetry. Then M_{ijkk} is

$$\begin{aligned}
M_{ijkk} &= (2\mu + 3\lambda + \beta)\delta_{ij} + \\
&\quad + (4\alpha + 3\beta + \gamma)h_i h_j.
\end{aligned}
\tag{7.24}$$

Therefore the effective stress coefficient for transversely isotropic rocks is

$$\begin{aligned}
\alpha_{ij} &= \left(1 - \frac{2\mu + 3\lambda + \beta}{3K_s}\right)\delta_{ij} - \\
&\quad - \frac{4\alpha + 3\beta + \gamma}{3K_s}h_i h_j.
\end{aligned}
\tag{7.25}$$

In order to understand how the rock microstructural anisotropy governs the pore pressure effects on the total stress, α_{ij} should be described by those elastic constants which directly depict rock microstructural anisotropy and are easy to measure in an experimental lab.. Following the notations proposed by Lekhnitskii (1963), here we use E , E_a , ν , ν_a , and μ_a to describe transversely-isotropic rocks. E and E_a are Young's moduli with respect to directions lying in the plane of isotropy and perpendicular to it, respectively; ν is Poisson's ratio which characterizes the transverse deformation in the plane of isotropy for loading in the same plane; ν_a is Poisson's ratio that describes the transverse deformation in the plane of isotropy for the loading in a direction normal to it; μ_a is the shear modulus for the planes normal to the planes of isotropy. We find

$$2\mu + 3\lambda + \beta = \frac{EE_a(1 + \nu_a)}{E_a(1 - \nu) - 2E\nu_a^2},
\tag{7.26}$$

and

$$4\alpha + 3\beta + \gamma = \frac{E_a^2(1 - \nu) - EE_a(1 - \nu_a)}{E_a(1 - \nu) - 2E\nu_a^2}.
\tag{7.27}$$

Thus, the expression of α_{ij} as in equation (7.13) becomes

$$\begin{aligned}\alpha_{ij} &= \alpha_0 \delta_{ij} + A_{ij} \\ &= \left(1 - \frac{EE_a(1 + \nu_a)}{3K_s[E_a(1 - \nu) - 2E\nu_a^2]}\right) \delta_{ij} + \\ &\quad + \frac{EE_a(1 - \nu_a) - E_a^2(1 - \nu)}{3K_s[E_a(1 - \nu) - 2E\nu_a^2]} h_i h_j.\end{aligned}\quad (7.28)$$

There are nine independent elastic constants to describe orthotropic rock behaviors. Let us assume three orthogonal planes of elastic symmetry with normal x , y , and z , there are three Young's moduli E_x , E_y , E_z , three shear moduli μ_{yz} , μ_{xz} , μ_{xy} , and three Poisson's ratios ν_{yx} , ν_{zx} , and ν_{zy} (Lekhnitskii, 1963). We find

$$M_{ijkk} = M_x l_i l_j + M_y m_i m_j + M_z n_i n_j \quad (7.29)$$

where l_i , m_i , and n_i are direction cosines of the symmetry axes x , y , and z , respectively, and

$$M_x = \frac{E_x E_y E_z (1 + \nu_{yx} + \nu_{zx} + \nu_{yx} \nu_{zy}) + E_x E_y^2 \nu_{zy} (\nu_{zx} - \nu_{zy})}{D}, \quad (7.30)$$

$$M_y = \frac{E_x E_y E_z \nu_{yx} (1 + \nu_{zx}) + E_y^2 [E_x \nu_{zx} (\nu_{zy} - \nu_{zx}) + E_z (1 + \nu_{zy})]}{D}, \quad (7.31)$$

$$M_z = \frac{E_x E_y E_z [\nu_{zx} + \nu_{yx} (\nu_{zx} + \nu_{zy})] + E_y^2 E_z \nu_{zy} + E_z^2 (E_y - E_x \nu_{yx}^2)}{D}, \quad (7.32)$$

where

$$D = E_y(E_z - 2E_x\nu_{yx}\nu_{zy}\nu_{zx} - E_y\nu_{zy}^2) - E_x(E_z\nu_{yx}^2 + E_y\nu_{zx}^2). \quad (7.33)$$

Thus the effective stress coefficient is

$$\alpha_{ij} = (\delta_{ij} - \frac{M_x l_i l_j + M_y m_i m_j + M_z n_i n_j}{3K_s}). \quad (7.34)$$

When the elastic symmetry axis x , y , or z is not consistent with any one of normal stress directions 1, 2, or 3, the pore pressure influences both the normal and shear stress components with different magnitudes on each of them. When x , y , and z are consistent with axes 1, 2, and 3, respectively, (7.34) becomes

$$\alpha_{ij} = (1 - \frac{M_x}{3K_s})l_i l_j + (1 - \frac{M_y}{3K_s})m_i m_j + (1 - \frac{M_z}{3K_s})n_i n_j. \quad (7.35)$$

7.3.4 Directions and magnitude sequences of effective principal stresses

The pore pressure in anisotropic porous rocks affects both the normal and shear stress components, and so the directions and magnitude sequences of effective principal stresses may differ from those of total principal stresses.

For transversely-isotropic rocks, the effective stress law can be written as

$$\bar{\sigma}_{ij} = \sigma_{ij} - P_p(\alpha_0 \delta_{ij} + \alpha_a h_i h_j), \quad (7.36)$$

where

$$\alpha_0 = 1 - \frac{EE_a(1 + \nu_a)}{3K_s[E_a(1 - \nu) - 2E\nu_a^2]}, \quad (7.37)$$

$$\alpha_a = \frac{EE_a(1 - \nu_a) - E_a^2(1 - \nu)}{3K_s[E_a(1 - \nu) - 2E\nu_a^2]}. \quad (7.38)$$

Given the total stress σ_{ij} as a principal stress state,

$$\begin{aligned} \sigma_{11} &= \sigma_1, \quad \sigma_{22} = \sigma_2, \quad \sigma_{33} = \sigma_3, \\ \sigma_{12} &= \sigma_{13} = \sigma_{23} = 0, \\ \sigma_1 &\geq \sigma_2 \geq \sigma_3, \end{aligned} \quad (7.39)$$

the effective stress $\bar{\sigma}_{ij}$ is

$$\begin{pmatrix} \bar{\sigma}_{11} & \bar{\sigma}_{12} & \bar{\sigma}_{13} \\ \bar{\sigma}_{21} & \bar{\sigma}_{22} & \bar{\sigma}_{23} \\ \bar{\sigma}_{31} & \bar{\sigma}_{32} & \bar{\sigma}_{33} \end{pmatrix} = \begin{pmatrix} \sigma_1 & 0 & 0 \\ 0 & \sigma_2 & 0 \\ 0 & 0 & \sigma_3 \end{pmatrix} - P_p \begin{pmatrix} \alpha_0 + \alpha_a h_1^2 & \alpha_a h_1 h_2 & \alpha_a h_1 h_3 \\ \alpha_a h_1 h_2 & \alpha_0 + \alpha_a h_2^2 & \alpha_a h_2 h_3 \\ \alpha_a h_1 h_3 & \alpha_a h_2 h_3 & \alpha_0 + \alpha_a h_3^2 \end{pmatrix}. \quad (7.40)$$

From (7.36) we see that a portion of the pressure effect is hydrostatic, and the other portion depends on the orientation of the symmetric axis in transversely-isotropic rocks. When the symmetric axis is not consistent with any of total principal stress directions, (7.40) indicates that effective principal stress directions $1', 2', 3'$ are not consistent with the axes 1, 2, 3, respectively.

The value of α_a in equation (7.36) may be positive or negative, depending on the relative magnitudes of E , E_a , ν , and ν_a . For the transverse isotropy induced by unidirectionally-aligned penny-shaped cracks, E_a is much smaller than E , and so α_a is positive. However, for the transverse isotropy induced by randomly oriented cracks in two dimension, E_a may be much bigger than E , and so α_a becomes negative. Consequently, the magnitude sequences of effective principal stresses, relying on total stress, pore pressure, and transversely-isotropic feature, have up to six possible arrangements.

For the orthotropic rocks with fluids, let us assume the total stress is of the form in (7.39), and the symmetric axes x, y, z are consistent with principal stress axes 1, 2, 3, respectively. Then the effective stress state is

$$\begin{pmatrix} \bar{\sigma}_1 & 0 & 0 \\ 0 & \bar{\sigma}_2 & 0 \\ 0 & 0 & \bar{\sigma}_3 \end{pmatrix} = \begin{pmatrix} \sigma_1 & 0 & 0 \\ 0 & \sigma_2 & 0 \\ 0 & 0 & \sigma_3 \end{pmatrix} - P_p \begin{pmatrix} 1 - \frac{M_x}{3K_s} & 0 & 0 \\ 0 & 1 - \frac{M_y}{3K_s} & 0 \\ 0 & 0 & 1 - \frac{M_z}{3K_s} \end{pmatrix}. \quad (7.41)$$

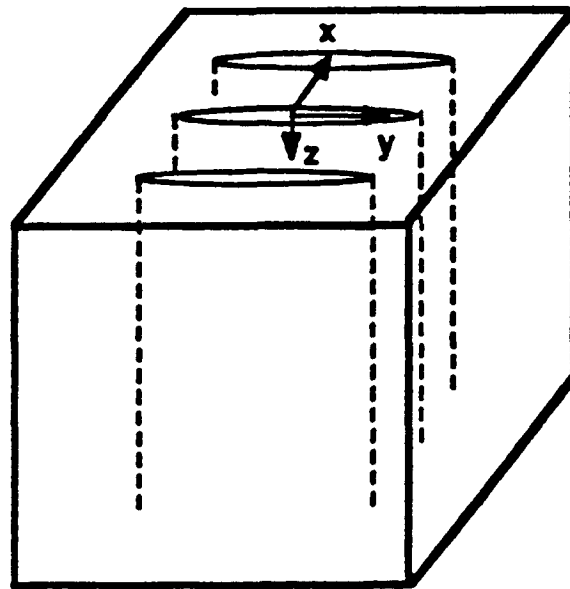
In order to compare the relative magnitudes of pore pressure effects on different directions, we consider a simple rock model with unidirectionally-aligned cracks as in Fig.7.1(a). The effective elastic constants can be computed by the boundary element method (Chen et al. 1990). Fig.7.1(b) compares the pore pressure effects on 1, 2, and 3 directions. When the pore pressure is in the same order as the total stress, the anisotropy effect will lead to different magnitude sequences of three effective principal stresses.

7.4 Applications

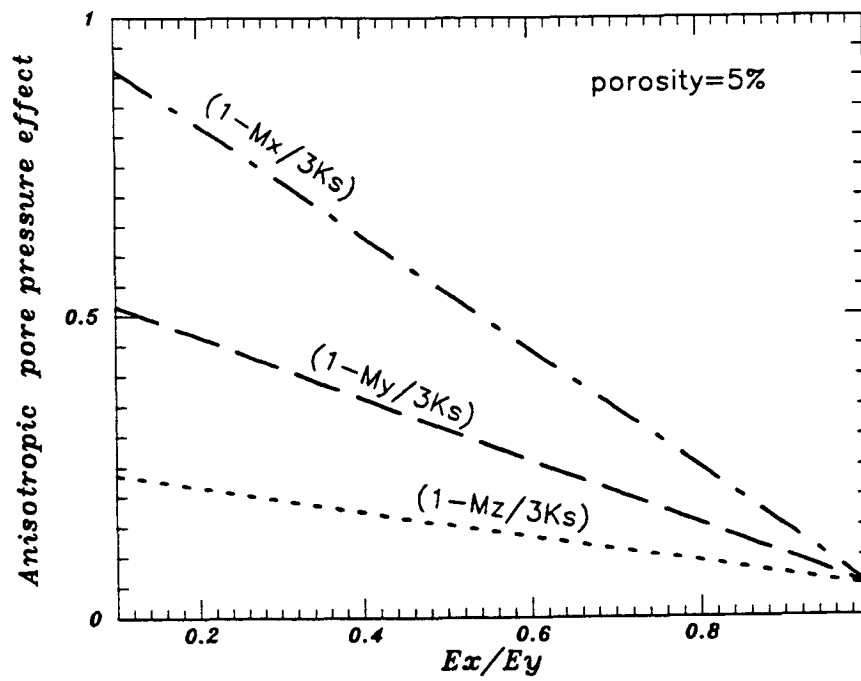
The pore pressure effect in anisotropic porous rocks can provide a new class of explanations and evaluations to many geological and geophysical phenomena especially earthquake activities. Here we discuss some problems related to the variations of stress directions and magnitudes, and provide explanations to them in terms of the above results.

7.4.1 Variation of fault slipping

The occurrence and slipping history of strike-slip faults, normal faults, and reverse faults in the crustal rocks are generally controlled by the directions and magnitude sequences of principal stresses (Anderson, 1951). It is generally recognized that the direction and magnitude of regional tectonic stresses are quite stable over a geological



(a)



(b)

Fig.7.1 (a) A rock model with unidirectionally-aligned cracks, (b) the relative magnitudes of pore pressure effects on different directions.

time. But many studies of active faults indicate that the slipping history of a fault may vary in slipping type and/or slipping rate. Since time-dependent pore pressure variation is quite possible in the crust (Nur and Walder, 1990), the pore pressure effect in anisotropic rocks may lead to the variation of effective stress directions and magnitude sequences from previous tectonic stress state, and this new state of effective stresses changes faulting types and slipping rate.

7.4.2 Variation of focal stress axes

The variations of effective stress directions and magnitude sequences render a reasonable explanation to the stress axis rotation observed in focal region prior to a mainshock (Nersesov and Simbireva 1968, Song et al. 1988). Several mechanisms have been proposed to explain the stress axis rotation. Kuo et al. (1973) suggested that plastic deformation in a focal region may change the focal stress state and direction. Brady (1974) used the inclusion theory to explain the stress axis rotation in terms of crack closure. Wu et al. (1980) proposed that the impacting of thermal fluids in surrounding regions causes the stress state and direction change. Indeed, the thermal fluids from surrounding and deep sources in the lithosphere have substantial effects on the crustal deformation and failure (Gold and Soter 1985, Zhang 1985; Sammis and Julian 1987; Nur and Walder 1990). With time-dependent hydraulic properties and stress-induced cracks/fractures in crustal rocks, the ascending fluids from the deep sources will have anisotropic pressure effects on the rocks, resulting in the changes of direction and magnitude sequence of effective stresses.

7.4.3 Pore pressure coefficient on a failure plane

For dry rocks with strong dependence on hydrostatic pressure, Jaeger and Cook (1976) modified Coulomb criterion to include anisotropic effects. When the pore pressure effect in anisotropic rocks is taken into account, the modified Coulomb criterion can be written as

$$\bar{\tau} = \tau'_0 + \xi'(\sigma - \alpha_f P_p), \quad (7.42)$$

where τ'_0 and ξ' are the cohesion and friction coefficient depending on anisotropic properties (Jaeger and Cook 1976, Donath et al. 1979), and α_f represents the anisotropic pore pressure coefficient on the potential failure plane.

Assume (l_0, m_0, n_0) as the direction cosines of the potential failure plane referenced to the coordinate system with orthogonal axes 1, 2, and 3, α_f is found related to α_{ij} as

$$\begin{aligned} \alpha_f = & \alpha_{11}l_0^2 + \alpha_{22}m_0^2 + \alpha_{33}n_0^2 + \\ & + 2\alpha_{12}l_0m_0 + 2\alpha_{13}l_0n_0 + 2\alpha_{23}m_0n_0. \end{aligned} \quad (7.43)$$

For the effective stress state given in (7.41), we have

$$\alpha_f = 1 - \frac{M_x l_0^2 + M_y m_0^2 + M_z n_0^2}{3K_s}. \quad (7.44)$$

Thus, α_f depends on both the rock anisotropy features and the orientation of a potential failure plane. When the pore pressure is in the same order as the total stress, the change of effective shear stress is mainly attributed to the variation of α_f .

7.4.4 Earthquakes induced by fluid extraction

Based on above results we can now construct the Mohr circle diagrams to show how the pore pressure buildup and decline in orthotropic rocks affect faulting instability. Assume that the normals of three symmetry planes are consistent with principal stress axes, then there are up to six possible arrangements of the normals x, y, and z with respect to the axes 1, 2, and 3.

Fig.7.2 shows that, when (x, y, z) are consistent with $(1, 2, 3)$, respectively, the pore pressure buildup stabilizes the faulting, and the pore pressure decline destabilizes the faulting. Fig.7.3 gives the opposite results when (x, y, z) are consistent with $(3, 2, 1)$, respectively.

Fig.7.4 shows the Mohr circle diagram with (x, y, z) corresponding to $(2, 1, 3)$. The pore pressure buildup destabilizes the faulting, but an important point is that, the faulting type governed by $\bar{\sigma}_1 > \bar{\sigma}_3 > \bar{\sigma}_2$ is quite different from that controlled by $\sigma_1 > \sigma_2 > \sigma_3$.

Fig.7.2(b) provides a good explanation to the faulting and earthquakes induced by fluid extraction from subsurface. When weakness planes, composed of unidirectionally-aligned cracks or fractures, or debonded layer interfaces, in porous rocks are perpendicular to the maximum principal stress direction, the fluid pressure decline in the rocks will probably lead to the faulting and trigger earthquakes. Furthermore, when the occurrences of weakness planes are vertical, and regional maximum principal stress is horizontal, the fluid extraction will lead to limiting stress state for thrust faulting or earthquakes of thrust-faulting focal mechanism.

In several oil fields where great amount of fluids are extracted from subsurface, many thrust faults and earthquakes of thrust-faulting focal mechanism just located above and beneath the fluid zone have been reported (Yerkes and Castle 1976, Segall 1985, Pennington et al. 1986, Wetmiller, 1986). The local stress fields in some of those fluid-extracted regions have been determined by other methods as horizontally-maximum stress fields (Wetmiller 1986, Grasso and Wittlinger 1990). Therefore, these seismic observations and measurements support the mechanism as proposed in this study.

On the other hand, when the local stress field is characteristic of maximum vertical stress field, a sufficient fluid pressure decline in the rock containing horizontal weakness planes such as layer interfaces will lead to the stress state for normal fault-

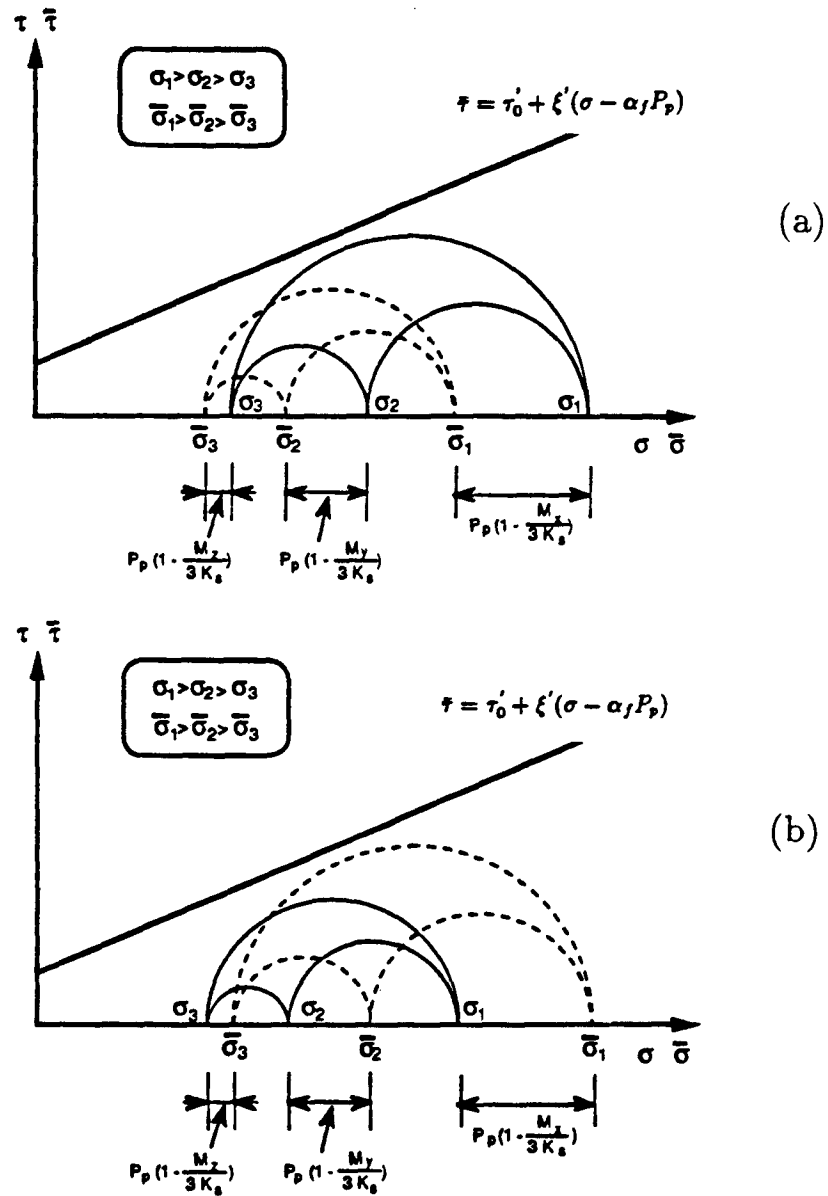


Fig.7.2 Mohr circle diagram for the effect of pore fluid pressure in orthotropic rock. (x,y,z) consistent with (1,2,3), respectively.
 (a) pore pressure buildup stabilizes faulting, (b) pore pressure decline destabilizes faulting

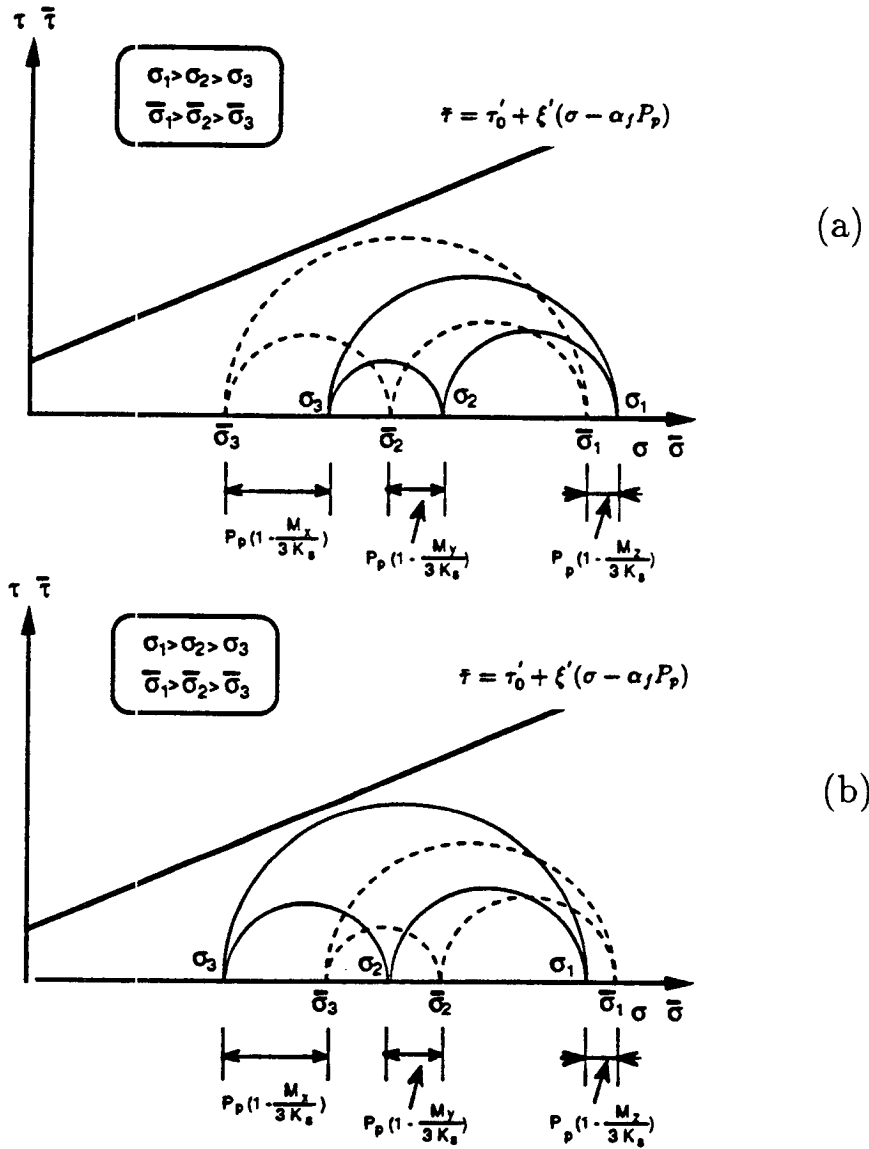


Fig.7.3 Mohr circle diagram for the effect of pore fluid pressure in orthotropic rock. (x,y,z) consistent with (3,2,1), respectively.
 (a) pore pressure buildup destabilizes faulting, (b) pore pressure decline stabilizes faulting

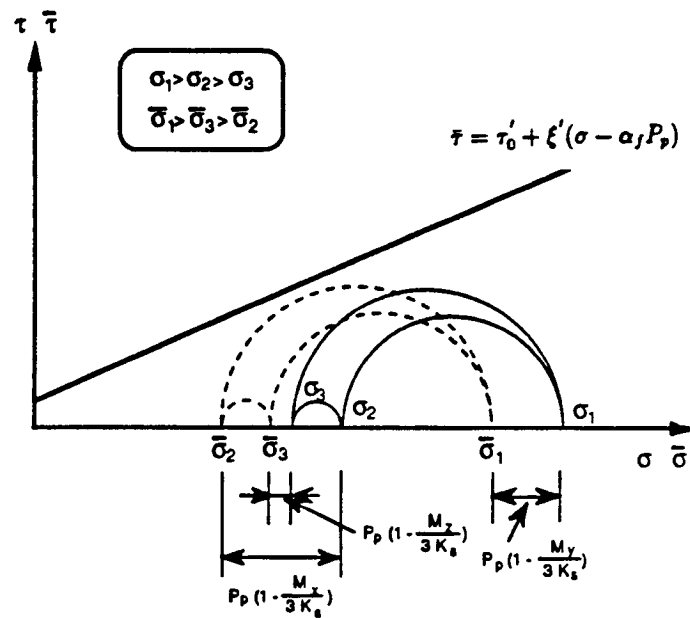


Fig.7.4 Mohr circle diagram for the effect of pore fluid pressure in orthotropic rock. (x,y,z) consistent with (2,1,3), respectively. The magnitude sequence of effective stresses differs from that of total stresses

ing and earthquakes of normal-faulting focal mechanism. This mechanism may be also useful to understand the normal faulting and earthquakes associated with fluid extraction in oil fields (Yerkes and Castle 1976, Segall 1989).

7.5 Conclusions

The general effective stress law for anisotropic porous materials is $\bar{\sigma}_{ij} = \sigma_{ij} - P_p \alpha_{ij}$. For isotropic porous materials, $\alpha_{ij} = \alpha \delta_{ij}$, and the critical concentration model of porous materials indicates that α is exactly the volume fraction of the critical concentration phase, $\alpha = \phi_2 / \phi_{cr}$, which is applicable to various elastic and inelastic deformation processes.

For anisotropic porous materials, $\alpha_{ij} = \alpha_0 \delta_{ij} + A_{ij}$, and we determine α_{ij} and A_{ij} in terms of directly-measurable elastic constants for the linearly elastic deformation in transversely-isotropic and orthotropic porous rocks.

The pore pressure effect in anisotropic porous rocks may lead to the departure of effective stress directions and magnitude sequence from those of total stresses. Consequently, not only the buildup but also the decline of pore pressure in anisotropic porous rocks may lead to faulting and earthquake instabilities. The result can provide explanations to many geological and geophysical phenomena, especially the faulting and earthquakes induced by extracting fluid from subsurface.

References

- Anderson, E. M., 1951, The dynamics of faulting and dyke formation with applications to Britain: Oliver and Boyd, Edingburgh, pp.206.
- Bernabe, Y., 1986, An effective pressure law for permeability in Chelmsford granite and Barre granite: *Int. J. Rock Mech. Miner. Sci. Geomech. Abstr.*, **23**, 267-275.
- Biot, M. A. 1941, General theory of three-dimensional consolidation: *J. Appl. Phys.*, **12**, 155-164.
- Biot, M. A. and D. G. Willis, 1957, The elastic coefficients of theory of consolidation: *J. Appl. Mech.*, 594-601.
- Boitnott, G. N. and C. H. Scholz, 1990, Direct Measurement of the effective pressure law: deformation of joints subject to pore and confining pressures: *J. Geophys. Res.*, **95**, 19,279-19,298.
- Brace, W. F., and R. J. Martin III, 1968, A test of effective stress law for crystalline rocks of low porosity: *Int. J. Rock Mech. Miner. Sci.*, **5**, 415-426.
- Brady, B.T., 1974, Theory of earthquakes, I. A scale independent theory of rock failure, *Pure and Appl. Geophys.*, **112**, 701-725.
- Carroll, M. M., 1979, An effective stress law for anisotropic elastic deformation: *J. Geophys. Res.*, **84**, 7510-7512.
- Chen, Q., Nur, A., Mavko, G., and J. Dvorkin, 1990, Modeling effective elastic moduli of porous rocks: *SRB*, **40**, Paper C.
- Chen, Q. and A. Nur, 1991, Pore pressure effects in anisotropic porous rocks, in *Proc. Int. Conference on Earthquake Prediction: State of the Art*, Strasbourg, France, 184-192.
- Dieterich, J. H., 1972, Time-dependent friction in rocks: *J. Geophys. Res.*, **77**, 3690-3697.
- Donath, F. A., K. W. Schuler, and J. R. Tillerson, 1979, Apparatus effects in the determination of strength variation in anisotropic rock: *Colloques internationaux du CNRS, N° 295, Comportement mécanique des solides anisotropies*, 819-832.
- Geertsma, J., 1957, The effect of fluid pressure decline on volumetric changes of porous rocks: *Trans. AIME*, **210**, 331.
- Gold, T. and S. Soter, 1985, Fluid ascent through the solid lithosphere and its relation

- to earthquakes, *Pure and Appl. Geophys.*, **122**, 492-530.
- Grasso, J. R., and G. Wittlinger, 1990, Ten years of seismic monitoring over a gas field: *Bull. Seis. Soc. Amer.*, **80**, 450-473.
- Handin, J., R. V. Hager, Jr., M. Friedman, and J. N. Feather, 1963, Experimental deformation of sedimentary rocks under confining pressure: Pore pressure tests: *Bull. Amer. Ass. Petrol. Geol.*, **47**, 717-755.
- Harrigan, T. and R. W. Mann, 1984, Characterization of microstructural anisotropy in orthotropic materials using a second rank tensor: *J. Mat. Sci.*, **19**, 761-767.
- Hubbert, M. K., and W. W. Rubey, 1959, Role of fluid pressure in mechanics of overthrust faulting: *Bull. Geol. Soc. Amer.*, **70**, 115-205.
- Jaeger, J. C. and N. G. W. Cook, 1976, *Fundamentals of rock mechanics*: 2nd ed., London, Chapman and Hall, pp.584.
- Kachanov, M., 1982, A micro-crack model of rock elasticity, Part 1. Frictional sliding on micro-cracks: *Mech. Mater.*, **1**, 19-27.
- Kanatani, K., 1984, Distribution of directional data and fabric tensor: *Int. J. Engng Sci.* **22**, 149-164.
- Kuo, T. C., Chin, P. Y., Hsu, W. Y., and C. Tang, 1973, A preliminary model for the development of the focus of an earthquake, *Acta Geophysica Sinica* (translated from Chinese version), **16**, 40-45.
- Lekhnitskii, S. G., 1963, *Theory of elasticity of an anisotropic elastic body*, Holden Day, Inc. San Francisco, pp.404.
- Manolis, G. D. and D. E. Beskos, 1989, Integral formulation and fundamental solutions of dynamic poroelasticity and thermoelasticity: *Acta Mechanica*, **76**, 89-104.
- Murrell, S. A. F., 1963, A criterion for brittle fracture of rocks and concrete under triaxial stress, and the effect of pore pressure on the criterion: in Fairhurst c (ed.), *Rock Mechanics, Proc. 5th Symp. Rock Mech.* New York, Pergamon Press, 563-577.
- Nersesov, I. L. and I. G. Simbireva, 1968, Regularities in the distribution of stresses in the foci of weak earthquakes in the Garm area and their relationship to seismicity, *Third All-Union Symposium of the Seismic Regime, Part I*, 147-181.
- Nur, A., and J. D. Byerlee, 1971, An exact effective stress law for elastic deformation of rock with fluids: *J. Geophys. Res.*, **76**, 6414-6419.

- Nur, A., and J. Walder, 1990, Time-dependent hydraulics of the earth's crust, in *The Role of Fluids in Crustal Processes*, National Academy Press, 113-127.
- Oda, M., 1983, A method for evaluating the effect of crack geometry on the mechanical behavior of cracked rock masses: *Mech. Materials*, **2**, 163-171.
- Oda, M., Nemat-Nasser, S., and M. M. Mehrabadi, 1982, A statistical study of fabric in a random assembly of spherical granules: *Int. J. Numer. Anal. Mech. Geomech.*, **6**, 77-94.
- Paterson, M. S., 1978, *Experimental rock deformation — the brittle field*: Springer-Verlag, Berlin, Heidelberg, New York, pp.254.
- Pennington, W., S. D. Davis, S. M. Carlson, J. Dupree, and T. E. Ewing, 1986, The evolution of seismic barriers and asperities caused by the depressuring of fault planes in oil and gas fields of south Texas: *Bull Seis. Soc. Amer.*, **76**, 939-948.
- Rice, J. R. and M. P. Cleary, 1976, Some basic stress diffusion solutions for fluid-saturated elastic porous media with compressible constituents: *Rev. Geophys. Space Phys.*, **14**, 227-241.
- Robin, P.-Y. F., 1973, Note on effective pressure: *J. Geophys. Res.*, **78**, 2434-2437.
- Robinson, L. H., Jr., 1959, The effect of pore and confining pressure on the failure process in sedimentary rock: *Colo. Sch. Mines Quart.*, **54**, 177-199.
- Rudnicki, J. W., 1985, Effect of pore fluid diffusion on deformation and failure of rock: In Z. Bazant (eds.), *Mechanics of geomaterials*, 315-347, John Wiley & Sons Ltd.
- Sammis, C. G. and B. R. Julian, 1987, Fracture instabilities accompanying dike intrusion, *J. Geophys. Res.*, **92**, B3, 2597-2605.
- Satake, M., 1978, Constitution of mechanics of granular materials through graph representation: *Theoret. Appl. Mech.*, **26**, 257-266.
- Satake, M., 1982, Fabric tensor in granular materials: in P. A. Vermeer and H. J. Ligar, eds., *Deformation and Failure of Granular Materials*, Balkema, Rotterdam.
- Schiffman, R. L., 1970, The stress components of a porous medium: *J. Geophys. Res.*, **75**, 4035-4038.
- Segall, P., 1985, Stress and subsidence resulting from subsurface fluid withdrawal in the epicentral region of 1983 Coalinga earthquake: *J. Geophys. Res.*, **90**, 9801-

9816.

Segall, P., 1989, Earthquakes triggered by fluid extraction: *Geology*, **17**, 942-946.

Skempton, A. W., 1961, Effective stress in soils, concrete and rock: Conference on Pore Pressure and Suction in Soils, 4-16, Butterworth, London.

Song, H. Z., Yuan, Y. G., Huang, L. R., and X. W. Hua, 1988, Analysis on the 1976 Tangshan earthquake process, *Seismology and Geology*, **10**, No.4, 98-108.

Terzaghi, K. V., 1923, Die Berechnung der Durchlässigkeitsziffer des Tones aus dem Verlauf der hydrodynamischen Spannungserscheinungen: *Sitzungsber. Akad. Wiss. Wien*, **132**, 105-124.

Terzaghi, K. V., 1936, The shearing resistance of saturated soils and the angle between the planes of shear: *Proc. Int. Confer. Soil Mech. Found. Engng*, **1**, 54-56. Harvard University Press, Cambridge, Mass..

Teufel, L. W., Rhett, D. W., and H. E. Farrell, 1991, Effect of reservoir depletion and pore pressure drawdown on in situ stress and deformation in the Ekofisk Field, North Sea: *Proc. 32nd U.S. Symp. Rock Mech. Roegiers, J. C. (ed.)*, 63-72. Rotterdam, Brookfield.

Wetmiller, R., 1986, Earthquakes near Rocky Mountain House, Albertas, and their relationship to gas production facilities: *Can. J. Earth Sci.*, **23**, 172-181.

Wu, J. X., Wang, Y. L., and S. Y. Li, 1980, The characteristics of forerunner field of underground water regime during Tangshan earthquake and its focal evolution process, *Seismology and Geology*, **2**, No.1, 65-78.

Yerkes, R. F., and R. O. Castle, 1976, Seismicity and faulting attributable to fluid extraction: *Engineering Geol.*, **10**, 151-167.

Zhang, Z. L., 1985, Investigation on the thermal force sources of 1976 Tangshan earthquake, *Acta Seismologica Sinica*, **7**, No.1, 45-56.

Zimmerman, R. W., Somerton, W. H., and M. King, 1986, Compressibility of porous rocks: *J. Geophys. Res.*, **91**, 12,765-12,777.

Chapter 8

Critical Concentration Strength Theory of Porous Materials

Abstract

A strength theory of porous materials is established on the basis of the critical concentration model. Pores and cracks of porous materials reduce the load-bearing area, induce the stress concentration, and lead to the critical porosity, which are all taken into account by redefining the actual stress from the nominal stress, average stress, to local stress. Such actual stresses are responsible for porous materials failure and fracture, and so the uniaxial tensile and compressive strength criteria, and linear and nonlinear shear strength criteria are investigated in terms of the actual stress. Then, the effect of transverse isotropy on porous material strengths is explored. Finally, the failure mechanism in transversely-isotropic porous materials is applied to the explanation of tectonic block rotations.

8.1 Introduction

The strength properties and fracture features of porous materials are closely related to their microstructures, or pore structures. Low-porosity porous materials are usually taken as cracked materials, and fracture mechanics has been widely used in describing the dependence of fracture strength and propagation on crack structures (Griffith, 1920; Irwin, 1958; Paris and Sih, 1965; Lawn and Wilshaw, 1975; Atkinson and Meredith, 1987; Aliabadi and Rooke, 1991). In particular, the micromechanical fracture criteria such as the Griffith criterion and its improvements of cracked materials are quite successful in predicting the strength and fracture propagation in low-porosity geomaterials (McClintock and Walsh, 1962; Murrell, 1963; Bertolotti and Fulrath, 1967; Rice, 1984; Krstic, 1988; Ingraffea, 1989; Lajtai et al., 1990; Gdoutos, 1990).

However, fracture mechanics based on a single crack or thin pore embedded in solid matrix can not describe the strong effects of porosity on porous material strengths and fracture features as indicated by numerous experimental studies. Most sedimentary rocks are characterized by broad range of porosity, and complicated pore geometry and connectivity. When the strength and fracture feature of such high-porosity rocks are concerned, far less well understood is how the strength properties change with porosity and other parameters characterizing the pore structures. The objective of this chapter is to develop a strength theory which is based on the critical concentration model of porous materials, and is focused on the uniaxial tensile, uniaxial compressive, and shear strength criteria of porous materials.

8.2 Critical Porosity and Actual Stress

Experiments show that all strength properties of porous materials fall with increase in porosity, which is attributed to two aspects of pore effect:

- (1) pores and cracks decrease the load-bearing area of the material and so decrease

the strength;

(2) stress concentration induced on the boundaries of pores and cracks reduces the strength.

Pore volume fraction (porosity) has been used as a major parameter of pore effect in empirical strength relations of porous materials, and it has been customary to regard porosity as an end member of two-phase material. However, more and more experimental data indicate that the uniaxial tensile and compressive strengths, and shear strengths of porous materials approach zero at finite porosities ranging from 20% to 80% (Schiller, 1958; Price, 1960; Smorodinov et al., 1970; Rzhnevsky and Novik, 1971; Dunn et al., 1973; Hoshino, 1974; Kendall, 1984; Lemaitre, 1985; Jizba, 1991). Such porosity is the critical porosity at which the porous material collapses, as defined in Chapter 3. Since the critical porosity is related to the pore geometry and connectivity, a rigorous strength theory of porous materials should take into account not only the pore volume fraction but also the pore geometry and connectivity. In other words, the first aspect of pore effect stated above should be described by both the porosity and critical porosity.

In experiments with porous material samples, the boundary applied stress is usually measured in terms of the whole section area of a porous material sample. Such stress is the nominal stress (Kachanov, 1986), or total macroscopic stress (Paterson, 1978). In order to quantify the pore effect on the material strength, one must study how such nominal stress and the macroscopic strength are related to the actual stress in the load-bearing solid skeleton of porous materials. For a statistically isotropic porous material, as analyzed in chapter 7, the boundary porosity $\frac{S-S_c}{S}$ is related to the critical porosity ϕ_{cr} by

$$\frac{S - S_c}{S} = \frac{\phi_2}{\phi_{cr}}. \quad (8.1)$$

If only the first aspect of pore effect is taken into account, the actual stress can

be defined in a way similar to that in damage mechanics (Lemaitre, 1985; Kachanov, 1986). With a uniaxial loading P , the actual normal stress σ_a is defined as

$$\sigma_a = \frac{P}{S_c} = \frac{P}{S(1 - \frac{\phi_2}{\phi_{cr}})} = \frac{\sigma}{(1 - \frac{\phi_2}{\phi_{cr}})}, \quad (8.2)$$

where σ is the nominal normal stress. With the same reason, the actual shear stress τ_a is defined as

$$\tau_a = \frac{\tau}{(1 - \frac{\phi_2}{\phi_{cr}})}, \quad (8.3)$$

where τ is the nominal shear stress.

The actual stresses in equations (8.2) and (8.3) represent the average stresses on the load-bearing solid skeleton of a porous material, which are the first-order approximation of nonhomogeneous stress state in the porous material.

Since our interest is to study how the material strength varies with the both aspects of pore effect, and it is generally recognized that pores and cracks can behave as stress concentrators and serve as fracture origins, the actual stress should be defined as the local stress which is the maximum stress in the nonhomogeneous stress field and responsible for the material failure and fracture. For a solid containing a single isolated pore or crack, it is possible to find the maximum stress concentration by means of elastic mechanics or fracture mechanics, but in porous materials containing a large number of pores and cracks, the maximum stress concentration is expected to be altered by all pore structure features, in other words, both the porosity and critical porosity. On the basis of equations (8.2) and (8.3), the stress concentration due to pore structures leads to the general definition of actual stress,

$$\sigma_a = \frac{\sigma}{(1 - \frac{\phi_2}{\phi_{cr}})^D}, \quad (8.4)$$

$$\tau_a = \frac{\tau}{\left(1 - \frac{\phi_2}{\phi_{cr}}\right)^D}, \quad (8.5)$$

where the parameter D represents the degree of stress concentration. In general, D can be determined by uniaxial experiments of porous materials.

The stress concentration near pore boundaries is related to pore size, geometry, and connectivity (Muskhelishvili, 1953; Timoshenko and Goodier, 1970; Jaeger and Cook, 1976; Rice, 1984; Krstic, 1988). Since the critical porosity is closely related to pore geometry and connectivity, we propose a formula to estimate D , by generalizing Rossi's hypothesis from effective moduli to failure strengths (Janowski and Rossi, 1967; Rossi, 1968; Bert, 1985),

$$D = D_0 \phi_{cr}, \quad (8.6)$$

where D_0 is the stress concentration factor defined as the maximum stress reached in the material divided by the applied stress. When a spheroidal pore with aspect ratio c/a (the ratio of pore length along loading direction to pore width) is considered, Rossi (1968) found

$$D_0 = 0.75 + (1.25a/c). \quad (8.7)$$

For example, $D_0 = 2$ for spherical pores, $D_0 \approx 1$ for needle-like pores parallel to loading direction, and $D_0 > 2$ for oblate pores.

8.3 Uniaxial Strength Criteria

From above analysis it is now reasonable to assume that the actual stress in the load-bearing solid skeleton is responsible for the deformation and failure of a porous

material. When the actual stress σ_a reaches the macroscopic strength for a specific loading, the porous material failure occurs.

8.3.1 Tensile strength criterion

Let σ_t represent the uniaxial tensile strength in a solid material without pores. For a tensile loading, the uniaxial tensile strength criterion of the porous material is thus

$$\sigma = \sigma_t \left(1 - \frac{\phi_2}{\phi_{cr}}\right)^D. \quad (8.8)$$

For comparison, some existing empirical criteria are of the forms

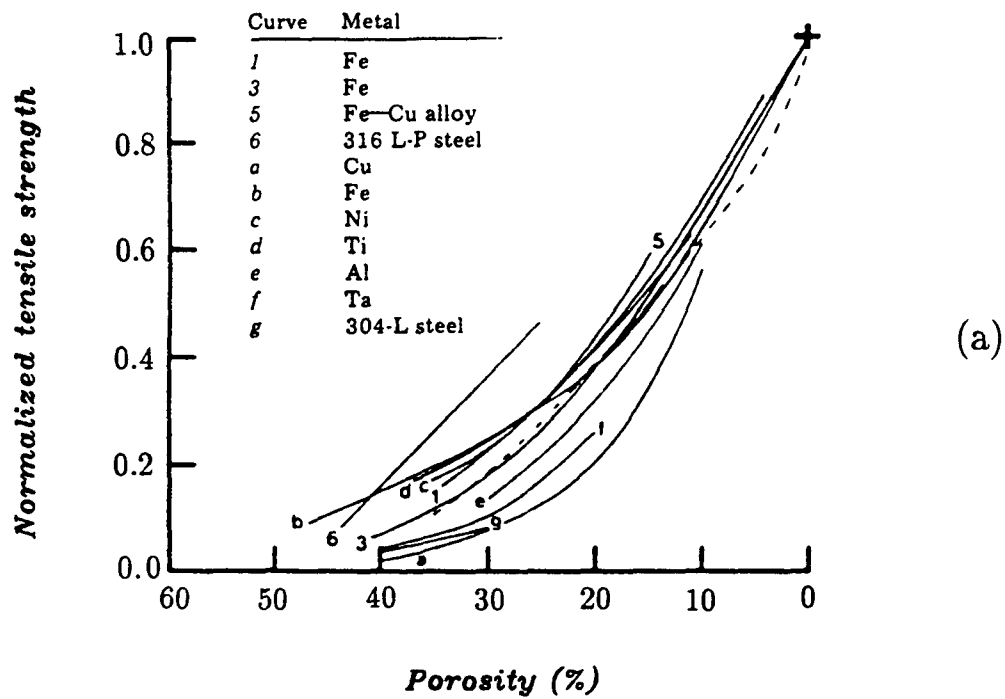
$$\sigma = \sigma_t (1 - \phi_2) \quad (8.9)$$

as suggested by Haynes (1971), and

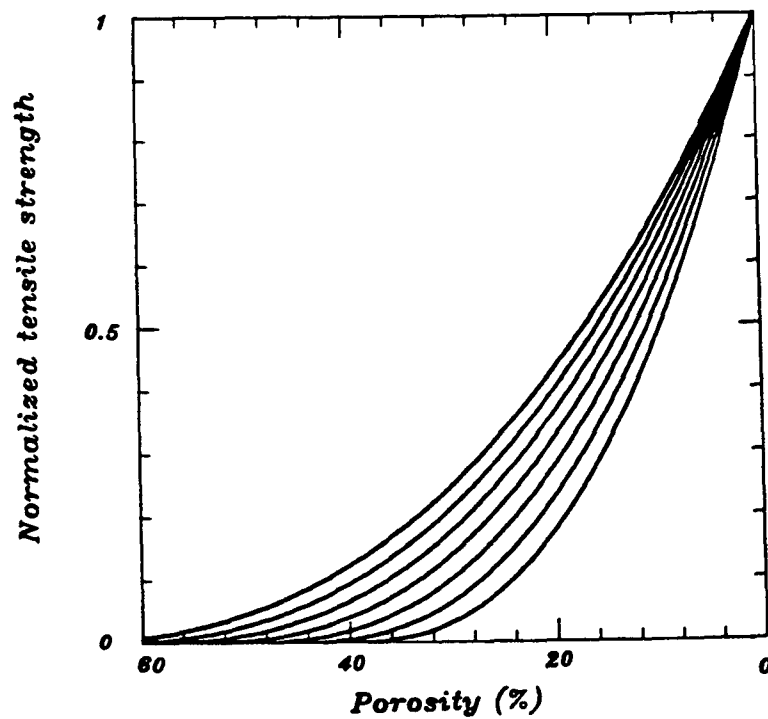
$$\sigma = \sigma_t (1 - c\phi_2^{2/3}) \quad (8.10)$$

as proposed by Eudier (1962) and Ishimaru et al. (1971), where the value of c , determined experimentally, is usually larger than 1.0. By using the concept of critical porosity, it is clear that $c > 1.0$ in criterion (8.10) implies the general existence of critical porosity in porous materials.

Fig.8.1(a) is a collection of experimental data of tensile strength versus porosity for sintered porous materials. The tensile strengths are normalized for different metals including aluminium, copper, copper-iron and copper-tin alloys, nickle, steel, and titanium. The estimated critical porosities range from 40% to 70%. By using the criterion in equation (8.8), the plot of normalized tensile strength (σ/σ_t) versus porosity ϕ_2 in Fig.8.1(b) provides better description of the experimental data in Fig.8.1(a).



(a)



(b)

Fig.8.1 (a) Experimental data of normalized tensile strength versus porosity for sintered porous materials (after Tharp, 1983), (b) Normalized tensile strength versus porosity predicted by critical concentration strength criterion in (8.8).

Kendall (1984) collected another set of tensile strength data for various porous materials including natural rocks and firebrick, alumina and zirconia, cement, and ice, as in Fig.8.2. The nonlinear decrease of tensile strength with porosity is remarkably similar for different porous materials and this fundamental feature is directly attributed to the stress concentration as reflected in the criterion (8.8).

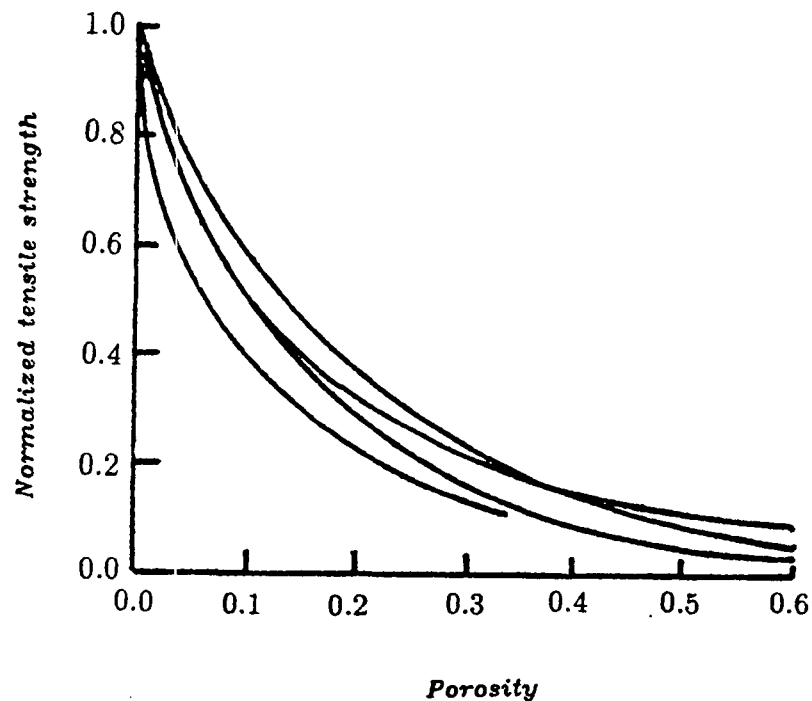


Fig.8.2 Normalized tensile strength versus porosity for various porous materials (after Kendall, 1984).

8.3.2 Compressive strength criterion

Let σ_c be the uniaxial compressive strength in a solid material without pores, the uniaxial compressive strength criterion of the porous material is

$$\sigma = \sigma_c \left(1 - \frac{\phi_2}{\phi_{cr}}\right)^D. \quad (8.11)$$

In the following we compare criterion (8.11) with the existing criteria and expe

imental data of uniaxial compressive strength of porous materials. Schiller (1958) proposed an empirical criterion for the uniaxial strength of porous solids,

$$\sigma = \sigma_c \left(1 - m \sqrt{\frac{\phi_2}{\phi_{cr}}}\right), \quad (8.12)$$

where m is a parameter depending on pore geometry. The stress concentration due to pore boundaries, compared with equation (8.11), is empirically included by a factor $(m/\sqrt{\frac{\phi_2}{\phi_{cr}}})$.

Rzhevsky and Novik (1971) reported another form of uniaxial compressive strength-porosity relation,

$$\sigma = \sigma_c (1 - \gamma \phi_2)^2, \quad (8.13)$$

where γ is a parameter determined experimentally. By comparing equation (8.11) and (8.13), we see that γ is related to the critical porosity by $\phi_{cr} = \frac{1}{\gamma}$, and that $D = 2$. The available experimental data of rock strengths show that the parameter γ for rocks may vary between 1.5 and 4 (Lama and Vutukuri, 1978), thus the critical porosity ϕ_{cr} ranges from 25% to 67%, consistent with the model results in chapter 3. Fig.8.3 shows the experimental data of compressive strength versus porosity for carbonates. Two curves predicted by (8.13) are drawn to be the upper and lower bounds of the data.

8.4 Shear Strength Criteria

Our approach to establish the shear strength criteria is to let the actual stress satisfy the Mohr condition originally proposed for the same material without pores. The basic requirement for such a strength criterion is that the predicted material strength should reduce to zero when the material porosity reaches the critical porosity.

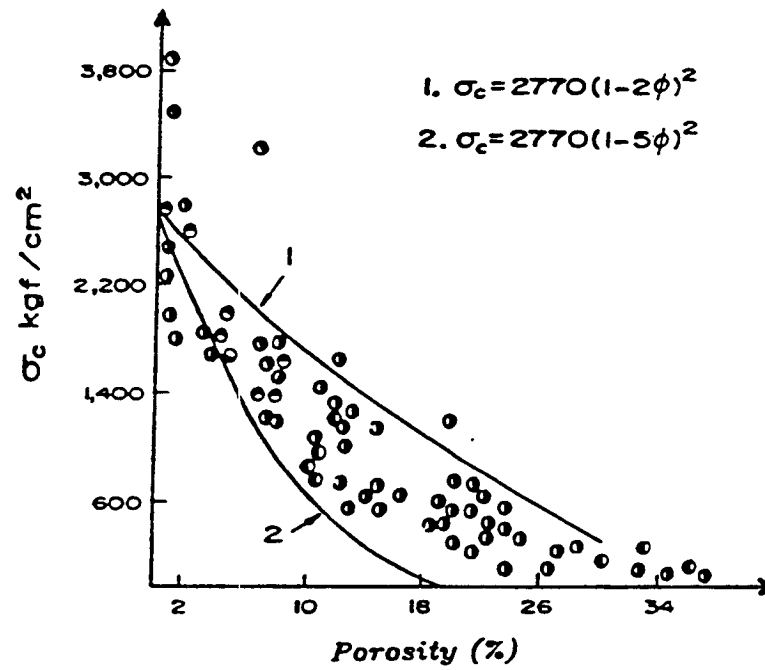


Fig.8.3 Experimental data of compressive strength versus porosity for carbonates, and bounding curves 1 and 2 predict 20% ~ 50% critical porosity (after Rzhevsky and Novik, 1971).

Assume that shear failure occurs on a given plane of a porous material when the actual stresses σ_a and τ_a on it satisfy a general relation

$$\tau_a = f(\sigma_a). \quad (8.14)$$

The linear and nonlinear forms of the function f are analyzed as follows.

8.4.1 Linear condition between τ_a and σ_a

Assume the actual stresses in the solid skeleton of a porous material satisfy the Coulomb condition, then

$$\tau_a = \tau_0 + \sigma_a \tan \varphi \quad (8.15)$$

where τ_0 and $\tan \varphi$ are the cohesive strength and coefficient of internal friction of the solid material itself. Substituting from equations (8.4) and (8.5) into (8.15) gives

$$\tau = \left(1 - \frac{\phi_2}{\phi_{cr}}\right)^D \tau_0 + \sigma \tan \varphi. \quad (8.16)$$

By comparing equation (8.16) with conventional Coulomb criterion, we notice that the first term on the right of (8.16) represents the effective cohesion of a porous material. This strength criterion predicts that shear strength increases linearly with the applied normal stress but decreases with the porosity. How much loading the porous material can bear depends on the porosity. When the porosity approaches the critical porosity, the porous material can bear little loading, and so the shear strength reduces to zero at the critical porosity.

8.4.2 Nonlinear condition between τ_a and σ_a

The above linear relationship between shear strength and normal stress may be just the first-order approximation to many rock experimental data (Paterson, 1978). For

solid materials, Murrell (1971) is credited for the popular forms of nonlinear strength criteria,

$$\tau^2 = c_0 + c_1\sigma, \quad (8.17)$$

$$\tau = c_0 + c_1\sigma^n, \quad (8.18)$$

where the constants c_0 , c_1 , and n are determined experimentally. Wang and Han (1977) used parabolic curves to fit the Mohr stress envelopes and obtained an explicit form of nonlinear strength criteria,

$$\tau^2 = \tau_0^2 + (\sigma_0 - 2\tau_0)\sigma, \quad (8.19)$$

where σ_0 is the uniaxial compressional strength of solid material. Comparing equations (8.17) with (8.19) yields $c_0 = \tau_0^2$ and $c_1 = (\sigma_0 - 2\tau_0)$.

In order to describe nonlinear relationships between shear strength, normal stress, and porosity of porous materials, we propose that the actual stresses satisfy the condition in the form of equation (8.19),

$$\tau_a^2 = \tau_0^2 + (\sigma_0 - 2\tau_0)\sigma_a. \quad (8.20)$$

Substituting from (8.4) and (8.5) into (8.20) yields

$$\tau^2 = \left(1 - \frac{\phi_2}{\phi_{cr}}\right)^{2D} \tau_0^2 + \left(1 - \frac{\phi_2}{\phi_{cr}}\right)^D (\sigma_0 - 2\tau_0)\sigma. \quad (8.21)$$

Fig.8.4 shows the strength experimental data of Nugget sandstones obtained by Logan (1987). The empirical equations in Fig.8.4(b) imply 25% ~ 45% critical porosity. Jizba (1991) recently conducted experiments to study the porosity effect on the

shear strengths of sandstones. The results indicate that the shear strength increases nonlinearly with the normal stress, but decreases almost linearly with porosity. Least-squares fits to these data indicate that the critical porosity is about 35% (Fig.8.5).

We apply equation (8.21) to explain the above dependence of shear strength on porosity and normal stress. In Jizba's experiments, the cohesive strength is very small, but the uniaxial compressive strength is quite large. For example, with 9% porosity in sandstone samples, the measured uniaxial compressive strength is in the order of 100 MPa. When $\phi_{cr} = 35\%$, $\tau_0 = 10\text{MPa}$, and $\sigma_0 = 420\text{MPa}$ are used in (8.21), the theoretical results are presented in Fig.8.6. Fig.8.6(a) indicates that the shear strength-normal stress relationship is nonlinear, similar to the feature in Fig.8.4(a). Fig.8.6(b) shows the relationship between shear strength and porosity, and the quasilinear feature is consistent with the data in Fig.8.4(b) and Fig.8.5.

8.5 Pore Pressure Effect on Strength

Above strength criteria are derived for dry porous materials. When these materials are saturated with fluid, the pore pressure effect on the strength can be understood and evaluated in terms of effective stress as analyzed in chapter 7.

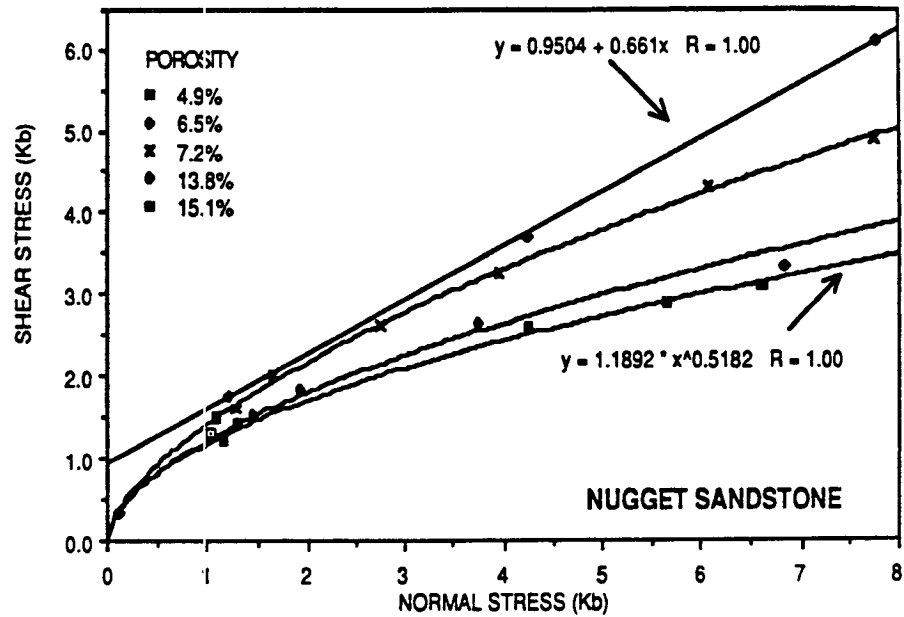
When an isotropic fluid-saturated porous material with pore fluid pressure P_p is considered, the effective stress on the potential failure plane $\bar{\sigma}$ is given by

$$\bar{\sigma} = \sigma - \frac{\phi_2}{\phi_{cr}} P_p. \quad (8.22)$$

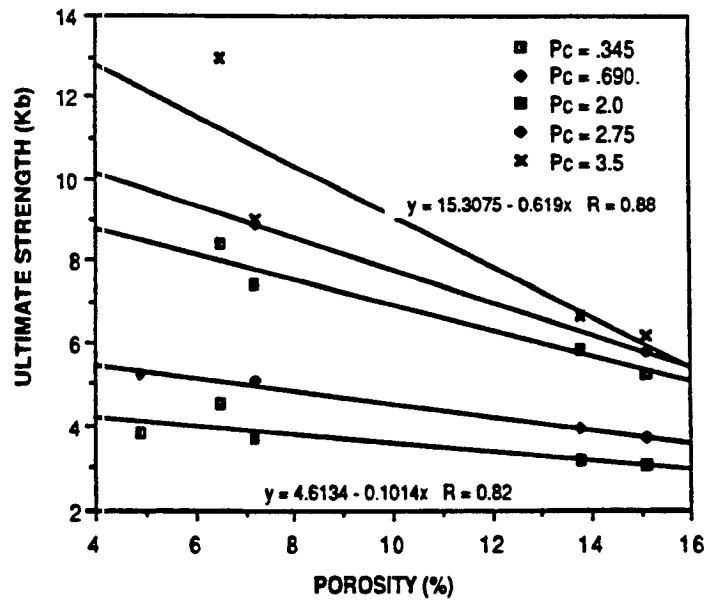
Then, corresponding to equation (8.16), the shear strength criterion for fluid-saturated porous materials is

$$\tau = \left(1 - \frac{\phi_2}{\phi_{cr}}\right)^D \tau_0 + \left(\sigma - \frac{\phi_2}{\phi_{cr}} P_p\right) \tan \varphi. \quad (8.23)$$

Similarly, another criterion, corresponding to equation (8.21), is



(a)



(b)

Fig.8.4 (a) Mohr diagram of Nugget sandstones. Data points are taken at failure of each experiment. Empirical equations for upper and lower curves are given. (b) Ultimate strength versus porosity for Nugget sandstones. Curves are for confining pressures indicated in kilobars. Empirical equations for the upper and lower curves are shown (after Logan, 1987).

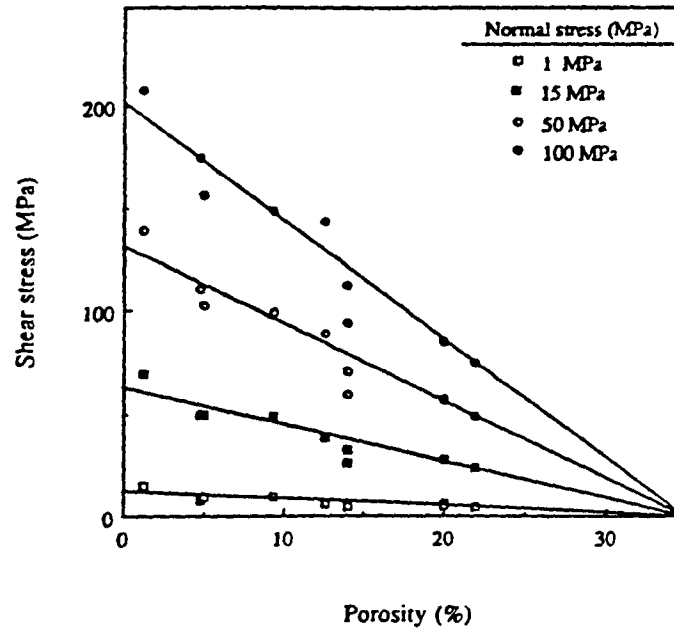


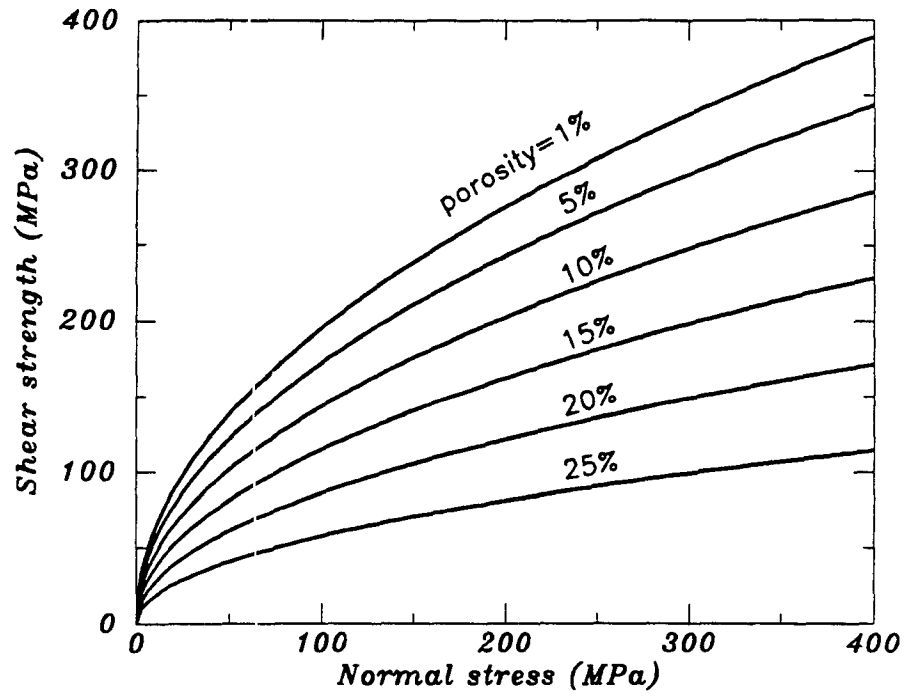
Fig.8.5 Experimental data of shear stress at failure versus porosity at different levels of normal stress for sandstones, and the least-squares fits indicate about 35% critical porosity (after Jizba, 1991).

$$\tau^2 = \left(1 - \frac{\phi_2}{\phi_{cr}}\right)^{2D} \tau_0^2 + \left(1 - \frac{\phi_2}{\phi_{cr}}\right)^D (\sigma_0 - 2\tau_0) \left(\sigma - \frac{\phi_2}{\phi_{cr}} P_p\right). \quad (8.24)$$

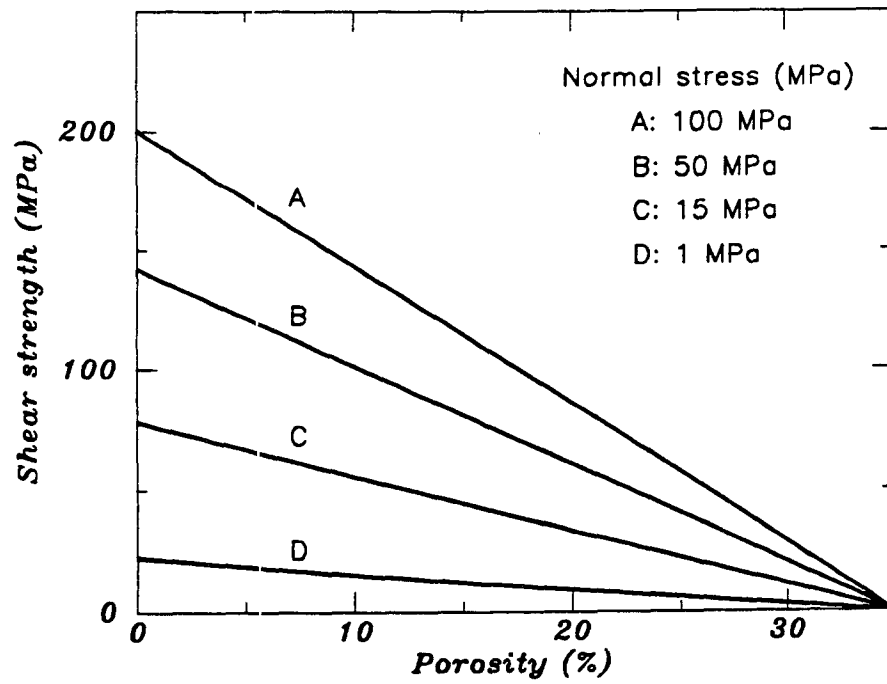
8.6 Transverse-isotropy Effect on Strength

Extensive surveys of strength criteria of anisotropic materials have been accomplished by Amadei (1983) and Rowlands (1985). For rock materials with strong dependence on hydrostatic pressure, however, the Coulomb criterion for isotropic materials is often modified and extended to anisotropic materials. Nova and Sacchi (1979) and Nova (1980) proposed tensorial forms of the Coulomb criterion for orthotropic and transversely-isotropic materials,

$$\tau_{mn} = c_{mn} + \xi_{mnr} \sigma_{rs}, \quad (8.25)$$



(a)



(b)

Fig.8.6 (a) Predicted nonlinear relationship between shear strength and normal stress from equation (8.19). (b) Predicted quasilinear shear strength-porosity relationship from equation (8.19).

where τ_{mn} and σ_{rs} are the shear and normal stresses on a potential failure plane; the cohesion c_{mm} varies as does the normal components of a second-rank tensor, and the quadruple tensor ξ_{mnr_s} can be physically linked to the internal friction of the material. For transversely-isotropic materials, equation (8.25) is involved with four strength parameters: the least cohesion c_t^s and the maximum cohesion $c_r^s \equiv \beta_c c_t^s$ ($\beta_c \geq 1$), the least friction coefficient ξ_t and the maximum friction coefficient $\xi_r \equiv \beta_\xi \xi_t$ ($\beta_\xi \geq 1$).

When this criterion is applied to the transversely-isotropic porous materials such as sedimentary rocks containing parallel weakness planes, as indicated by equation (8.16), only the cohesions c_t^s and c_r^s should be replaced by the effective cohesions c_t and c_r , respectively, where $c_t = (1 - \frac{\phi_2}{\phi_{cr}})^D c_t^s$, and $c_r = (1 - \frac{\phi_2}{\phi_{cr}})^D c_r^s$.

A failure plane is defined as the plane on which equation (8.25) is satisfied. Let ψ be the inclination of an incipient failure plane to the axis of least principal stress σ_3 , or the angle between the normal of that plane and the axis of maximum principal stress σ_1 . ψ can be therefore determined by comparing the shear stress due to external boundary loading and the shear strength resulted from equation (8.25). In the reference frame of Fig.8.7, equation (8.25) is expressed as

$$\begin{aligned} \frac{\sigma_1 - \sigma_3}{2} \sin 2\psi &= c_t [\beta_c \cos^2 (\psi + \theta) + \sin^2 (\psi + \theta)] + \\ &+ \xi_t [\beta_\xi \sigma_r \cos^2 (\psi + \theta) + \sigma_t \sin^2 (\psi + \theta) + \tau_{tr} \sin^2 (\psi + \theta)], \end{aligned} \quad (8.26)$$

where θ is the inclination of weakness plane to the axis of maximum principal stress σ_1 , and the stresses σ_r , σ_t , and τ_{tr} are the stresses on the planes normal to the principal axes of strength anisotropy,

$$\sigma_r = \sigma_1 \cos^2 \theta + \sigma_3 \sin^2 \theta, \quad (8.27)$$

$$\sigma_t = \sigma_1 \sin^2 \theta + \sigma_3 \cos^2 \theta, \quad (8.28)$$

$$\tau_{tr} = \frac{\sigma_1 - \sigma_3}{2} \sin 2\theta. \quad (8.29)$$

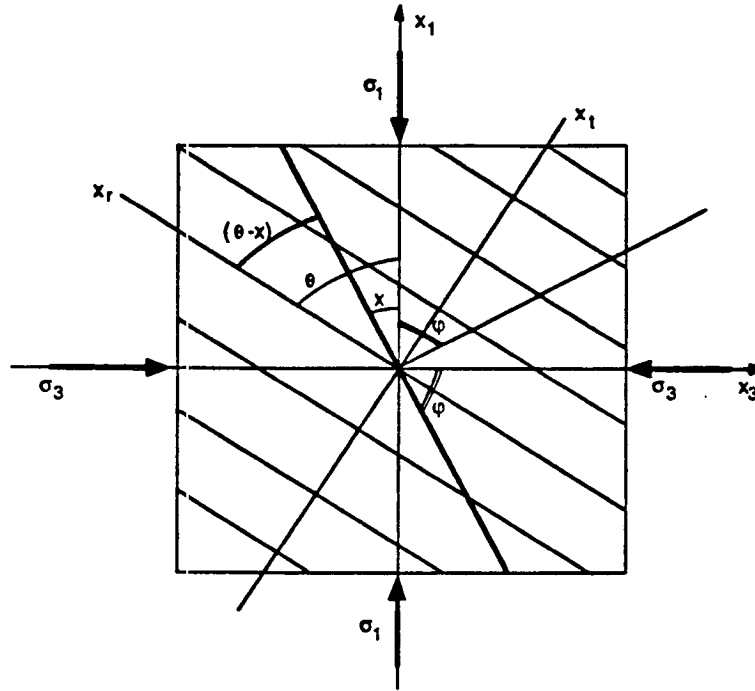


Fig.8.7 Reference frame of transversely-isotropic porous materials under boundary loading.

Given the principal stresses at failure σ_1 and σ_3 , and the inclination of the weakness plane θ , the only unknown in equation (8.26) is therefore the angle ψ . Equation (8.26) yields only one value of ψ for each angle θ ,

$$\tan \psi = \frac{\sigma_1 - \sigma_3 + [c_t(\beta_c - 1) + \xi_t(\beta_\xi \sigma_r - \sigma_t)] \sin 2\theta - 2\xi_t \tau_{tr} \cos 2\theta}{2[(\beta_c c_t + \beta_\xi \xi_t \sigma_r) \cos^2 \theta + (c_t + \xi_t \sigma_t) \sin^2 \theta - \xi_t \tau_{tr} \sin 2\theta]}. \quad (8.30)$$

Consequently, for transversely-isotropic porous rocks, there exists only one possible failure plane for each angle of weakness plane, and the inclination of the failure plane

depends on all four strength parameters, besides the stresses σ_1 and σ_3 and the angle θ . This theoretical result is completely different from the concept of **conjugate** failure planes of isotropic materials.

8.7 Application to Tectonic Block Rotations

8.7.1 Existing block rotation model

Based on accumulating paleomagnetic, structural, and seismic evidence, the concepts and models of tectonic block rotations have developed as an attractive approach to crustal deformation in regions with distributed faulting. The kinematic model originally proposed by Freund (1970, 1974) indicates that, due to the geometrical constraints at the boundaries of tectonic domains, faults and the rigid blocks bounded by them will slip and rotate away from the direction of maximum compressive principal stress. Nur et al. (1986, 1989) applied the Coulomb criterion with variable cohesions for existing fracture sliding and intact rock failure to Freund's model, and found that new fault sets should be required to accommodate block rotations greater than 45° , as depicted in Fig.8.8

The mechanism of an initial set of shear fractures in intact rocks, as indicated in Fig.8.8(a), can be well understood from the failure and fracture theories of isotropic materials. The mechanical process of a new set of shear fractures in the faulted rocks, as shown in Fig.8.8(b), involves the failure and faulting in anisotropic materials, but is only qualitatively explained in Nur's block rotation model as the same occurrence as the initial set of fractures. This section is intended to rationalize Nur's block rotation model by analyzing the failure and faulting in transversely-isotropic rocks.

8.7.2 Relationship between failure and weakness planes

After a set of parallel or subparallel fractures occur in an intact, isotropic rock mass, the rock mass is no longer isotropic. In order to study the occurrence of sequential

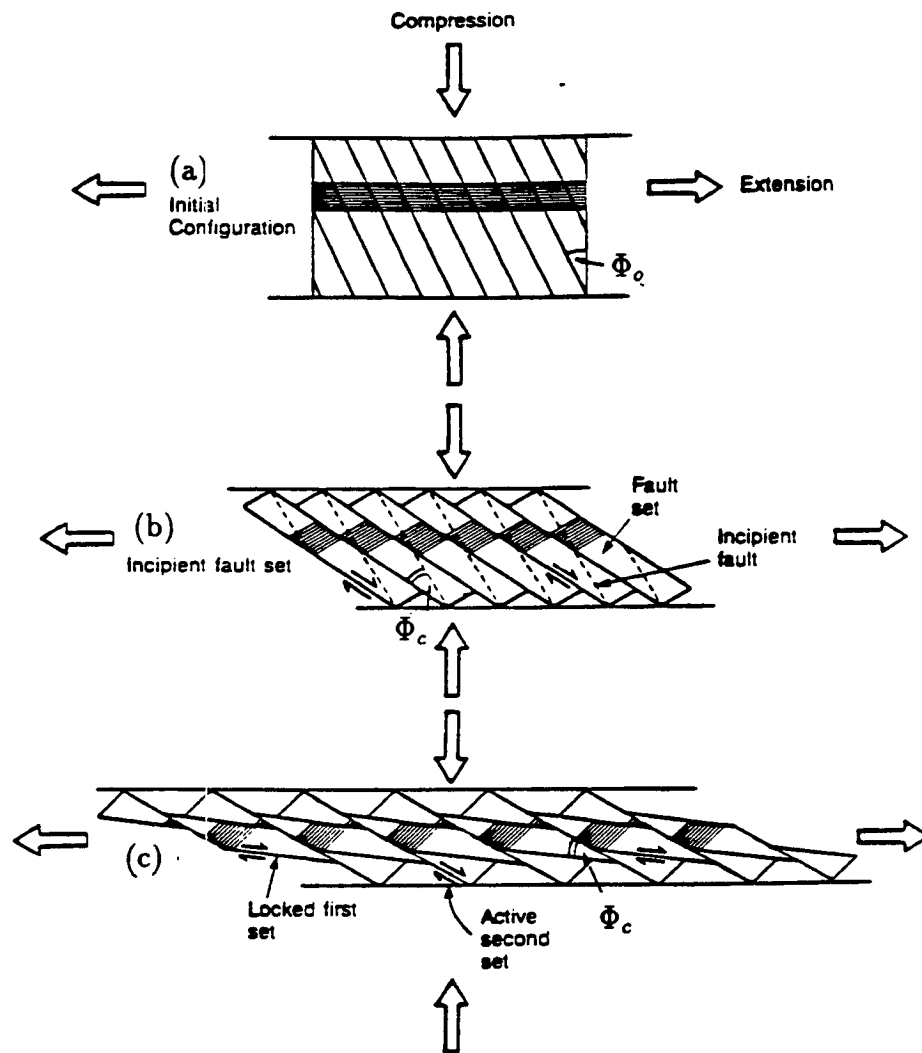


Fig.8.8 Tectonic block rotation of sequential fault sets (after Nur et al., 1989)

(a) Initial configuration of the first set of fractures occurred in intact rocks, and the angle Φ_o is the inclination of fracture plane to the axis of maximum principal stress.

(b) Configuration of rotation of the first set and inception of the second set, and the angle Φ_c is the critical angle between sequential sets.

(c) Configuration after rotation of the second set, with the locked first set.

fractures, the rock mass as in Fig.8.8(a) can be reasonably taken as a macroscopically-continuous and transversely-isotropic porous material, and such anisotropy is structurally-anisotropic, since each fracture in the rock mass in fact represents a deformation zone or a bunch of subparallel weakness planes.

Our main interest is to identify the occurrence of failure plane in transversely-isotropic porous rocks with respect to the initial weakness plane. Fig.8.9 compares above failure analysis with Penrhyn slate data obtained by Attewell and Sandford (1974), and the strength parameters used in this case are:

$$c_t = 22.2 \text{ MPa}; \quad \xi_t = 0.503; \quad \beta_c = 3.3; \quad \beta_\xi = 2.7.$$

Fig.8.9(a) compares theoretical and experimental deviatoric stress at failure ($\sigma_1 - \sigma_3$) versus the inclination of weakness plane θ . Both theory and experiment show that the least strength plane is the plane with $\theta \sim 30^\circ$, which is consistent with many other experimental observations (McLamore and Gary, 1967). Fig.8.9(b) compares the inclination of failure plane χ ($\chi = 90^\circ - \psi$) with the inclination of weakness plane θ . Several useful conclusions can be drawn from Fig.8.9(b):

1. The theoretical results are in good agreement with the experimental data, especially at higher pressure. Since both theoretical and experimental results generally depart from the line $\chi = \theta$, the failure plane does not occur, in general, along the weakness plane.

2. When $\theta \sim 30^\circ$, the failure plane occurs along the weakness plane, now the least strength plane in the sense of deviatoric stress ($\sigma_1 - \sigma_3$).

3. With θ much greater than 30° , the failure plane occurs at $35^\circ \sim 40^\circ$ of angle χ . On these failure planes, the overall strengths in the sense of ($\sigma_1 - \sigma_3$) in Fig.8.9(a) are much less than those one would expect from an isotropic rock with strengths equal to $\beta_c c_t$ and $\beta_\xi \xi_t$.

4. With the increase of angle θ to $65^\circ \sim 75^\circ$, the angle χ will reach its maximum

value ($\sim 40^\circ$). When post-failure behaviors of such incipient failure planes are considered, the probable slip along the failure plane, or the faulting of rocks will occur along the failure plane whose χ approaches its maximum value. Consequently, the angle difference ($\theta - \chi$) will be $25^\circ \sim 40^\circ$.

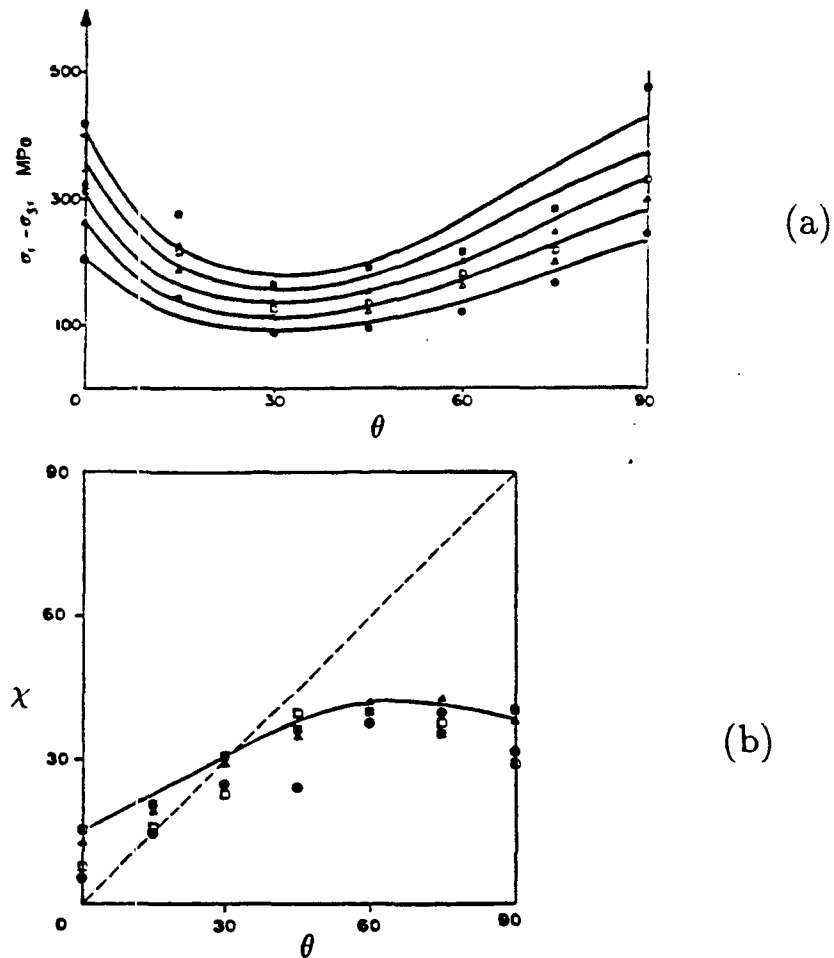


Fig.8.9 (a) Comparison of theoretical and experimental deviatoric stress vs the inclination of weakness plane; (b) Comparison of inclinations of failure plane and weakness plane (after Nova, 1980)

8.7.3 Faulting and rotation of tectonic blocks

When applied to tectonic block rotations, the above failure analysis of transversely-isotropic porous rocks renders a rigorous mechanism to the faulting and rotation of tectonic blocks as in Fig.8.7.

The Coulomb criterion for isotropic rocks predicts conjugate failure planes in intact rocks. Due to the boundary constraint, only one set of fractures prevail in intact rocks. Since the internal friction coefficient of most rocks is about 0.6, the inclination of fracture plane Φ_o is about 30° , as in Fig.8.7(a).

With the axes of regional principal stresses unchanged, faulting will occur in the fractured rocks and the slipping will begin along the initial fracture planes since they are the least-strength weakness planes ($\theta \sim 30^\circ$) according to above failure analysis. Simultaneously the rotation of faulted blocks occurs in accordance with the rule of Freund's model, that is, blocks rotate counterclockwise (CCW) when slip is right handed and clockwise (CW) when slip is left handed. For a moderately increase of θ from its initial value of 30° resulted from the block rotation, the strength of the rocks is like that of an isotropic material characterized by the strength parameters c_t and ξ_t , as shown in Fig.8.9(a). Consequently, the large shear stress components on these weakness planes with $\theta \sim 45^\circ$ keep the slipping or faulting along these planes. With further rotation of faulted blocks, the increase of angle θ approaches $65^\circ \sim 75^\circ$, and the inclination of failure plane will reach its maximum value ($\sim 40^\circ$). These failure planes are just the incipient fault set as in Fig.8.7(b). Once faulting along these planes begins, more block rotations are accumulating, and the initial set of fracture planes, being simply the weakness planes in the rock mass, no longer activate, as indicated in Fig.8.7(c). Consequently, the angle between the weakness plane and currently-active faulting plane ($\theta - \chi$), ranging $25^\circ \sim 40^\circ$, is in fact equivalent to the critical angle Φ_c defined in Nur's block rotation model.

CRITICAL ANGLE OF BLOCK ROTATION

By using constant friction coefficient ξ and variable cohesions c_t and c_i for preexisting fracture plane and intact rock failure, respectively, Nur et al. (1986) determined the critical angle Φ_c as

$$\begin{aligned}
\Phi_c &= \frac{1}{2} \cos^{-1} \left[1 - \frac{2(c_i - c_t) \cos(\tan^{-1} \xi)}{\sigma_1 - \sigma_3} \right] \\
&= \frac{1}{2} \cos^{-1} \left[1 - \frac{(1 - c_t/c_i)}{1 + (\xi \sigma_0/c_i)} \right], \tag{8.31}
\end{aligned}$$

where σ_0 is effective overburden pressure. For general rock properties and crustal stress levels, Φ_c ranges $25^\circ \sim 40^\circ$. Only for the extreme cases $c_t = 0$ and $\xi = 0$ (or $\sigma_0 = 0$), can the upper limit of Φ_c reach 45° .

From the failure analysis of transversely-isotropic rocks in the above, we know that the strengths on the new set of fracture planes are rather lower than those characteristic of $\beta_c c_t$ and $\beta_\xi \xi_t$. Thus, when the angle $(\theta - \chi)$ is taken as equivalent to the critical angle Φ_c as defined above, the parameter β_ξ should be equal to 1 to meet the condition of constant friction coefficient, and the cohesion c_i is not equivalent to αc_t but a value moderately smaller than $\beta_c c_t$ and larger than c_t .

The angle $(\theta - \chi)$ is therefore a generalized definition of the critical angle Φ_c , and from equations (8.26) to (8.30) we can find

$$(\theta - \chi) = \tan^{-1} \left(\frac{\tan \psi - \cot \theta}{1 + \cot \theta \tan \psi} \right). \tag{8.32}$$

Many experimental data indicate that the cohesive strengths of various intact rocks vary from tens of *MPa* to hundreds of *MPa* (Jaeger and Cook, 1976; Paterson, 1978). The cohesive strengths on preexisting fracture planes, however, are much smaller, even approach zero (Byerlee, 1978). The cohesive strength ratio β_c of transversely-isotropic rocks as defined in the above, is therefore in a wide range. On the other hand, the friction coefficients on the preexisting fracture planes, in general, are smaller than but in the same order as those of intact rocks, thus the friction coefficient ratio β_ξ is rather low. In order to see clearly how the transverse isotropy and crustal stress level affect the angle $(\theta - \chi)$, we use rock properties and crustal

stress conditions similar to those in Nur et al. (1986) to visualize equation (8.32) in Fig.8.10 and Fig.8.11.

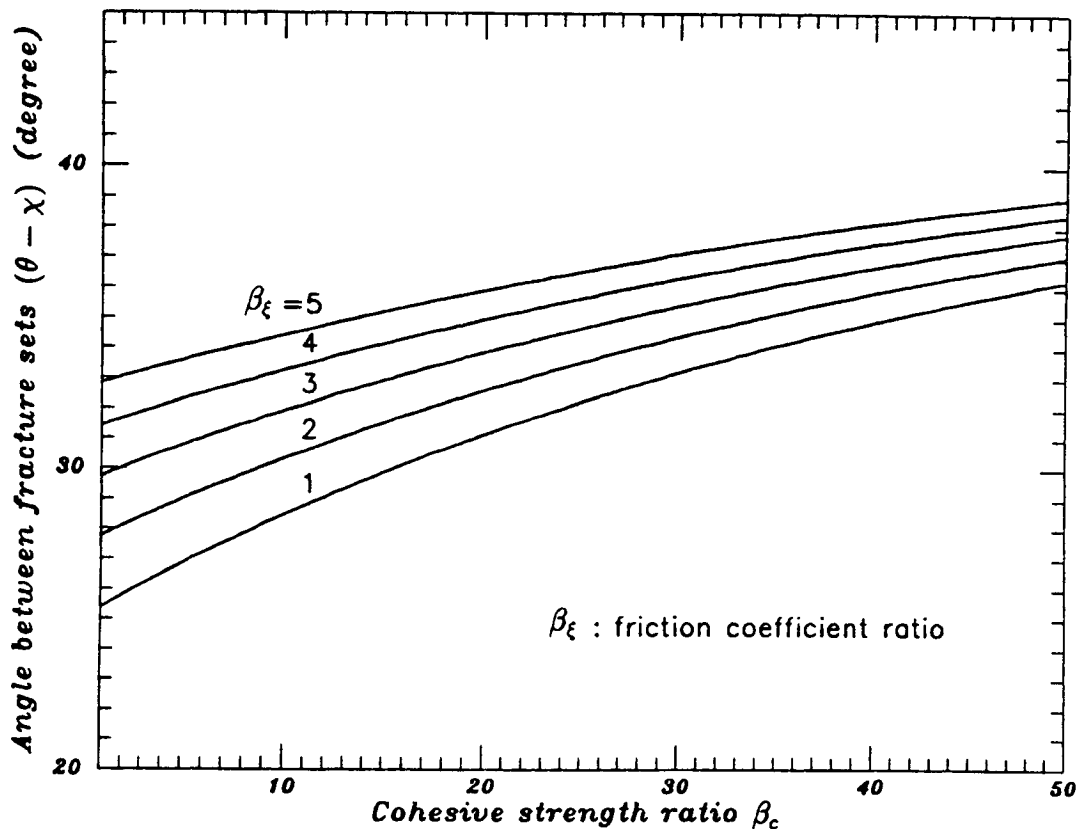


Fig.8.10 Generalized critical angle $(\theta - \chi)$ versus anisotropic strength ratios β_c and β_ξ , with $\sigma_1 = 400MPa$, $\sigma_3 = 100MPa$, and $\theta = 70^\circ$

Given stresses at failure $\sigma_1 = 400MPa$ and $\sigma_3 = 100MPa$, and a large inclination of weakness plane $\theta = 70^\circ$, the critical angle $(\theta - \chi)$ versus β_c and β_ξ is shown in Fig.8.10 With β_c ranging $1 \sim 50$ and β_ξ ranging $1 \sim 5$, the angle between fracture sets $(\theta - \chi)$ ranges $25^\circ \sim 40^\circ$. Recent studies by Ron et al. (1986, 1990) show that in-situ measurements of the angle between fracture sets are indeed $25^\circ \sim 40^\circ$.

The block rotation model proposed by Nur et al. (1986), as well as present study, can be applicable to both strike-slip and dip-slip multiple sets. Of course, the crustal

stress conditions for them may be quite different. Fig.8.11 shows how the angle $(\theta - \chi)$ depends on the stresses: σ_1 and σ_3 . When $\beta_c = 5$, $\beta_\xi = 2$, and $\theta = 70^\circ$ are used, we see that the angle $(\theta - \chi)$ ranges $10^\circ \sim 40^\circ$, and that $(\theta - \chi)$ increases with the deviatoric stress at failure $(\sigma_1 - \sigma_3)$.

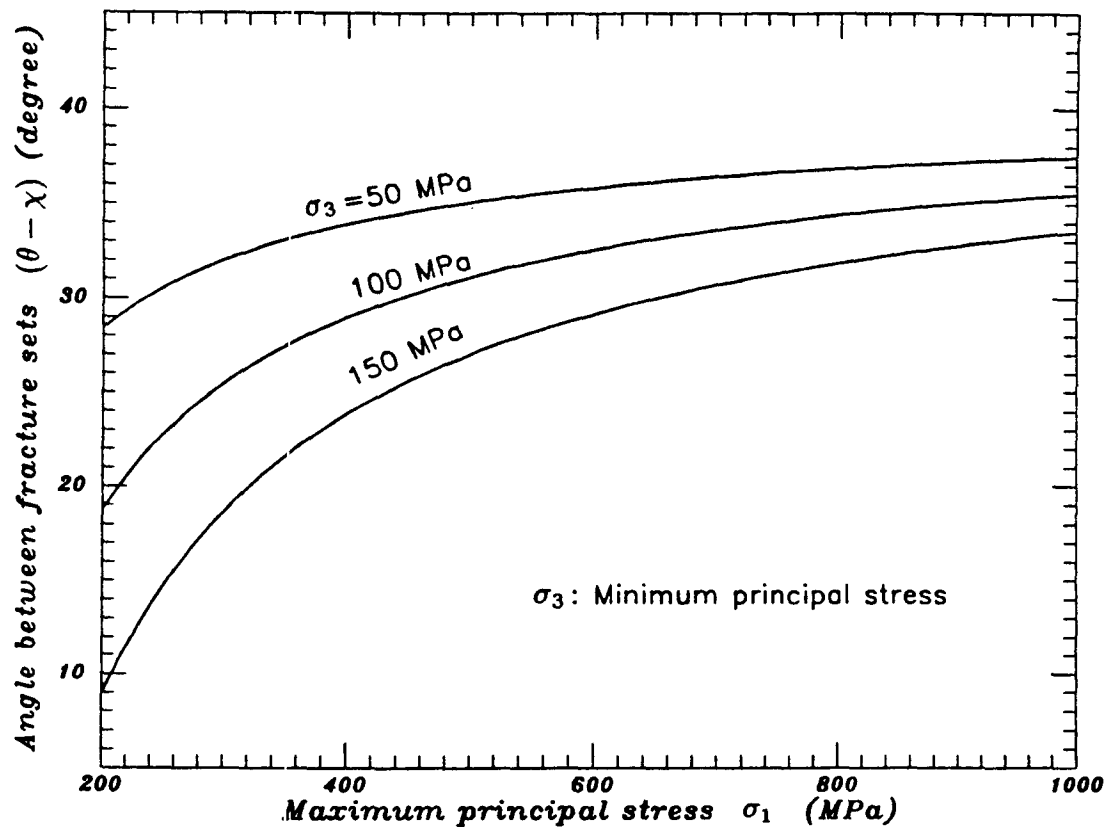


Fig.8.11 Generalized critical angle $(\theta - \chi)$ versus principal stresses at failure σ_1 and σ_3 , with $\beta_c = 5$, $\beta_\xi = 2$, and $\theta = 70^\circ$

8.8 Conclusions

Pores and cracks of porous materials reduce the load-bearing area, induce the stress concentration, and lead to the critical porosity, which are all taken into account by re-defining the actual stress from the nominal stress, average stress, to local stress. The

uniaxial tensile and compressive strength criteria, and linear and nonlinear shear strength criteria in terms of such actual stress are proposed and compared with available experimental data. The effects of pore pressure and transverse isotropy on porous material strengths are explored. Finally, the failure mechanism in transversely-isotropic porous materials is applied to the rationalization of existing block rotation models.

References

- Amadei, B., 1983, Rock anisotropy and the theory of stress measurements, Lecture Notes in Engineering, edited by Brebbia, C.A. and S. A. Orszag, Springer-Verlag, New York, pp.478.
- Atkinson, B. K. and P. G. Meredith, 1989, The theory of subcritical crack growth with applications to minerals and rocks, in *Fracture Mechanics of Rock*, edited by B. K. Atkinson, Academic Press, London, 111-166.
- Attewell, P. B. and M. R. Sandford, 1974, Intrinsic shear strength of a brittle, anisotropic rock, I – experimental and mechanical interpretation, *Int. J. Rock Min. Sci. & Geomech. Abstr.*, **11**, 423-430.
- Bert, C. W., 1985, Prediction of elastic moduli of solids with oriented porosity, *J. Mat. Sci.*, **20**, 2220-2224.
- Bertolotti, R. L. and R. M. Fulrath, 1967, Effect of micromechanical stress concentrations on strength of porous glass, *J. Amer. Ceram. Soc.*, **50**, 558-562.
- Byerlee, J., 1978, Friction of rocks, *Pure and Applied Geophysics*, **116**, 615-626.
- Dunn, D. E., La Fountain, L. J., and R. E. Jackson, 1973, Porosity dependence and mechanism of brittle fracture in sandstones, *J. Geophys. Res.*, **78**, 2403-2417.
- Freund, R., 1970, Rotation of strike-slip faults in Sistan, southeastern Iran, *J. Geology*, **78**, 188-200.
- Freund, R., 1974, Kinematics of transform and transcurrent fault, *Tectonophysics*, **21**, 93-134.
- Goodier, J. N., 1933, Concentration of stress around spherical and cylindrical inclusions and flaws, *J. Appl. Mech.*, **1**, 39-44.
- Griffith, A. A., 1920, The phenomena of rupture and flow in solids, *Phil. Trans. R. Soc., Ser. A* **221**, 163-198.
- Hegemier, G. A. and H. E. Read, 1985, On deformation and failure of brittle solids: some outstanding issues, *Mach. Mater.*, **4**, 215-259.
- Hoshino, K., 1974, Effect of porosity on the strength of the clastic sedimentary rocks, in *Advances in Rock Mechanics, Proc. 3rd Congr. Int. Soc. Rock Mech.*, Denver, Nat. Acad. Sci., Vol. II, Part A, 511-516.
- Ingraffea, A. R., 1989, Theory of crack initiation and propagation in rock, in *Fracture*

- Mechanics of Rock, edited by B. K. Atkinson, Academic Press, London, 71-110.
- Irwin, G. R., 1958, Fracture, in *Handbuch der Physik*, Vol. VI, *Elastizität und Plastizität*, Flügge, S. (ed.), Berlin-Heidelberg-New York, Springer, 551-590.
- Jaeger, J. C. and N. G. W. Cook, 1976, *Fundamentals of Rock Mechanics*, 2nd ed., London, Chapman and Hall, pp.585.
- Jizba, D., 1991, *Mechanical and acoustical properties of sandstones and shales*, PhD dissertation, Stanford University, California.
- Kachanov, L. M., 1986, *Introduction to continuum damage mechanics*, Martinus Nijhoff Publishers, Dordrecht, Boston, and Lancaster, pp.135.
- Kendall, K., 1984, Connection between structure and strength of porous solids, in Johnson, D. L. and P. N. Sen (ed.), *Physics and Chemistry of Porous Media*, AIP Conf. Proc. 107, Amer. Inst. Physics, 78-88.
- Krstic, V. D., 1988, Porosity dependence of strength in brittle solids, *Theoret. Appl. Fracture Mech.*, **10**, 241-247.
- Lajtai, E. Z., Carter, B. J., and M. L. Ayari, 1990, Criteria for brittle fracture in compression, *Engng. Fract. Mech.*, **37**, 59-74.
- Lama, R. D. and V. S. Vutukuri, 1978, *Handbook on Mechanical Properties of Rocks*, **3**, Trans. Tech. Publications, pp.406.
- Lawn, B. R. and T. R. Wilshaw, 1975, *Fracture of Brittle Solids*, Cambridge, Univ. press, pp.240.
- Lemaitre, J., 1985, A continuous damage mechanics model for ductile fracture, *J. Engng. Mat. Tech.*, **107**, 83-89.
- Logan, J. M., 1987, Porosity and the brittle-ductile transition in sedimentary rocks, in Banavar, J. R., Koplik, J., and K. W. Winkler (ed.), *Physics and Chemistry of Porous Media II*, AIP Conf. Proc. 154, Amer. Inst. Phys., 229-242.
- McClintock, F. A. and J. Walsh, 1962, Friction on Griffith cracks under pressure, *Proc. 4th National Congr. Appl. Mech.*, **2**, 1015-1021.
- McLamore, R. and K. E. Gary, 1967, The mechanical behaviour of anisotropic sedimentary rocks, *J. Engng. Ind.*, **89**, 62-76.
- Murrell, S. A. F., 1963, A criterion for brittle fracture of rocks and concrete under triaxial stress, and the effect of pore pressure on the criterion, in *Rock Mechanics*,

- Fairhurst, C. (ed.), Proc. 5th Symp. Rock Mech., New York, Pergamon Press, 563-577.
- Nova, R. and G. Sacchi, 1979, A generalized failure condition for orthotropic solids, *EUROMECH 115-Mechanical Behaviour of Anisotropic Solids*, Villard de Lans, 623-641.
- Nova, R., 1980, The failure of transversely-isotropic rocks in triaxial compression, *Int. J. Rock Min. Sci. & Geomech. Abstr.*, **17**, 325-332.
- Nur, A., H. Ron, and O. Scotti, 1986, Fault mechanics and the kinematics of block rotation, *Geology*, **14**, 746-749.
- Nur, A., H. Ron, and O. Scotti, 1989, Kinematics and mechanics of tectonic block rotations, *Stanford Rock & Borehole Project*, **37**, Paper K.
- Paterson, M. S., 1978, *Experimental rock deformation in the brittle field*, Springer-Verlag, Berlin, Heidelberg, New York, pp.254.
- Paris, P. C. and G. C. Sih, 1965, Stress analysis of cracks, in *Fracture Toughness Testing and its Applications*, Spec. Tech. Publ., **381**, Am. Soc. Test. Mater., Philadelphia, 30-81.
- Price, N. J., 1960, The compressive strength of coal measure rocks, *Coll. Eng.*, **37**, 283-292.
- Rice, R. W., 1984, Pores as fracture origins in ceramics, *J. Mat. Sci.*, **19**, 895-914.
- Ron, H., A. Aydin, and A. Nur, 1986, Strike slip faulting and block rotation in the Lake Fault system, *Geology*, **14**, 1020-1023.
- Ron, H., A. Nur, and Y. Eyal, 1990, Multiple strike-slip fault sets: a case study from the Dead Sea Transform, **9**, 1421-1431.
- Rowlands, R. E., 1985, Strength (failure) theories and their experimental correlation, in: G. C. Sih and A. M. Skudra. eds., *Failure Mechanics of Composite*, Handbook of Composites, III, Ch.2.
- Rzhevsky, V. and G. Novik, 1971, *The Physics of Rocks*, Moscow, MIR Publishers, pp.320.
- Schiller, K. K., 1958, Porosity and strength of brittle solids (with particular reference to gypsum), *Proc. Conf. Mech. Prop. Non-metallic Brittle Materials*, London, 35-45.

Smorodinov, M. I., E. A. Motovilov, and V. A. Volkov, 1970, Determinations of correlation relationships between strength and some physical characteristics of rocks, Proc. 2nd Cong. Int. Soc. Rock Mech., Belgrade, **2**, 35-37.

Wang, W. and Y. Han, 1977, Mechanical analysis of conjugate fracture structure, in Collected Papers and Notes on Geomechanics, **4**, 64-75, Science Press, Beijing, China.

Chapter 9

Discussions and Conclusions

9.1 Main Contributions

The main contributions of this dissertation are summarized as follows.

1. Critical porosity and concentration are recognized as the general features of porous materials, and they are of first-order effects on the mechanical and acoustic properties of porous materials.

2. New theoretical models of porous materials are developed by incorporating the concept of critical porosity and critical concentration phase into the description of porous material microstructures.

3. New theoretical solutions are proposed to relate wave velocities or effective elastic moduli to pore structure parameters. These solutions

- are extensions of nondilute solutions;
- are in good agreement with most experimental data;
- and provide physical interpretations to empirical relations.

4. The new models and solutions are widely applied to other aspects of Rock

Physics:

- Strength criteria;
- Effective stress laws;
- Clay effects;
- Permeability;
- and Anisotropy.

9.2 Discussions

1. Effective elastic moduli

For dry and fluid-saturated porous materials, clay-free and clay-bearing porous materials, and consolidated rocks and unconsolidated sediments, we have developed a series of material models to describe their microstructural variations, to establish relationships between effective elastic moduli, porosity, critical porosity, clay content and location, and fluid property. The developments from dilute to nondilute concentration models and solutions, and from nondilute to critical concentration models and solutions, are significant in both theory and practice.

2. Porous material strengths

Porous material strengths strongly depend on pore structure features such as pore volume fraction, pore geometry, pore connectivity, and pore surface roughness. The concept of critical concentration in porous materials leads us to propose the critical concentration strength theory. It is neither the nominal stress nor the average stress, but the local stress on the load-bearing materials skeleton that governs the strength feature. The uniaxial tensile and compressive, and shear strength criteria based on such actual stresses are able to describe accurately most existing strength data of various porous materials.

3. Effective stress laws

The critical concentration model of fluid-saturated porous materials provides a new explanation of pore pressure effect. It is the critical concentration phase that loads the pore pressure on the material skeleton, thus its volume fraction is the general expression of effective stress coefficient. In contrast with the conventional concept of pore pressure in isotropic porous materials, pore pressure in anisotropic porous materials affect both the normal and shear stress components, leading to the possible variations of effective stress directions and magnitude sequences. The direct application of such anisotropic pore pressure effects is useful in explaining the faulting

and earthquake instabilities induced by subsurface fluid extraction.

4. Porosity and permeability in sediments

Clay content, clay location, and clay cementation state in sediments are of considerable effects on effective properties especially porosity and permeability. The application of the concept of critical concentration makes it possible to quantitatively describe relationships between effective properties and clay-bearing microstructures, which are very useful in reservoir exploration and production.

5. Wave velocities

There are more than a dozen of factors affect the wave velocities in porous materials. Critical porosity, closely related to pore geometry and connectivity, is identified as a basic parameter whose effect on P and S wave velocities may be an order higher than other factors. The proposed models and solutions allow us to fully consider the clay effect and provide physical interpretations to several empirical relations between velocity, porosity, and clay content.

9.3 Further Studies

This dissertation presents only some preliminary applications of the proposed material models and solutions. Some further applications include

- A. Acoustic well logging interpretation**
- B. Seismic tomography modeling and interpretation**
- C. Reservoir property evaluation**
- D. Near wellbore damage analysis**
- E. Hydraulic fracturing design**
- F. Induced faulting and seismicity**

While I finish the thesis writing, I realize that there are more related problems emerging from current study than I faced years ago. Maybe that is why Stanford Rock Physics Project can run year after year. An obvious problem is the Frequency

and Confining Pressure Effects.

The wave velocities in fluid-saturated geomaterials studied in this paper are calculated from the effective elastic moduli in static state, and so they are appropriate at low frequency domains. When the frequency and confining pressure effects on wave velocities are concerned, Biot theory of wave propagation has been verified as the fundamental one applicable to a wide range of porous materials (Biot, 1956a, b, 1962; Plona, 1980; Schmitt, 1986; Charles et al., 1988; Winkler, 1989). According to Biot theory, sound wave velocity and attenuation depend on frequency, elastic properties of matrix grain and pore fluid, porosity, grain size and pore geometry, permeability, and effective stress. Thus 13 parameters are required as model inputs. Among others, the effective bulk and shear moduli of dry porous materials have been the subject of many studies (Berryman, 1980a, b; Ogushwitz, 1985). The critical concentration model and its formulation in this study render several solutions to the effective elastic moduli which are important inputs for Biot theory. One of our further studies is to incorporate the critical concentration model and solution into Biot theory to investigate the acoustic, transport, and microstructural properties of poroelastic geomaterials.

REFERENCES

- Berryman J. G., 1980a, Long-wavelength propagation in composite elastic media I. spherical inclusions, *J. Acoust. Soc. Am.*, **68**, 1809-1819.
- Berryman J. G., 1980b, Long-wavelength propagation in composite elastic media II. ellipsoidal inclusions, *J. Acoust. Soc. Am.*, **68**, 1820-1831.
- Biot, M. A., 1956a, Theory of propagation of elastic waves in a fluid-saturated porous solid, I. Low frequency range, *J. Acoust. Soc. Am.*, **28**, 168-178.
- Biot, M. A., 1956b, Theory of propagation of elastic waves in a fluid-saturated porous solid, II. Higher frequency range, *J. Acoust. Soc. Am.*, **28**, 179-191.
- Biot, M. A., 1962, Generalized theory of acoustic propagation in porous dissipative media, *J. Acoust. Soc. Am.*, **34**, 1254-1264.
- Charles, W. H. et al., 1983, The Biot-Stoll sediment model: an experimental assessment, *J. Acoust. Soc. Am.*, **84**, 1437-1443.
- Plona, T. J., 1980, Observation of a second bulk compressional wave in a porous medium at ultrasonic frequencies, *Appl. Phys. Lett.*, **36**, 259-261.
- Schmitt, D. P., 1986, Full-waveform synthetic acoustic logs in saturated porous media, Annual Report, MIT, Full waveform acoustic logging consortium, 105-330.
- Watt, J. P., G. F. Davies, and R. J. O'Connell, 1976, The elastic properties of composite materials, *Review of Geophysics and Space Physics*, **14**, 541-563.
- Zimmerman, R. W., W. H. Somerton, and M. S. King, 1986, Compressibility of porous rocks, *J. Geophys. Res.*, **91**, B12, 12,765-12,777.